UNIVERSITY OF
BIRMINGHAM

CLAY DERIVED MATERIALS FOR ENVIRONMENTAL MANAGEMENT

By

SELINA ILUNAKAN OMONMHENLE

Supervisor: Dr Ian J. Shannon

A Thesis submitted to The University of Birmingham for
The degree of Doctor of Philosophy

The School of Chemistry
College of Engineering and
Physical Sciences
The University of Birmingham
July 2014

ABSTRACT

Hydrotalcite-like compounds with Mg^{2+}/Al^{3+} and Zn^{2+}/Al^{3+} cations in the layer at different mole ratios with different anions in the galleries were synthesised in this study. The materials have been characterised by a range of techniques. The influence of layer cations, and interlayer anions, which in turn influences the crystallinity, can affect the properties of the hydrotalcites.

Dodecylsulfate (DS) and dodecylbenzenesulfonate (DBS) anions were intercalated successfully into the galleries and characterisation studies by the same technique that were used for the parent hydrotalcites show that the hydrotalcites structure was maintained and the interlayer space expanded, suggesting that intercalation of other organic compounds or other surfactants may be possible. The intercalated dodecylsulfate and dodecylbenzenesulfonate anions arranged themselves in monolayer and bilayer configuration in the interlayer. These modified hydrotalcites have well-ordered layered structures, divalent/trivalent mole ratios that are close to those of the host precursors, and hydrophobic properties. SEM images show that the modification with DS and DBS led to many of the particles being broken down into smaller pieces due to thermal pre-treatment and regeneration with organic anions, but overall morphology was maintained as the host. They show thermal transitions that are comparable to the host, exhibiting three decomposition steps but with increase in the temperature at which weight losses are completed. They show capacity to uptake phenol and 2-chlorophenol (2-CP) from aqueous solution with the compounds containing DBS anions showing higher sorption capacities for 2-CP than the corresponding DS-

containing compounds. A pseudo second order reaction best described the sorption process.

ACKNOWLEDGEMENT

My unfathomable thanks go to God Almighty, the benefactor of life and source of all knowledge, for the gift of life, the blessings of a sound mind and excellent health. I appreciate Him for sustaining me through this programme and for keeping my family while I was away from them.

My sincere and profound gratitude goes to my supervisor, Dr Ian J. Shannon for his patient supervision, guidance, support and also for giving me the opportunity to attend the 50th Anniversary Annual Meeting of the Clay Mineral Society held at the University of Illinois, USA. I also like to thank the past members of Dr Shannon's research group, my predecessors, Dr Marco Antonio Lopez Martinez, Dr Suparb Tamuang (Ying), Dr Chao Zhao (Ivan) for the brilliant science discussions, the sharing of experiences and ideas, pleasure of working together amicably. I say the entire time shared will certainly not be forgotten in a hurry.

I would also acknowledge all the people whose inestimable diligence guided me through the use of the different machines and techniques employed in the course of this research, Dr Louice Male for technical assistance with XRD, Dr Jacqueline Deans for training me on the XRF, FTIR and TGA machines, Dr Chi Tsang, for advice and technical assistance with HPLC, Dr Paul Stanley for training me on the scanning electron microscope, and some of my past colleagues like Dr Cathryn Hancock and Dr Yasmin Begum who taught me how to use some softwares for data analysis. The brilliant discussions with you ladies helped in data analysis. My acknowledgements will be incomplete without expressing my profound gratitude to Mr John Wedderburn of Materials and Metallurgy department who assisted with surface area measurements,

N.G Marsh of University of Leicester for his valuable advice that helped us to develop modified fused beads preparation method. The technical officers, Rachel Sturman, Katie Topham, Sharon and Theresa Morris who were always there whenever I needed help in the laboratory.

Not left out are all other members of staff of the school of Chemistry who by the diligent discharge of their duties have helped in one way or another to successful completion of this research.

I also appreciate the good advice, support and friendship of Dr John Zheng-yun Zhao, Dr Nicola Gurusinghe, Dr Omowumi Iyang, Dr Shinga Masango, Hart Abbarasi, Christopher Karl, Shaven Win, Rowena Fletcher-wood and a host of other outside Uni friends for their fervent prayers which facilitated the successful completion of this research. I also like to thank the 4th floor (office 418) members for an enjoyable friendship shared. I would like to say that the period spent with you in the office make up a reasonable fraction of the indelible memories of my time in the school of Chemistry, University of Birmingham.

I lack the perfect vocabulary to express my heartfelt appreciation to my children for their understanding and patience, my husband, Sir W.E Omonmhenle for his personal support, love, encouragement and great patience at all-time which propels me through this four years journey in Birmingham alone. My siblings for their absolute support throughout, as always, for which, I am most grateful.

I am especially grateful to the Tertiary Education Trust Funds (TETFUND) for funding, the University of Benin, for granting me training leave and the Advance West Midlands for research facilities.

DEDICATION

This thesis is dedicated to God Almighty, the Immortal, Invisible, Omnipotent, Omniscient and Omnipresent, for diligently working out His plan and purpose for my life to His glory.

LIST OF ABBREVIATIONS

Abbreviation	Description
a	Unit cell in HTlc (inter-metal-distance in brucite-like layers)
c	Unit cell parameter (total thickness of brucite-like layer and interlayer distance)
c′	Interlayer distance
BET	Brunauer-Emmett-Teller method
3c′ or 2c′	(unit cell parameter in c-direction)
d	Distance between two planes
dhkl	Distance between reflection planes (hkl)
Fig.	Figure
Figs.	Figures
FTIR	Fourier transform infrared spectroscopy
Hr(s)	Hour(s)
HT	Hydrotalcite
HTlc	Hydrotalcite-like compound
HTlcs	Hydrotalcite-like compounds
λ	Wavelength of X-ray radiation (1.5064 Å for Cu Kα radiation)
m	The amount of interlayer water in hydrotalcite-like compounds
n	Symbol of IR vibrational mode
x	Mole ratio of gallery cations in hydrotalcite
θ	Diffraction angle in the X-ray diffraction measurements (^{o})
T	Temperature
TGA	Thermogravimetric analysis
DTA	Differential thermal analysis
XRD	X-ray diffraction
qe	The amount of adsorption at equilibrium (mmol/g)
qt	The amount of adsorption at time t (mmol/g)
k_i	Rate constant of pseudo first order process (min^{-1})
k_2	Rate constant of pseudo second order process ($gmmol^{-1}min$)
R^2	Linear regression correlation coefficient
SEM	Scanning electron microscopy
MS	Mass spectrometry

CONTENT

List of Figures

LIST OF TABLES

CHAPTER ONE

INTRODUCTION

1.1 A brief description of Clay

The term clay is somewhat ambiguous unless specifically defined. It is perceived differently by different professionals. Clay is viewed as a raw material for shales by the geologists, as a dynamic system that supports plant life by the soil scientist; the ceramist considers it as a body to be processed in preparation for nitrification, while Chemists and Technologists see it as a layered material composed of sheet-like structures that can be used as a catalyst, adsorbent, filler, coater, or source of aluminium compound. Grim (1968) perceived clays as "composed primarily of extremely small crystalline particles of one or more members of a small group of minerals called clay minerals"[1]. These minerals are the most important constituents of nearly all clays and to a great extent determine their properties. Velde (1995)[2] described "clay" as a term applicable to materials having a particle size of less than 2μm and belonging to the family of minerals with common chemical compositions and crystal structure characteristics. Bhattacharyya and Agupta (2008) agreed with Velde and described clays as "hydrous aluminosilicates consisting of those minerals that makeup the colloid fraction (<2μm) of soils, sediments, rocks and water"[3]. According to them, clays are complex materials that occur naturally and include mixtures of fine grained clay minerals and clay-sized crystalline substances of other minerals such as quartz, feldspar, carbonates and metal oxides. The metal oxides/hydroxides popularly known in soils include those of iron, aluminium and manganese. The main derivation of these metal oxides/hydroxides is the chemical weathering of various primary minerals in soil which liberates these metals

through hydrolytic oxidation or from the precipitation of translocated materials [4, 5, 6]. A clay deposit usually contains non clay-like minerals considered as impurities, although these impurities may actually be essential in determining the unique and specially desired properties of particular clay. Clays are distinct from other soil types by their fine particles composition which are often colloidal and their capability to be moulded. Table 1.1 shows the classification of phyllosilicate clay minerals.

Generally, clays can be distinguished into two broad classes, namely cationic clays (more widespread in nature) and anionic clays. The latter is our main focus in this study. The anionic clays occur naturally though not common in nature but are relatively simple and cheap to prepare. Anionic clays are composed of positively charged metal hydroxide layers with charge neutralising anions and water molecules located in the spaces between the layers and are bound to them forming interlayers [7]. This is in contrast to their cationic counterparts, which have negatively charged sheets with positively charged cations between the sheets or layers to balance the charge, which result as a consequence of the Isomorphous substitution of divalent for trivalent cations in the dioctahedral sheet, for instance, in Montmorillonite clay.

TABLE 1.1: Classification Scheme of Phyllosillicate Clay Minerals (T = Tetrahedral, O = Octahedral [8])

Structure Type	Charge per Unit Cell	Group	Mineral Examples	Ideal Composition	Notes
1:1 (TO)	0	Kaolin- Serpentine	Kaolinite, dickite, nacrite	$Al_4Si_40_{10}(OH)_8$	Kaolin subgroup, dioctahedral, nonswelling
			Halloysite	$Al_4Si_40_{10}(OH)_8 \cdot 4H_20$	Kaolin subgroup, dioctahedral, swelling
			Chrysotile, antigorite, Lizardite	$Mg_6Si_40_{10}(OH)_8$	Serpentine subgroup, trioctahedral, nonswelling
2:1 (TOT)	0	Pyrophyllite	Pyrophyllite	$Al_4Si_80_{20}(OH)_4$	Dioctahedral, nonswelling
			Talc	$Mg_6Si_80_{20}(OH)_4$	Trioctahedral, nonswelling
	0.5-1.2		Beidellite	$[(Al_4)(Si_{7.5\text{-}6.8}\,Al_{0.5\text{-}1.2})\,0_{20}(OH)_4]Ex_{0.5\text{-}1.2}$	Dioctahedral, swelling
			Montmorillonite	$[(Al_{3.5\text{-}2.8}Mg_{0.5\text{-}1.2})(Si_8)\,0_{20}(OH)_4]Ex_{0.5\text{-}1.2}$	
		-talc	Nontronite	$[(Fe_{4.0})(Si_{7.5\text{-}6.8}\,Al_{0.5\text{-}1.2})\,0_{20}(OH)_4]Ex_{0.5\text{-}1.2}$	
		Smectite	Saponite	$[(Mg_6)(Si_{7.5\text{-}6.8}\,Al_{0.5\text{-}1.2})\,0_{20}(OH)_4]Ex_{0.5\text{-}1.2}$	Trioctahedral, swelling
			Hectorite	$[(Mg_{5.5\text{-}4.8}Li_{0.5\text{-}1.2})(Si_8)\,0_{20}(OH)_4]Ex_{0.5\text{-}1.2}$	
	1.2-1.8		Vermicullite	$[(Al_4)(Si_{6.8\text{-}6.2}\,Al_{1.2\text{-}1.8})$	Dioctahedral, swelling

				$0_{20}(OH)_4]Ex_{1.2\text{-}1.8}$	
			Vermicullite	$[(Mg_6)(Si_{6.8\text{-}6.2}\ Al_{1.2\text{-}1.8})$ $0_{20}(OH)_4]Ex_{1.2\text{-}1.8}$	Trioctahedral, swelling
		Vermiculite			
		IIIite	IIIite	$[(Al_4)(Si_{7.5\text{-}6.5}\ Al_{0.5\text{-}1.2})$ $0_{20}(OH)_4]K_{0.5\text{-}1.2}$	Dioctahedral, nonswelling
			Glauconite	IIIite rich in Fe	
	2	Mica			
			Muscovite	$[(Al_4)(Si_6Al_2)0_{20}(OH,F)_4]K_2$	Dioctahedral, nonswelling
			Celadonite	$[(Fe_2Mg_2)(Si_8)0_{20}(OH,F)_4]K_2$	
			Phlogopite	$[(Mg_6)(Si_6Al_2)0_{20}(OH,F)_4]K_2$	Trioctahedral, nonswelling
			Taenolite	$[(Li_2Mg_4)(Si_8)0_{20}(OH,F)_4]K_2$	Trioctahedral, lithium mica
	4	Brittle mica	Margarite	$[(Al_4)(Si_4Al_4)0_{20}(OH,F)_4]Ca_2$	Dioctahedral, nonswelling
2:1 channels or inverted ribbons	Variable	Palygorskite-sepiolite	Palygorskite	$[(Mg,Al)_4(Si_{7.5\text{-}7.75}\ Al_{0.5\text{-}0.25})$ $0_{20}(OH)_2(OH_2)_4]Ex_{var}$	Dioctahedral, nonswelling
			Sepiolite	$[(Mg,M)_8(Si,M')_{12}$ $0_{30}(OH)_4(OH_2)_4]Ex_{var}$	Trioctahedral (M = Al, Fe(III); M' = Fe(II), Fe(III), Mn(II)
2:1:1	Variable	Chlorite	Clinochlore		[TOT]O[TOT] structure

Source: Adapted from ref. 8

1.2 Cationic Clays

This group of clays consists of negatively charged metal (most times alumino) - silicate layers and gallery cations. The basic foundational unit of cationic clays are the tetrahedral Si (O, OH) and octahedral M (O, $OH)_6$ (where M = $Al^{3+,}$ $Mg^{2+,}$ Fe^{3+} or $Fe^{2+)}$, which form two dimensional tetrahedral and octahedral sheet, respectively. The combinations of these two different types of sheets give rise to the precise electro neutral structures of the layers. In nature, the occurrence of isomorphous substitution of Si^{4+} in the tetrahedral sheet and/or Al^{3+} or Mg^{2+} in the octahedral sheet by atoms with lower valence, results to the development of excess negative charges, which are balanced by exchangeable interlayer cations, such as Na^{+}, Ca^{2+}, K^{+}, $NH4^{+}$ or Mg^{2+} [9, 10, 11, 12] . The synthesis of the pure form of this type of clay is relatively difficult and complicated, compared to the synthesis of anionic clays.

1.2.1 Mineralogy and structure of clay

Clays may be crystalline or amorphous. Most natural clays (cationic) have a phyllosilicate or sheet structure, whose crystalline structure is based on a combination of coordinated polyhedrons, arranged along planes as mentioned earlier. In each tetrahedron, a silicon atom is surrounded by four oxygen atoms to form the tetrahedron. The chemical composition of each tetrahedron may be expressed as SiO_4 (Fig.1.1a). Separate or distinct tetrahedrons share edges (three out of four oxygens) to form tetrahedral sheets. These tetrahedra of silica are linked together by covalent bonding through sharing of oxygen to form a hexagonal network of the composition $Si\text{-}O_4$ when

repeated indefinitely (Fig.1.2). The top of the four tetrahedra all point in one direction and the base are in one plane (Fig.1.1b). In the tetrahedral structural units, the interlinked oxygen is the basal oxygen, and they are arranged such that they leave a hexagonal-shaped hole or cavity in the network of oxygen atoms. To the opposite end of the linked tetrahedral sheet lie the apical oxygen atoms and they point away from the interlinked tetrahedral bases. This apical oxygen is shared with other series of cations to form another polyhedron.

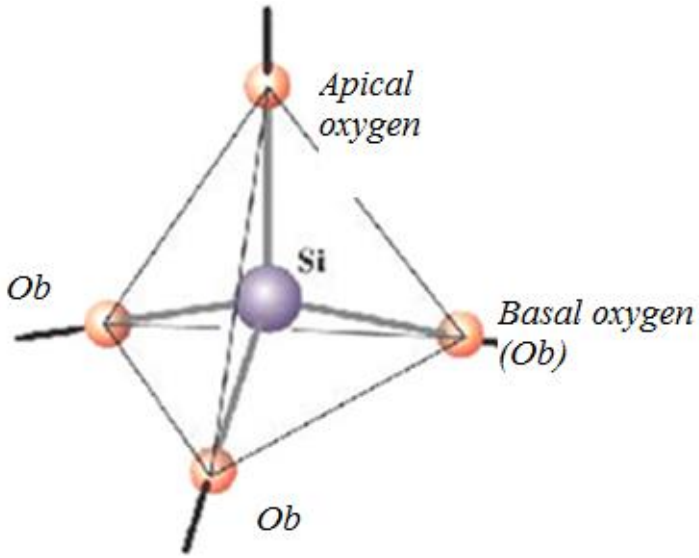

Fig.1.1a: Single silica tetrahedron

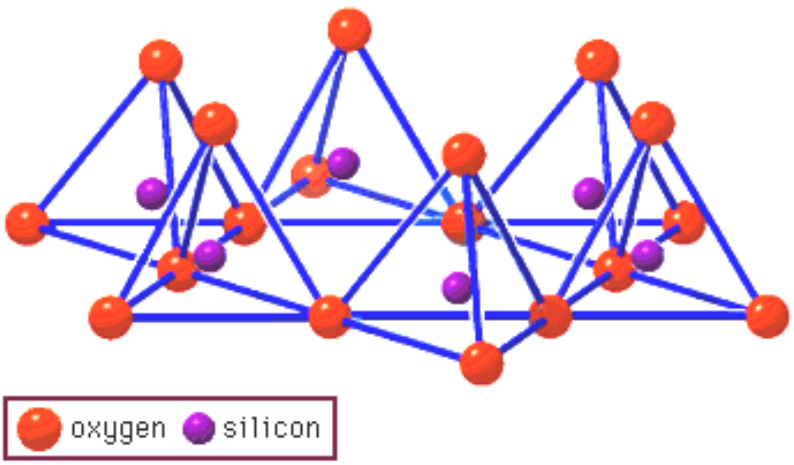

Fig.1.1b: Hexagonal combining form that gives tetrahedrons in the silica layer

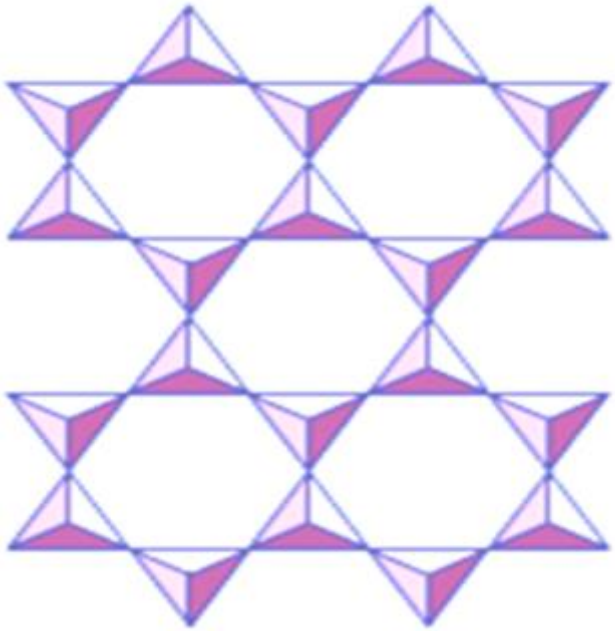

Fig.1.2: Hexagonal arrangement of the basal oxygen of the linked silica tetrahedral layer[8]

Aluminium may be substituted for silicon in the tetrahedral layer resulting in the development of excess negative charge. Based on the charge difference, the negative charge on the shared oxygen between Al and Si tetrahedra is not satisfied, hence the excess negative charges. The second basic unit responsible for the pattern of construction of the different clay minerals is AlO_6 octahedra in which six hydroxyl groups or oxygen atoms are arranged such that each forms the vertices of an octahedron held together by an aluminium atom at the centre (Fig.1.3a). The octahedra formed are linked together laterally by sharing edges in the sheets known as alumina or octahedral sheets. In these sheets, the six hydroxyl groups that form each octahedron are jointly shared by three adjacent octahedra. The cell consists of four aluminium atoms and six hydroxyl groups in such a way that the top and bottom of the alumina sheet are hydroxyl terminated surfaces. An arrangement in a hexagonal pattern is also possible.

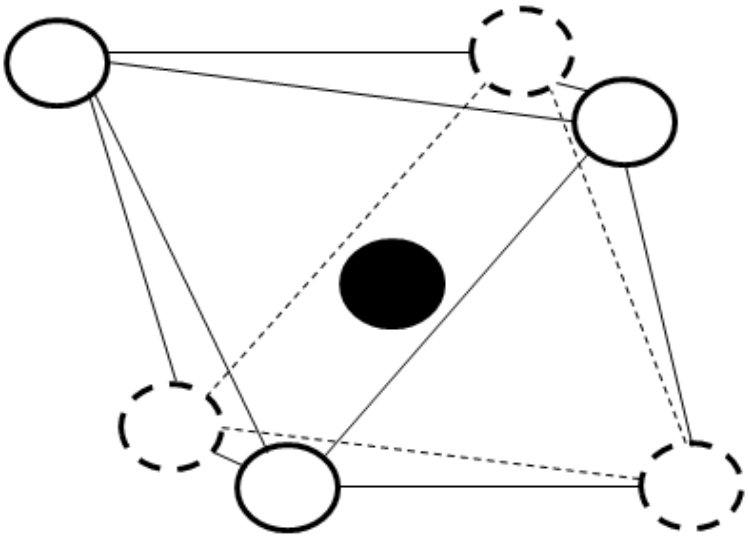

(a)

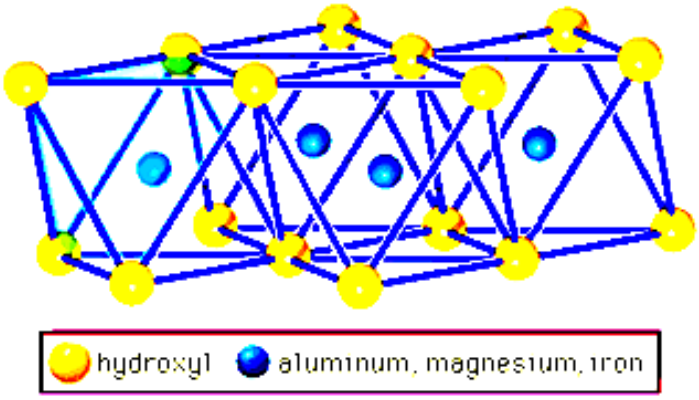

(b)

Fig.1.3: (a) single alumina octahedron and (b) alumina octahedral sheet (Showing lateral sharing of edges)[8].

Aluminium, iron, or magnesium atoms can be embedded in the octahedral coordination sites (and more rarely, chromium, lithium, manganese, etc. (Fig.1.3b). When it is aluminium that is present in the octahedral coordination sites, only two-thirds of the possible positions are filled to balance the charge of the structure, giving what is known

as the gibbsite structure, with formula $Al_2(OH)_6$. When magnesium is substituted for aluminium, all the possible positions are filled to balance charges leading to the brucite structure, $Mg_3(OH)_6$[1]. The octahedral sheet is in coordination with oxygen from the tetrahedral sheet. When tetrahedral and octahedral sheets are taken together, a layer is formed. The individual layers may be joined to each other by interlayer cations, Van der Waals and electrostatic forces or hydrogen bonding.

1.2.2 Classification of clay minerals

There are considerable differences of opinion regarding the proper basis for a satisfactory classification of clay minerals. Different classifications have been adopted by different clay researchers/professionals based on their research interest. Three principal types/groups may be identified, which are Kaolinite, Smectite (Montmorillonite) and Chlorite. All three types principally consist of tiny crystals with platy shapes of layers of molecules which are stacked one on another and are made up of different combinations of the tetrahedral and octahedral sheets (1:1 clay mineral like Kaolinite, Halloysite etc.); the three sheets layer structure of silica–alumina–silica consisting of the Montmorillonite, Vermiculite and the Illite groups.

1.2.2.1 The 1:1 Mineral (two layer-group clay minerals)

Different combinations of tetrahedral and octahedral sheets fashion different clay minerals. Basically, all clay minerals are made of two sheets, namely tetrahedral and octahedral sheets. The combination of one silica sheet with one octahedral sheet forms a basic layer of the two layer-group clay mineral. When there is no absorbed water molecules existing inside the structure, the mineral is referred to as Kaolinite, $[Si_4(Al_4)O_{10}(OH)_8]$. The basic building blocks are layers of silica tetrahedra and layers of alumina octahedra in a 1:1 relationship. These sheets are stacked in sequence to build up the platy crystals firmly bound together. The bonding present between the layers is effective through hydrogen bonding and Van der Waals forces. (Fig.1.4a), Kaolinite is a non-expanding clay. Fig.1.4b shows the SEM image.

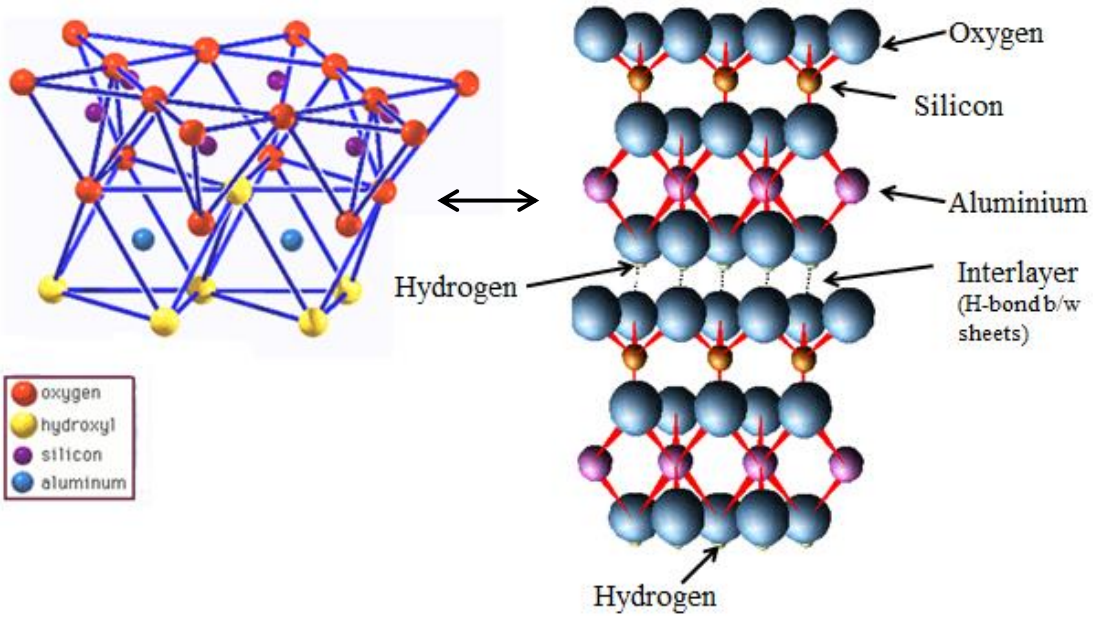

Fig.1.4a: Structure of Kaolinite showing silica tetrahedral and alumina octahedral in 1:1 relationship. The surface on one sheet holds hydrogen ions while the other contains only oxygen ions.

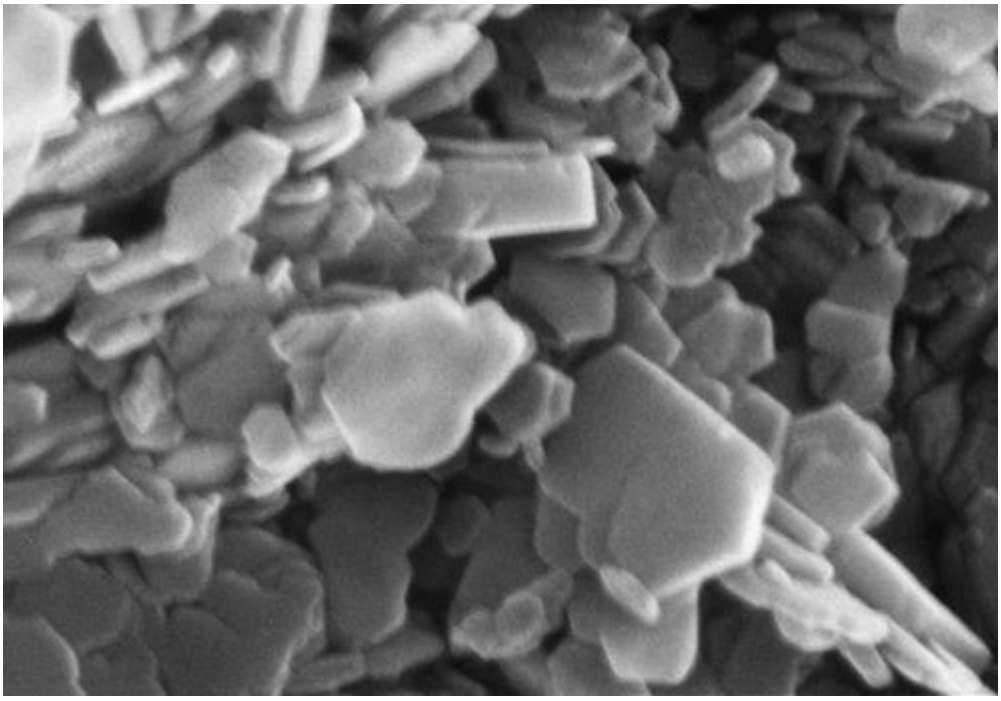

Fig.1.4b showing the SEM image of Kaolinite, Acc.V = 20.0kV, WD = 10mm, Magn = 70.0Kx and 100nm scale.

Also included in this group is a similar mineral known as hydrated halloysite, which though, has resemblance to Kaolinite, possesses four additional water molecules per layer [$Si_4(Al_4)O_{10}(OH)_8.4H_2O$]. The microscopic crystalline particles are elongated, not equidimensional in shape (Fig.1.5) as in Kaolinite.

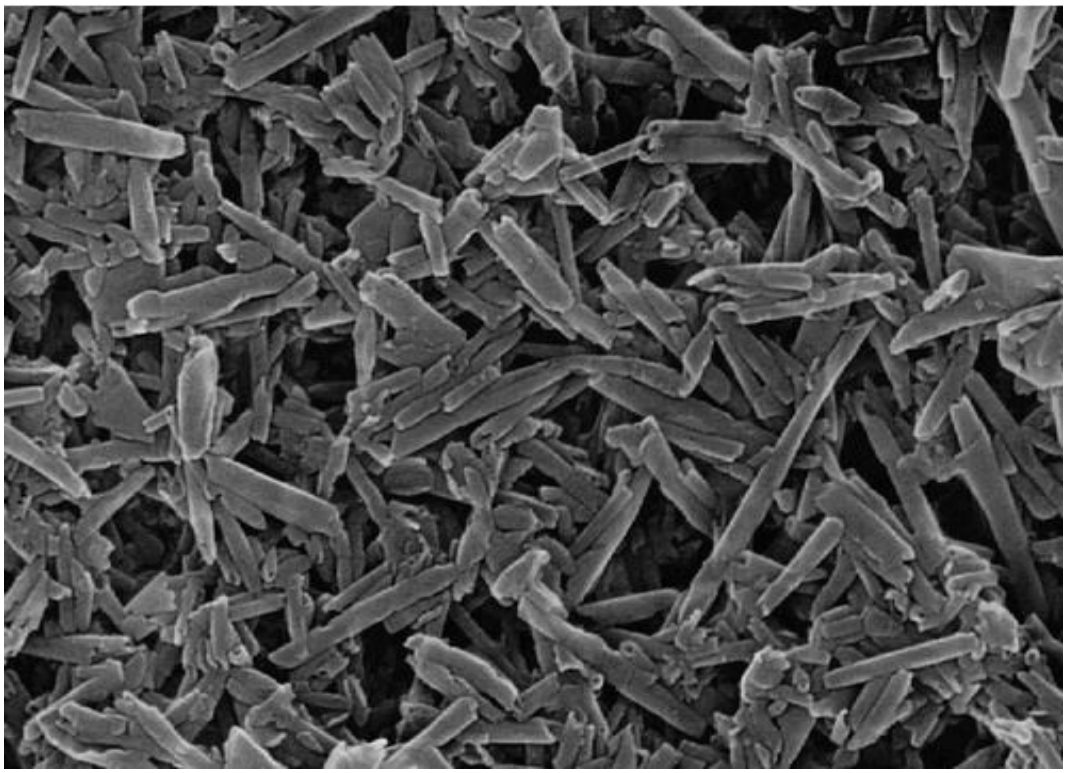

Fig.1.5 showing the SEM image of halloysite, Acc.V = 25.0kV, WD = 10mm, Magn = X40.0K and 750nm scale [13]

Ross and Kerr (1934)[14], identified two types of halloysite, which are; light- coloured, porous and friable, and the dense, nonporous and porcelain-like (less hydrous). Usually, the tetrahedral cation sites in the 1:1 layer type are all occupied by Si^{4+} and the octahedral sites all by Al^{3+} or Mg^{2+}. The minerals of this group show almost no isomorphous substitution occurring in them, such that charge per unit cell is almost zero thus there are no compensating cations located in the interlayer space unlike in the three layer clay minerals. Kaolinite is the most abundant mineral in most kaolin. It is the most useful and important industrially. The kaolin family of minerals also includes other minerals such as halloysite, dickite and nacrite which are formed from hydrothermal or pneumatolytic alteration. Pure deposits are mined and find use in ceramics, paints, paper, plastic, ink[15] and are also used in beauty therapy and pharmaceutical industries[16, 17].

1.2.2.2 The 2:1 Clay Mineral (Three-layer clay minerals)

These have platy crystals which are constituted from an octahedral layer sandwiched between two tetrahedra thereby giving three layers of silica - alumina - silica per layer. There is a coordination of the octahedral unit through shared or linking oxygen to two layers of tetrahedrally coordinated ions with hydroxyls found only in the intermediate layer of the octahedrally coordinated structural unit [18]. Ionic substitution can occur in either the tetrahedral or octahedral sheets. Cations that are small enough to enter into tetrahedral coordination with oxygen do so leaving net negative charges on the layer. Cations such as Fe^{3+} and Al^{3+} can substitute for Si^{4+} in the tetrahedral sheet. Likewise, in the octahedral sheet, cations like Mg^{2+}, Fe^{2+}, Fe^{3+}, Li^{+}, Ni^{2+}, Cu^{2+} can substitute for Al^{3+}. Alkali and alkaline earth cations such as K^{+}, Na^{+}, Cs^{+}, Mg^{2+} and Ca^{2+} can be located between the layers (called interlayer cations) and it is also found that F may sometimes substitute for (OH) in some clay minerals. It can sometimes, therefore be difficult to distinguish between members of this group, because there are a number of them, all with very similar crystal structures. Members of the 2:1 layer clay minerals spread into different groups that may be differentiated on the basis of the extent or degree of isomorphous substitution, the type of octahedral layer present, and also on the way the layers are bound together. However, three main divisions may be identified and they are Illite, Smectite and Vermiculite. In Illite, there is isomorphous substitution in the tetrahedral and octahedral sheets and this substitution is larger than in the other two minerals, thus a higher charge deficiency such that the layers are stacked together by frontal sharing of K^{+} ions. The bond between K^{+} and the layers is very strong such that the minerals are stable under normal conditions and do not swell chemically (Fig.1.6a). The unhydrated, firmly fixed interlayer ion is prominently potassium if not exclusively.

If the octahedral sheet is exclusively occupied by Al^{3+} (gibbsite), the mineral is called Muscovite and if Mg^{2+} (brucite) is present, the mineral is Phlogopite. Vermiculites not only have a smaller isomorphous substitution, but also display a different bonding between layers, (di and trioctahedral Vermiculites also exist, though of unknown composition). Molecules of water are available between the layers and are linked with exchangeable cations that shield the electrical charge of the layers. Most common cations found in the interlayer space are Mg^{2+} and Ca^{2+} (Fig.1.7a). Substitutions of Al^{3+} for Si^{4+} result in charge imbalance and these may be partially balanced by other substitutions within the unit structure (octahedral substitution). Heating Vermiculite to a moderate temperature of up to 500^{o}C, abstracts water from its layers, and on exposure to moisture at room temperature, the mineral quickly rehydrates. If the mineral is heated up to 700^{o}C and beyond, there will be no more expansion and rehydration becomes difficult or impossible. The optical image is shown in Fig.1.7b.

The other group of 2:1 minerals is Smectite, the most common mineral being Montmorillonite with both dioctahedral and trioctahedral sheets, similar to talc ($Mg_3Si_4O_{10}(OH)_2$). The Montmorillonite group is very sticky, expands when it comes on contact with water and shrinks when dried. It has good plasticity, high capacity to absorb and hold water and other substances within their layers, due to their internal crystal structure. The tetrahedral- octahedral-tetrahedral sheets are weakly bonded to each other because they are joined by weak Van der Waals bond and by outer complexes of cations, surrounded by water molecules and therefore can easily be separated by water (Fig.1.8a). It could be that it is the exchangeability of cations and water molecules within the galleries of these minerals that makes them show great swelling potential and some of the “clayey” behaviour. The cations replacing aluminium

in the dioctahedral sheet are mainly magnesium, iron, and zinc. The net negative charge of Montmorillonite is satisfied by cations, which pre-surround the negatively charged mineral. The SEM image is shown in Fig.1.8b.

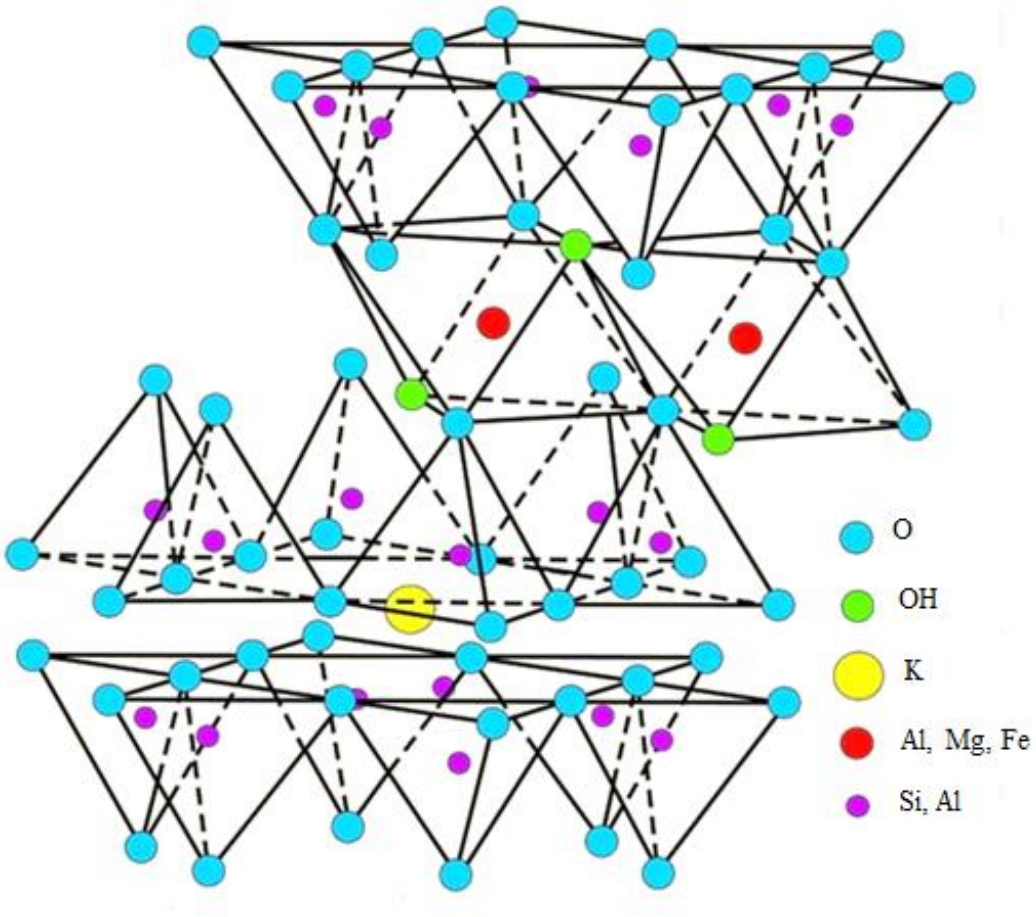

Fig.1.6a: Three-sheet layer structure of Illite (adopted from [19])

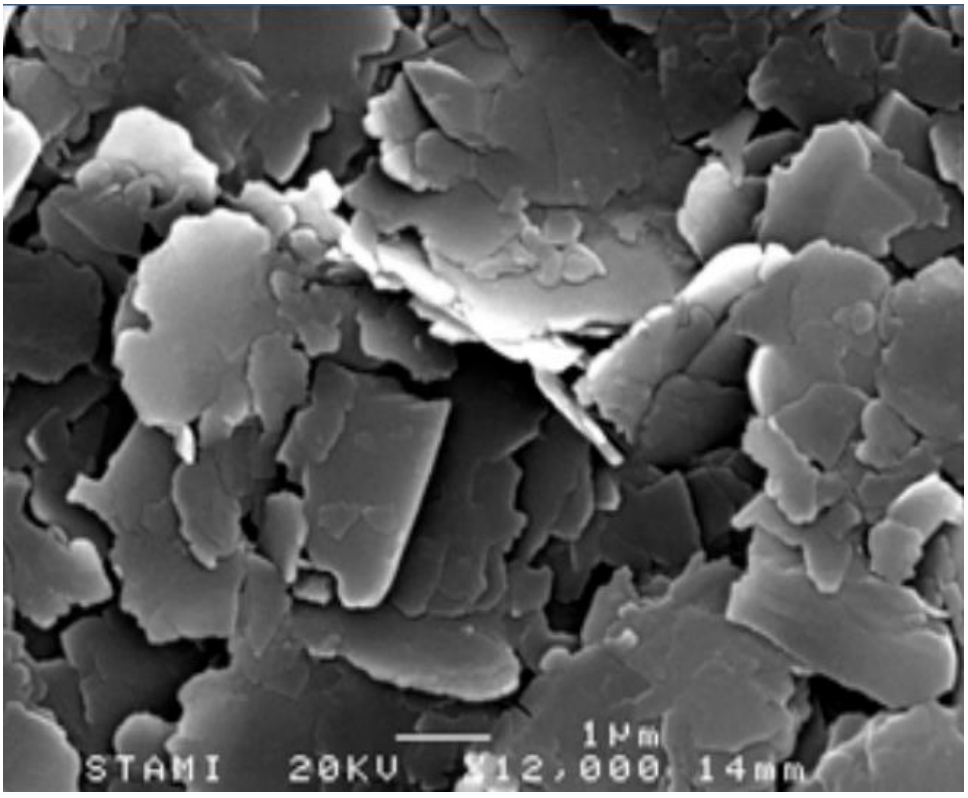

Fig.1.6b showing the SEM image of Illite

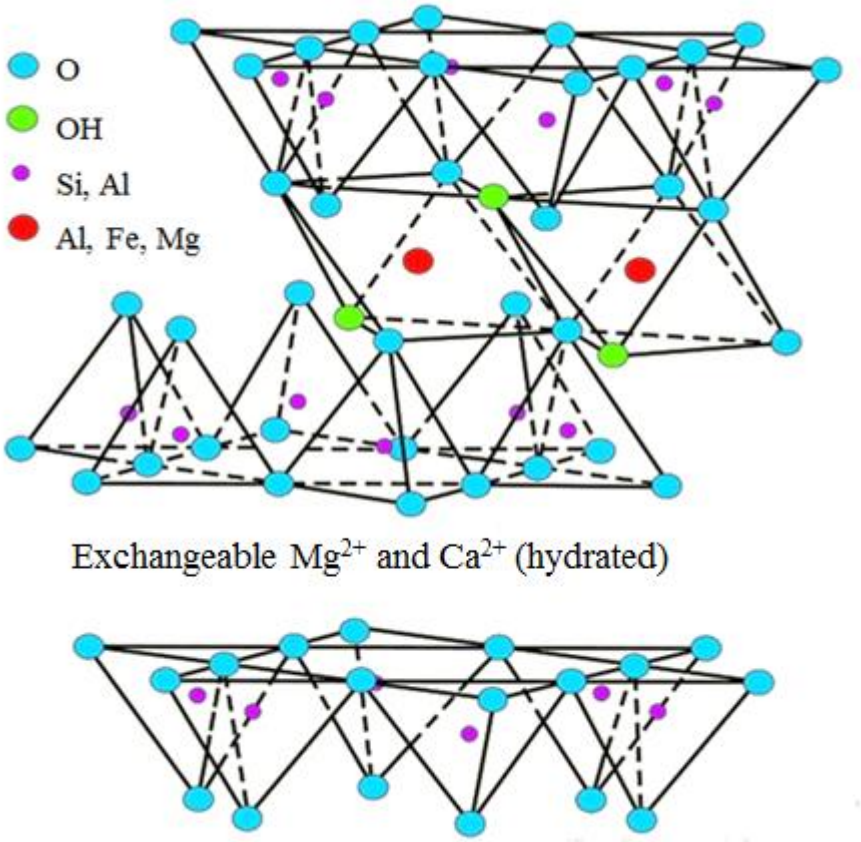

Fig.1.7a: Three-sheet layer structure of Vermiculite

Fig.1.7b showing the Optical image of Vermiculite

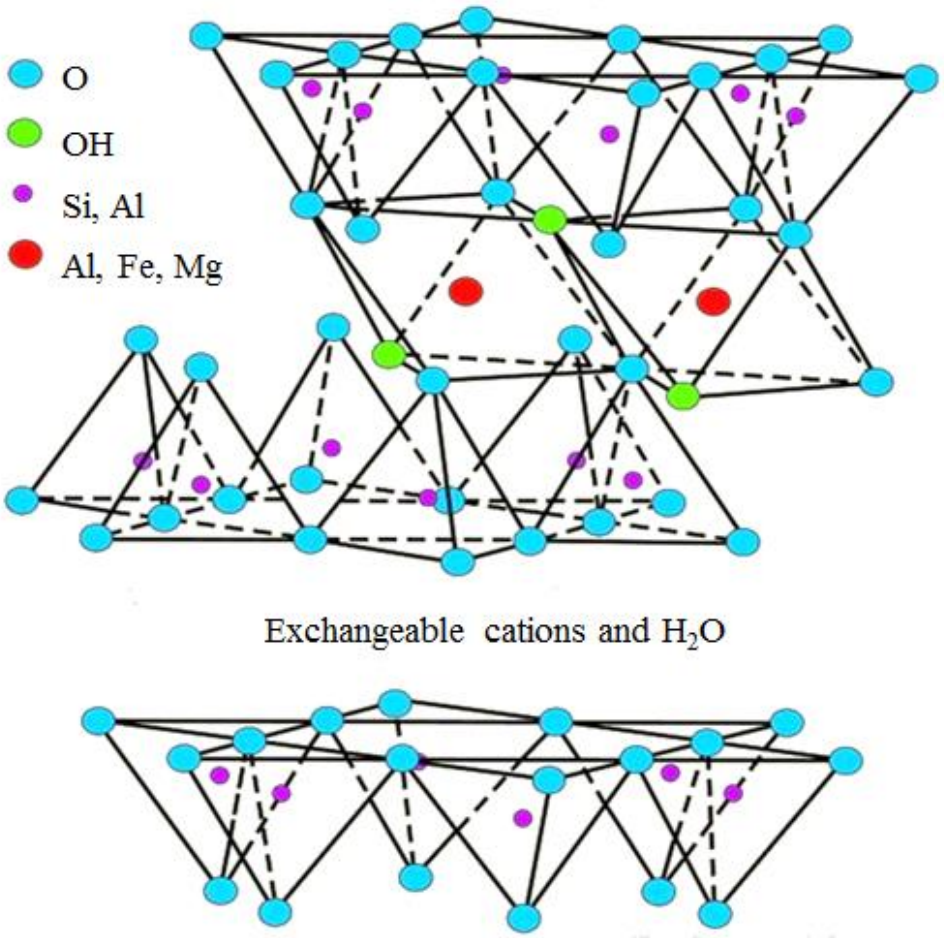

Fig.1.8a: Structure of Montmorillonite (Adapted from [19])

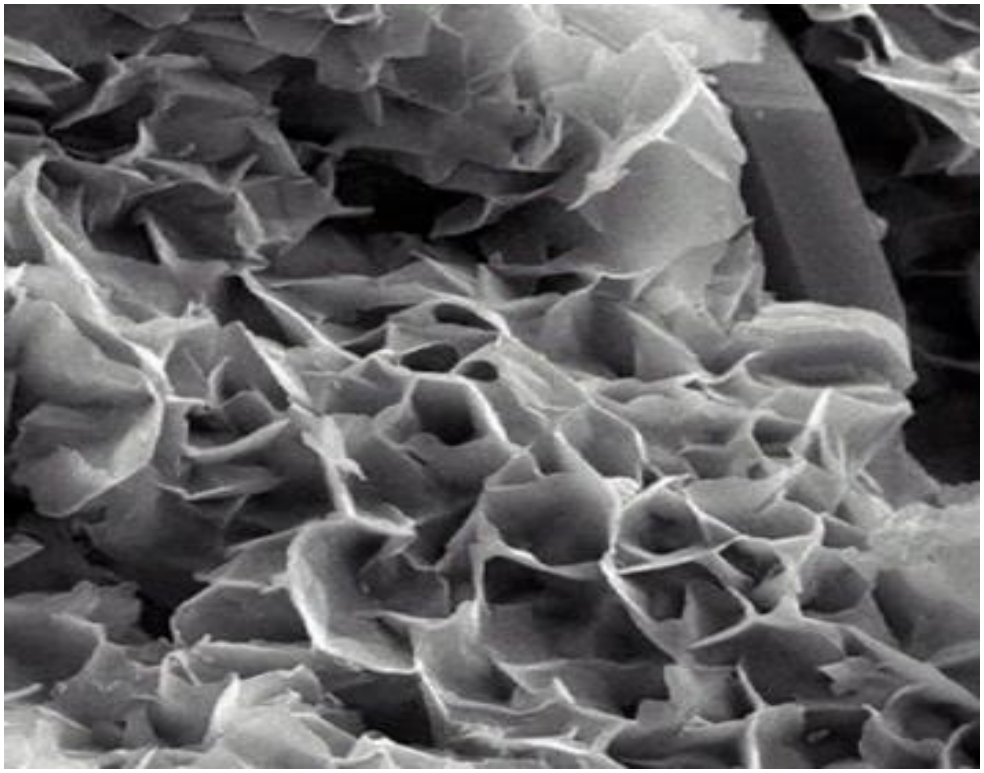

Fig.1.8b showing the SEM image of Montmorillonite, Acc.V = 20.0kV, WD = 10mm, Magn = 1.5Kx and 6.67µm scale.

Other 2:1 clay minerals are talc [$Mg_3Si_4O_{10}(OH)_2$] and pyrophyllite[$Al_2Si_4O_{10}(OH)_2$] which contain trioctahedral and dioctahedra members respectively. There are no tetrahedral or octahedral substitutions, no layer charge and no layer materials. All the same, there is often some small amount of substitution in the natural minerals, but this only gives a small amount of ionic attraction between layers that supplement Van der Waals bonding. This weak force may be the reason that these materials are soft, have good cleavage, slipperiness and exhibit varying degree of stacking disorder[20]

1.2.2.3 The 2:1:1 layer clay minerals

The mineral of this kind of clay results from the additional hydroxide interlayer added to the structure of a 2:1 layer or mineral [Fig.1.9a]. In 2:1:1 layer silicates with interlayer brucite, each 2:1 part of the structure is separated by a brucite layer. The most important mineral in this group is chlorite:

$$\text{Talc} + \text{brucite} \longrightarrow \text{chlorite } [Mg_6Si_4O_{20}(OH)_8]$$

Al may substitute for Si between Si_7Al and Si_4Al_4 and may also substitute for Mg between $Mg_{11}Al$ and Mg_8Al_4. Replacement of Fe^{2+} for Mg^{2+} and Fe^{3+} for Fe^{2+} is also possible. Vermiculite is the most common in this group and it is a Mg containing octahedral clay mineral with primary substitution being of Al for Si in the tetrahedral layer of the talc structural unit. Interlayer cations (mainly Mg) compensate for the resulting charge imbalance. The Mg occurs in a double sheet of H_2O and not all water sites are occupied. The water molecules form a distorted hexagonal pattern. Each of the waters is linked to oxygen of the tetrahedral layer by a hydrogen bond. The resulting structure resembles that of chlorites, except that the brucite sheet is only partially filled, which results in a [H_2O - Mg - H_2O] double sheet. Two thirds of the available water molecule sites are filled along with one third of the cation sites. Swelling in organic liquids and in water occurs with minerals of this group [21]. The SEM image is displayed in (Fig.1.9b):

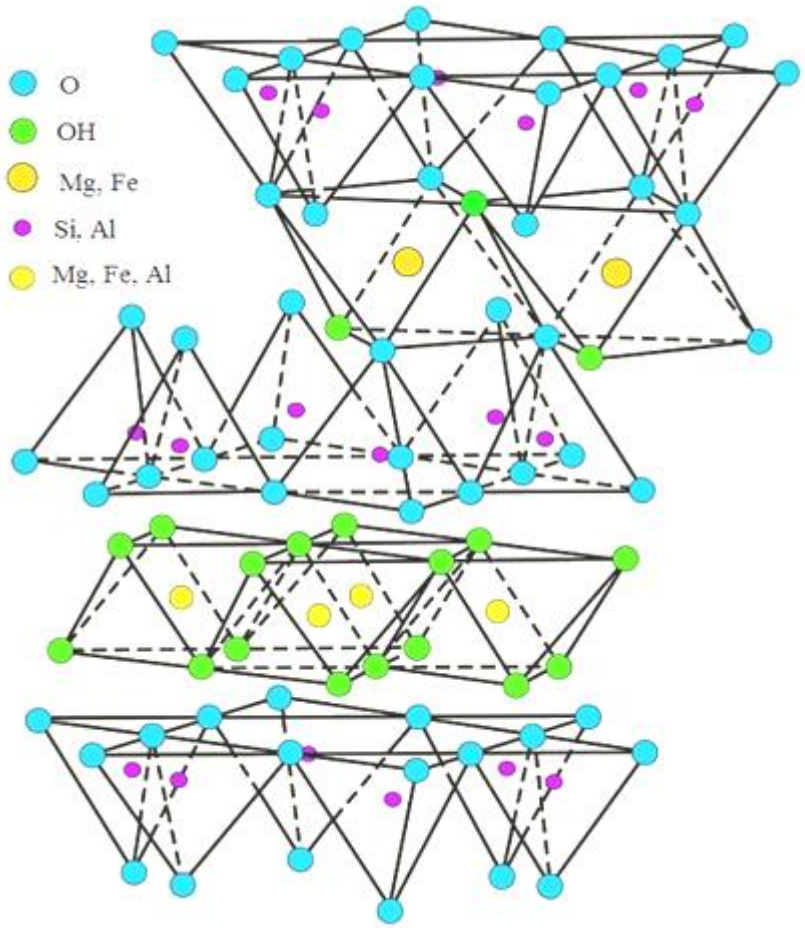

Fig.1.9a: Chlorite (2:1), non-expanding, minimum swelling.

Fig.1.9b showing the SEM image of chlorite

1.3 Anionic clays

The anionic clays may be described as either natural or synthetic sheet-like alternating layers of mixed hydroxides having interlayer space composed of exchangeable anions [22, 23]. They were first discovered in Sweden about 1842, and at about the same time, a mixed hydroxycarbonate of Mg and Fe called pyroaurite was also discovered which was later identified to be isostructural with hydrotalcite and have similar characteristics. Hydrotalcite is the most prominent of the anionic clay group. Different names can be used to describe this type of clay, and the name used depends on the composition and polytype forms of the minerals. Most often used are the general terms hydrotalcite-type or hydrotalcite-like compound (HT/HTlc)), or layered double hydroxides (LDHs), based

on the early work of Feithnecht who called them “doppelschichtstrukturen” (double sheet structure). The mineral hydrotalcite has the molecular formula, $Mg_6Al_2(OH)_{16}CO_3.4H_2O$. The hydrotalcite structure emanated from the stacking of brucite-like-layers [$Mg(OH)_2$] consisting of positive residual charge resulting from the partial isomorphous substitution of trivalent cations like Al^{3+} for Mg^{2+} cations. This excess positive charge is balanced by interlayer anions which maintain the overall charge neutrality[24, 25].

1.3.1 The Structure of HT $([M^{2+}_{1-x}M^{3+}_{x}(OH)_2]^{b+}[A^{n-}_{b/n}].\ mH_2O)$

The structure of HT can be clearly described as the piling of positively charged layers with anions in their interlamellar space, i.e. brucite like layers (Fig.1.10a) consisting of Mg^{2+} ions that are coordinated octahedrally by hydroxyl groups with the octahedral units sharing edges to form charged neutral sheets[26, 27] (Fig.1.10a). These sheets are heaped orderly on each other, and held together by both ionic and hydrogen bonding [23. 28]. Isomorphous replacement of some of the Mg^{2+} with trivalent cations like Al^{3+}, Fe^{3+}, Cr^{3+} etc bring about the positive charges on the layers allowing the presence of gallery charge balancing anions (to maintain electrical neutrality) while molecules of water of crystallization occupy the remaining gallery space[29, 30, 31] (Fig.1.10b).

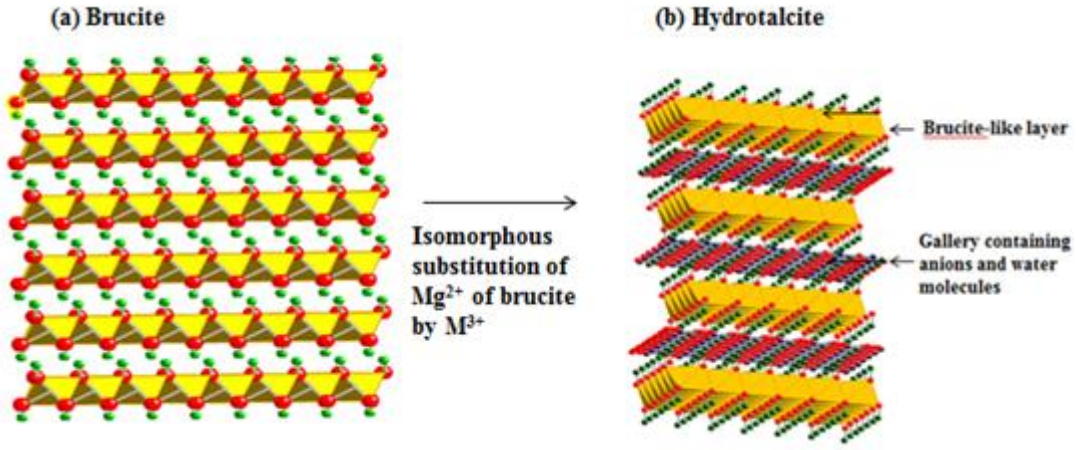

Fig.1.10: (a) Brucite ($Mg(OH)_2$ structure to (b) Hydrotalcite structure by isomorphous substitution M^{2+} by M^{3+} cations. Cations occupy the centre of the octahedra with hydroxide ions at the vertices and intercalated anions and water are situated at the gallery.

Hydrotalcite-like compounds have a range of length scale. They are represented by the general formula $[M^{II}_{1-x} M^{III}_{x} (OH)_2]^{b+} [A^{n-}_{b/n}]. mH_2O$. Where;

- M^{II} = (Ca^{2+}, Mg^{2+}, Zn^{2+}, Co^{2+}, Ni^{2+}, Cu^{2+}, Mn^{2+}, Fe^{2+}), or monovalent cation Li^{+}
- M^{III} = (Al^{3+}, Cr^{3+}, Fe^{3+}, Co^{3+}, Mn^{3+}, Ga^{3+})
- A = Interlayer anions of the valence n (Cl^-, NO_3^-, ClO_4^-, Br^-, F^-, OH^-, CO_3^{2-}, SO_4^{2-}, organic anions etc)
- x = the metal ratio $M^{3+}/(M^{2+} + M^{3+})$
- m = moles of co-intercalated solvent, generally water of crystallization

In this study, hydrotalcite-like compounds are referred to as $M^{2+}M^{3+}A$ for example, Mg_2AlCO_3.

1.3.2 Inside the Hydroxide Layers

There are a great variety of combinations of divalent and trivalent cations that can be accommodated in the brucite-like layers (hydroxide layers). This includes binary combinations of metal cations, ternary, quaternary and multicomponent combination of metal cations[32], mainly some metal cations of the third and fourth periods of the periodic table of elements. They must meet the radius requirement to qualify to be accommodated in the holes of the close packed arrangement of OH group in the octahedral hydroxide layer. Mg^{2+} ions have an ionic radius of 0.65Å (six coordination number), and the trivalent ions that substitute for Mg^{2+} ion should have ionic radii not too different from that of Mg^{2+}. Cations that are too small, such as Be^{2+}, or too large like Cd^{2+} or Ca^{2+}, may give other types of compounds[33, 34, 35]. For instance, larger ions like Cd^{2+} can be introduced into the metal hydroxide layer but will distort the stacking arrangement of the layers or join with other M(II) or M(III) ions as in MgCdAl[36]. While with Ca^{2+}, the hydrotalcite-like structure converts into that of hydrocalcumite ($Ca_2Al(OH)_6Cl.3H_2O$), a more general representation of the group being $[Ca_2 M^{III}(OH)_6]^{b+} [A^{n-}_{b/n} .mH_2O]$, where $M^{III} = Al^{3+}$, Fe^{3+}, Cr^{3+}, Ga^{3+} etc and $A^{n-} = SO_4^{2-}$, CO_3^{2-}, or Cl^-. Monovalent [37, 38, 39] and tetravalent cations[40, 41] can also be incorporated into the brucite-like layers to some extent but not as common as the trivalent cations. In this study, our focus is the $M^{II}M^{III}$ hydrotalcites. Natural hydrotalcite exists with an x value of 0.25, and it is possible to synthesise a number of compounds similar to natural hydrotalcite ($Mg_6Al_2(OH)_{16}CO_3.4H_2O$), with different stoichiometry possessing a wider range of x value. Some researchers[22, 42, 43] are of the view that x values of 0.2 - 0.33 are necessary to obtain pure hydrotalcites or LDHs. Deviation from this value of x may give impurities or compounds with different structures.

Mascolo and Marino[44] supports a M^{2+}/M^{3+} ratio of between 2 and 4 in order to obtain pure HTlcs. Braterman et al[30] are also of the view that the overall ratio of M^{2+} to M^{3+} cations should be kept between 0.2-0.4. Values of x other than this range, $0.2 \leq x \leq 0.33$ may result to pure hydroxides or compounds with entirely different structures.

Table 1.2 shows the ionic radii of selected divalent and trivalent cations that can exist within the hydroxide layers. The charge density of the hydrotalcite may be controlled by varying the M(II) / M(III) ratio within the layers.

Table 1.2: The ionic radii (r) of selected divalent and trivalent cations with coordination number 6

Divalent cation (M^{2+})	Be	Mg	Cu	Ni	Co	Zn	Fe	Mn	Cd	Ca
Radius (Å)	0.30	0.65	0.69	0.72	0.74	0.74	0.76	0.80	0.97	0.98
Trivalent cations (M^{3+})	Al	Ga	Ni	Co	Fe	Mn	Cr	V	Ti	In
Radius (Å)	0.50	0.62	0.62	0.63	0.64	0.66	0.69	0.74	0.76	0.81

Taken from[22]

1.3.3 Between the Layers

The most common anion that is found between the layers of natural hydrotalcite is carbonate (CO_3^{2-}), but there is no restraint as to the nature of the charge balancing anions that can be accommodated within the galleries of hydrotalcite-like compounds, therefore, in practice, different charge balancing anions can occupy the galleries of the hydrotalcite as long as they possess adequate charge density in one cross section and would not remove the metal ions from the hydroxide layers. Possible charge

neutralising anions are halides, oxo-anions, silicates, polyoxometalate anions, complex anions, iso and heteropolyanion, metallorganic complexes, inorganic and organic anions [27, 45]. The interlayer anions can be displaced by several inorganic and organic anions and the water molecules by other polar molecules[42, 46]. By varying the ratio of M^{2+}/M^{3+}, the anion exchange capacity can be controlled thus controlling the number and arrangement of charge balancing anions in the HT. When the interlayer anion is not carbonate, it is often difficult to avoid contamination from CO_2 (from the atmosphere) during the preparation of the compounds. This is because the carbonate anion is so tenaciously incorporated and is held very firmly due to the high preference of HT for carbonate anion, and so the direct preparation of pure, non-carbonate LDHs or hydrotalcites is not very easy to accomplish. Notwithstanding, the synthesis of a number of compounds of different stoichiometry are possible as long as there is the right environment and the choice of value of x exists in the right range. Miyata 1983[47] showed that the affinity of hydrotalcite for different anions is in the order $CO_3^{2-} > SO_4^{2-} > OH^- > F^- > Cl^- > Br^- > NO_3^- > I^-$.

Anions differ from one another in structure, charge and size. Despite this difference, they are all held between the gallery space (interlayer layers). This unique characteristic is depicted by the interlayer spacing, and the orientation of the anions is such that their interaction with their surroundings is maximised. A good example can be represented by the CO_3^{2-} anion arranged within the brucite-like layer in a parallel position such that the three oxygen atoms form hydrogen bonds due to effective interaction with the layer hydroxyl groups. This facilitates the maximization of the electrostatic interaction between the CO_3^{2-} anions and the positively charged layers because the height of the gallery is minimized. In the case of the nitrate anion with larger interlayer space, the

molecular plane is tilted at high x values and parallel to the hydroxide layer within the interlayer even though it has the same shape as a carbonate anion[48]. The tetrahedral anions like the ClO_4^-, ClO_4^{2-}, SO_4^{2-} etc can exhibit two different arrangements, pyramidal and perpendicular (Fig.1.11). In the former, it is arranged with one of its C_3 axes standing upright to the hydroxide layer while in the latter, it presents the edge configuration with one C_2 axis oriented uprightly to the hydroxide layer giving rise to smaller height [45].

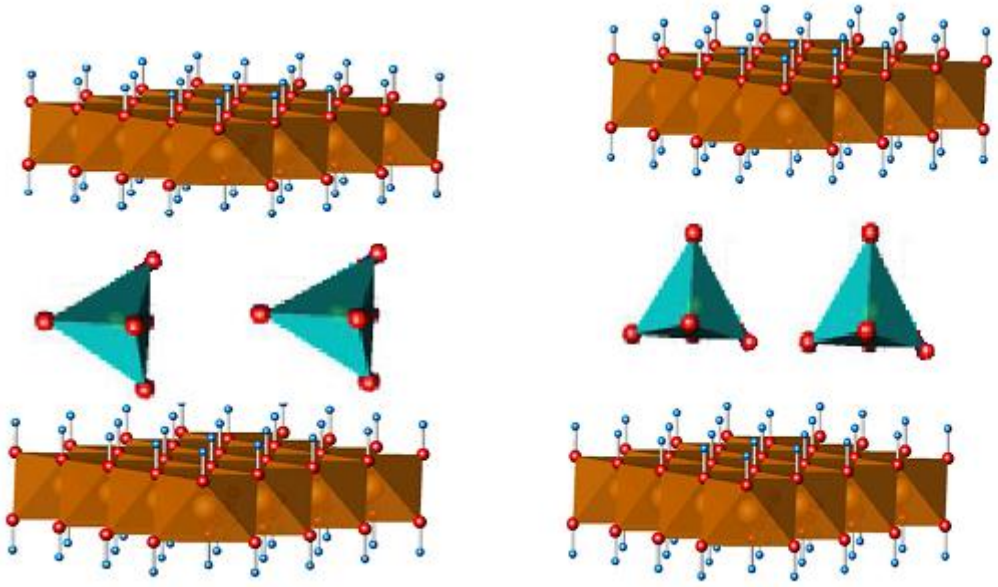

(a) (b)

Fig.1.11: Intercalation of tetrahedral anions (a) pyramidal and (b) perpendicular.

For aliphatic monocarboxylate, sulphates and sulfonates, the organic anions may exhibit three possible orientations, monolayer, simple bilayers and interpenetrating or perpendicular bilayers (Fig.1.12-1.13).

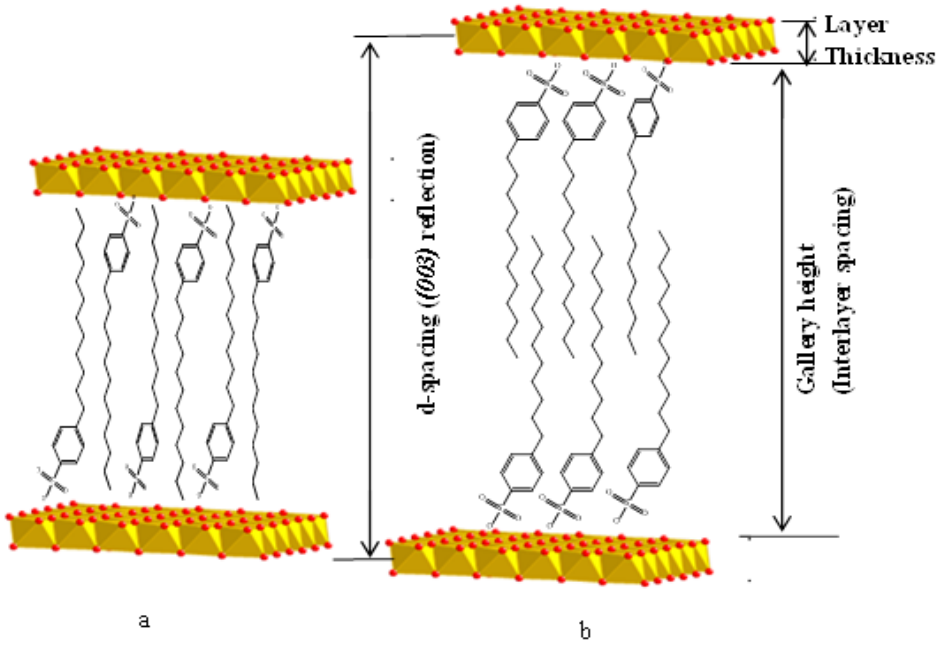

Fig.1.12: Schematic illustration of possible (a) Perpendicular monolayer and (b) bilayer orientations of SDBS within the interlayer of host hydrotalcite.

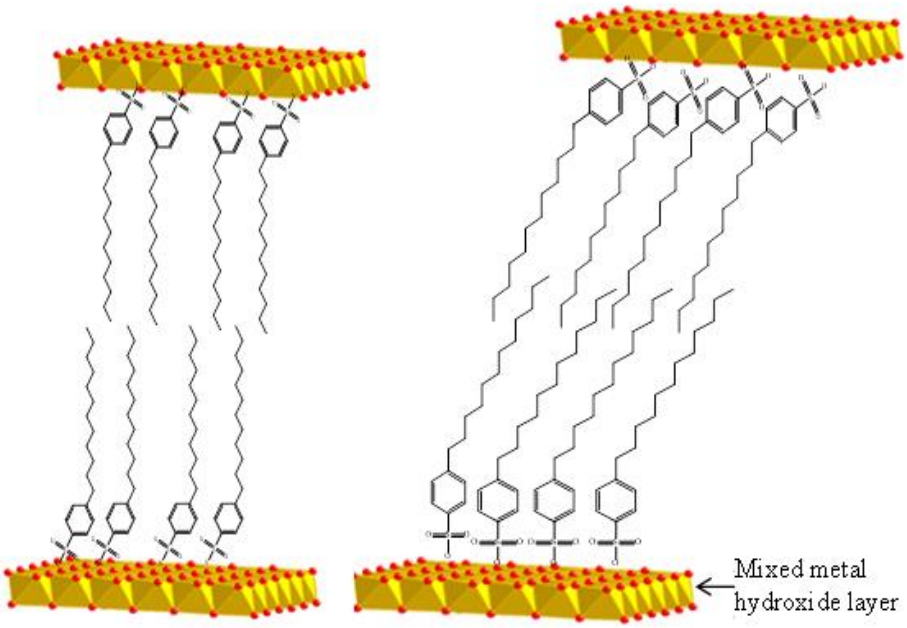

Fig.1.13: Schematic illustration of the arrangement of DBS between the brucite-like layers of organo-HTlc (Left) perpendicular bilayer and (right) tilted interpenetrating bilayer orientation

1.4 Stacking and Polytypism

Natural and synthetic hydrotalcites usually crystallise in two polymorphs (Fig.1.14); rhombohedral symmetry, one with a three layer repeat unit stacking sequence (where the unit cell parameters are *a* and *c* and *c* = 3*c*', polytype 3R) and hexagonal symmetry, one with a two-layer repeat stacking sequence (where the unit cell parameters are *a* and *c* and *c* = 2*c*', Polytype 2H). For natural hydrotalcites, *a* and *c* are reported to be 3.054 and 22.81Å respectively[49], with the value of *c*' being 7.60Å calculated from $d_{(003)}$ reflection[47]. The unit cell parameter *a* is the cation-cation distance within the cationic layer and the parameter *c* is the interlayer separation related to the total thickness of the hydroxide layer and the interlayer distance [50, 51, 52, 53]. These lattice parameters define the length of the edges of a unit cell and the angles between them.

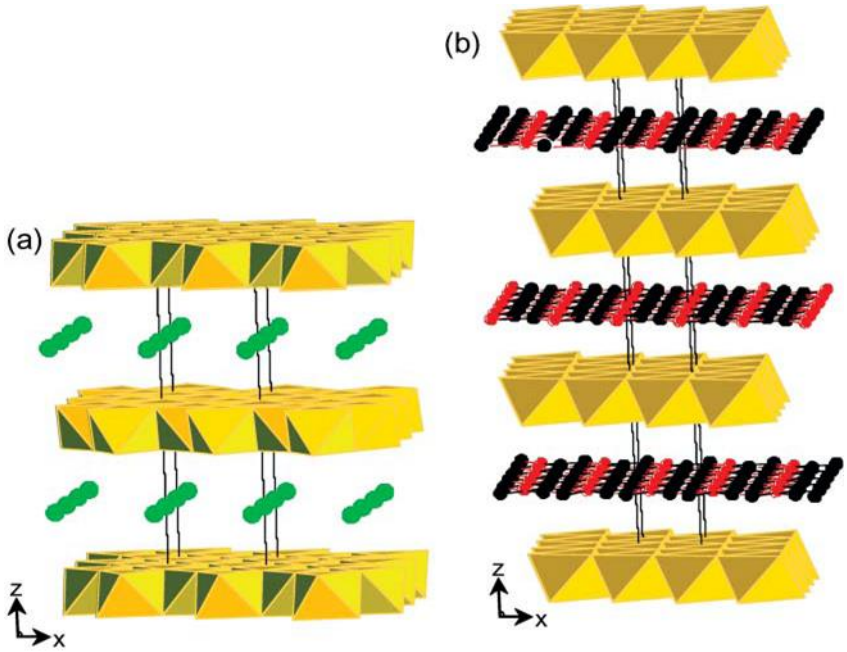

Fig.1.14: Showing the different stacking patterns of hydrotalcite (a) Hexagonal and (b) Rhombohedral [adapted from[54]]

A number of polytype structures can be obtained from the stacking of metal hydroxide layers in a variety of ways. For instance, a trigonal prismatic orientation of the interlayers can be obtained from the vertical arrangement of the OH groups above one another, while an offset placement of these aforementioned groups results in an octahedral orientation[53, 55]. The hexagonal polytype has three possible stacking orientation of layers denoted as $2H_1$, $2H_2$ and $2H_3$ in which the $2H_1$ has all prismatic interlayers, the $2H_2$ octahedral and the $2H_3$ has both the prismatic and octahedral interlayers. The rhombohedral symmetry on the other hand gives nine possible polytypes of which seven have hexagonal symmetries thus leaving only two($3R_1$ and $3R_2$) with the rhombohedral symmetry[55, 56, 57] Fig.1.15.

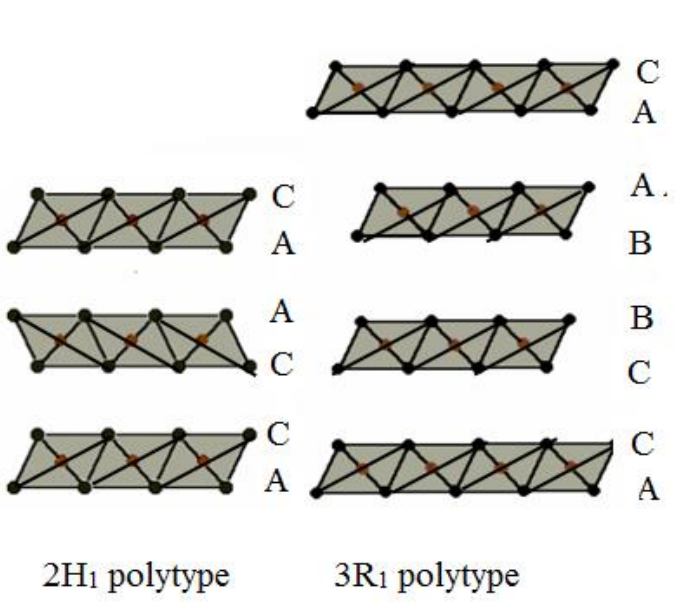

One layer

AC – AC – AC… 1H

Two layers

AC=CA=AC… $2H_1$

AC – AB – AC… $2H_2$

AC – BA=AC… $2H_3$

Three layers

AC=CB=BA=AC… $3R_1$

AC – BA – CB – AC… $3R_2$

And 7 others: $3H_{1.7}$

= stands for prismatic interlayer site while – for octahedral interlayer site.

Fig.1.15: Schematic representation of polymorphism in hydrotalcite (two-layer and 3-layer polytype)

1.5 Synthesis of hydrotalcites or Anionic Clays

There are various methods for synthesizing HTs or LDHs, and the choice of method is a function of composition required and properties of the compounds desired. Some of these methods are:

- Co-precipitation
- urea hydrolysis method
- Sol gel method
- Microwave irradiation method
- Combustion synthesis
- Steam activation,
- Solvothermal method.
- Structural reconstruction method after calcination
- Anion exchange of a precursor LDH method

The most commonly utilised methods are co-precipitation and urea hydrolysis methods and others; most relevant to our study are the reconstruction method after calcination and the anion exchange methods which are discussed in more details below

I.5.1 Co-precipitation method

This is the most widely used method for synthesising hydrotalcites (HTs) or layered double hydroxides (LDHs) due to its high reliability and reproducibility. Co-precipitation involves precipitating all cations in a controlled ratio or set by the starting solution and it involves adding steadily a solution containing the metal cations and

another base (usually sodium hydroxide solution with a solution of the guest anion) together at the same time to a reactor with stirring and regulated flow rate. This method was developed by Feitknecht in 1938[58], when he used dilute salt solutions to synthesise hydrotalcite or layered double hydroxide in the presence of a base. Usually, M^{2+} and M^{3+} hydroxides are nucleated and grown from an aqueous solution of the anion that is to be inserted into the hydrotalcite-like compounds (HTlc). The anions must have high affinity for the hydroxide layers to avoid contamination and the process is carried out at constant or increasing pH under low or high supersaturation condition. According to Ogawa and Kaiho[59], low supersaturation condition is preferred because it gives products that are more crystalline when compared to those from high supersaturation condition. After precipitation at the chosen supersaturation condition, ageing simultaneously with thermal treatment under pressure is carried out for periods ranging from hours to days [7, 42, 46]. When anions other than carbonate are the interlayer anions, vigorous stirring with nitrogen purging is a necessary condition and decarbonated ultrapure water is also an important factor. It is possible to synthesis a number of compounds that are similar to the natural hydrotalcite, ($Mg_6Al_2(OH)_{16}CO_3.4H_2O$) by this method and the method requires certain conditions to be controlled in order to obtain a pure product (HT/LDHs) of high quality, such as the pH of the resulting suspension, flow rate of bringing the two solutions together over time, stirring degree and temperature of the reaction process. To increase the yield and crystallinity of the poorly crystallised HT/LDH or amorphous materials which may form, hydrothermal treatment followed the reaction process and an inert atmosphere was required for HTs/LDHs other than carbonates to minimize or avoid competition from CO_3^{2-} resulting from atmospheric CO_2 contamination. There are two main types of co-precipitation

methods that can be used: precipitation at constant pH value and at variable pH value. In the former, the reaction system is maintained at the same pH throughout the preparation process giving rise to the co-precipitation of the two metal cations at low supersaturation[60] leading to pure intercalated hydrotalcites with good crystallinity. The guest anions are usually present in excess and have a high attraction to the HT/LDH layers. This is the method employed in this study. The variable pH method comprises of mixing the mixed metal salt solution with the base solution containing the guest anions under vigorous stirring producing a continuous change in pH value. The material formed at high saturation is relatively less crystalline than that synthesized at low supersaturation[24].

1.5.2 Urea hydrolysis method

This method involves treating the precipitated samples at moderate temperatures below and above 100°C for a few hours. It employs urea as the precipitating agent and the process proceeds slowly leading to low supersaturation during the precipitation process thus giving HTlc with well-defined hexagonal shape with carbonate as the interlayer anion plus a good degree of crystallinity. Though NaOH can be used to replace urea, the use of urea is better because of the aforementioned reasons. Urea is well known in gravimetric analysis where it is often used as a precipitating agent for a number of metal ions as hydroxides or as insoluble salts from homogeneous solution in the presence of suitable anion(s)[61]. The following mechanism was proposed by Costantino[62] for the hydrolysis of urea. Urea is a very weak Bronsted base with pK_b of 13.8 and is highly water soluble. Its controlled hydrolysis in aqueous solution yields ammonium cyanate or its ionic form (NH_4^+, NCO^-), and prolonged hydrolysis gives CO_2 in acidic medium or CO_3^{2-} in basic medium:

$$CO(NH_2)_2 \longrightarrow NH_4CNO$$

$$NH_4CNO + 2H_2O \longrightarrow (NH_4)_2CO_3 \text{ or}$$

$$NH_4CNO + 2H^+ + 2H_2O \longrightarrow 2NH_4^+ + H_2CO_3$$

Costantino and co-workers[62] used the urea hydrolysis procedure to prepare hydrotalcites of varying cations (Mg/Al, Zn/Al and Ni/Al) from their chloride precursors. They varied the urea/Al + Mg and Al/Al + Mg molar fraction in the solution, the temperature and time and they obtained different materials with different levels of crystallinity; and thus inferred that the best crystallinity could be obtained when the total metal ion concentration was 0.5 mol/dm^3 and molar fraction of urea/metal cation is 3.3 or 4.0. The control of the reaction temperature is another important factor which not only affects the crystallinity level but also the uniformity and particles size. According to Kustrowski and co-workers[63], larger particles are obtained at lower temperatures as a result of a lower nucleation rate and smaller and more uniform particles are produced at elevated temperatures. Rao et al.,[64] used this method to prepare MgAl hydrotalcite with a Mg/Al ratio of 1. They claimed that it was the first time this material was successfully synthesised, which could not be achieved by using conventional co-precipitation method where Mg /Al ratio is in the range of 2-5. Ogawa and coworker[59] used the urea hydrolysis method to synthesize hydrotalcite and studied the effect of temperature and concentration of reactants on the particle size. Their results showed that the particle size was controlled in the range of 2-20 μm by the reaction temperature and concentration of reactants. The morphology of hydrotalcite was retained even after the thermal decomposition had occurred. Similarly, Oh et al.,[65] observed that as the aging time increased and metal concentration decreased,

crystallinity of hydrotalcite increased, because the decomposition rate of urea in aqueous solution depends on temperature, the particle size distribution was controlled by altering the reaction temperature.

1.5.3 Structural reconstruction method after calcination

This method involves calcining the as-synthesised hydrotalcite-like compounds at a moderate (intermediate) temperature such that the host hydrotalcite-like compounds retain their memory (known as memory effect). This produces semi-amorphous mixed metal oxides which when reacted with/or exposed to aqueous solution containing the guest molecules or anions to be intercalated, reconstructs into the host hydrotalcite-like compound structure with intercalation of the guest anions or molecules[66-70]. This method is importantly useful for preparing both inorganic and organic anion-intercalated hydrotalcite-like compounds[71, 72, 73, 74, 75]. The selection of an appropriate temperature of calcination is dependent on the composition of the precursor hydrotalcite. Usually the hydrotalcite structure is easily generated when the calcination temperature is not too far from the temperature at which the hydrotalcite structure crumbles (usually $\leq 500^{o}C$). Above this, the products will transform to three-dimensionally ordered spinel phases which are not able to reconstruct to the hydrotalcite structure. Therefore a high temperature of calcination can irreparably damage the precursor hydrotalcite structure and destroy the memory effect. Carlino et al[76] recommend using a slow temperature ramping technique to control the rate of anion expulsion and water removal. On attempting to regenerate new hydrotalcite phases with different anions, an inert environment is necessary because of the ease of CO_2 contamination[77]. The extent of intercalation by use of this method depends on the reaction medium, the composition of the precursor host layers and the nature of the

guest anions. Several researchers have incorporated various guest anions into hydrotalcites by using this method[70, 73, 78, 79, 80, 81].

1.5.4 Anion Exchange method

This method is a direct utilisation of the anion exchange property of hydrotalcite and a wide range of different anions can be introduced through this method. Miyata et al[47, 82] derived a sequence of ease of exchange for simple inorganic anions which follows the order NO_3^- > Br^- > Cl^- > F^- > SO_4^{2-} > CO_3^{2-}. Generally, nitrate and chloride forms of hydrotalcites are selected as most suitable precursors for the preparation of organo-hydrotalcites, because nitrate and chloride anions are easily displaced from the gallery space, unlike the carbonate anion which is most difficult to exchange. The ion exchange method is based on the capacities of the interlayer anions and it is performed by simply dispersing the precursor host hydrotalcite-like compound in aqueous solution containing an excess of the guest anion that is to be incorporated. To retain the precursor host structure with the same M^{2+}/M^{3+} ratio maintained, the mixed metal hydroxide layer must be stable and the guest anion to be incorporated must also be stable at the pH of exchange[73, 74]. The height of the gallery expands upon incorporation of bulky or supra molecules such as oxometallate ions, DNA or long alkyl chain organic molecules. For more complicated anions like the polyoxometalates, the reaction process can proceed via an intermediate hydrotalcite possessing relatively simpler anions such as the terephthalate anion[83].

1.6 Application of Anionic clay (Hydrotalcite)

Hydrotalcites have the ability to act as host materials just like various other layered materials (e.g. 2:1 phyllosilicates, graphite, transition metal phosphates/phosphonates) through the incorporation of guest species into them to generate novel solids with physical and chemical properties that are desirable. In the last two decades, a wide range of potential technological applications has been made possible because of their unique intercalation properties[45, 84]. Hydrotalcites have been applied in different areas such as in ceramics, pottery/decoration, petroleum refining, medicine and cosmetics[85, 86], agriculture[87, 88], paper coatings/fillings, as adsorbents, catalysts/catalyst supports [22, 89, 90, 91], ion-exchangers[47], optical fibres, polymers, and remediation of polluted environments[92].

The crave for growth of technology and increased development to improve the quality of life has created an imbalance in the environment by way of increased hazardous and toxic wastes generated by industries into the environment. A high proportion of these wastes are recalcitrant toxic organic compounds and heavy metals. The increased amounts of these heavy metal ions and pernicious organic compounds (chlorinated and other synthetic organic chemicals) in our ecosystem have presented ultimate importance due to the virulent effect they pose to both man and animals. This concern has directed efforts towards developing effective treatment technology and/or effective and environmentally friendly scavengers for these generated wastes. Lately, different methods have been selected and employed to get rid of these contaminants from water and industrial wastewaters. Methods like precipitation, ion-exchange, conventional coagulation, reverse osmosis and adsorption have been adopted. The choice of method

to be adopted to treat water/wastewater depends on a number of factors such as the extent of pollution, the adsorption capacity and the efficiency/cost ratio of the method. Adsorption has been regarded as a most general and efficient method of environmental clean-up in regards to getting rid of hazardous heavy metals ions and organic compounds from industrial wastewater, aqueous solution and water.[93, 94, 95, 96]. Some factors are importantly considered when choosing sorbent type such as cost, availability, ease of regeneration or recovery, and environmental friendliness. The sorbent that has displayed considerably recorded success in this respect due to its high ability to uptake both metal ions and organic molecules, its high surface area, micro-porous structure and special reactivity[97], is activated carbon. However its use is limited by its high cost, intra-particle resistance in adsorption processes[98, 99] and the difficulty of recovery. Therefore, these drawbacks have limited its use, and so a lot of work has been driven towards obtaining new adsorbents that are cheap, can effectively remove these pollutants from the environment without posing any further threat on the environment. A lot of researchers have settled for substituting activated carbon with other adsorbents ranging from various agricultural by-products to clay minerals, zeolites and others [100, 101, 102, 103]. Hydrotalcite, a clay based material is a promising adsorbent. However, hydrotalcite in its natural form has low sorption attraction for organic compounds or NOCs/HOCs because of its hydrophilic nature[104, 105]. Intercalating organic anions like the surfactants into its interlayer can change its surface quality from hydrophilic to hydrophobic thus increasing its capacity to uptake organic molecules or pollutants. Previous studies[106- 109] have shown the potential of organically modified hydrotalcites to remove some contaminants or pollutants from water such as trichloroethylene and tetrachloroethylene[110], radioactive anion pollutants like TcO_4^-, ReO_4^- and I^-[111, 112],

heavy metals like chromates, selenate/selenite and phenolic compound like trichlorophenol (TCP)[110, 113, 114, 115], pesticide and herbicides. For instance, Mg_3-Al HT was modified by You et al[73] using sodium octylsulfate (SOS), sodium dodecylsulfate (SDS), sodium 4-octylbenzenesulfonate (SOBS), and sodium dodecylbenzenesulfonate (SDBS), following ion exchange method. The various organo-hydrotalcite-like compounds were used to adsorb the organic pollutants, 1,2,4-trichlorobenzene and 1,1,1-trichloroethane. Their results showed that all organo-HTs synthesised could adsorb the two organic pollutants within the concentration range studied and that adsorption was due to partitioning with uptake affinity greatly influenced by the surfactant type. Zhao and Nagy[116] used organo-LDH (SDBS modified HT) and the parent or original LDH to remove TCE and PCE from water. They reported that the adsorption ability of the organo-LDH for the two organic compounds was considerably higher than for the original LDH materials. They also attributed the adsorption to a partition mechanism. Dekany et al 1997 also agree that intercalating organic anions into the gallery of hydrotalcite or LDH is capable of changing the surface properties thereby increasing their sorption ability for non-ionic contaminants. Dekany[117] and co-workers synthesised calcium aluminium LDH ($[Ca_2Al(OH)_2]NO_3.2H_2O$), modified it with SDS and SDBS and the internal and external surface area were hydrophobised causing the adsorption capacity toward organic liquids (propanol and toluene) to increase strongly with preferential adsorption of propanol by the dodecylbenzenesulfonate derivative. While on the contrary, the dodecylsulfate derivative adsorbed propanol and toluene in slightly different amounts. Esumi and Yamamoto[118] studied the sorption of 2-Naphthol using SDS-hydrotalcite and reported that 2-naphthol is effectively sorbed into the gallery of the hydrotalcite. They also said that at low SDS concentration, the amount of

2-naphthol adsorbed increased substantially, but decreased slowly with SDS concentration. Bruna et al[119], observed that the adsorption capacities of different organo-hydrotalcites depends on their structure, nature and the polarity of the pollutant to be sorbed. The pollution by organic compounds is becoming an ever increasing concern globally. This is because the majority of these compounds are toxic, particularly those associated with wastewater generated from industrial sectors like the timber industries, petroleum, petrochemical, pesticide, dye, plastic and refineries. For instance, high exposure to phenol and chlororphenol can commonly affect vital organs like the kidney, liver, eyes, skin and central nervous system. Therefore US Environmental Protection Agency (EPA), European Environmental Agency (EEA) and World Health Organisation (WHO) have listed phenol and chlororphenol as priority pollutants. The US Environmental Protection Agency (USEPA) has set the allowable limit at 1.0mg/l. In this study, organo-hydrotalcites of MgAl and ZnAl as adsorbents of phenol and chlorophenol were prepared. Sodium dodecylsulfate (SDS) and sodium dodecylbenzenesulfonate (SDBS) were selected as the guest species. A study of the changes in surface properties of these MgAl and ZnAl organo-hydrotalcites and the configuration of SDS and SDBS in the interlayer is required. Hence the relevance of this research as its overall objective was to examine the synthesis and characterisation of this clay base sorbent, its selectivity to phenol/derivatives from water, because understanding its structure and properties is essential for its application in environmental management.

1.7 Aim and Objectives

The aim of this research is to develop clay-based materials for environmental management in pollution control and wastewater treatment, and investigate their use as sorbents for the removal of organic pollutants from industrial effluents and water. Our key focus was to study the different alkylsulfate and akylsulsulfonate exchange clays, to tune the hydrophobic/hydrophilic properties within the galleries and to optimise the adsorption properties, for phenol and chlorophenol.

1.8 Specific objectives of the research

The specific objectives of this study were;

- The preparation of anionic clay hosts – hydrotalcites by co-precipitation and urea hydrolysis methods
- The modification with alkylsulfate/alkylsulfonate anions
- Physicochemical characterization of host hydrotalcites and derivative organo-hydrotalcites.
- To study the adsorption of phenol and chlorophenol by these organo-hydrotalcites adsorbents to investigate pH and time of adsorption on the properties.

CHAPTER TWO

CHARACTERISATION TECHNIQUES

2.1 Introduction

This chapter describes the range of techniques used in this study to characterise the synthesised and modified hydrotalcites in order to have reliable data with which to describe our synthesised hydrotalcites and to compare them with other laboratory-made or commercial hydrotalcites. X-ray diffraction was used throughout our study while FT-IR was also used to establish whether our synthesised hydrotalcites were modified by intercalation of organic anions into the interlayers, replacing the initial inorganic anions. Other techniques employed in this study include TGA, XRF, SEM and BET SA.

2.2 X-Ray Diffraction (XRD)

X-ray powder diffraction is a non-destructive rapid analytical technique suited for the characterization and identification of materials. It is used for phase identification and to obtain information about the chemical composition and crystallographic structure. The XRD pattern of a pure substance is a fingerprint of that substance and it is unique to that substance. Usually, the same substance will always have the same pattern and in a mixture of substances each substance gives its own pattern independent of the others.

2.2.1 Boundary behaviour of waves

When a series of waves strikes an obstacle, for example, a boundary surface between two different media, several phenomena are observed. As the wave hits the boundary surface, part of it is reflected within the incident medium and part is transmitted into the second medium. The angle which the incident wave makes with the normal to the

boundary surface is equal to the angle between the reflected wave and the normal. Due to the differences in the wave speed in the second medium, the transmitted wave is weakened and refraction occurs. Diffraction involves a change in direction of waves as they pass through an opening or around a barrier in their path. The extent of diffraction depends on the magnitude of the wavelength of the wave front relative to the size of the barrier encountered. The amount of diffraction (the sharpness of the bending) increases with increasing wavelength and decreases with decreasing wavelength. In fact, when the wavelength of the waves is smaller than the obstacle, no noticeable diffraction occurs. If two waves pass through the same region of space (travelling along the same medium), they combine by a process called superposition. The superposition principle is that the resultant wave formed by the simultaneous influence of two or more waves is the vector sum of the displacements due to each wave acting independently. The waves are in phase with each other if they interfere constructively with a resultant gain in intensity due to displacement in the same direction as the two interfering waves combine. Destructive interference occurs at any location along the medium where the two interfering waves give a translational displacement in opposite direction. They do not combine, so their addition produces a resultant wave with a zero phase difference. The waves are completely out of phase with each other. The phase difference of interfering waves from coherent source is often due to a difference in path length as the waves are diffracted by a barrier.

2.2.2 Principle of Powder X-ray Diffraction (XRD)

X-rays are highly penetrating electromagnetic waves. The principle of X-ray diffraction is based on constructive interference of monochromatic radiation from diffraction from a crystalline material. As for all electromagnetic waves, X-rays diffract when they meet

a barrier and exhibit interference when two or more of them meet at the same point. Powder X-ray diffraction studies the pattern of scattered radiation from crystalline materials when they are bombarded with X-ray radiation. These X-rays are generated by an X-ray tube and by a single crystal monochromator are converted to monochromatic (single wavelength) X-rays which are impinged on the crystalline material. Basically the crystalline material is a three-dimensional structure composed of regular repeating planes of atoms that form the crystal structure. XRD studies the interaction of X-rays and this crystalline material and what happens (effects produced) during this interaction. Information obtained can be used to identify and characterise, or determine the crystal structure of the material or rough check the purity of the material.

2.2.2.1 Generation of X-rays

X-rays are high energy electromagnetic waves with short wavelength (0.1 - 100Å)[120] and high frequencies (10^{16} - 10^{20} Hz)[121]. They are found between gamma-rays and the ultraviolet rays in the electromagnetic spectrum. They were discovered by the German physicist, Wilhelm Röntgen in 1895. These X-rays can be produced in an X-ray tube (Fig.2.1) e.g. a cathode ray tube. For XRD, single wavelength or a narrow range of wavelengths (monochromatic radiation) are desired, therefore, a filter is usually necessary to remove the K_β line and the white radiation, so that the K_α line is selected. A monochromator (single crystal) is used which utilises the Braggs Law to select the single wavelength. Filters are made of metal foil of element with atomic number one below that of the metal target. Once this single wavelength is selected, it is collimated and is directed to interact with the sample. An X-ray tube consists of an evacuated chamber with a tungsten filament at one end of the tube known as the cathode, and a metal target at the other end called the anode. Electricity is run through the tungsten

filament causing it to emit electrons which are accelerated due to a high potential difference (20 - 50kV) maintained between the anode and cathode. This generates currents between 10 - 50mA in the tube[122]. The high velocity electrons are allowed to strike the metal target (often Cu fixed to the anode) which is cooled with water. As these high energy accelerated electrons continuously bombard the metal anode, they are decelerated by the metal target due to collision with the electrons of the target producing a broad continuous spectrum of X-rays known as background or white radiation (originally called bremstrahlung meaning breaking radiation). Upon this background intense and sharp peaks (K_α and K_β) are superimposed. The collision of these high energy electrons and the electrons of the anode generates X-rays (quantized transition) perpendicular to the path of the electron beam which exit through the beryllium windows. Only a fraction of the generated energy is released as X-rays while the remaining energy is released as heat, hence the need to continuously chill the anode with cold water to avoid meltdown of the target[120]. There are two types of X-rays tubes, namely, sealed and rotating anode tube. The former comprises of an anode coupled with cathode housed in a metal/ceramic or metal/glass envelope. The rotating anode tube on the other hand is designed to improve the X-ray tube input power. It consists of a massive disk-shaped anode which rotates continuously at a high speed while also being constantly chilled with cold water.

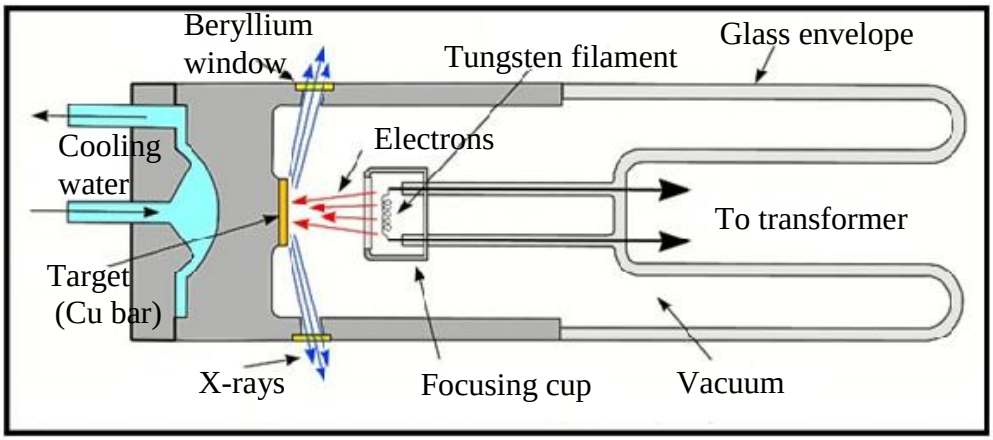

Fig.2.1: Schematic design of a typical X-ray tube Adapted from[12 1]

The spectra of X-rays emitted by the anode in the X-ray tube is composed of two components as mentioned earlier; the broad continuous spectrum of wavelengths (white radiation caused by energy loss of X-rays as they enter the metal) and a series of sharp peaks (Fig.2.2). For X-ray diffraction analysis applications, a monochromatic beam of X-rays is most desirable. The white radiation or continuous spectra is composed of a range of wavelengths of X-rays with minimum wavelengths and intensity (measured in counts/sec) and depend only on the target metal and accelerating voltage of the X-ray tube. The second type, the X-rays produced from electron transition within the atoms of the target metal (anode), possess wavelengths characteristic of the target metal. In order to generate this characteristic monochromatic X-rays for XRD, the bombarding electrons must possess sufficient energy to initiate ionisation of the target metal. Therefore a sufficiently high accelerating voltage ($\geq$ 10kV) is required to accelerate the electrons[122]. Meeting this requirement results in core electrons of the atom of the target metal being knocked out and the X-rays which are element specific or characteristic of the metal target are produced by decay. Whenever a core electron makes a transition

from their lowest energy level (K shell or n=1 state) to an unoccupied energy level a vacancy is left in the K shell. Electrons in the L shell (n=2) or the M shell (n=3) immediately descends to occupy the vacant K shell, simultaneously releasing electromagnetic radiation with energy of several keV (characteristic X-rays of the anode metal). Transitions from the L shell gives the K_α lines and transitions from the M shell gives the K_β lines. These lines are closely spaced doublets and are actually unresolved.

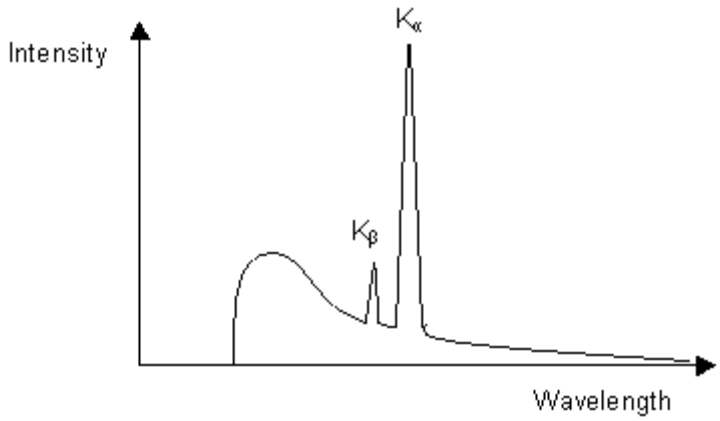

Fig.2.2: Characteristic X-ray emission spectrum

For instance, for Cu target, the K_α line consists of two lines corresponding to $K_{\alpha1}$ (λ=1.54051Å) and $K_{\alpha2}$ (λ=1.54433Å) produced from two L to K transitions with $K\alpha_1$ having a slightly shorter wavelength and twice the intensity of $K_{\alpha2}$ because of the spin multiplicity of the 2p electrons that make the transition[122, 123]. In some XRD experiments, particularly in powder diffractometry at low angle, diffraction by the two Kα radiations are not resolved so a single peak is shown instead of a doublet. However several diffraction peaks may be seen in other experiments and this can be overcome by removing the weaker beam from the incident radiation [122]. Some commonly used target metals are Cr, Fe, Cu, Mo and Ag. A beryllium window is created in the tube (Be is

transparent to X-rays and has low atomic number) to allow the X-ray beams to escape from the tube to provide information on the internal arrangement of atoms in the crystal on which the beam of X-rays are impinged.

2.2.2.2 Bragg's Law

Diffraction of waves by objects produce scattered radiation giving a pattern of intensity maxima and minima. W.H and W.L Bragg proposed a model which describes how X-ray diffraction (XRD) can be used as a means of structure determination. This model regards the crystal structure as consisting of an orderly arrangement of atoms built up in layers or planes such that each acts as a semi-transparent mirror that can reflect waves. Therefore the Bragg equation treats diffracted X-rays as reflections from planes of atoms within the crystal lattice. However only at specific orientation of the crystal with respect to the source and detector are X-rays reflected from the planes. With XRD, reflection only occurs when the conditions for constructive interference are satisfied. A simple set of three integers (Miller indices) denoted *hkl* can be used to describe a plane surface within a crystal. Miller indices can be determined by considering two parallel planes, one of which encloses a point taken to be the origin of the unit cell. The x, y and z vectors originating from this origin will at some point be cut by the other plane, and these intercepts are some fraction of the unit cell dimension, a, b and c. Therefore the Miller indices that describe such planes can be calculated as follows:

$$h = \frac{a}{x} \qquad (2.1)$$

$$k = \frac{b}{y} \qquad (2.2)$$

$$l = \frac{c}{z} \qquad (2.3)$$

Thus the Miller indices of a plane are determined by the reciprocal on the intercept made on the axis by the plane nearest the origin[124]. The spacing between parallel planes described by Miller indices (*hkl*) is the d- spacing and is denoted as d_{hkl}. Accordingly, the d-spacing between a set of planes (*hkl*) within an orthogonal crystal with lattice parameters a, b and c is given by:

$$\frac{1}{dhkl^2} = \frac{h^2}{a^2} + \frac{k}{b^2}^2 + \frac{l^2}{c^2} \qquad (2.4)$$

Following from the above, Bragg conditions for X-ray diffraction can easily be derived by considering two parallel X-rays incident at an angle θ upon parallel planes of atoms as illustrated in figure 2.3.

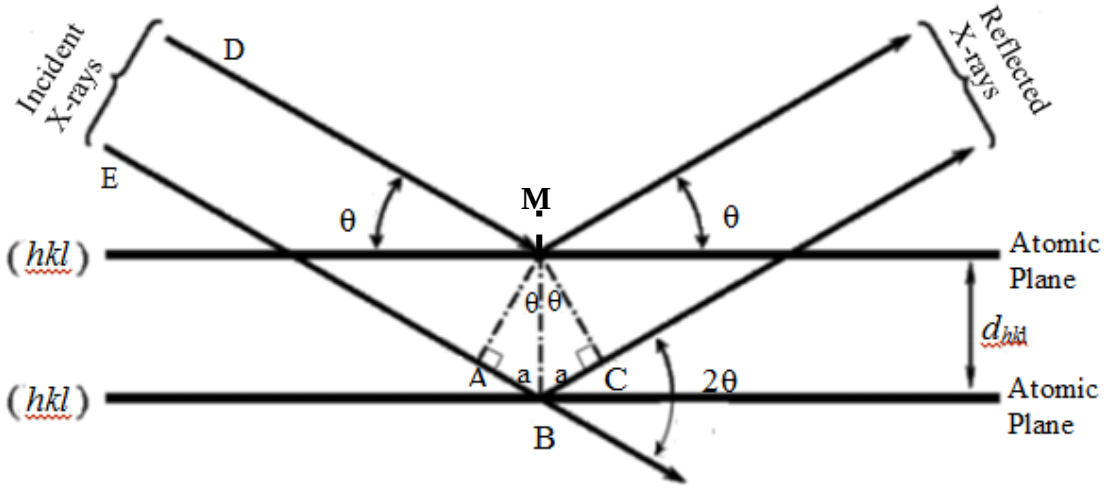

Fig.2.3: Schematic diagram of Bragg's Law

The atoms in the crystal interact with the X-ray waves and produces interference. When the beam of monochromatic rays hit the sample, ray D is reflected off the upper atomic plane at an angle θ equal to its angle of incidence. Ray E reflects off the lower atomic plane at the same angle θ after penetrating the crystal and travelling a further distance a,

than ray D. If this distance a is equal to an integer number of wavelengths (nλ), then rays D and E are in phase as they exit from the crystal and constructive interference occurs and a single beam of reasonable intensity emerges. On the other hand, if the distance a, is not an integer number of wavelengths, then destructive interference will occur and the waves that enter the crystal will not be strong enough. Based upon this therefore, the condition for constructive interference to occur is $n\lambda = 2a$. This means that the path lengths of the interfering beams differ by an integral number of wavelengths nλ. So following the spacing between atomic planes and from trigonometry

$$a = d_{hkl} \sin\theta \qquad (2.5)$$

The difference in path length between the two beams (D and E), if AB and BC are drawn at right angles to the beam is equal to 2a (a + a).

Thus,

$$2a = 2d_{(hkl)} \sin\theta \qquad (2.6)$$

Since $n\lambda = 2a$

$$\text{Then } n\lambda = 2d_{hkl} \sin\theta \qquad (2.7)$$

This is known as Bragg's equation[124, 125]. It relates the spacing between crystal planes $d(hkl)$ to the Bragg angle θ_{hkl} at which reflection from the atomic planes are observed. Diffraction only occurs if the rays are in phase when they emerge and such will occur at appropriate values of n (1, 2, 3, 4 etc) and θ. The integer n is the order of reflection and most often takes the value of 1 (n = 1). Intensity peaks are detected for all different values of 2θ depending on the symmetry of the crystal under investigation because all X-rays detected are a direct result of the interference of incident X-rays reflected from

different planes. The XRD pattern observed for a crystal has direct relationship with the size and symmetry of the crystal and is quite characteristic[120, 126]. Generally, crystals with high symmetry (e.g. isometric system) tend to have relatively few peaks, whereas crystals with low symmetry tend to have a large number of possible peaks in the XRD pattern.

2.2.3 Powder X-ray diffraction

X-ray powder diffraction (XRD) is a non-destructive analytical technique commonly employed to identify the phases of a crystalline substance. It provides information on unit cell dimensions, chemical composition; crystallisation and microstructure of materials. The techniques were developed by Debye and Scherrer and separately by Hull in 1914-1919[124]. The sample to be analysed is finely ground and homogenised, the composition of the average bulk is determined by placing the sample into a plastic circular holder, pressed down with a transparent tape or glass slide (in order to obtain a random arrangement of crystal) and then mounted into the diffractometer. The principle behind the design of powder diffraction experiments is the random orientation of crystals in the powdered sample. Because the sample powdered crystals are randomly oriented, all sets of the planes (*hkl*) in the powder are in the correct orientation (usually horizontal) with respect to the X-ray source to satisfy Bragg's law for the θ angle. The more finely ground the powder, the more likely that all orientations are present in abundance. The D8 diffractometer used in this study moves both the X-ray source and the detector through arcs of θ values (Fig.2.4) and sends the periodic signals which is proportional to the average diffracted X-ray intensity to the computer providing the intensities for diffracted beams as a function of the diffraction angle θ (or 2θ). If a

sample is of an already known phase, this can often be identified from the powder diffraction data using the ICDD. Both intensity and 2θ or (hkl) values are required for a search which could lead to unique match with a known powder diffraction pattern. Where the observed diffraction data does not exactly match the standard data for a given sample, then identification becomes more challenging, Therefore additional information based on chemical data and physical property is needed to confirm results for the sample.

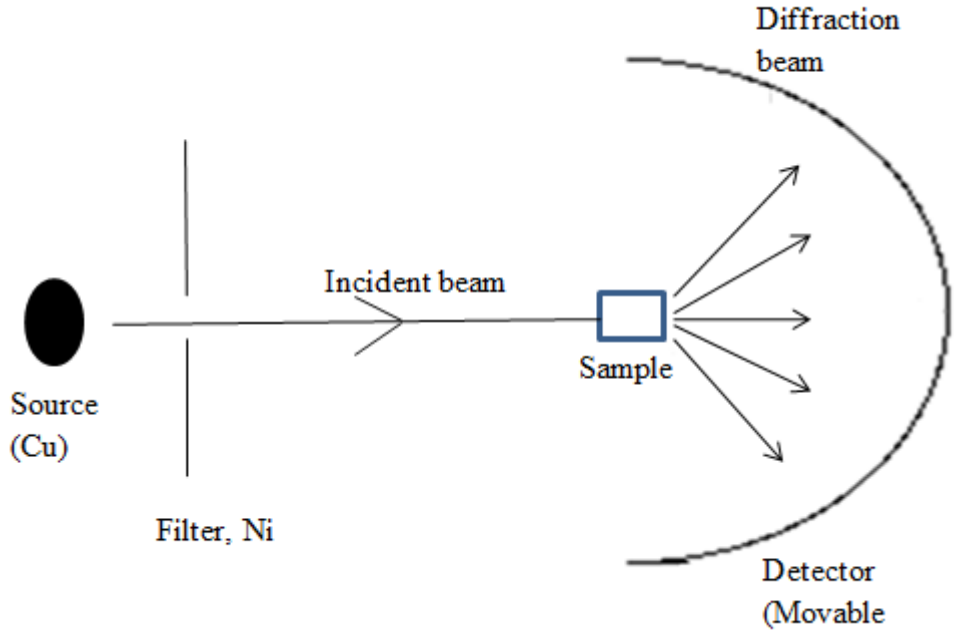

Fig 2.4: Simple sketch of X-ray source (X-ray tube), the X-ray detector, and the sample during an X-ray scan. The X-ray tube and the detector both move through the angle theta (θ), continues diffraction arc (cones) derived from scattering from the sample (crystalline material) and the sample remains stationary.

2.2.4 Instrumentation of Powder X-ray Diffraction

X-ray diffractometers can perform in both reflection and transmission geometries. Sample preparation is the same in both operations. It always tends towards getting samples which contains a random arrangement of crystal orientations. If this is not the

case, then preferred orientation exists and this can introduce errors into the measured intensities. In this study, all room temperature powder XRD data were collected with Bruker D8 ADVANCE X-ray diffractometer operating in 2Theta transmission geometry with Cu $K\alpha_1$ radiation ($\lambda_{CuK\alpha_1}$ = 1.54056 Å) equipped with a Lynx-Eye PSD detector. Data were collected using a step size of 0.02° and time of detection of 65.8s for routine characterization and identification of materials. The 2θ range is from 5° to 80°. Variable temperature powder XRD data were collected using Bruker D8 ADVANCE X-ray diffractometer operating in reflection mode. Some data were also collected with the D5005 diffractometer operating in reflection mode from 2θ of 1° to 70°, using a step size of 0.014746° for 30mins.

2.3 X-Ray Fluorescence Spectroscopy

2.3.1 X-Ray Fluorescence Spectroscopy

X-Ray Fluorescence (XRF) is a non-destructive analytical technique used for qualitative and quantitative elemental analysis of a sample with a different number of elements. It is used for the identification and characterisation of materials because it enables the determination of concentrations of elements present in a sample which could be solid, powder, or liquid. This technique works on a wavelength dispersive spectroscopic principle and can identify elements with atomic number greater than 8 within a sample by comparing the peak intensities at the appropriate wavelengths with a calibration chart that enables quantitative analysis of constituent elements of a sample to be performed[122].

2.3.2 Principle of X-ray fluorescence

X-ray fluorescence is an emission technique that is a consequence of changes that take place within an atom as a result of the interaction with a high energy X-ray source. When substances are impinged with high energy, short wavelength radiation like X-rays, their atoms get ionised and if the radiation is high enough to remove a core electron (K shell electron) that is most tightly held to the element of the substance, it becomes unstable; therefore to restore equilibrium an outer electron (L shell electron) quickly jumps in to fill the void created. The difference in energy produced as the electron moves between these energy levels is released as secondary X-rays (Fig.2.5) which is characteristic of the element resulting in a characteristic X-ray emission spectrum.

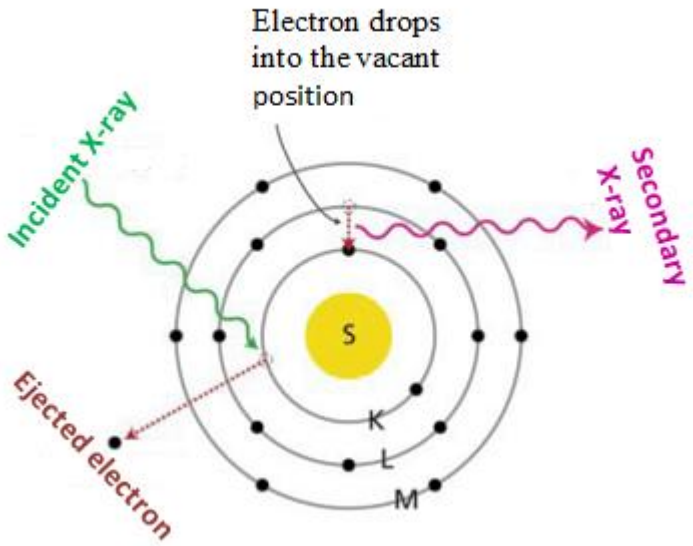

Fig.2.5: Diagram showing source of fluorescence

The emitted radiation is of lower energy than the primary incident X-rays and is termed fluorescent radiation. The outer shell electron is bound to the atom of the element with

lesser energy than the innermost shell electron, so when the outer shell electron moves in to fill the inner shell vacancy created. The energy difference is accounted for by the energy of the emitted X-ray. The elements present in the substance can be identified by locating the energy peaks of these emitted X-rays along the horizontal axis (qualitative analysis). Because the energy of the emitted photon is characteristic of a transition between specific electronic orbitals in a particular element, the resulting fluorescent X-rays can be used to detect the abundances of elements that are present in the sample. Since in theory, the number of X-rays produced is proportional to the number of atoms present in a sample, then from the net intensities of the energy peaks, quantitative elemental concentrations can be determined. In this study, XRF was used to confirm the mole ratios of the divalent/trivalent cations and to confirm the consistency of stoichiometry of the modified hydrotalcites to the synthesised host hydrotalcites.

2.3.3 Sample preparation

This is simple, fast and reproducible if appropriate standards are available. Usually samples are prepared as solid disks (ceramics and hard alloys) or fused beads (light element analysis as in clay minerals) or as loose powder or pressed pellets. The basic necessity here is that a homogeneous sample with a scratch free, flat smooth surface is desired and care must be taken to avoid introducing inter-element interferences, matrix interferences and particle size effects.

2.3.4 Instrumentation

A typical XRF spectrometer is composed of the following major components:

- X-rays Source, used to irradiate the sample.

- The Sample.
- The detector to detect the emitted fluorescent X-rays.

The XRF spectrum obtained displays intensity of X-rays (usually in counts per second) as a function of energy (usually in eV). There are basically two types of XRF spectroscopy. Energy Dispersive XRF (EDXRF) and Wavelength Dispersive XRF (WDXRF), which differ primarily in the way the fluorescent X-rays, are detected and analysed. The type employed in this study is the Energy Dispersive XRF. This type of XRF spectroscopic system directly records the different energies of the emitted X-rays from the sample. It generates an XRF spectrum by counting and plotting the relative numbers of X-rays at various energies. On the other hand, the wavelength dispersive detection system remarkably distributes the X-rays according to their wavelengths. The X-rays are guided to a crystal, which break up or bend the X-rays in diverse directions according to their wavelengths (energies). On a regular successive system, a detector is placed at a fixed position, and the crystal is rotated so that different wavelengths are picked up by the detector. The XRF spectrum is built up point by point. In a simultaneous system, a number of crystal/detector units are used, such that a range of elements can be detected at the same time.

2.4 Thermal Analysis

2.4.1 Thermal gravimetric analysis (TGA)

Thermogravimetric analysis is a technique used to characterise materials that exhibit weight loss or gain due to decomposition, oxidation or dehydration. It measures the properties of the solids, such as weight change or absorption (or evolution) of heat with

respect to temperature or time under controlled atmosphere. A TGA measurement can be used to determine the composition of materials and also to predict their thermal stability at temperatures up to 1200°C. TGA can provide information on oxidative stability of materials, decomposition kinetics of materials, composition of multicomponent systems, and estimated lifetime of a product, the effect of reactive or corrosive atmospheres on materials, and the moisture and volatiles content of materials among others. Thermogravimetric curves, characteristic of the materials under study are generated based on chemical composition and structure of the material and the physicochemical changes occurring over specific temperature ranges and heating rates. The instrument is composed of a high precision balance with two platinum crucibles, one to load the sample and the other as reference. The crucibles are positioned in a small electrically heated oven containing a thermocouple located in the furnace chamber. Prior to analysis, the chamber is purged with an inert gas (nitrogen referred to as the purge gas) to avoid contamination from oxidation or other undesirable reactions that may possibly occur within the furnace chamber. Several instruments/devices may be combined with this TGA instrument in order to analyse the composition of species evolved from the material as it is heated over time or temperature under controlled atmosphere. When TGA is used in combination with other devices such as a mass spectrometer (TGA-MS), infrared spectrometer (TGA-FT-IR), and gas chromatograph (TGA-GC) or gas chromatograph/ mass spectrometer (TGA-GC-MS), detailed analysis of the evolved gas products are possible. All TGA data presented in this study were obtained on a Netzsch STA 449 FI Jupiter® apparatus, connected to a quadrupole mass spectrometer, Netzsch QMS 403 Aëolus® (TGA-MS) (Fig.2.6).

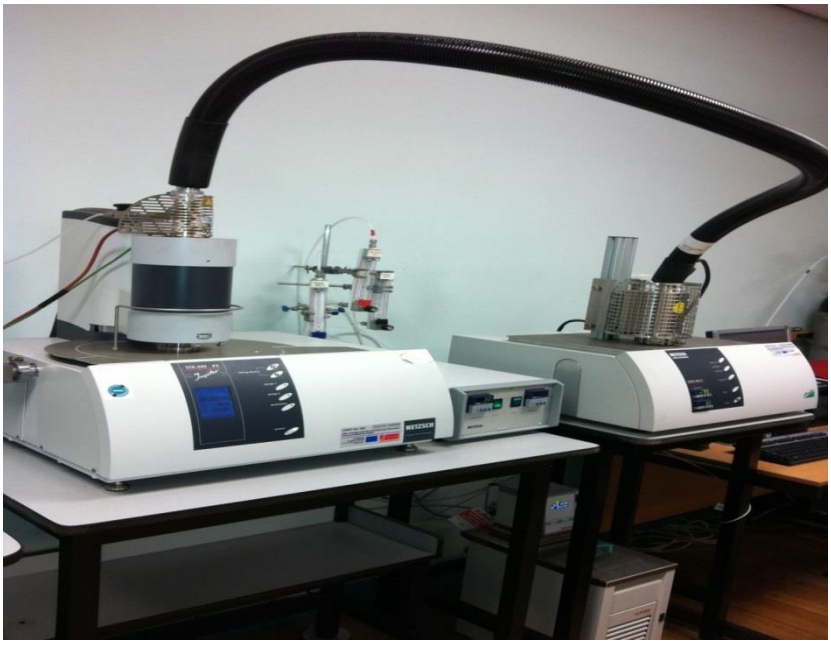

Fig.2.6: TGA-MS Instrument

2.4.2 Differential Thermal Analysis (DTA)

Differential thermal analysis (DTA) is a technique that measures the difference in temperature between a sample and a control material that remains inert upon heating and cooling. This technique is useful for determining phase changes. Plotting the differential temperature against temperature or time depicts peaks which show clear endotherms and exotherms where changes in phases occur thereby providing information on the nature of transformations taking place as well as the temperature ranges over which these phase changes happen. The instrument is composed of a sample holder which consists of thermocouples, sample and a temperature programmer.

2.5 Scanning Electron Microscopy (SEM)

2.5.1 Electron Microscopy

The topology, morphology and composition of a solid material can be studied using electron microscopy. It can also be used to obtain information on the composition and arrangement of atoms in a material. Electron Microscopy is a technique that uses a beam of highly energetic electrons to investigate the material with the resolution ranging from the micrometer scale down to the atomic scale[127]. When a material is exposed to an electron beam, several processes are induced or prompted due to the interaction of the primary electrons and the studied material. When atoms are bombarded with electrons, depending on the incident energy of the electron beam, some of the electrons can simply backscatter or collide inelastically and transfer their energy to secondary electrons while others pass through the material with or without experiencing energy loss.

2.5.2 Scanning Electron Microscopy (SEM)

In scanning electron microscopy (SEM), a focused beam of high energy electrons is used to generate a series of signals at the surface of the material investigated (solid sample). The signals obtained from the interactions between the electron beam and the sample discloses relevant information about the sample external morphology (texture), chemical composition and crystalline structure and orientation of components that make up the sample. The image of a sample is thus obtained by scanning it in a raster pattern[127]. In this study, a Philips XL 30 Scanning Electron Microscope (XL 30 ESEM-FEG) equipped with a LaB_6 emission source was used to study the external

morphology of synthesised parent hydrotalcites and their hybrids after modification. The XL 30 ESEM-FEG was used because of its ability to examine the natural state of materials without prior complicated sample preparation or modification.

2.5.3 Basic Principles of SEM

The sample is irradiated by a beam of electrons and interactions occur inside the irradiated sample having effects on the electron beam. These interactions and effects are detected and transformed into an image. Streams of electron are generated at the gun, accelerating towards the sample to illuminate it and, depending on the incident energy of these electrons, they are scattered in a variety of signals (elastic and inelastic scattering) due to interaction between the sample and these impinging electrons (electron-sample-interaction). Some of the accelerating electrons can pass through the sample without interaction. The signals (Fig.2.7) that are obtained from the sample-electron-interactions disclose textural information, and information about the chemical composition (EDS), crystalline structure and orientation of the material components. EDSD). The best imaging resolution is obtained from Auger and Secondary electrons (SE) due to the electron interaction volume (the different depths within the sample at which each of the electron emission generation develops after the high energy beam has impinged on the sample). Auger and SE have the smallest volume near the surface of the sample while backscattered electrons (BSE) are generated over a large volume thus producing images of intermediate resolution. Each signal has different imaging and analytical resolution. In essence, SEM works by using an electron beam to trace over the indentation of a sample and produce a replica image. The microscope controls the movement of electron beams with scanning coils that create magnetic field using

alternative voltage. It manipulates the electron beams, moving them back and forth over a defined area of the sample (magnification) producing clear SEM images.

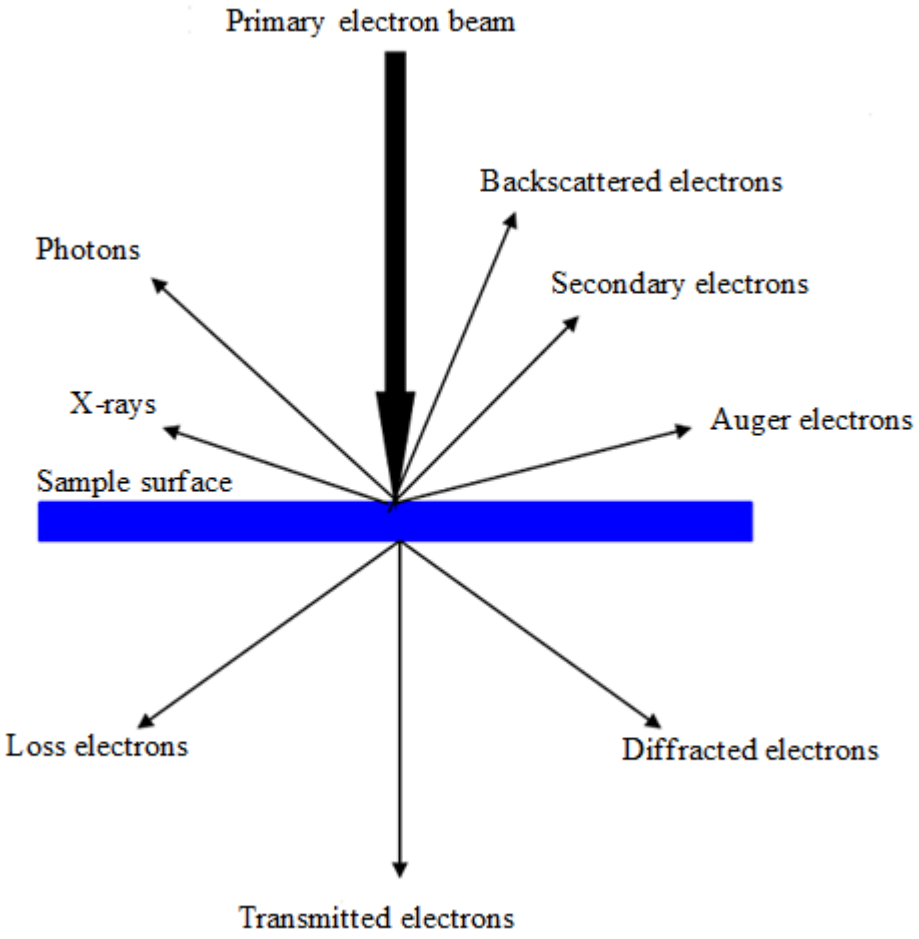

Fig.2.7 Interaction between primary electrons and the sample

2.5.4 Instrumentation

SEM consists of the following important components:

- Electron source, the gun: This is where the steady stream of electrons, required by SEM to operate, is produced. It is of two typical types, namely thermionic gun and field emission gun. The former is the most common type and it applies

thermal energy to a filament, made of tungsten, to pull electrons away from the gun towards the sample being investigated. A strong electric field is formed by the latter to induce a force capable of pulling electrons away from the atoms of the sample they are associated with. Usually electron guns are located either at the top or bottom of the microscope and instigate a beam of electrons at the sample.

- Electron lenses: Just like an optical microscope, SEM uses lenses, in this case made of magnets to produce clear and detailed images. They are capable of bending the path of the electrons to get them focused thereby controlling the electron beam and directing them where they ought to be at any point in time.
- Sample chamber: This is the sample holder and it is usually sturdy and well insulated from vibration to enable it to keep the sample still so that clear images can be obtained.
- Detectors: These devices detect the various ways that the sample and electron beams interacts (eye of the microscope). Some detectors record secondary electrons (electrons ejected from the outer surface of the samples). These detectors are able to provide the most detailed images of the sample surfaces. Other detectors like the backscattered electron detectors and X-ray detectors produce information about the composition of the sample investigated.
- Vacuum chamber: Every scanning electron microscope needs a vacuum chamber to operate, because without a vacuum, the beam of electrons generated by the electron gun would experience constant interferences from air particles in the atmosphere thereby blocking the path of electron beam, and air could also be swept onto the sample thus distorting the surface.

2.5.5 Sample preparation

A Scanning Electron Microscope operates in a vacuum and relies on an electric field for operation so sample surfaces must be kept clean to prevent build-up of surface charges. Most often, the sample (particularly for conducting samples) is coated with gold or platinum through sputter coating to prevent sample damage due to the electron beam and also to prevent build-up charges.

2.6 Fourier Transform Infrared spectroscopy (FT-IR)

FT-IR spectroscopy is a non-destructive and reliable analytical technique (qualitative and quantitative) used for the identification of materials. It is a very useful technique for the determination of the presence or absence of a range of functional groups in a material. When infrared radiation is allowed to pass through a material or sample, some of the radiation is absorbed by the sample while some passes through the sample (transmission). Based on the molecular absorption and transformations that occur within the sample, an absorption spectrum is produced which contains information about the chemical bonds and molecular structure of the sample. This resulting spectrum is equivalent to the molecular fingerprint of the sample[128]. Like with fingerprints, no two molecular structures produce the same infrared spectrum. Therefore, FT-IR spectroscopy is useful for the identification of an unknown material, determination of the different components that make up the material (qualitative) and determination of the amount of these components in the material (quantitative). The spectrum is a plot of intensity of absorption peaks (which corresponds to the frequencies of vibration between the bonds of the atoms that make up the material/sample) versus the frequency.

FT-IR spectroscopy employs interferometer, an optical device that measures all infrared frequencies simultaneously rather than individually. This interferometer generates a type of signal that contains all the infrared frequencies encrypted into it thus permitting fast measurement. The interferometer consists of a beamsplitter and a pair of mirrors at right angles to one another; it produces an interferogram from the source radiation. The beamsplitter takes incoming infrared beam, divides it into two optical beams, of which one reflects off a flat fixed in place mirror, and the other reflects off a flat moving mirror. These two beams reflect off their respective mirrors and are combined as they meet at the beamsplitter producing the interferogram from the source radiation. The interferogram holds information about the intensity of all infrared radiation at all frequencies simultaneously. This then passes through the sample into the detector. At arrival at the detector, the interferogram can be decoded by a mathematical technique called Fourier transformation. This gives the intensity of the infrared radiation at each frequency separately. This transformation is performed by a computer which produces a graph of % transmittance against wavenumber (spectrum). This spectrum is interpreted to make the identification of the sample.

2.6.1 Principle

Infrared (IR) radiation lies between the visible and microwave portions of the electromagnetic spectrum. IR waves have longer wavelengths and lower frequencies than visible light but shorter wavelengths and higher frequencies than microwaves. The infrared region is divided into near, mid and far infrared regions and it is a lower energy area than visible and ultraviolet portions of the spectrum. The particular IR portion of interest to our study ranges from 2.5×10^{-4} to 2.5×10^{-3}cm (4000-400cm^{-1}), the area

most commonly utilised by IR spectrophotometers. Within a material, molecular bonds vibrate at different frequencies based on the elements and the kind of bonds present. The types of vibrational excitation that can occur are stretching and bending vibrations. The latter occurs at lower energy while the former at higher energy. For a given bond, there are several specific frequencies at which this vibration occurs and energy (relatively small) is absorbed and released. Electromagnetic radiations are propagated in photons, and transfer of energy only occurs if the energy being transferred exactly matches the energy of the transition being carried out by the molecule.

2.6.2 Instrumentation

A FT-IR spectrometer (with ATR sampling accessory) consists of the following instrumental components:

- Sample compartment: This comprises of a sample holder made of diamond or germanium. The IR radiation enters the sample compartment where it is directed into the sample and transmitted through the sample or reflected off the sample surface, depending on analysis type. Here specific frequencies of energy which are uniquely characteristic of the sample are absorbed.
- The energy source: The IR energy is radiated from a glowing black body source and emitted beams pass through an opening which controls the amount of energy that reaches the sample and ultimately the detector.
- The interferometer: This is where the ‘spectra encoding’ takes place. The beams enter the interferometer and an interferogram is produced which then exit the interferometer.

- Detectors: These are specially designed detectors that can measure the special interferogram signals. The final beams are passed to the detector for measurement. The output of the detector is digitized.
- The computer: This is where the Fourier transformation takes place. The computer obtains the measured signals and uses the digitized signal to produce a spectrum.

2.6.3 Sample preparation/Analysis

There is no special sample preparation needed for most samples for attenuated total reflection (ATR). The ATR method is used where the sample is placed on a crystal made of diamond or germanium and the IR beam directed on it by a mirror is reflected back from the upper surface before being guided into the detector by a second mirror. A small amount (ca. 1mg) of the solid sample is required, placed on the sample holder and a good contact with surface of the crystal is required. A background spectrum is also required because there is a need for a relative scale for the absorption intensity to ensure that all instrument characteristics are removed. This is done by carrying out the measurement without the sample in the beam and when the sample is measured; it is then compared with the sample measurement to produce percent transmittance. This shows that all the spectra characteristics presented are strictly due to the sample. For polymer materials, a cast film is sometimes used. The cast film is made by dissolving the solid sample in a solvent like methylene chloride and then evaporating off the solvent (by placing the solvent onto a single plate), leaving the original sample on the plate. Alternatively, solid samples may be milled with KBr forming a very fine powder which is compressed into pellets. Liquid samples are analysed in liquid cells (and gases

in gas cells) made of infrared transparent materials, or a drop of the liquid sample can be placed between two sodium chloride plates, where a thin film of the drop is formed between the plates.

FT-IR measurements carried out in this study were recorded on a Varian 660 FT-IR spectrometer to identify the anions in the interlayer of our synthesised host hydrotalcites, and also to confirm the intercalation of dodecylsulfate and dodecylbenzenesulfate anions replacing the original inorganic anions within the gallery of the host hydrotalcite after modification. The ATR method was adopted and no prior sample preparation was required, the analysis was performed on the samples from wavenumber range of 700 – 4000cm^{-1}.

2.7 Ultraviolet-Visible (Uv-vis) Spectrophotometry

Uv-vis spectroscopy is a non-destructive analytical technique used to determine the identity (quantitative and qualitative) of a material. The ultraviolet and visible regions of the electromagnetic spectrum are those regions where most molecules and functional groups are transparent. These regions show wavelengths range from 190nm to 800nm, and information derived from these regions of the spectrum can be used for structural elucidation. Absorption spectroscopy is often also referred to as electronic spectroscopy, whereby light of ultraviolet and visible region is absorbed by molecules. When ultraviolet radiation is imparted on a material, some of the radiation may be absorbed by the material causing the atoms or molecules to pass from one energy level to another energy level i.e. from a ground state (low energy level) to an excited state (higher energy level). The remaining unabsorbed energy if allowed to pass through a prism to yield a spectrum. The electromagnetic radiation which is absorbed must have energy

which conforms exactly to the energy difference between the two energy levels or states. Most molecules that have the σ-orbitals corresponding to σ- bonds have the lowest energy occupied molecular orbitals while the π-orbitals that hold the unshared pair of electrons stand at higher energy level. The non-bonding (n-bonding caused by lone pairs of electrons) orbitals are at higher energies than the π-orbitals. The orbitals of highest energy are the unoccupied or anti-bonding orbitals (π* and σ*). The majority of the absorption that takes place in the Uv-vis spectroscopy is as a result of π-electron transition or n-bonding electron transitions. In each case, the right quantum of energy is required to trigger the transition in the electronic energy levels of the bonds in a molecule for excitations of electrons from the ground state (HOMO) into an excited state (LUMO). A Uv-vis spectrometer records the degree of absorption by the material at various wavelengths giving a spectrum of plot of absorbance (A) against wavelength (λ). The wavelength at which the material absorbs the highest amount of light (energy) is the λ_{max} of the material and this depends on pH, temperature and solvent.

Two important pieces of information can be obtained from Uv spectroscopy: the position of absorbance (λ_{max}) and molar absorptivity or extinction coefficient. The latter is a constant for a given molecule at a given wavelength and it is a measure of the ease of transition caused by the absorption of radiation at a given time. For Uv-vis spectra analysis, if the transition is allowed, the molar absorptivity Ɛ value will be large ($> 10^3$) and vice versa. Hyperchromic substituents increase Ɛ value and hypochromic substituents decrease Ɛ value. Beer-Lambert Law helps to correlate the intensity of absorption of Uv-visible radiation to the amount of species present in a sample. The law relates the molar absorptivity Ɛ and the concentration of the absorbing species (chromophore) in mol L^{-1} expressed by the Beer-Lambert Law as:

$$\log_{10} \frac{Io}{I} = \varepsilon l c$$

It states that there is a logarithmic dependence between the transmission of light through a material and the product of the absorption coefficient of the material and the path length of the material. These relationships are written as:

$$A = \log_{10} \frac{Io}{I} = \varepsilon l c \text{ or}$$

$$A = \varepsilon l c$$

Where I_o = Intensity of incident light

I = intensity of transmitted light

C = the concentration in mol L^{-1}

l = the path length of absorbing solution in cm

ε = molar absorptivity in L mol^{-1} or M^2 mol^{-1}

A is the absorbance = log (I_o / I)

As long as the solution is sufficiently dilute and no molecules are in the shadow of another, the law is obeyed.

CHAPTER THREE

SYNTHESIS AND CHARACTERISATION OF HYDROTALCITE-LIKE COMPOUNDS (HTLCS)

3.1 Methods of Synthesising HTlcs

This chapter describes the methods employed in this study to synthesise the hydrotalcite-like compounds, their characterisation and properties optimisation for the desired application in this study. A series of hydrotalcite-like compounds of different composition of layers (containing Mg^{2+}, Zn^{2+} and Al^{3+}) and interlayers composed of different anions (CO_3^{2-}, NO_3^- and Cl^-) have been synthesised with M^{II}/M^{III} ratio $R = 1 - x/x$ ranging from $2.0 \leq R \leq 4.0$. Two different methods have been used for the synthesis. The methods are co-precipitation and urea hydrolysis methods. A series of experiments were performed to establish reproducibility.

3.2 Experimental

3.2.1 Materials

Salts of metal nitrates of Mg, Zn and Al; metal chlorides of Zn, Mg, Al, sodium hydroxide, sodium chloride, sodium nitrate used in this synthesis were of high purity. Table 3.1 shows the materials used in this synthesis, their supplier and their chemical purity.

Table 3.1: List of chemicals for the synthesis of CO_3^{2-}, NO_3^- and Cl^- HTlcs

Chemical Name	Formulae	MW $gmol^{-1}$	Supplier	Purity (%)	Source
Magnesium nitrate hexahydrate	$Mg(NO_3)_2.6H_2O$	256.41	Sigma Aldrich	99 ACS	Japan
Aluminium nitrate hexahydrate	$Al(NO_3)_3.9H_2O$	375.13	Sigma Aldrich	98 ACS	Germany
Zinc nitrate hexahydrate	$Zn(NO_3)_2.6H_2O$	297.49	Sigma Aldrich	98 reagent grade	Germany
Magnesium chloride hexahydrate	$MgCl_2.6H_2O$	203.30	Sigma Aldrich	99	NA
Aluminium chloride hexahydrate	$AlCl_3.6H_2O$	241.43	Sigma Aldrich	99	Japan
Aluminium (III) chloride	$AlCl_3$	133.34	BDH laboratory supplies	98	England
Zinc(II) chloride	$ZnCl_2$	136.32	Sigma Aldrich	98 ACS	USA
Sodium nitrate	$NaNO_3$	85.00	Sigma Aldrich		Japan
Sodium chloride	NaCl	58.44	Sigma Aldrich		USA
Sodium hydroxide	NaOH	40.00	Fisher Scientific	Analytical reagent	UK
Sodium Carbonate	Na_2CO_3	105.99	Sigma Aldrich	99	NA

3.2.2 Methods

Two methods have been used in this study. A urea hydrolysis method to synthesise $Mg_2Al(OH)_2(CO_3)_{0.5}.mH_2O$ and $Zn_2Al(OH)_2(CO_3)_{0.5}.mH_2O$ and a co-precipitation at controlled pH. The co-precipitation method has been employed to synthesise various

hydrotalcite-like compounds of magnesium aluminium hydroxyl carbonate (MgAl-CO_3) and zinc aluminium hydroxyl carbonate **(**ZnAl-CO_3) of varying M^{2+}/M^{3+} ratios ranging from 2-4 by following the procedures of Miyata[82], and Reichle[24]. Throughout this procedure, the mole fraction of aluminium was kept constant.

3.2.2.1 Co-precipitation method for the synthesis of CO_3^{2-} hydrotalcite-like compounds (HTlcs).

A mixed solution of the metals salts $Mg(NO_3)_2.6H_2O$ or $Zn(NO_3)_2.6H_2O$ and $Al(NO_3)_3.9H_2O$ in the appropriate stoichiometry to give M^{2+}/M^{3+} ratios of 2:1 in a total molar concentration of 0.8mol/dm^3 was prepared in 100cm^3 deionised water. Another solution comprising of NaOH (3.63M) and Na_2CO_3 (1.06M) was also made in another 100cm^3 deionised water. These two solutions were added together slowly and simultaneously into a reactor under vigorous stirring condition, at room temperature, maintaining the solution pH of between 9-10 for Zn-Al and 12-13 for Mg-Al hydrotalcite like compounds. After the addition was complete, the mixture was allowed to stir for a further 30-45mins before the resulting suspension was aged at 110°C for 18 hrs[22, 62] in polypropylene bottles. Thereafter, the products were separated by filtration and the precipitates washed 3-4 times with deionised water. Then, the precipitates were dried at 60°C in a drying oven for 24hrs. The resultant white solids were ground and stored in sample bottles for further analysis. Hydrotalcite-like compounds with Mg/Al and Zn/Al stoichiometric ratios of 4:1 and 3:1 were also prepared by this same procedure. A total of six samples were synthesised.

3.2.2.2 Synthesis of nitrate hydrotalcite-like compounds (NO_3^- HTlcs)

The precursor Mg/Al and Zn/Al hydroxyl nitrate hydrotalcites were also prepared by the pH control co-precipitation of metal nitrate salts[22, 30] followed by hydrothermal treatment at 110°C for 18hrs. An aqueous mixed solution of aluminium [$Al(NO_3)_3.9H_2O$] and zinc [$Zn(NO_3)_2.6H_2O$] or magnesium [$Mg(NO_3)_2.6H_2O$] of 1mol/dm^3 concentration, consisting of Mg/Al and Zn/Al in appropriate stoichiometry to form mole ratio of 3:1 with the mixed base solution of sodium hydroxide and sodium nitrate in required stoichiometry to give ~ 3.0 mol/dm^3, were prepared. The two solutions were added together drop wise slowly each time within about 60mins under vigorous stirring, and under a nitrogen atmosphere at room temperature. The resulting mixtures (pH 8.0-9.0 for Mg/Al and 6.0-7.2 for Zn/Al) were stirred briefly after the additions were completed before being placed in an oven to age. Deionised deaereated water was used throughout to minimise the risk of carbon dioxide contamination. After the aging process, the mixtures were allowed to cool to room temperature, filtered, washed and dried at 60°C to give white solids which were pulverised and stored in an air tight glass sample bottles. The same procedure was followed to synthesize hydrotalcite-like compounds with MgAl and ZnAl stochiometric ratios of 4 and 2.

3.2.2.3 Synthesis of chloride hydrotalcite-like compounds (Cl^- HTlcs)

Six hydrotalcite-like compounds (containing magnesium or zinc aluminium hydroxyl chloride) have been synthesised with nominal Mg/Al or Zn/Al molar ratios in the range of 2-4. A similar synthesis procedure as in 3.2.2.2 was followed. A solution with the amounts of metal (specified in Table 3.1) salts in 100cm^3 of deionised water was prepared in suitable stoichiometry to give the x value of 0.20 in a total M^{2+}/M^{3+} molar

ratio of 1mol/dm^3. Another solution was prepared containing NaOH and NaCl in the required stoichiometry to give ~ 3.5mol/dm^3 (3.5M). The various amounts were calculated taking into account the theoretical formula of the hydrotalcite-like compounds, $M^{II}_{1-x}M^{III}_{x}(OH)_2Cl.mH_2O$ where M^{II} = Mg or Zn and M^{III} = Al. Both solutions were added together simultaneously in a dropwise manner under vigorous stirring at room with continuous nitrogen bubbling to minimise carbon dioxide contamination. The reaction was allowed to proceed at the solution pH which was in the range of 6.3-6.8. After completing the addition of the solutions, the suspension was aged for 18 hrs at 110^oC in a polypropylene bottle. The resultant solid was recovered by filtration, washed 4-5 times with deionised deaerated water and finally dried in a drying oven at 60^oC for 24 hrs. The ultimate solids were ground and stored in air tight glass sample containers. The same procedure was followed to prepare hydrotalcite-like compounds with Mg/Al and Zn/Al stoichiometric ratios of 3:1 and 4:1.

3.2.2.4 Synthesis of Carbonate hydrotalcite-like compounds (CO_3^{2-} HTlcs) by urea hydrolysis method:

Mg_2AlCO_3 and Zn_2AlCO_3 HTlcs were synthesised using the urea hydrolysis method in accordance with the method described by Costantino et al[13, 59]. In a typical experiment, solid urea, 1.65mol/L (comprising of urea/Mg + Al or urea/Zn + Al in a molar ratio of 3.3) was dissolved in an aqueous solution containing the desired metal precursors, magnesium [$Mg(NO_3)_2.6H_2O$] and aluminium [$Al(NO_3)_3.9H_2O$] or aluminium [$Al(NO_3)_3.9H_2O$] and zinc [$Zn(NO_3)_2.6H_2O$] (Mg:Al or Zn:Al) in appropriate ratio to give a total concentration of 0.5mol/L. The resulting clear solution was refluxed at 90°C, with constant vigorous stirring, for 48 hrs. The mixtures were filtered thereafter,

washed and dried at 60°C for 24 hrs. The derived solids were ground and stored in air tight container. The synthesis of higher mole ratios could not be achieved. All attempts failed as the products were reverting to the 2:1 Mg/Al and Zn/Al mole ratio.

Table 3.2: List of the synthesised hydrotalcite-like compounds with composition of layers/interlayers and reagent types.

Hydrotalcite	Metal salts		Base type
$Mg_2Al(OH)_6NO_3$	$Mg(NO_3)_2.6H_20$	$Al(NO_3)_3.9H_2O$	$NaOH/NaNO_3$
$Mg_3Al(OH)_8NO_3$	$Mg(NO_3)_2.6H_20$	$Al(NO_3)_3.9H_2O$	$NaOH/NaNO_3$
$Mg_4Al(OH)_{10}NO_3$	$Mg(NO_3)_2.6H_20$	$Al(NO_3)_3.9H_2O$	$NaOH/NaNO_3$
$Zn_2Al(OH)_6NO_3$	$Zn(NO_3)_2.6H_2O$	$Al(NO_3)_3.9H_2O$	$NaOH/NaNO_3$
$Zn_3Al(OH)_8NO_3$	$Zn(NO_3)_2.6H_2O$	$Al(NO_3)_3.9H_2O$	$NaOH/NaNO_3$
$Zn_4Al(OH)_{10}NO_3$	$Zn(NO_3)_2.6H_2O$	$Al(NO_3)_3.9H_2O$	$NaOH/NaNO_3$
$Mg_2Al(OH)_6Cl$	$MgCl_2.6H_2O$	$AlCl_3.6H_2O$	NaOH/NaCl
$Mg_3Al(OH)_8Cl$	$MgCl_2.6H_2O$	$AlCl_3.6H_2O$	NaOH/NaCl
$Mg_4Al(OH)_{10}Cl$	$MgCl_2.6H_2O$	$AlCl_3.6H_2O$	NaOH/NaCl
$Zn_2Al(OH)_6Cl$	$ZnCl_2$	$AlCl_3$	NaOH/NaCl
$Zn_3Al(OH)_8Cl$	$ZnCl_2$	$AlCl_3$	NaOH/NaCl
$Zn_4Al(OH)_{10}Cl$	$ZnCl_2$	$AlCl_3$	NaOH/NaCl

3.3 Characterisation of Materials

3.3.1 X-ray diffraction (XRD)

Powder X-ray diffraction analysis was performed on the synthesised hydrotalcites for identification of the materials. Data were collected using 2 theta transmission geometry with CuKα_1 radiation ($\lambda_{CuK\alpha_1}$ = 1.54056 Å) on a Bruker D8 ADVANCE X-ray diffractometer equipped with a Lynx-Eye PSD detector. A step size of 0.02° and detection time of 65.8s was used for routine characterization and identification of materials. The samples were collected in the 2θ range from 5° to 80°. Diffrac Plus XRD commander and Eva software (Materials Data, Inc.) was used to manipulate the data; identification of the crystalline phases was based on comparison with pre-existing JCPDS diffraction data files. Cell refinements were carried out using Celref, using the parameters obtained from the JCPDS as starting values.

3.3.2 X-ray Fluorescence Spectrometry (XRF)

The elemental compositions of the synthesised hydrotalcite-like compounds were determine using X-ray fluorescence spectrometry (Bruker S8 TIGER wavelength dispersive X-ray fluorescence spectrometer) with high intensity rhodium X-ray tube, two collimeters (0.23° and 0.46°) and five analyzer crystals to determine the elemental composition of our materials. The fused beads analysis method was adopted for the major oxides which involves dissolving usually 1.0g of sample in 10g of flux, di-Lithium tetraborate. In a typical experiment, approximately 0.35g of sample was mixed with 3.50g of flux, di-Lithium tetraborate ((99.9% purity; product of I.C.P.H, France).

The mixtures were put into a platinum/gold alloy crucible and placed in a muffle furnace at 1250°C for 6mins. After which, the crucible and content were brought out and a pinch of ammonium iodide (Sigma-Aldrich, Germany) was added. The crucible and mixture were swirled gently and returned into the furnace for another 5mins. Thereafter, brought out and swirled gently again (to remove air bubbles) and then returned into the furnace for another 3-5mins. Finally, the crucible and content were removed from the furnace and allowed to cool before XRF measurements were carried out without any additional sample preparation.

3.3.3 Fourier- Transform Infra-red Spectroscopy (FT-IR)

IR data were collected on a Varian 660 FT-IR spectrometer to identify the anions in the interlayer of the various synthesised hydrotalcites. 16 scans were taken to improve the signal-to-noise ratio in the range of 700–4000 cm^{-1}. The resolution used was 4 cm^{-1} with sensitivity of 1. The attenuated total reflection (ATR) method with a diamond sample holder was used.

3.3.4 TGA/DTA and Mass Spectrometry

Simultaneous thermogravimetric (TG) and differential thermal analyses (DTA) were performed from 25 to 900˚C under oxygen atmosphere for the CO_3^{2-} - HTlcs and under nitrogen atmosphere (for the NO_3^- and Cl^- - HTlcs at heating rate of 5°C/min with a Netzsch STA 449 FI Jupiter® apparatus, connected to a quadrupole mass spectrometer (Netzsch QMS 403 Aëolus®) to measure the thermal stability of the synthesised HTlcs and to analyse gases evolved during sample heating. Mass numbers *m*/*z* (18-H_2O; 30-NO/46-NO_2; 36-HCl; 51-ClO; 67-ClO_2 or 70-Cl_2 and 102/103-Cl_2O_2; and 44-CO_2) were

continually monitored. Approximately 50-60 mg of dried sample was used for each measurement.

3.3.5 Scanning Electron Microscopy (SEM)

SEM was carried out on the synthesised HTlcs to determine particle size and morphology using a PhilipXL 30 Scanning Electron Microscope. This technique was used to view the shape of the crystallite compounds and also to see how the various particles are assembled. The sample to be analysed was spread over a carbon tape that was placed on a silicon wafer substrate which was in turn placed on a stud and then coated slightly with gold on the surface of the particles to prevent any electron charge on the sample surface.

3.4 Results and discussion

3.4.1 X-ray diffraction results for $MgAlCO_3$ HTlcs with different layers

Fig. 3.1 shows the powder XRD patterns of the synthesised hydrotalcite-like compounds with $1-x/x$ value of 0.20, 0.25 and 0.33 **(**Mg^{2+}/Al^{3+} molar ratio of 4, 3 and 2) prepared by co-precipitation, and molar ratio 2 by urea hydrolysis method. All the samples show sharp and symmetric peaks at low 2θ angles with high intensity and broad asymmetric peaks at high 2θ angles which are indicative features of materials with a layered structure. No other phases were detected showing that the materials synthesised consisted of one crystallised phase (hydrotalcite) similar to natural hydrotalcite ($Mg_6Al_2(OH)_{16}(CO_3).4H_2O$) pattern. All the samples show good agreement with each other, all showing high structural order with little variation in peak positions. The lattice parameters '*a*' and '*c*' for these samples were calculated with a hexagonal crystal system using celref[129] and all samples show 3R symmetry, unit cell '*a*' and '*c*'; $\alpha = \beta =$ 90° and $\Upsilon = 120°$. The '*a*' parameter gives the cation-cation distance within the cationic (octahedral) layer while the '*c*' parameter is related to the total thickness of the hydroxide (brucite-like) layer and the interlayer distance[22]. Table 3.3 gives the unit cell parameters (*a, c*) and the *d* values of the first two peaks $d_{(003)}$ and $d_{(006)}$. The observed $d_{(003)}$ reflections of the series of $MgAlCO_3$ samples were observed at ~7.76Å, 8.00Å and 8.01Å, corresponding to basal spacings of ~23.27Å, 24.01Å and 24.02Å respectively. The various observed changes in the crystallographic parameters (samples by co-precipitation method) may be due to different Mg^{2+}/Al^{3+} mole ratios in the layers of the hydrotalcite-like compounds.

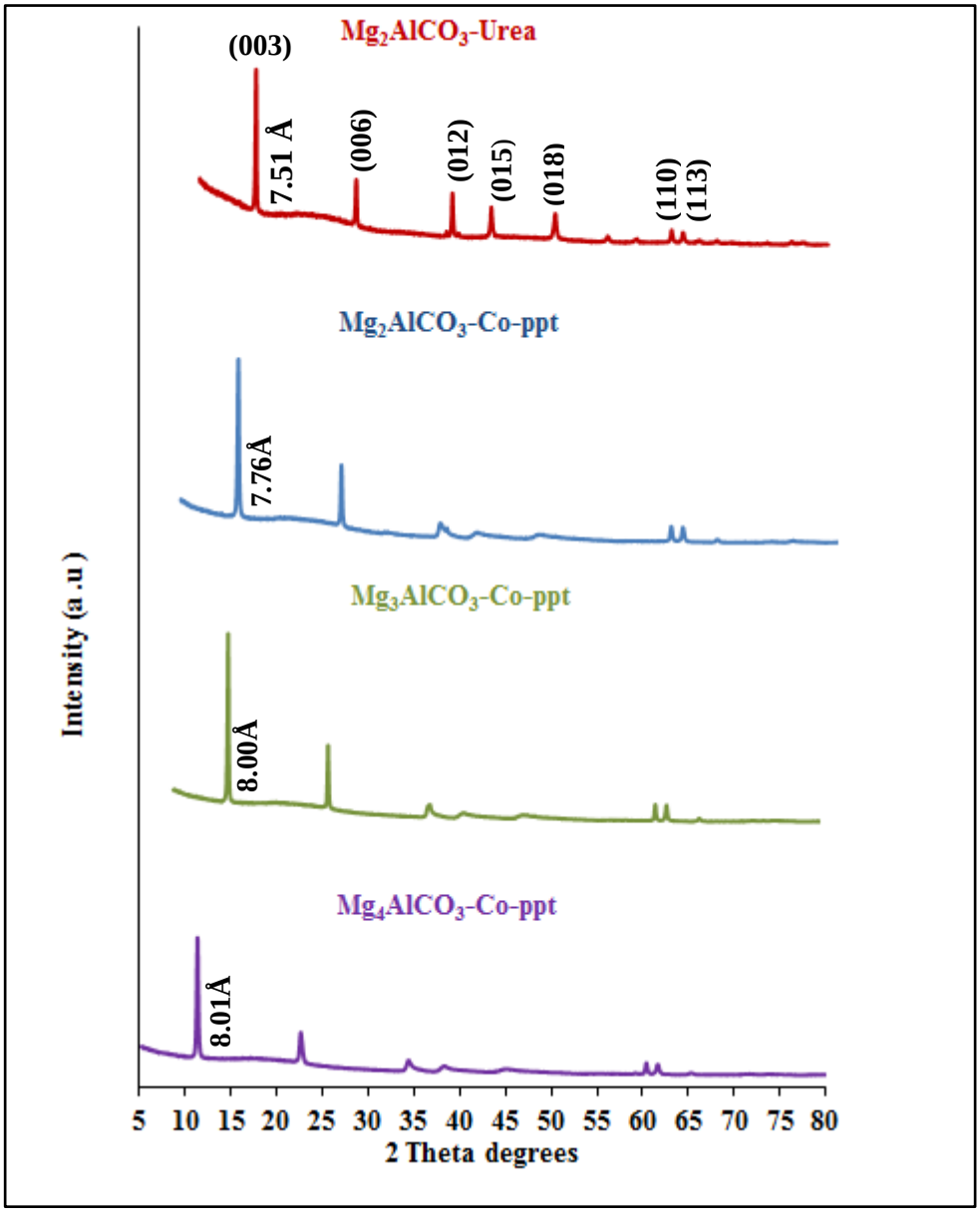

Fig.3.1: Powder X-ray diffraction patterns of the series of Magnesium aluminium hydroxylcarbonate ($MgAlCO_3$) hydrotalcites (as-synthesised) with different composition of layers. Co-precipitation method = (co-ppt) and urea hydrolysis method = (urea).

There is a very slight shift of the $d_{(003)}$ and $d_{(006)}$ peaks to lower 2 theta angle with increasing Mg^{2+} content meaning decreasing Al^{3+} content, thus giving a slight increase in the lattice parameters (Table 3.3). This may be due to the decreased ionic interaction between the metal hydroxide layers and the gallery carbonate anions. [22, 131, 132, 133]. Furthermore, these series of $MgAlCO_3$ HTlcs show peak broadening around 2θ°, 35-50° which reflects lower structural order of these samples as compared to the Mg_2AlCO_3 synthesised by the urea method. Within the series also, Mg_3AlCO_3 HTlc shows the most intense and sharpest peaks (most prominent peaks) while the Mg_4AlCO_3 HTlc showed the weakest intensity and least sharp peaks suggesting that Mg_3AlCO_3 HTlc showed higher crystallinity and has relatively larger crystallites. Whereas Mg_4AlCO_3 HTlc possesses relatively smallest particles with planes of lowest electron density, therefore crystallinity may be said to decreases with increasing M^{II}/M^{III} ratio and this can be attributed to increasing presence of water content. These results are consistent with previously reported results in literature [22, 24, 129, 130].

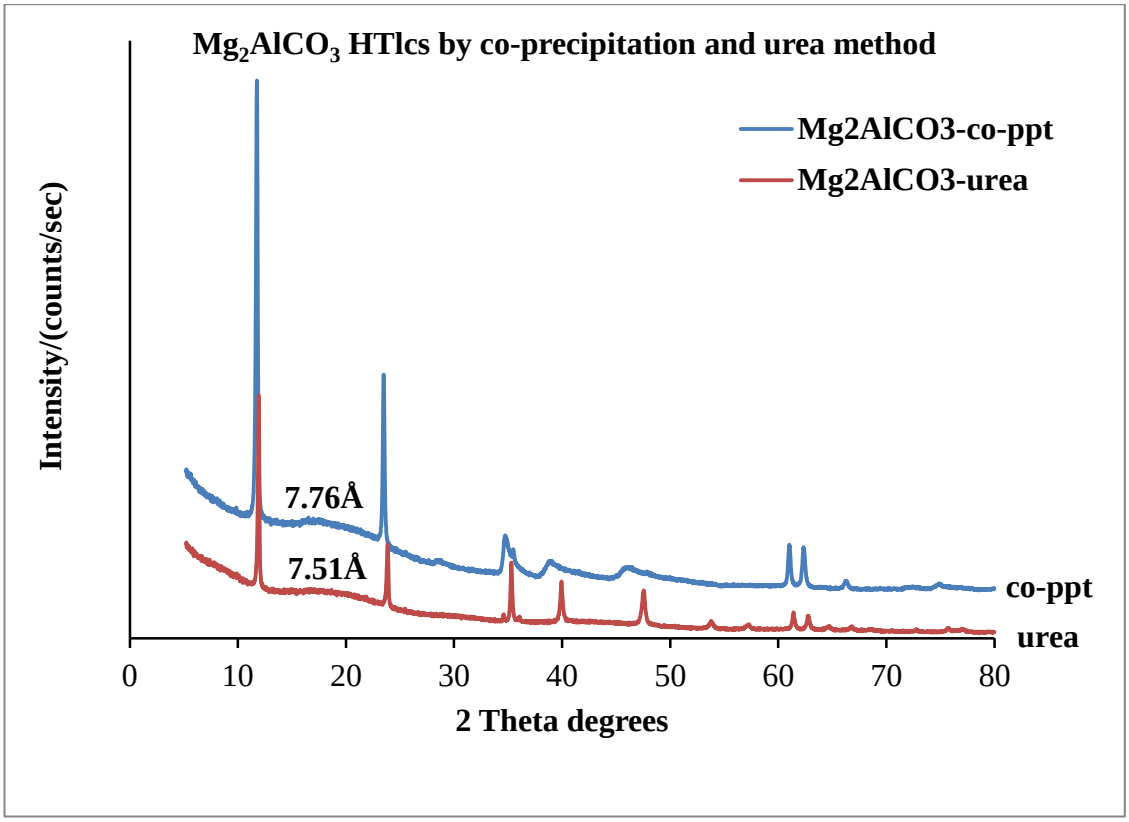

Fig.3.2: Powder X-ray diffraction patterns of Mg_2AlCO_3 HTlc prepared by co-precipitation and urea methods. Top to bottom: Mg_2AlCO_3 HTlc prepared by co-precipitation and Mg_2AlCO_3 HTlc prepared by urea method.

Fig.3.2 shows the powder XRD pattern of Mg_2AlCO_3 HTlc prepared by co-precipitation and urea methods. Comparing Mg_2AlCO_3 HTlc synthesised by the urea method and Mg_2AlCO_3 HTlc synthesised by the co-precipitation method, it was observed that Mg_2AlCO_3 HTlc by co-precipitation gave more intense peaks with slightly bigger unit cell, but Mg_2AlCO_3 HTlc synthesised by the urea method gave slightly sharper peaks with relatively smaller unit cell. This may be attributed to better crystallinity and bigger particles in the sample synthesised by the urea method, but denser sample from the co-precipitation method. Furthermore, the series of $MgAlCO_3$ HTlcs synthesised by the co-precipitation method showed peak broadening around 2θ, 35-50° which reflects that

Mg_2AlCO_3-urea (Fig 3.1) showed better structural order with less stacking faults. A key difference between these preparation methods is that, in the co-precipitation method (involving hydrothermal treatment), the system is under high pressure, while often at high pressure one would expect a denser phase with small unit cell to be produced, but in this case, a denser phase with larger unit cell was observed which may be due to more water being included in the interlayer region of Mg_2AlCO_3 synthesised by the co-precipitation method. This result ties with the TGA results, where greater overall weight loss, (42.38%) is indeed, observed for hydrothermal samples (33.38% overall weight loss for urea sample, [section 3.9]). The Sample prepared by urea hydrolysis (Mg_2AlCO_3-urea) may be said to be more highly crystalline than Mg_2AlCO_3-co-precipitation, which may account for the differences in relative intensity and d- spacing observed.

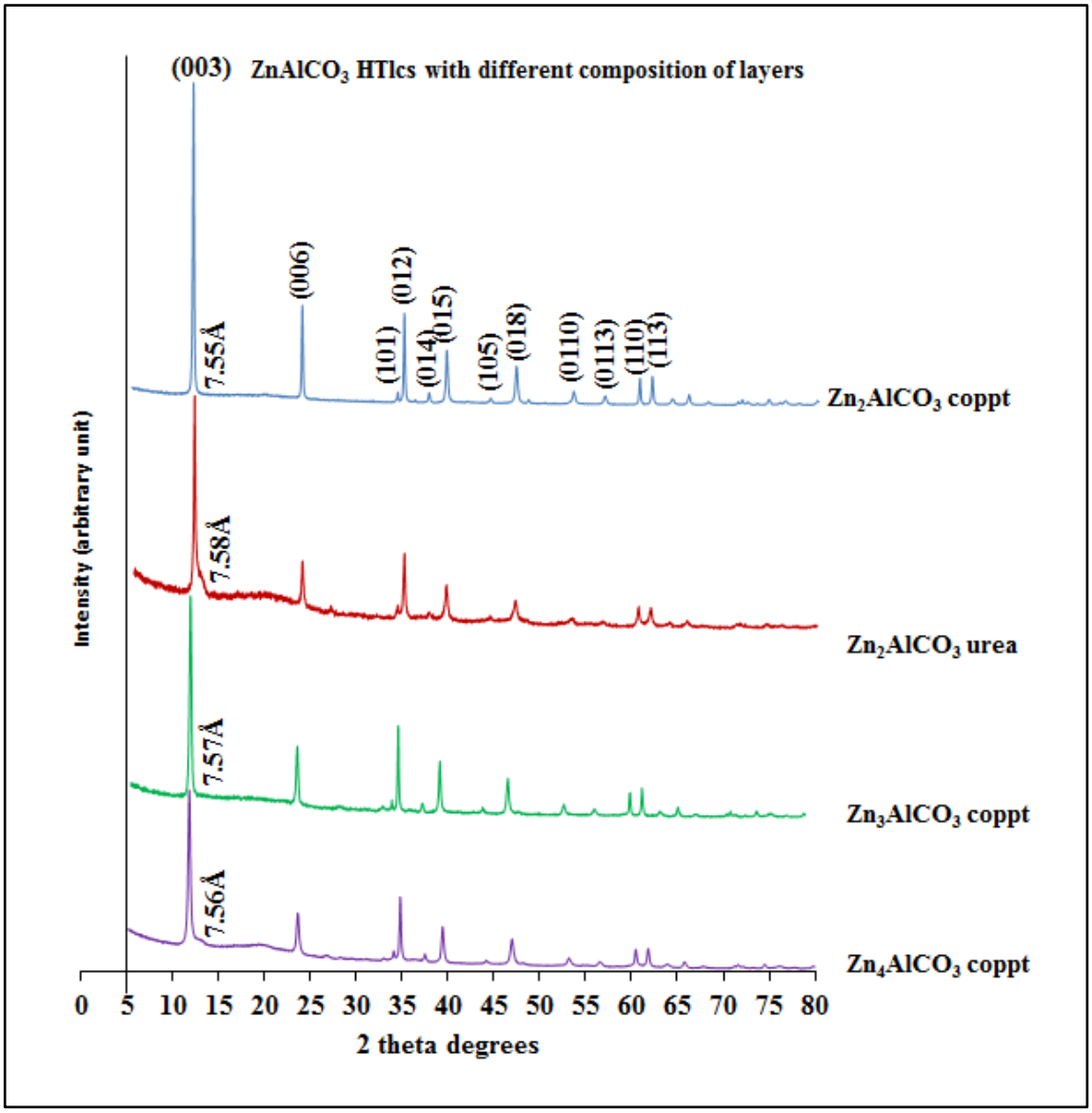

Fig.3.3: Powder X-ray diffraction patterns of the various $ZnAlCO_3$ hydrotalcites with different layers synthesised by co-precipitation (co-ppt) and urea hydrolysis method (urea).

3.4.2 X-ray diffraction results for $ZnAlCO_3$ HTlcs with different composition layers.

The powder X-ray diffraction patterns of the Zinc aluminium hydroxylcarbonate hydrotalcites are shown in Figs.3.3-3.5. These materials also showed patterns

characteristic of hydrotalcites. No impurity phases were observed, and all the samples showed formation of a single hydrotalcite phase. There is a slight variation in peak positions, increasing mole ratio of Zn/Al, HTlc peaks are slightly shifted towards lower angles due to decreased charge density leading to a slight increase in interlayer spacings (Fig.3.3 and Table 3.3). This may be attributed to lowering ionic interaction between the mixed metal hydroxide layers and the interlayer carbonate anions. It was further observed that, this variation in the Zn/Al mole ratio also influences the crystallinity and this was observed to decrease with increasing Zn/Al mole ratio.

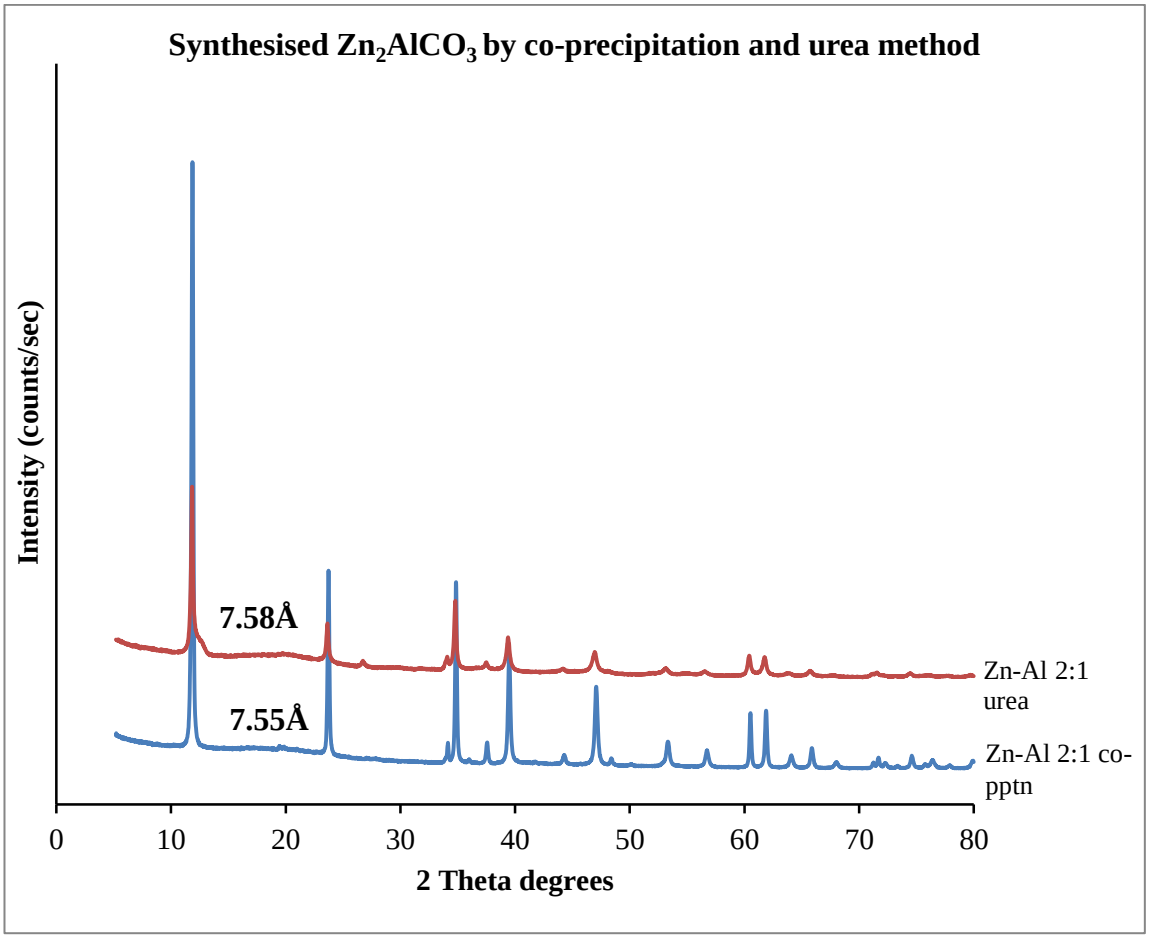

Fig 3.4: Powder X-ray diffraction patterns of Zn_2AlCO_3 HTlc prepared by co-precipitation (blue) and urea method (red). Bottom to top: [Zn_2AlCO_3] HTlc by co-precipitation method; d_{003}= 7.55Å, and [Zn_2AlCO_3] HTlc by urea method; d_{003}= 7.58Å

Fig.3.4 shows that Zn_2AlCO_3 prepared by co-precipitation gave higher intensity and sharper peaks than Zn_2AlCO_3 prepared by the urea method. The sample prepared by co-precipitation method gave a denser phase with small unit cell (Table 3.3) as is expected unlike in the case of Mg_2AlCO_3 synthesised by the urea method and Mg_2AlCO_3 by co-precipitation method where the opposite trend is observed.

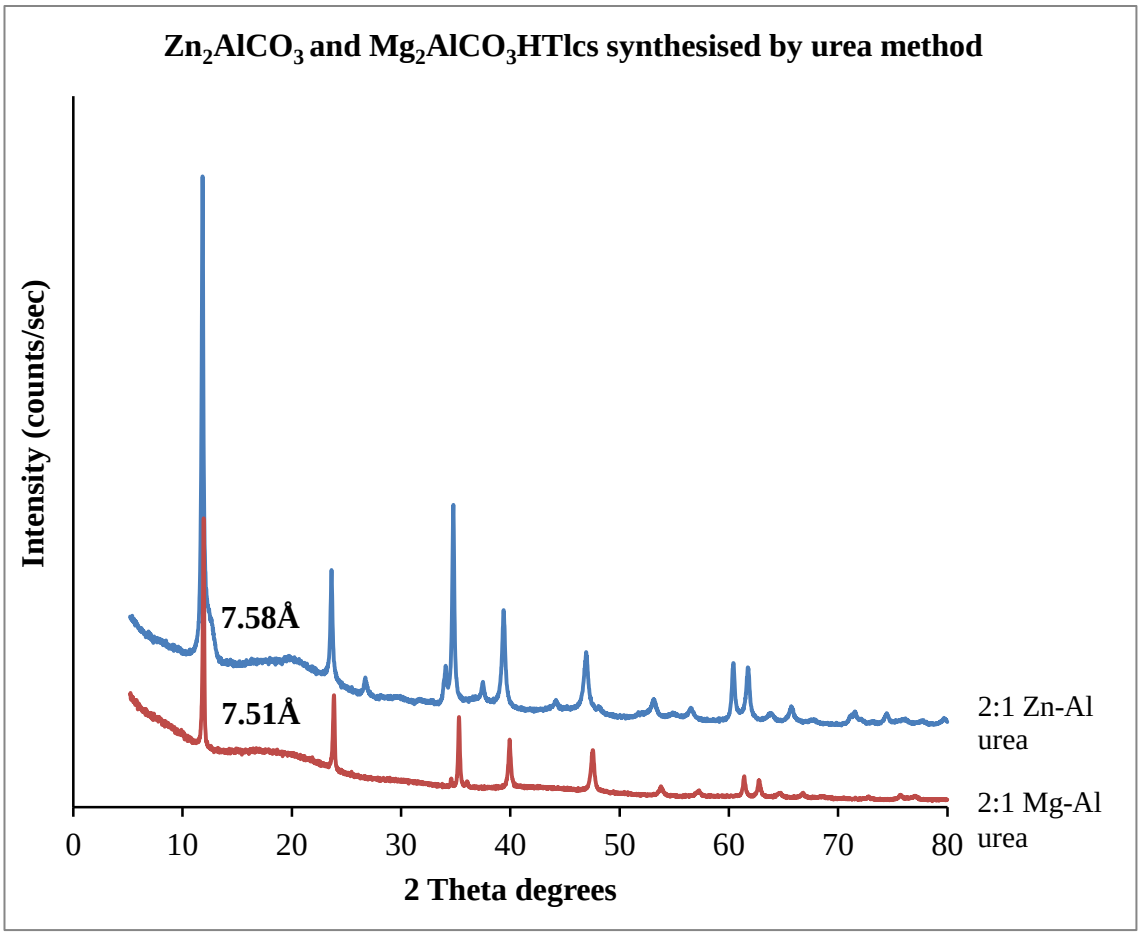

Fig.3.5: Powder X-ray diffraction patterns of Zn_2AlCO_3 and Mg_2AlCO_3 hydrotalcites synthesised by urea hydrolysis.

Fig.3.5 shows the powder XRD patterns of Zn_2AlCO_3 HTlc and Mg_2AlCO_3 HTlc with both samples prepared by urea hydrolysis method. The powder XRD patterns are

similar and both demonstrate their layered structures are very similar. The $d_{(003)}$ reflection of Zn_2AlCO_3 HTlc is observed at approximately 7.58Å, corresponding to a unit cell parameter *c* of 22.73Å while for Mg_2AlCO_3-HTlc, it is observed at ~7.51Å corresponding to a unit cell parameter *c* of 22.53Å. Mg_2AlCO_3-HTlc also showed sharper peaks indicating better crystallinity, which may be an indication of better order in Mg_2AlCO_3-HTlc.

Table 3.3: Unit cell parameters a(Å), c(Å) and $d_{(003)}$ for the various CO_3^{2-}-HTlcs.

Sample	**Cations mole ratio**	***a* (Å)**	***c* (Å)**	***d* $_{(003)}$ (Å)**	**$d_{(006)}$(Å)**
Mg_2AlCO_3HTlc	Mg/Al 2:1	3.0438(71)	23.2675(40)	7.7554	3.8777
Mg_3AlCO_3HTlc	Mg/Al 3:1	3.0590(19)	24.0093(20)	8.0031	4.0015
Mg_4AlCO_3HTlc	Mg/Al 4:1	3.0651(49)	24.0159(08)	8.0053	4.0027
Mg_2AlCO_3_urea	Mg/Al 2:1	3.0269(11)	22.5340(14)	7.5113	3.7557
Zn_2AlCO_3-HTlc	Zn/Al 2:1	3.0679(11)	22.6419(4)	7.5474	3.7737
Zn_3AlCO_3-HTlc	Zn/Al 3:1	3.0688(09)	22.7169(5)	7.5724	3.7862
Zn_4AlCO_3-HTlc	Zn/Al 4:1	3.0685(10)	22.6940(5)	7.5645	3.7823
$Zn_2Al\ CO_3$_urea	Zn/Al 2:1	3.0708(13)	22.7261(6)	7.5754	3.7877

Calculated with celref software using hexagonal crystal system

3.5 X-ray diffraction results of nitrate hydrotalcites

This section shows the series of Mg/Al and Zn/Al nitrates hydrotalcite-like compounds with different composition of layers. Fig.3.6 shows the X-ray diffraction patterns of the series of $MgAlNO_3$ HTlcs with varying mole ratio. No additional phase or phases were

observed. The $d_{(003)}$ values of the three different Mg/Al molar ratios, intercalated with nitrate anions are larger than their carbonate counterparts. This may be due to the size, amount and orientation of NO_3^- anion in the galleries of the hydrotalcites which is influenced by the $Mg^{2+/}Al^{3+}$ mole ratio. Further changes are noted in the unit cell parameters; parameter *c* increases with increasing charge density and parameter *a* decreases with increasing charge density. Changes in *c* are controlled by the balance between increased ionic interactions between the hydroxide layers and the interlayer nitrate anions and the increased number of NO_3^- anions required to be accommodated, while *a* decreases due to the higher fractional substitution of the smaller Al^{3+} cation. In addition, all samples show broad peaks with relatively weaker intensity which is an indication of reduced crystallinity, meaning smaller crystal diameter when compared to the carbonate hydrotalcites. The $d_{(110)}$ and $d_{(113)}$ peaks of the Mg_2AlNO_3 and Mg_3AlNO_3 hydrotalcite-like compounds overlapped, which could be because of changes in nitrate content which may have caused disturbance in the MgAl hydroxide layers during nitrate intercalation. The Mg/Al mole ratio may also influence this disturbance because it is observed to increase with increased charge density, meaning that, differences in the distribution of electrostatic charges (M^{2+}/M^{3+} mole ratio) can suggest differences in distortion within the brucite-like layers.

The increase in basal spacing with increasing charge density observed in these materials is opposite to the observation in the carbonate hydrotalcite-like compounds which may be due to repulsion of large anions in the interlayers, coupled to the number of anions present and the packing mode adopted in the gallery. Within the nitrate hydrotalcite series, it is also noted that the Mg_4AlNO_3 hydrotalcite sample is most crystalline and densest, while Mg_3AlNO_3 are less crystalline. This imperatively places the Mg_2AlNO_3

hydrotalcite-like compound in mid-way. The basal spacings of the as-synthesised nitrate hydrotalcites (for instance, at x = 0.33, it is 8.99Å) is consistent with the literature[47, 134, 135].

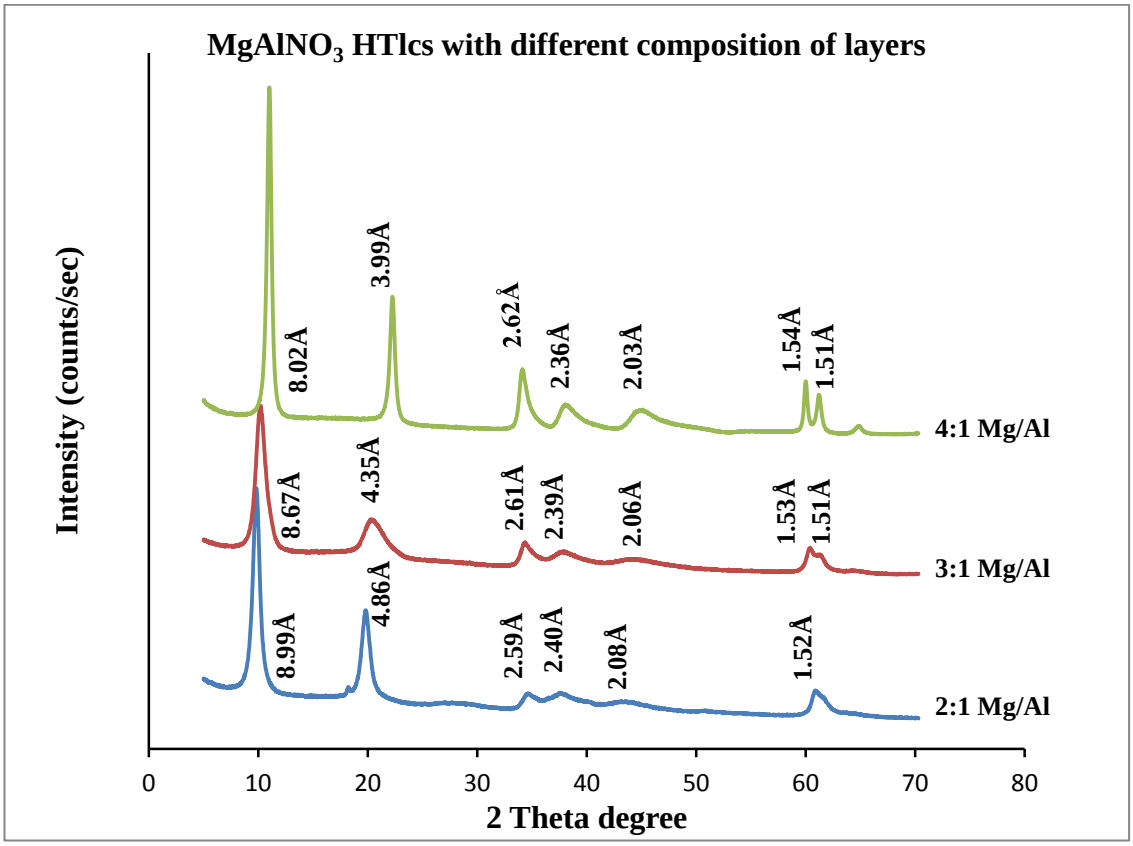

Fig.3.6: Powder X-ray diffraction patterns of the various $MgAlNO_3$ hydrotalcites (as-synthesised) with different layer compositions.

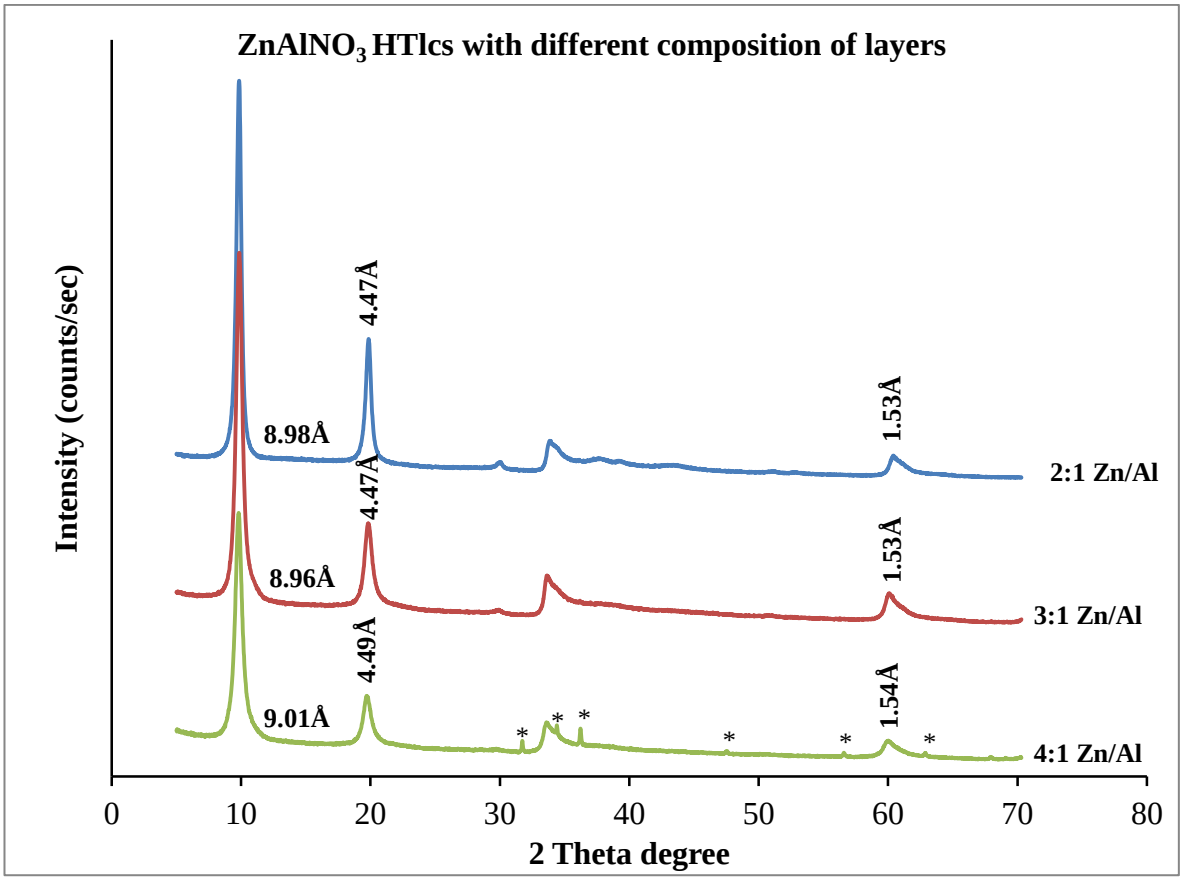

Fig.3.7: Powder X-ray diffraction patterns of the various $ZnAlNO_3$ hydrotalcites (as-synthesised) with different layers. The peaks labelled asterisks are artefacts due to presence of some ZnO and small unreacted starting material – NaCl

Fig.3.7. illustrates the XRD patterns for the as-synthesised $ZnAlNO_3$ hydrotalcite-like series with different layer compositions (Zn^{2+}/Al^{3+} ratios of 2-4). The XRD pattern are characteristic of the hydrotalcite structure just like previous samples, and similar to those described by other researchers[22, 82,]. An additional ZnO phase was observed in the 4:1 sample as indicated by asterisks in Fig.3.7. This may be due to stacking fault created on the hydrotalcite as fractional Zn^{2+} intercalation increased. The unit cell parameters calculated from Bragg's law assuming a hexagonal cell with rhombohedral symmetry (R-3m) are shown in Table 3.4. The first peak of the XRD pattern gave the interplanar distance (*003*), and the peak or reflection around 60-61° corresponds to the

(110) plane, and they define the unit cell parameters *a* and *c* listed in Table 3.4. The parameter *c* values were calculated from the average of the *00l* peaks, and the *a* parameter from the expression, a = $2d_{(110)}$ [136, 137, 138]. These patterns show elimination of some peaks (peaks beyond ~35° to 50° 2θ°) leaving only one peak at around ca. 35° 2θ°, suggesting high disorder from faults in stacking of successive mixed metal hydroxide layers. According to Forano and co-workers[137], stacking faults in synthetic hydrotalcites may be due to the co-existence of the two polytypes. They explained that when both polytypes grow together or one grows into the other, a random sequence is expected based on equal brucite-like and interlayer topology of the two polytypes which then causes random orientation about c-axis thus removing some (*hkl)* reflections. Also observed is a slight shift in the prominent peak positions towards lower 2θ° with increasing molar ratio of Zn/Al which also indicates lower charge density, and increased interlayer distance and unit cell parameters. This increase in interlayer distance could be due to a decrease in the electrostatic interaction between the positive [ZnAlOH] layers and negative interlayers.

Within this group, Zn_2AlNO_3 HTlc showed the most intense and sharpest *(003)* and *(006)* peaks, and because the level of crystallinity can be directly linked to the sharpness and intensity of the most prominent peaks in powder X-ray diffraction patterns (if all other factors are true), then Zn_2AlNO_3 sample could be said to be the better crystalline of the group. While the Zn_4AlNO_3 sample showed relatively broader (*003)* and (*006)* peaks with the weakest intensities indicative of least dense sample with smaller crystallites (lower crystallinity)

Comparing these samples with those of the groups considered earlier, these samples may be more crystalline than $MgAlNO_3$ group but less than the $MgAlCO_3$- HTs groups. The crystallinity of the hydrotalcite-like compounds increased as follows: $MgAlCO_3$ > $ZnAlCO_3$ > $ZnAlNO_3$ > $MgAlNO_3$ and similarly the basal spacing increased as follows: $MgAlNO_3$ > $MgAlCO_3$ and $ZnAlNO_3$ > $ZnAlCO_3$.

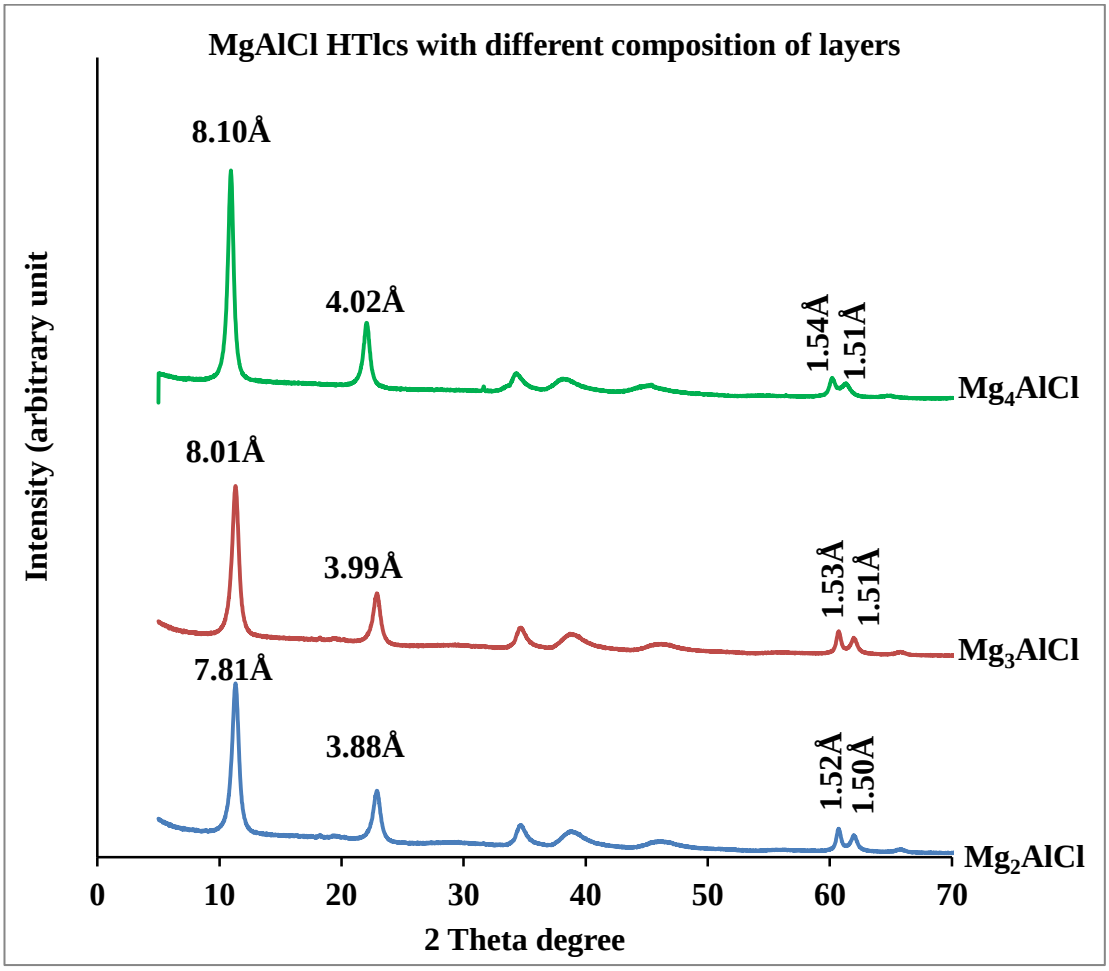

Fig.3.8: Powder X-ray diffraction patterns of the various MgAlCl hydrotalcites (as-synthesised) with different composition of layers.

The X-ray diffraction patterns of the chloride intercalated hydrotalcites are shown in Fig.3.8 and Fig.3.9.The patterns are similar to published hydrotalcite patterns[139]. All

samples show relatively broader peaks with weaker intensities when compared with the carbonate hydrotalcites, this could express lower crystallinity and/or smaller crystal diameter. The unit cell parameters *a* and *c* are displayed in Table 3.4. This slight increase in these crystallographic parameters with decreasing charge density may be due to decreased electrostatic attraction between the MgAl hydroxide layer and the intercalated chloride anion and water. In this group, Mg_2AlCl appeared to be most crystalline because showed most intense and sharpest (*003*) and (*006*) peaks.

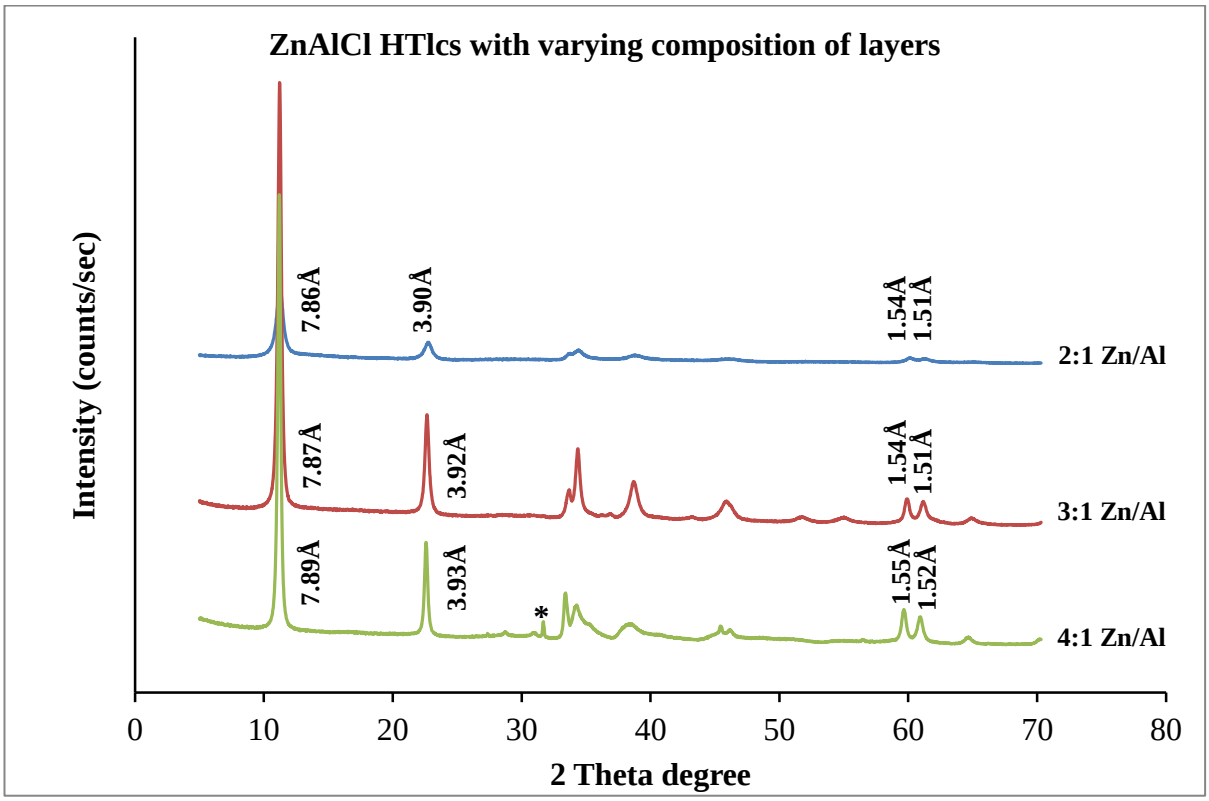

Fig.3.9: Powder X-ray diffraction patterns of the various ZnAlCl hydrotalcites synthesised with varying cation ratio. The peak labelled by asterisk is artefact due to presence of ZnO phase.

Table 3.4: Unit cell parameters of the various as-synthesised nitrate and chloride hydrotalcite-like compounds.

Sample	***(003)***		***(006)***		***(110)***		***a*(Å)**	***c*(Å)**	**Cations mole ratio in synthesis mixture**
	2θ°	*d*(Å)	2θ°	*d*(Å)	2θ°	*d*(Å)			
Mg_2AlNO_3	9.832	8.9886	18.246	4.8582	60.903	1.5199	3.04	26.97	2:1- Mg/Al
Mg_3AlNO_3	10.192	8.6722	20.411	4.3475	60.388	1.5314	3.06	26.02	3:1-Mg/Al
Mg_4AlNO_3	11.016	8.0250	22.250	3.9904	60.008	1.5404	3.08	24.07	4:1-Mg/Al
Zn_2AlNO_3	9.841	8.9810	19.856	4.4679	60.400	1.5314	3.06	26.94	2:1 Zn/Al
Zn_3AlNO_3	9.863	8.9606	19.830	4.4736	60.308	1.5335	3.07	26.88	3:1 Zn/Al
Zn_4AlNO_3	9.808	9.0111	19.727	4.4968	60.055	1.5393	3.08	27.03	4:1 Zn/Al
Mg_2AlCl	11.315	7.8137	22.901	3.8801	60.727	1.5239	3.05	23.44	2:1 Mg/Al
Mg_3AlCl	11.035	8.0111	22.280	3.9870	60.330	1.5330	3.07	24.03	3:1 Mg/Al
Mg_4AlCl	10.158	8.0965	22.045	4.0288	60.174	1.5366	3.07	24.29	4:1 Mg/Al
Zn_2AlCl	11.250	7.5884	22.753	3.9050	60.116	1.5379	3.08	23.58	2:1Zn/Al
Zn_3AlCl	11.231	7.8718	22.655	3.9218	59.908	1.5427	3.09	23.62	3:1Zn/Al
Zn_4AlCl	11.199	7.8946	22.593	3.9323	59.663	1.5485	3.08	23.68	4:1Zn/Al

3.6. X-Ray Fluorescence (XRF) Spectrometry

The elemental composition of the synthesised hydrotalcite-like compounds were determined by X-ray fluorescence spectroscopy to ascertain if the molar ratios of $M^{2+/}M^{3+}$ are consistent with stoichiometry in the synthesis mixture. The fused beads method was used to determine the mole ratio of the most prominent elements using a Bruker S8 Tiger λ dispersive X-ray fluorescence spectrophotometer. The results are shown in Table 3.5 below. The results indicated that the M^{2+}/M^{3+}mole ratios conform well to the expected ratios of Mg/Al and Zn/Al in the various samples which are an indication that the precipitation was in perfect correlation to the metal ratios in the starting materials used for synthesis. The only exception was Zn_4AlCl HTlc which precipitated as almost a 3:1 HTlc. This may be due to stacking faults on the hydrotalcite with high fractional Zn^{2+} incorporated into the hydroxide layer.

Table 3.5 Elemental analysis data and mole ratio of as-synthesised hydrotalcite-like compounds (HTlcs)

Synthesised Hydrotalcite	**Wt % ZnO**	**Wt % Al_2O_3**	**Wt % MgO**	**Mole ratio Mg/Al**	**Mole ratio Zn/Al**
Mg_2AlCO_3 by co-pptn	-	20.20	37.20	2.36:1	-
Mg_3AlCO_3	-	16.70	41.39	3.13:1	-
Mg_4AlCO_3	-	13.40	44.02	4.15:1	-
Mg_2AlCO_3 by urea	-	39.45	63.90	2.04	-
Zn_2AlCO_3 by co-pptn	69.90	20.10	-	-	2.18:1
Zn_3AlCO_3	86.16	14.40	-	-	3.75:1
Zn_4AlCO_3	79.60	12.80	-	-	3.90:1
Zn_2AlCO_3 by urea	121.9	36.90	-	-	2.07:1
Mg_2AlNO_3	-	19.45	30.67	2.05:1	-
Mg_3AlNO_3	-	15.92	38.52	3.05:1	-
Mg_4AlNO_3	-	13.21	43.88	4.20:1	-
Zn_2AlNO_3	52.29	16.36	-	-	2.05:1
Zn_3AlNO_3	59.89	12.34	-	-	3.04
Zn_4AlNO_3	65.31	8.93	-	-	4.58:1
Mg_2AlCl	-	31.77	51.89	2.07:1	-
Mg_3AlCl	-	27.30	67.83	3.14:1	-
Mg_4AlCl	-	15.46	44.01	3.60:1	-
Zn_2AlCl	54.88	16.92	-	-	2.03:1
Zn_3AlCl	64.01	12.33	-	-	3.25:1
Zn_4AlCl	65.84	9.58	-	-	4.30:1

3.7. FT-IR Analysis

Fourier Transform Infrared Spectroscopy (FT-IR) was carried out to identify the anions in the gallery of the various synthesised hydrotalcites. This section shows the FT-IR spectra in the region between 700 - 4000cm^{-1} and hydroxyl stretching regions of the synthesised hydrotalcite-like compounds. The FT-IR spectra of the carbonate hydrotalcite samples with Mg/Al molar ratios of 2.0 - 4.0 are shown in Fig.3.10. The broad peaks around 3400cm^{-1} - 3600cm^{-1} for each of the samples are attributed to the water hydroxyl stretching vibrations in the brucite-like layers and interlayer water molecules. The increase in the Mg/Al molar ratio caused a slight shifting of the OH^- stretching bands toward higher frequencies suggesting hydrogen bond weakening with decreasing charge density. It was also observed that the samples Mg_2AlCO_3 prepared by co-precipitation and urea both possess each a shoulder around higher frequency region and this may have been caused by increased interaction involving hydrogen bonding between the OH^- on the layers, CO_3^{2-} anions and H_2O molecules situated in the interlayer space. This hydrogen bonding effect is stronger in the Mg_2AlCO_3 HT synthesised by the urea method typified by the degenerates observed around 3300-3500cm^{-1} suggesting stronger Mg-Al hydroxide layer and interlayer interactions, higher crystallinity and long range order. This is supported by XRD results (section 3.4). However, the contamination of the sample by a little amount of urea during synthesis cannot be ruled out because of the following observations; splitting observed around 3250-3500cm^{-1}, and the appearance of the band observed around 1580cm^{-1} which could both be due to vibration bands due to NH_2 from urea. The weak broad bands presented around 1640-1660cm^{-1} are attributed to the bending vibration of water. Again

Mg_2AlCO_3 HT (urea rout) shows splitting of this OH bending band which may suggest stronger hydrogen bonding and better ordering of cations within the hydroxide octahedral layers and the interlayer region. The sharp intense vibration bands observed around 1367 cm^{-1} indicate CO_3^{2-} from $\nu_3(CO_3^{2-})$ and is a confirmation of the intercalation of carbonate in the interlayer spaces of these samples synthesised. The shifting of this band to lower frequency in the Mg_2AlCO_3 HT (urea method) and splitting of the band is due to greater order of the CO_3^{2-} and water molecules in the interlayer region. Also the absorption due to the carbonate anion shows sharper and more intense band in the Mg_2AlCO_3 HT (co-precipitation) consistent with the PXRD results showing this sample as having denser overall packing.

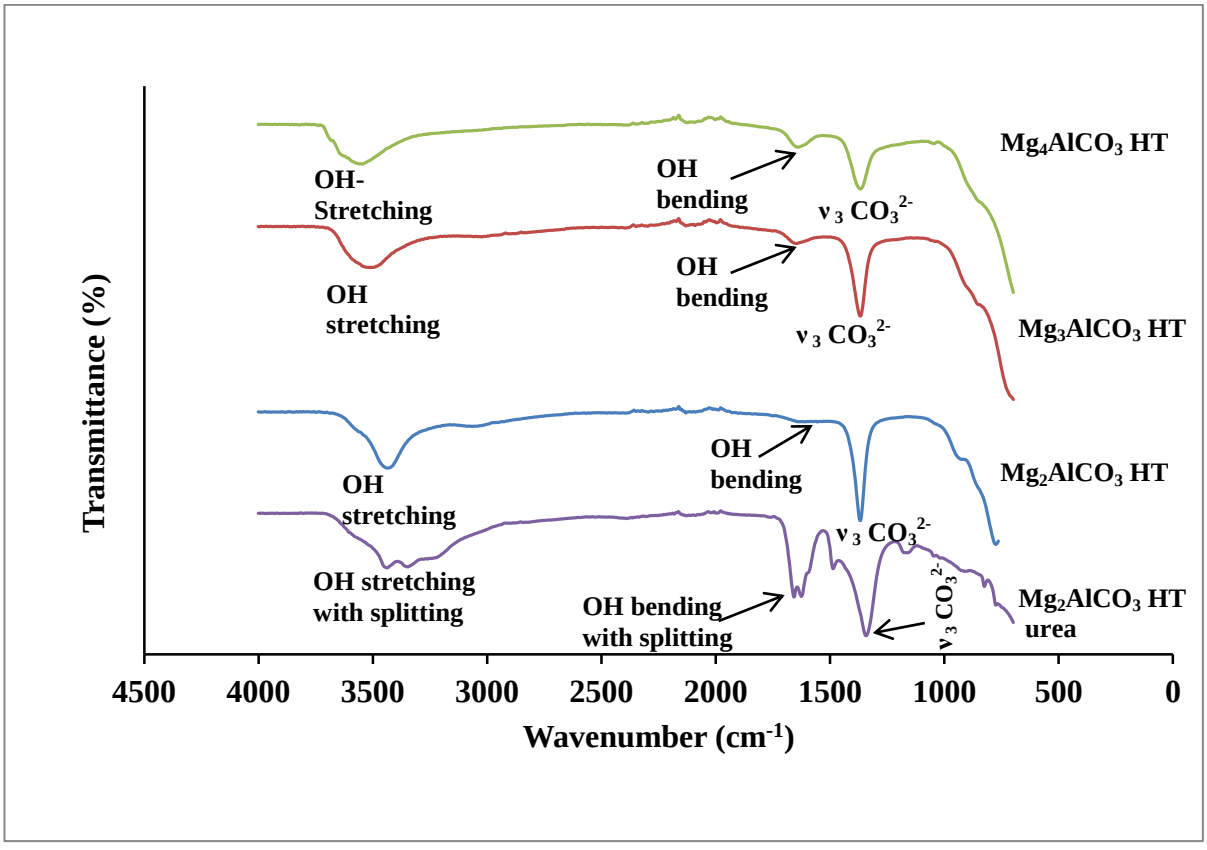

Fig.3.10: FT-IR spectra of the series of as- synthesised $MgAlCO_3$ hydrotalcites with varying composition of layers by co-precipitation (co-pptn) and urea hydrolysis methods (urea).

Fig.3.11: shows the FT-IR spectra of $ZnAlCO_3$ hydrotalcite- like compounds of Zn/Al mole ratios of 2, 3 and 4. The broad absorption bands between 3391 and 3500cm^{-1} are attributed to the hydrogen bond stretching of O–H group and hydrogen bonding between water and interlayer CO_3^{2-} anion[140]. The absorption peaks at 754cm^{-1} for Zn_2AlCO_3 by urea; 769cm^{1} for Zn_3AlCO_3; 766cm^{-1} for Zn_4AlCO_3; and 779cm^{-1} for Zn_2AlCO_3 by co-precipitation method are related to the metal–oxygen v(M–O–M) thus confirming the structure of a layered double hydroxide. The peaks located at about 1359 cm^{-1} (Zn_2AlCO_3 by urea); 1361 cm^{-1} (Zn_3AlCO_3); 1361 cm^{-1} (Zn_4AlCO_3); 1360 cm^{-1} (Zn_2AlCO_3 by co-pptn) are attributed to O-C-O stretching vibrations of the carbonate anions which confirms the presence of CO_3^{2-} as the intercalated anion in the interlayer region. There are significant variations in the band positions of the spectra of these samples and this may be due to a possibility of differences in order/disorder present in the stacking of the layers.

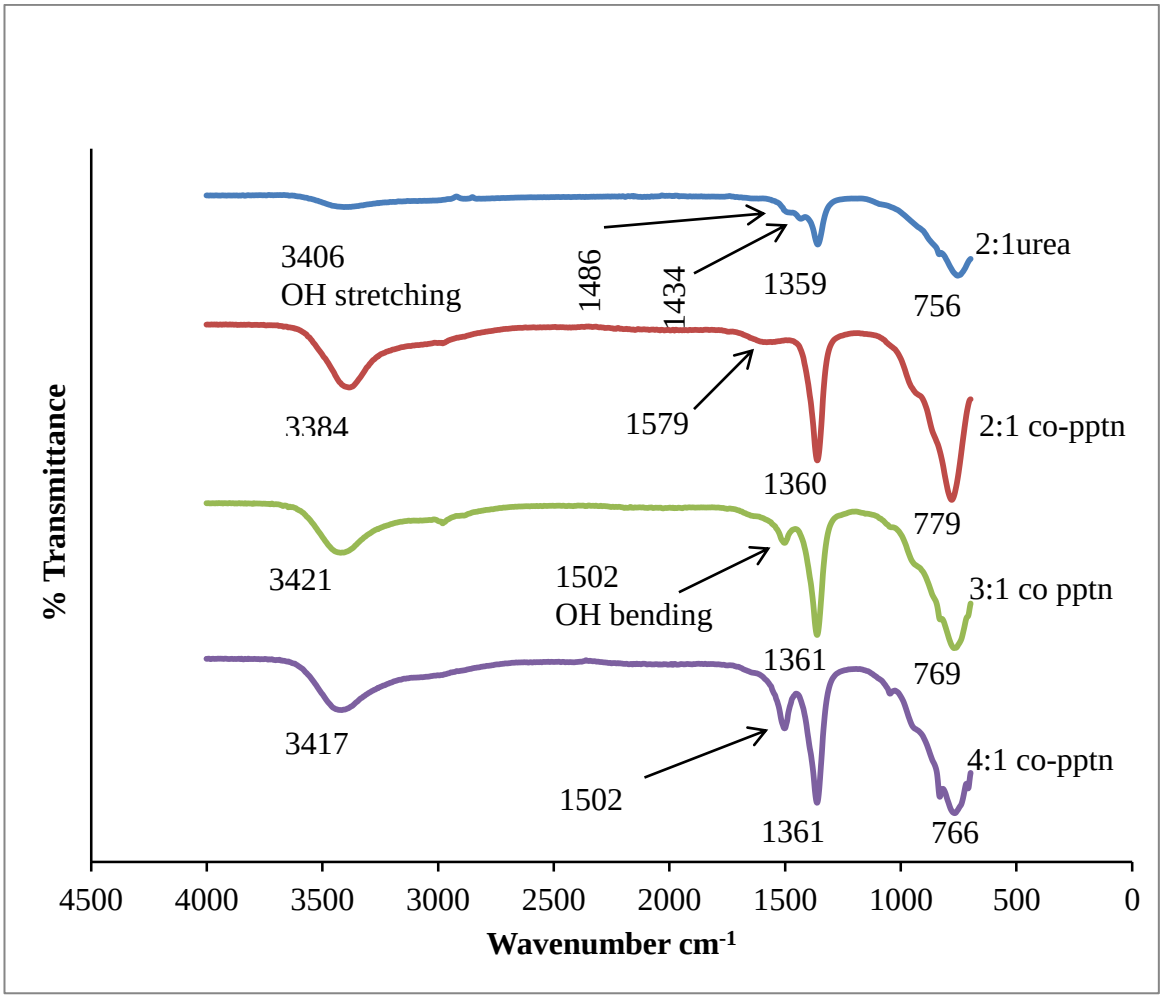

Fig.3.11: FT-IR spectra of the series of as- synthesised $ZnAlCO_3$ hydrotalcites with varying composition of layers by co-precipitation (co-pptn) and urea hydrolysis methods (urea).

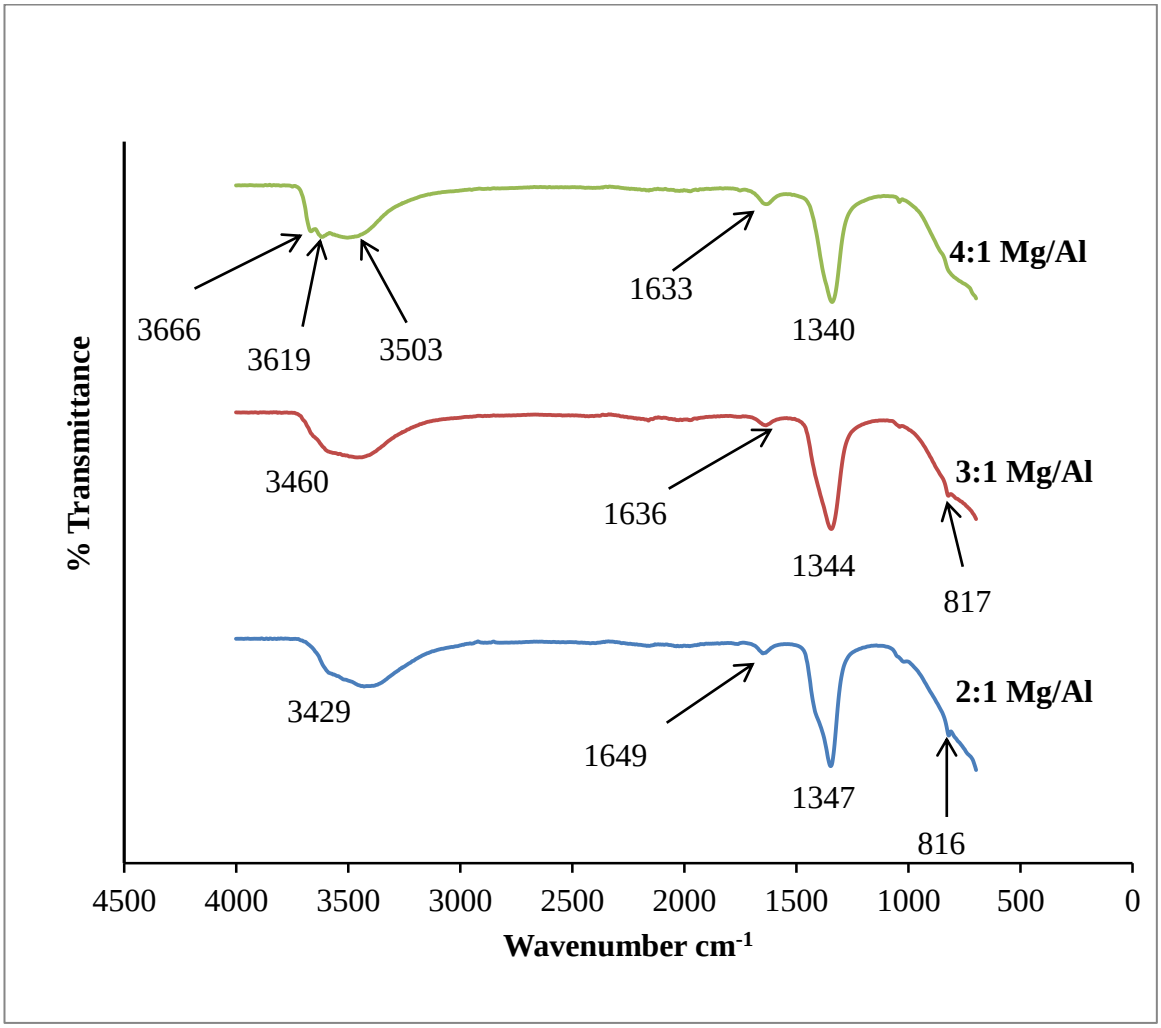

Fig.3.12: FT-IR spectra of the various $MgAlNO_3$ hydrotalcite-like compounds synthesised with varying layer composition by co-precipitation method.

The spectra in Fig.3.12 shows the absorption peaks of the synthesised nitrate hydrotalcite-like compounds. They show good agreement with each other and with the literature, but with variations in band positions also. The broad bands around 3400 – 3600cm^{-1} are attributed to the stretching modes of the OH groups that exist in the hydroxide layer and the gallery space water molecules and anions[22, 141]. The observed degenerates in Mg_4AlNO_3 HT may be due to the decreased effect of nitrate content and hydrogen bonding caused by reduced charge density and decreased electrostatic

interaction between the MgAlOH layers and the interlayer NO_3^- anions. This decreased charge density may also be responsible for the shifting of the bands to higher frequencies from Mg_2AlNO_3 to Mg_4AlNO_3, from differences in the amount of water and nitrate anions accommodated in the interlayer regions. The weak bands around $1633-1649cm^{-1}$ are attributed to the bending vibration of water while the relatively sharp and intense peaks at $1340cm^{-1}$ (Mg_4AlNO_3); $1344cm^{-1}$ (Mg_3AlNO_3) and $1347cm^{-1}$ (Mg_2AlNO_3) showed absorption bands of nitrate thus confirming the intercalation of nitrate within the interlayer gallery space.

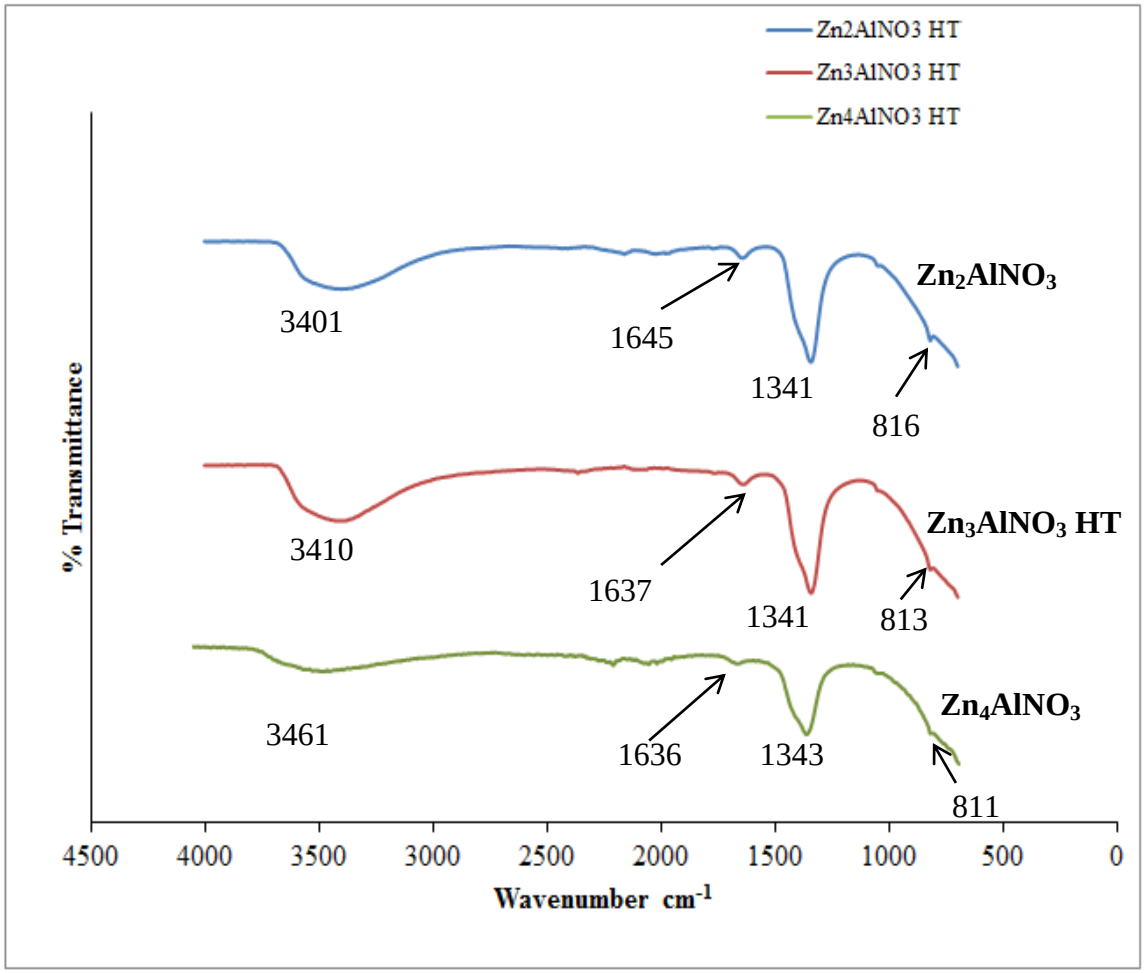

Fig.3.13: FT-IR spectra of the various $ZnAlNO_3$ hydrotalcites synthesised with varying with varying layer composition by co-precipitation.

FT-IR study of the Zinc aluminium hydroxynitrate hydrotalcites was also carried out to identify the presence of anionic groups in these HTlcs. The spectra are shown in Fig.3.13. Like the previous hydrotalcite-like compounds, the broad absorption peaks around 3300-3500 cm^{-1} are attributed to water hydroxyl stretching vibration in the brucite like layers and hydrogen bonding between water and nitrate anion in the interlayer region[25, 144, 145]. The weak bands around 1635-1645cm^{-1} are attributed to the bending vibration of water which may be due to interlayer water while the relatively sharp and intense peaks at 1343 cm^{-1} (Zn_4AlNO_3) and 1341cm^{-1} (Zn_2AlNO_3 HTlc and Zn_3AlNO_3) show absorption of nitrate. The slight asymmetry to the nitrate band suggests that there may be a small amount of residual carbonate present.

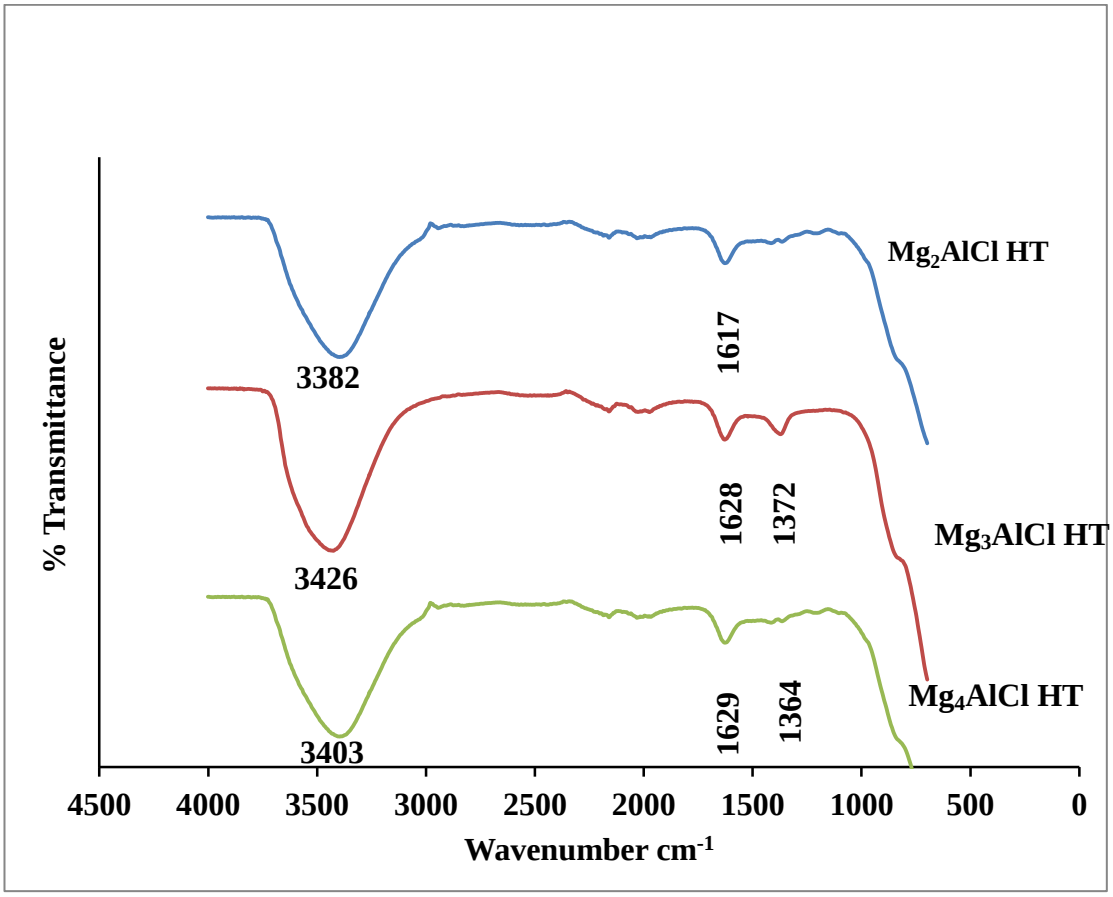

Fig.3.14: FT-IR spectra of the series of MgAlCl hydrotalcites synthesised with varying layer composition.

FT-IR spectra of MgAlCl hydrotalcite-like compounds illustrated in (Fig.3.14) show similar features to previous samples. OH stretching vibrations between 3380cm^{-1} and 3500cm^{-1} and bending vibrations of water at 1617 cm^{-1}-1628 cm^{-1}. Additional vibration bands at 1372 cm^{-1} (Mg_3AlCl) HTlc, and 1364cm^{-1} (Mg_4AlCl_3) HTlc) may be due to stretching vibration of the carbonate anion indicating the presence of carbonate anion in these samples. Hydrotalcites are known to have high affinity for carbonate such that despite the precautions observed, samples were still contaminated by carbonate from atmospheric CO_2.

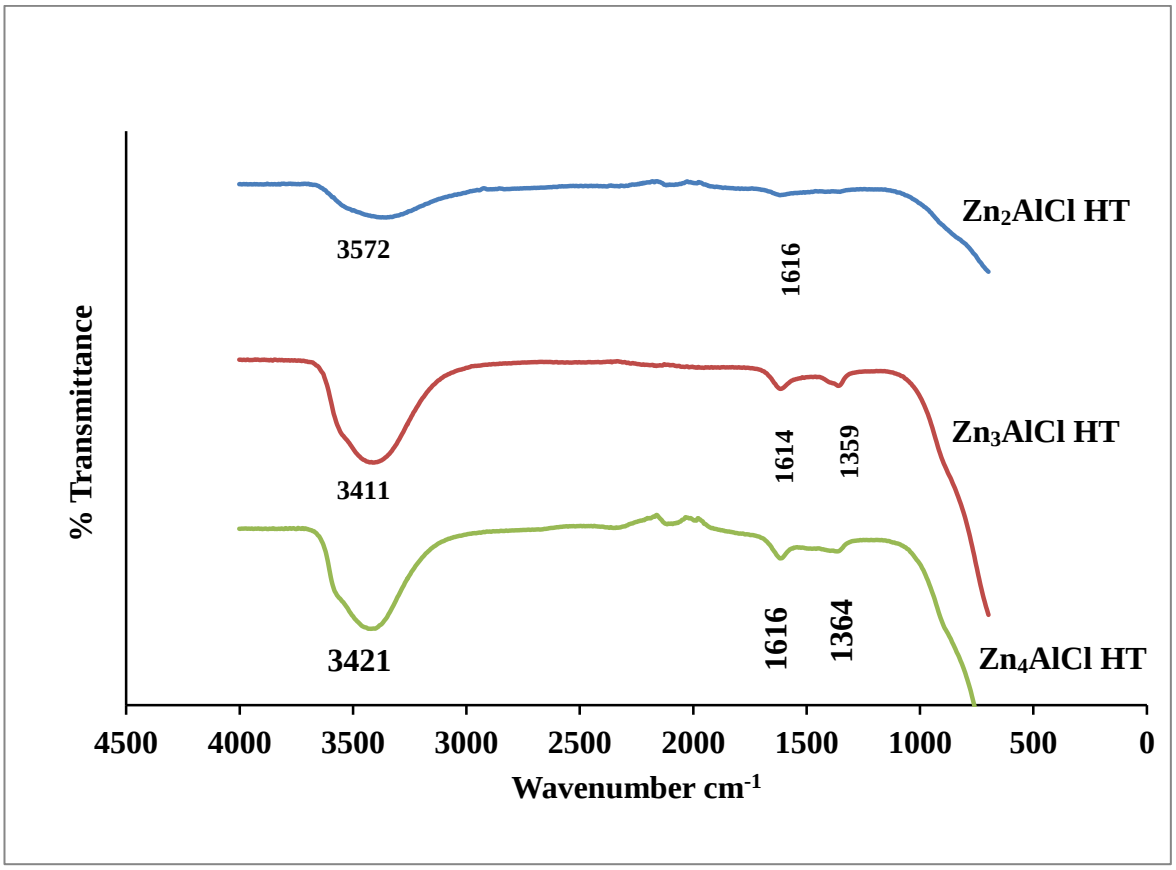

Fig.3.15: FT-IR spectra of the series of ZnAlCl hydrotalcites synthesised with varying layer composition by co-precipitation.

These spectra of the series of ZnAlCl hydrotalcites are consistent with their counterparts considered previously. The Zn_3AlCl and Zn_4AlCl hydrotalcites also showed traces of carbonate contamination.

3.8 Thermal analysis

This section shows the thermal behaviour of the various hydrotalcite-like compounds. Figs.3.16-3.23 show the TGA-MS plots and the ion current curves for the series of CO_3^{2-}-hydrotalcite-like compounds synthesised while Figs.3.24-3.35 show those of NO_3^- and Cl^- hydrotalcite-like compounds (HTlcs).

3.8.1: Thermal analysis of $MgAlCO_3$ hydrotalcite-like series

Thermogravimetric analysis measurements were carried out to investigate the phase changes during the thermal analysis of these samples. The first wt. loss occurred at lower temperature below 280^{o}C (precisely between 40-280^{o}C) and this can be attributed to the removal of water from the interior of the gallery surfaces and also water physiosorbed on the external sample surfaces. This step is reversible as it does not alter or affect the structure of the hydrotalcite-like compounds. The ion current curve showed that this water was removed at ca. 266^{o}C for Mg_2AlCO_3, 256^{o}C for Mg_3AlCO_3 and 226^{o}C for Mg_4AlCO_3 hydrotalcites. This process accounts for 16% for Mg_2AlCO_3, 15% for Mg_3AlCO_3 and 13% for for Mg_4AlCO_3 hydrotalcites. The second weight loss step occurred at higher temperature (310-500^{o}C), and this may be due to withdrawal of water from the metal hydroxide layers (loss of hydroxyl group) as well as breakdown of the

carbonate anion present in the galleries to release CO_2. The ion current curve shows that Mg_2AlCO_3 lost water at 422^oC and CO_2 gas at 424^oC while Mg_3AlCO_3 lost water at 423^oC and CO_2 at 428^oC, and Mg_4AlCO_3 hydrotalcite lost water at 406^oC and CO_2 gas at 403^oC. It is clearly observed that the loss of hydroxyl groups from the hydroxide layers (dehydroxylation) occurred at the same time as the removal of carbonate (decarbonation) from the galleries in all three samples. At this point, the hydrotalcite structure is broken down leading to the formation of defect metal oxides which gradually gain stability as the thermal temperature increases. The hydrotalcite-like compounds can still be regenerated from these metal oxides at these temperatures (400-500^oC) where simultaneous dehydroxylation and decarbonation happened, but once the temperature is elevated beyond 500^oC, restoring or recovering the hydrotalcite structure is difficult or may be impossible. This process accounts for a wt loss of 23.5% for Mg_2AlCO_3, 22.2% for Mg_3AlCO_3 and 29% for Mg_4AlCO_3 hydrotalcite. Heating the $MgAlCO_3$ hydrotalcite series synthesised in this study beyond 500^oC through to 900^oC transforms them into metal oxides and then into stable spinel with no further weight loss steps accompanying the transformation as can be seen in the TG-DTA curves. The total weight loss at 900^oC is thus 43.4% for Mg_2AlCO_3, 43.2% for Mg_3AlCO_3 and 42.8% for Mg_4AlCO_3. The point at which this material loses water from the layers and interlayers and, at the same time losing the intercalated carbonate anions and then collapsing, can be taken as an indication for thermal stability, and is as follows: Mg_4AlCO_3< Mg_2AlCO_3< Mg_3AlCO_3, meaning that Mg_3AlCO_3 HTlc is more stable than the Mg_2AlCO_3 HTlc while Mg_4AlCO_3 HTlc showed the lowest stability. The decrease in stability in the 4:1 sample may be as a result of decreased layer charge, while generally

stability would be expected to increase as the Mg^{2+} content increases[146, 147]. A delay in dehydroxylation of the layers demonstrates a more stable hydrotalcite-like compound.

Other observations (thermal transitions and temperature) are in line with the findings of other researchers[47, 148, 149, 150, 151]. They also observed thermal transitions with similar decomposition domains which they attributed to the removal of interparticle pore water in some instance, loss of surface adsorbed and interlayer water, the removal of structural water from the hydroxide layers happening together with the removal of carbonate from the gallery, and the thermal transition that produced the mixed oxides of the metal cations. The following thermal break down processes may be proposed for this sample (Mg_2AlCO_3 HTlc):

$$Mg_2Al(OH)_6(CO_3)_{1/2}.mH_2O \longrightarrow Mg_2Al(OH)_6(CO_3)_{1/2} + m\ H_2O$$

$$Mg_2Al(OH)_6(CO_3)_{1/2} \longrightarrow Mg_2AlO_{3.5} + \frac{1}{2}CO_2 + 3\ H_2O$$

$$Mg_2AlO_{3.5} \longrightarrow \frac{1}{2}MgAl_2O_4 + \frac{3}{2}MgO$$

The following reactions may be proposed for the break down process for Mg_3AlCO_3 and Mg_4AlCO_3 hydrotalcites:

$$Mg_3Al(OH)_8(CO_3)_{1/2}.mH_2O \xrightarrow[\text{Dehydration}]{105 - 280^oC} Mg_3Al(OH)_8(CO_3)_{1/2} + m\ H_2O$$

$$Mg_3Al(OH)_8(CO_3)_{1/2} \xrightarrow[\text{Dehydroxylation/ dehydration}]{430^oC} Mg_3AlO_{4.5} + \frac{1}{2}CO_2 + 4\ H_2O$$

$$Mg_3AlO_{4.5} \xrightarrow[\text{Decomposition}]{600^oC - 900^oC} 2.5\,MgO + \frac{1}{2}MgAl_2O_4$$

$$Mg_4Al(OH)_{10}(CO_3)_{1/2}.mH_2O \longrightarrow Mg_4Al(OH)_{10}(CO_3)_{1/2} + mH_2O$$

$$Mg_4Al(H_2O)_{10}(CO_3)_{1/2} \longrightarrow Mg_4AlO_{5.5} + \frac{1}{2}CO_2 + 5\,H_2O$$

$$Mg_4AlO_{5.5} \longrightarrow \frac{1}{2}\,MgAl_2O_4 + \frac{7}{2}\,MgO$$

XRD analysis of calcined and TGA products confirmed these processes and products of thermal break down. The drying procedure of hydrotalcites, the influence of layer cations, and the stability of interlamellar molecules can affect the stability of hydrotalcites[152].

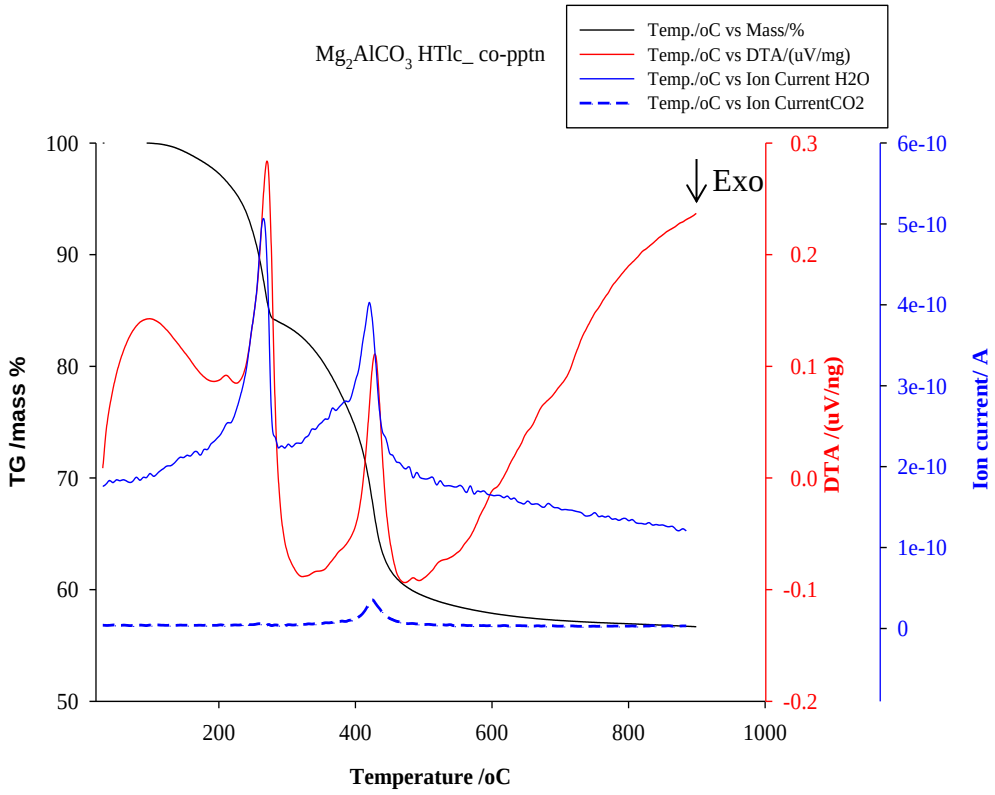

Fig.3.16: TG, DTA and gas evolution ion current curves of Mg_2AlCO_3 HTlc

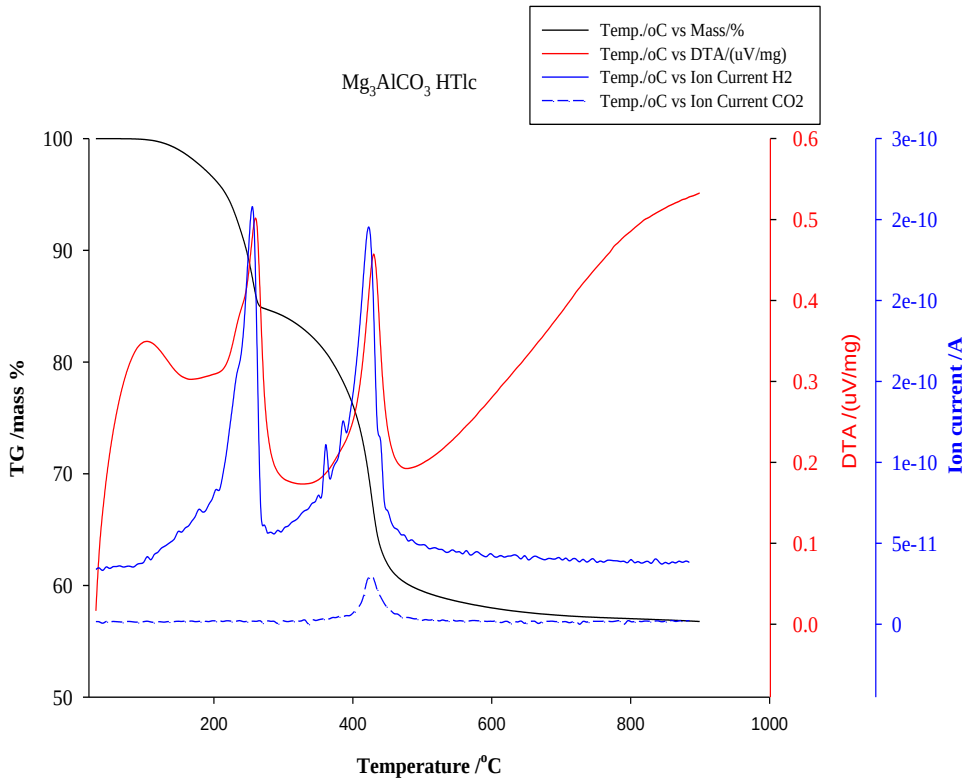

Fig.3.17: TG, DTA and gas evolution ion current curves of Mg_3AlCO_3 HTlc

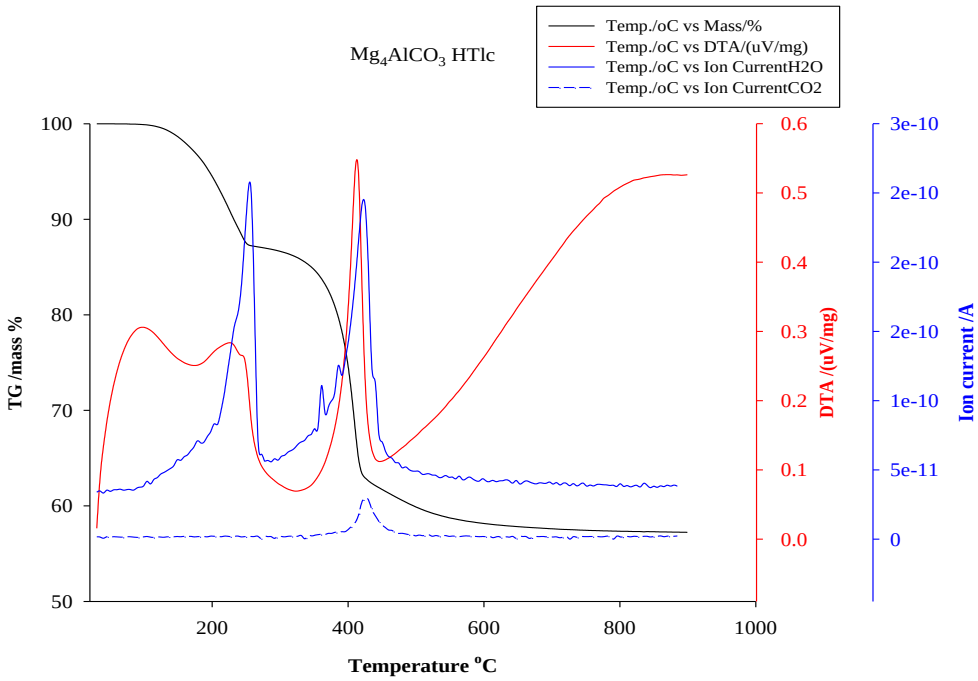

Fig.3.18: TG, DTA and gas evolution ion current curves of Mg_4AlCO_3HTlc.

PXRD patterns of TGA derivatives after heat treatment up to 900^{o}C under an oxygen atmosphere at the ramp rate of 5°C/min showed metal oxide phases. The phases were identified using the powder diffraction file (PDF- 4 + 2012) database maintained by the International Centre for Diffraction Data (ICDD)[153] and showed good match with the peak of magnesium aluminium oxide ($Mg_{0.97}Al_{0.03}O$ corresponding to PDF card number 04-006-8246). The formation of the defect magnesium aluminium oxide is due to evolution of water and carbon dioxide from the lattice structure. The FT-IR spectra of the TGA derivative confirms the removal of water and carbonate anion.

The variable temperature X-ray diffraction (VTXRD) pattern of as-synthesised Mg_2AlCO_3 HTlc is shown in Fig.3.19. It was observed that between 50-150^{o}C, the hydrotalcite retains its well-ordered structure with no variation in d-spacing. Between 200-250^{o}C, a slight change in d-spacing was noted with its integrity still maintained but by 300^{o}C, the amorphous form of the hydrotalcite emerged. This was closely followed by the first appearance of broad weak peaks of the periclase MgO at 350^{o}C which was maintained till 500^{o}C and thereafter significantly sharpened up till the emergence of the spinel phase at 900^{o}C. These observations are consistent with TGA results.

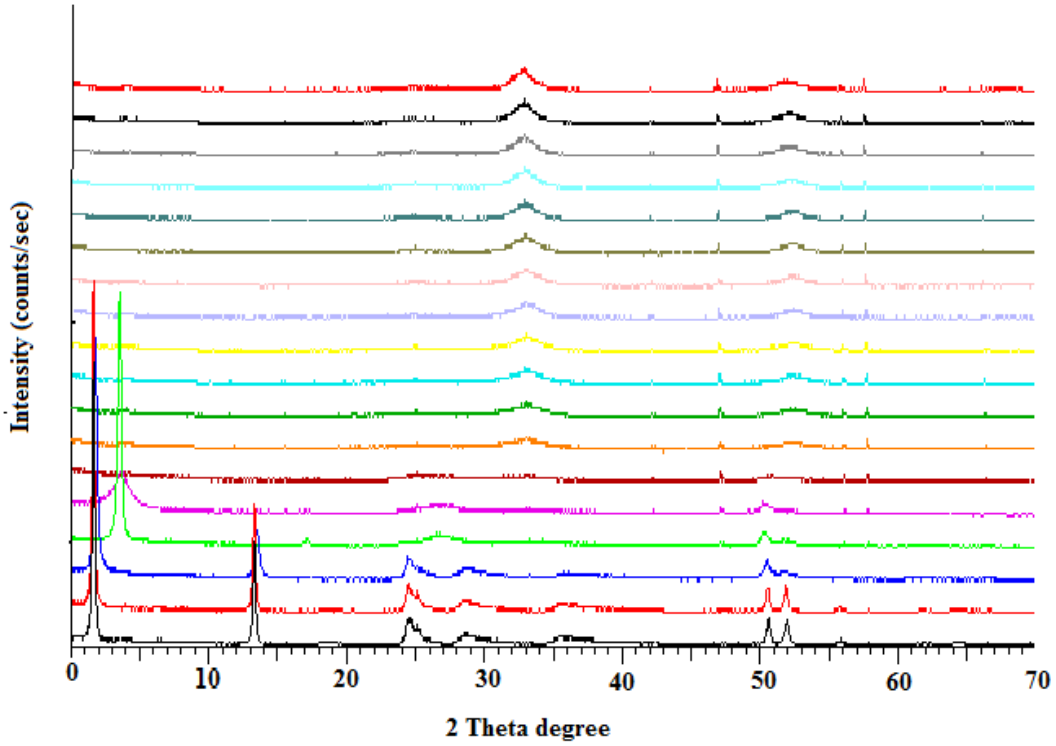

Fig.3.19: Powder XRD patterns of Mg_2AlCO_3 HTlc at different temperatures from 50°C to 900°C with step size of 50°C in air.

3.8.2: Thermal analysis of Mg_2AlCO_3 HTlcs prepared by the urea method.

Thermal analysis of Mg_2AlCO_3 hydrotalcite synthesised by the urea hydrolysis method is shown in Fig.3.20. The thermal analysis of this sample basically followed the same trend as the preceding compounds with a total mass loss of 33.4%. The first wt. loss at lower temperature is observed to occur between 40-240^oC. The DTA represents this process as a broad endothermic peak centered at 105^oC and another, a little less broad with maximum at 233^oC. This is also shown on the ion current curves that water was lost in two steps, at ca. 146^oC and at 234^oC. The other wt. loss involving the simultaneous removal of interlayer (gallery) carbonate, water and abstraction of

hydroxyl groups from the layers occurred at ca. 432^{o}C (DTA). This sample show a total wt. loss of 33.4%, and like the other samples, the final phase is the spinel.

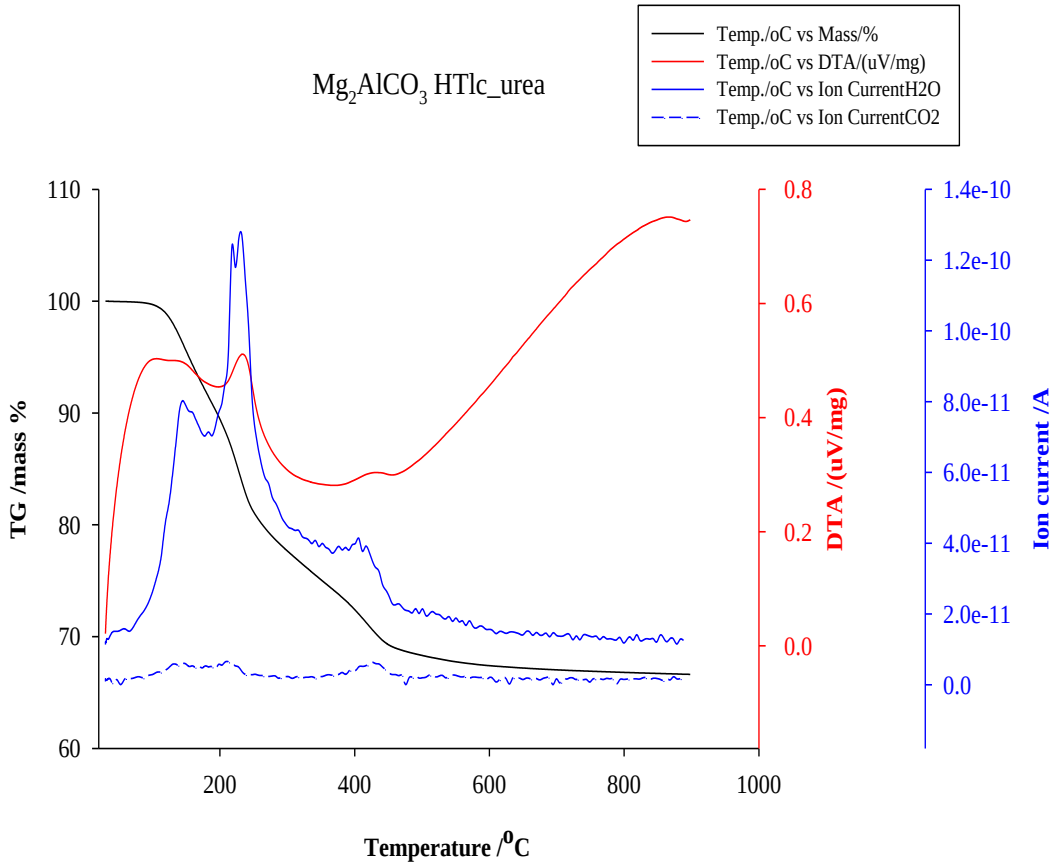

Fig.3.20: TG, DTA and gas evolution ion current curves of Mg_2AlCO_3 HTlc by urea method.

3.8.3: Thermal analysis of $ZnAlCO_3$ HTlcs

The thermal behaviours of $ZnAlCO_3$ HTlcs with different molar ratios are shown in Figs.3.21–3.25. Generally, hydrotalcites exhibit thermal behaviour characterised by two transition stages as described previously in section 3.9.1. These stages or steps are not clearly resolved on the TG curves for the $ZnAlCO_3$ hydrotalcite series. There appeared to be series of overlapping processes[154] during the decomposition of these samples. However, the DTA clearly show three endothermic peaks in all three samples. The first

change that occurs during thermal analysis of this type of sample is associated with the removal of water physisorbed on the surfaces of the hydrotalcites and from the interior surfaces of the galleries and it usually occurs at low temperature. For these samples, this may have happened around 90-140^{o}C, followed by the second step involving simultaneous abstraction of water from the layers and carbonate from the internal galleries leading to collapse of the structure. This step and the former may have overlapped and is represented on the DTA by the endothermic peak cantered at 235^{o}C for Zn_2AlCO_3 HT, 222^{o}C for Zn_3AlCO_3 HT and at 212^{o}C for Zn_4AlCO_3 HT. The mass spectrometry analysis showed the evolution of H_2O in a single step at 231^{o}C and CO_2 at 225^{o}C for Zn_2AlCO_3 HT, H_2O at 216^{o}C and CO_2 at 218^{o}C for Zn_3AlCO_3 HT and for Zn_4AlCO_3 HT, H_2O is released in 2 steps at 200^{o}C and 246^{o}C while CO_2 is released at 268^{o}C. By 350^{o}C, evolution was complete for these samples. The strong endothermic peaks around 740°C - 800°C may be due to heat absorbed during the formation into the spinel phase, $ZnAl_2O_4$[155, 156]. Total weight losses of 32, 31 and 30% respectively were derived. The less defined transitions in the thermograms of these materials as compared to their $MgAlCO_3$ counterparts are due to decomposition of carbonate and dehydroxylation of the layers occurring at a lower temperature in the ZnAl compounds. The stability of this series is in the order Zn_2AlCO_3> Zn_3AlCO_3> Zn_4AlCO_3 and they are less stable than their $MgAlCO_3$ counterparts. The proposed equations for the decomposition processes are given below:

$$Zn_2Al(OH)_6(CO_3)_{1/2}.\,mH_2O \longrightarrow Zn_2Al(OH)_6(CO_3)_{1/2} + mH_2O$$

$$Zn_2Al(OH)_6(CO_3)_{1/2} \longrightarrow Zn_2AlO_{3.5} + 3\,H_2O + \frac{1}{2}CO_2$$

$$Zn_2AlO_{3.5} \longrightarrow \frac{3}{2}ZnO + \frac{1}{2}ZnAl_2O_4$$

$$Zn_3Al(OH)_8(CO_3)_{1/2}.\ mH_2O \longrightarrow Zn_3Al(OH)_8(CO_3)_{1/2} + mH_2O$$

$$Zn_3Al(OH)_8(CO_3)_{1/2} \longrightarrow Zn_3AlO_{4.5} + 4H_2O + \frac{1}{2}CO_2$$

$$Zn_3AlO_{4.5} \longrightarrow 2.5\ ZnO + + \frac{1}{2}\ ZnAl_2O_4$$

$$Zn_4Al(OH)_{10}(CO_3)_{1/2}.\ mH_2O \longrightarrow Zn_4Al(OH)_{10}(CO_3)_{1/2} + mH_2O$$

$$Zn_4Al(OH)_{10}(CO_3)_{1/2} \longrightarrow Zn_4AlO_{5.5} + 5H_2O + \frac{1}{2}CO_2$$

$$Zn_4AlO_{5.5} \longrightarrow 3.5ZnO + \frac{1}{2}ZnAl_2O_4$$

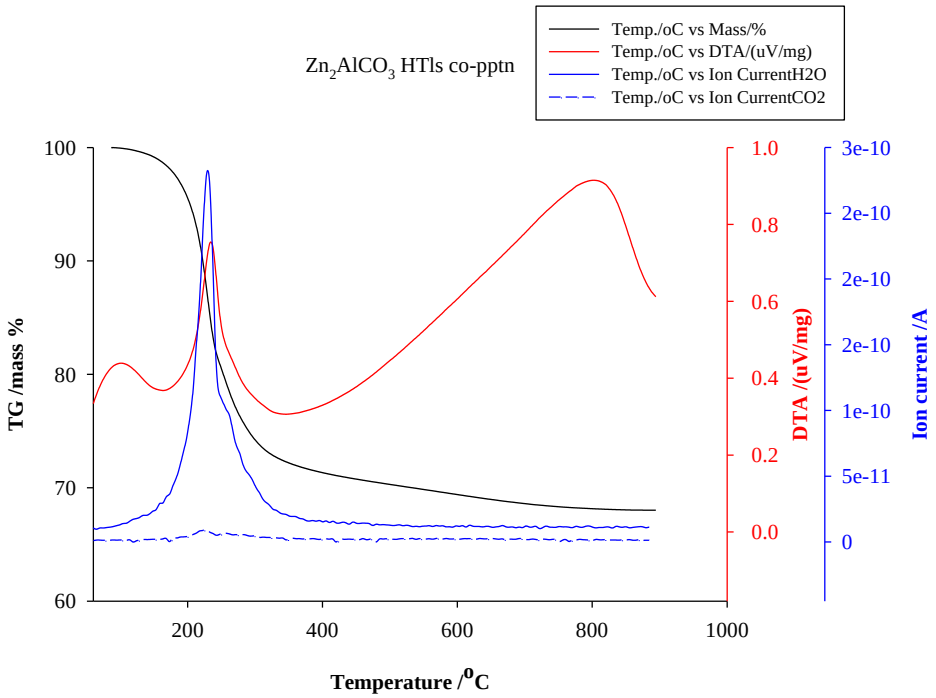

Fig.3.21: TG, DTA and gas evolution ion current curves of Zn_2AlCO_3 HTlc by co-precipitation method.

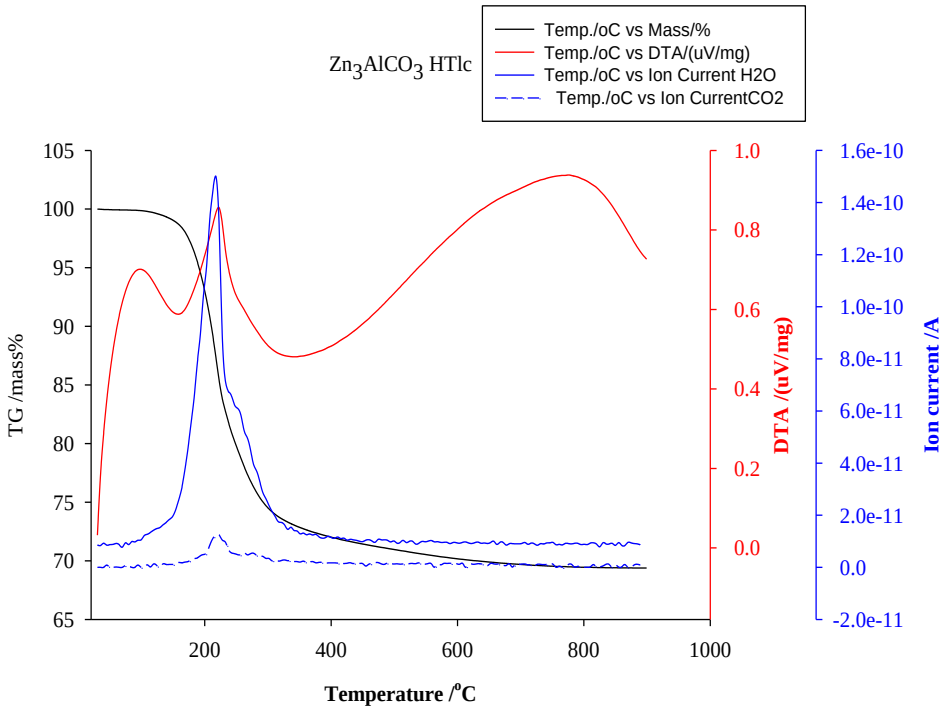

Fig.3.22: TG, DTA and gas evolution ion current curves of Zn_3AlCO_3 HTlc by co-precipitation method.

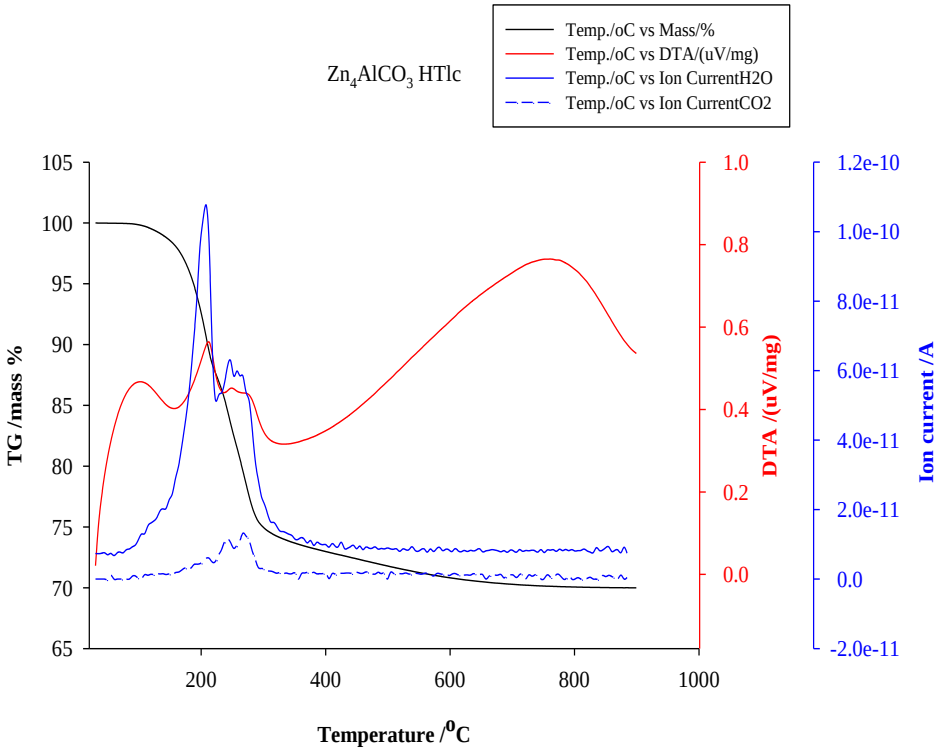

Fig.3.23: TG, DTA and gas evolution ion current curves of Zn_4AlCO_3 HTlc by co-precipitation method.

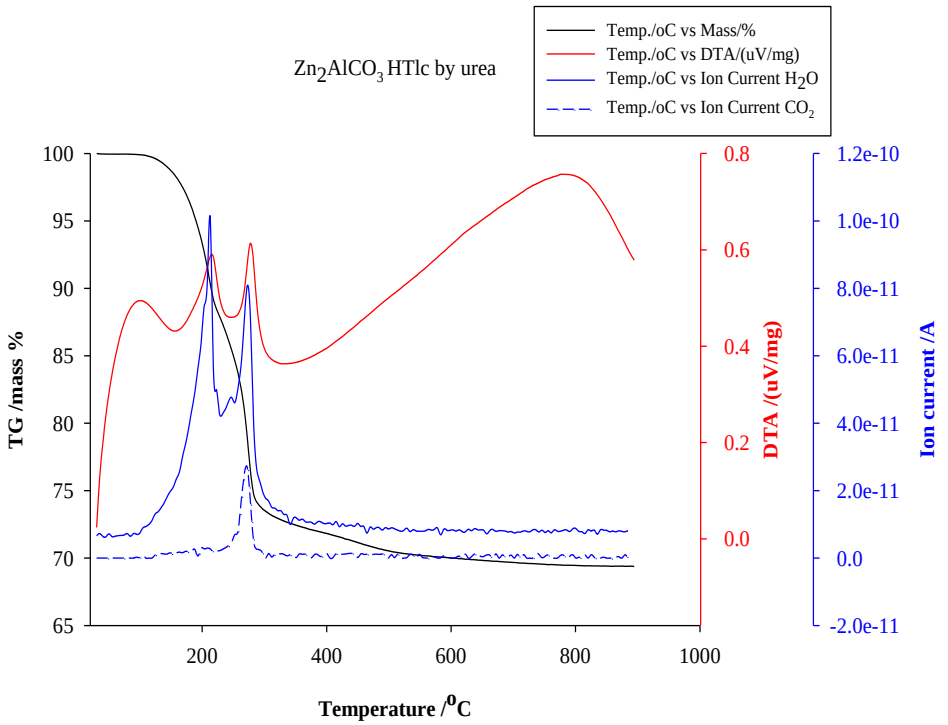

Fig.3.24: TG, DTA and gas evolution ion current curves of Zn_2AlCO_3 HTlc by urea

For the Zn_2AlCO_3-urea sample, the weight losses observed in the TG curve are slightly better resolved, due to improved order, though the same trend of thermal behaviour was observed. Here the first process is represented by two endothermic peaks on the DTA centered at ca. 101 and 216^oC. This accounts for 12% wt. loss. The mass spectrometry analysis shows that water was released at ca. 211^oC. The other wt. loss step is centered at ca.278^oC and it represents the process in which the sample starts to crumble due to loss of carbonate (at ca.271^oC) from within the galleries, and abstraction of water (at ca. 274^oC) from the layers. This step accounts for 19% wt. loss. By about 400^oC, the removal of the carbonate anion from the gallery would have been almost complete, and further heating would transform the hydrotalcite into ZnO and $ZnAl_2O_4$ just as it is with other samples.

3.8.4: Thermal analysis and structural stability of $MgAlNO_3$ HTlcs

The thermal curve comprising TG, DTA and MS curves is illustrated in Figs.3.25-3.27. The thermal curve is basically depicting similar thermal behaviour as previous samples with little variations in the onset and offset temperatures, weight changes and residual weights. For instance, the weight loss for Mg_2AlNO_3 HTlc, began at about 130^{o}C and terminates at about 240^{o}C for the first transition step. This is shown on the DTA as a broad endothermic peak with a maximum at 173^{o}C and is ascribed to the elimination of gallery water. The second weight loss step is centered at 423^{o}C, with mass spectrometry analysis of outflowing gases showing water removal at 414^{o}C, NO at 410^{o}C and CO_2 at 414^{o}C. By 520^{o}C dehydroxylation of the layers and the removal of nitrate from the galleries (interlayers) was completed.

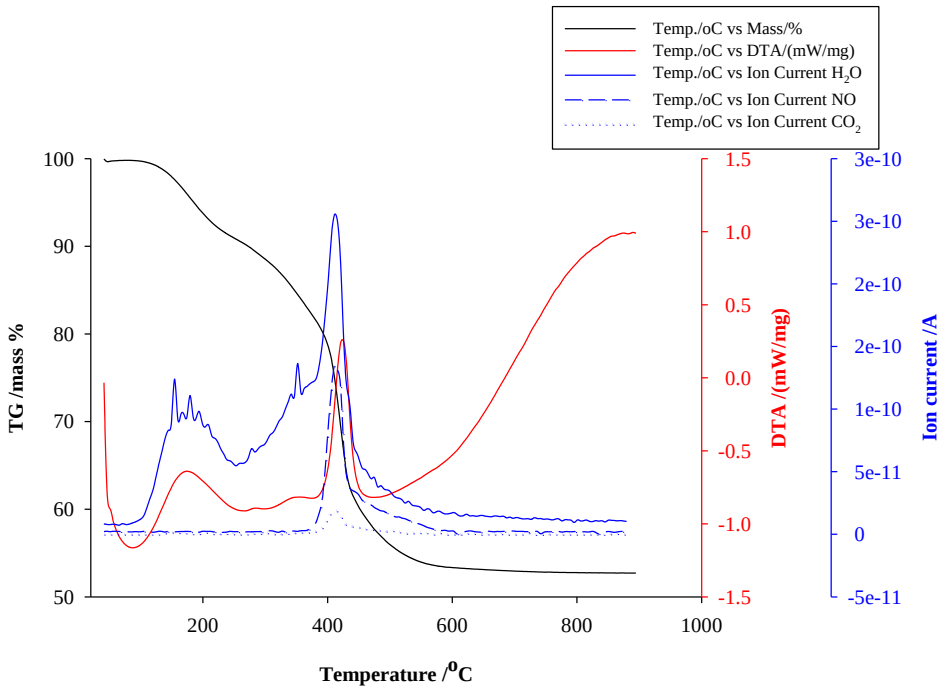

Fig.3.25: TG, DTA and gas evolution ion current curves of Mg_2AlNO_3 HTlc

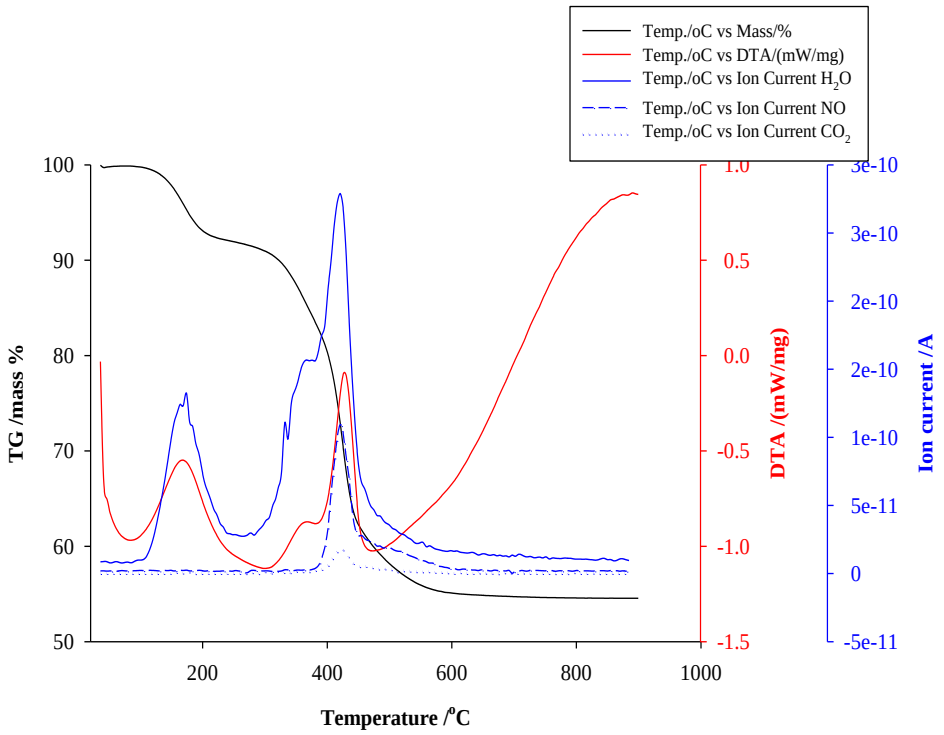

Fig.3.26: TG, DTA and gas evolution ion current curves of Mg_3AlNO_3 HTlc

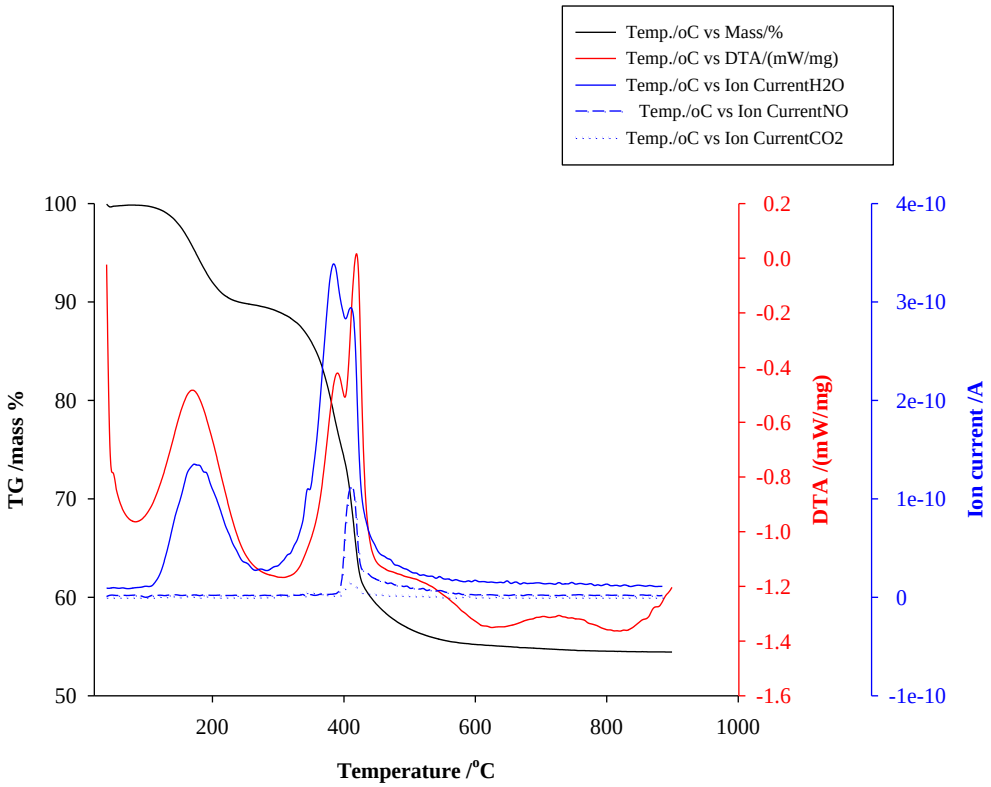

Fig.3.27: TG, DTA and gas evolution ion current curves of Mg_4AlNO_3 HTlc

The total weight loss at 900^{o}C is 47.3%. Mg_3AlNO_3 and Mg_4AlNO_3 HTlcs showed similar behaviour, Mg_3AlNO_3 showed a wt. loss centered at 168^{o}C and another centered at 428^{o}C with a shoulder at 367^{o}C. Its mass spectrometry analysis showed elimination of water at 175 and 422^{o}C and CO_2 and NO at 422^{o}C respectively giving a total wt. loss of 45.5% at 900^{o}C. Similarly, Mg_4AlNO_3 showed a wt. loss centered at 169^{o}C and another centered at 419^{o}C with a shoulder at 391^{o}C. Its mass spectrometry analysis showed elimination of water at 171^{o}C and 385^{o}C, 409^{o}C and CO_2 and NO at 409^{o}C and 414^{o}C respectively giving a total wt. loss of 46% at 900^{o}C. The offset temperatures for the second stage are 520^{o}C, 550^{o}C and 510^{o}C for Mg_2AlNO_3, Mg_3AlNO_3 and Mg_4AlNO_3 respectively and the temperature at which dehydroxylation of the layers and decomposition of the nitrate anions plus residual carbonate in the interlayer occurred are ca. 423.4^{o}C, 427.9^{o}C and 419.2^{o}C respectively. These results are consistent with variable temperature XRD analysis.

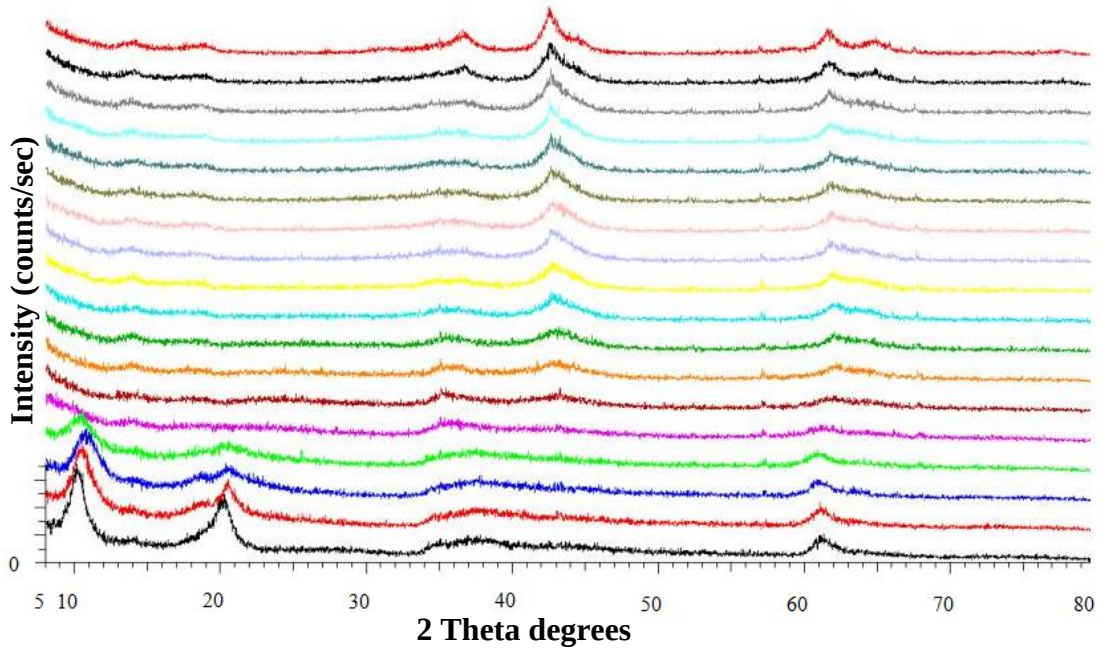

Fig.3.28: Powder XRD patterns of Mg_2AlNO_3 HTlc at different temperatures from 50°C to 900°C with step size of 50°C

Following the simultaneous evolution of H_2O, and residual CO_2 and NO gases at temperature around 400-430°C, the hydrotalcite structures at this point, have broken down into mixed metal oxides as revealed by variable temperature XRD patterns. These results agree with the literature[146, 157, 158].

3.8.5: Thermal analysis and structural stability of $ZnAlNO_3$ HTlcs

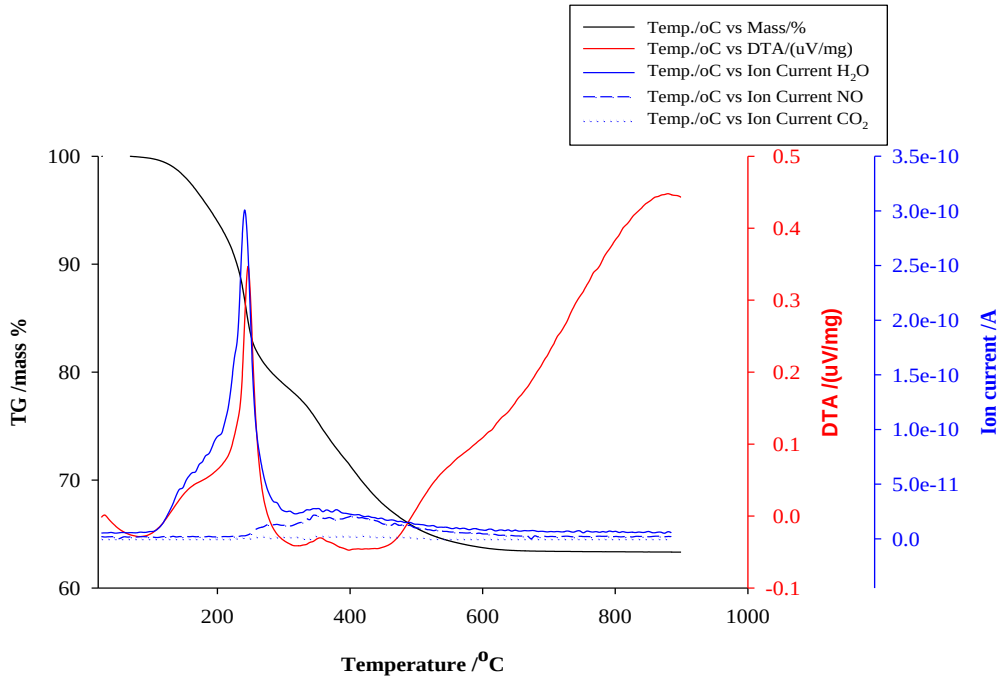

Fig.3.29: TG, DTA and gas evolution ion current curves of Zn_2AlNO_3 HTlc

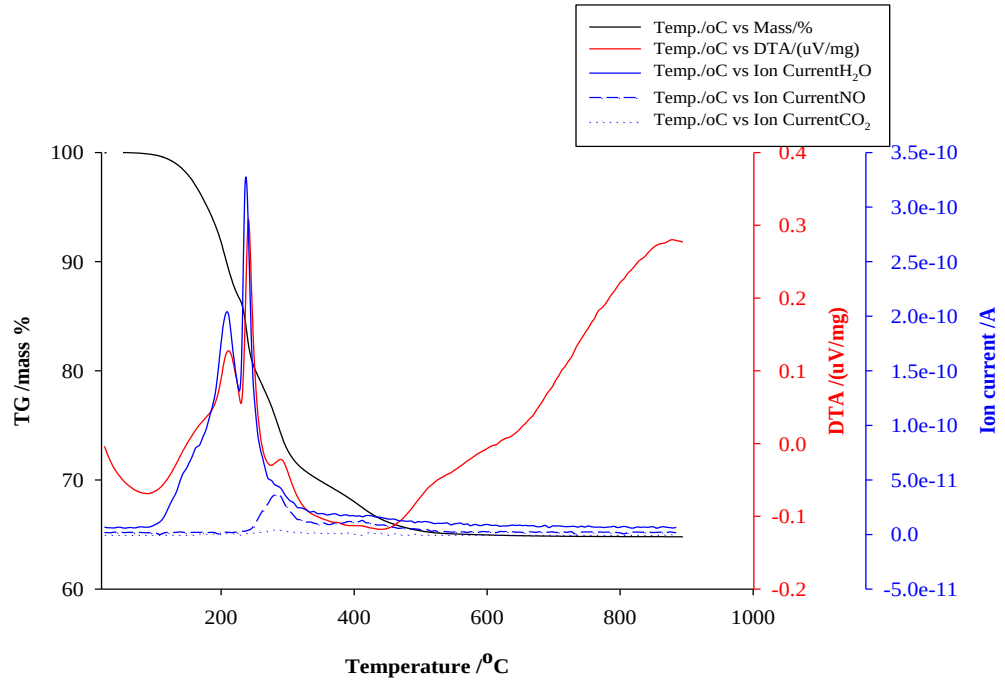

Fig.3.30: TG, DTA and gas evolution ion current curves of Zn_3AlNO_3 HTlc

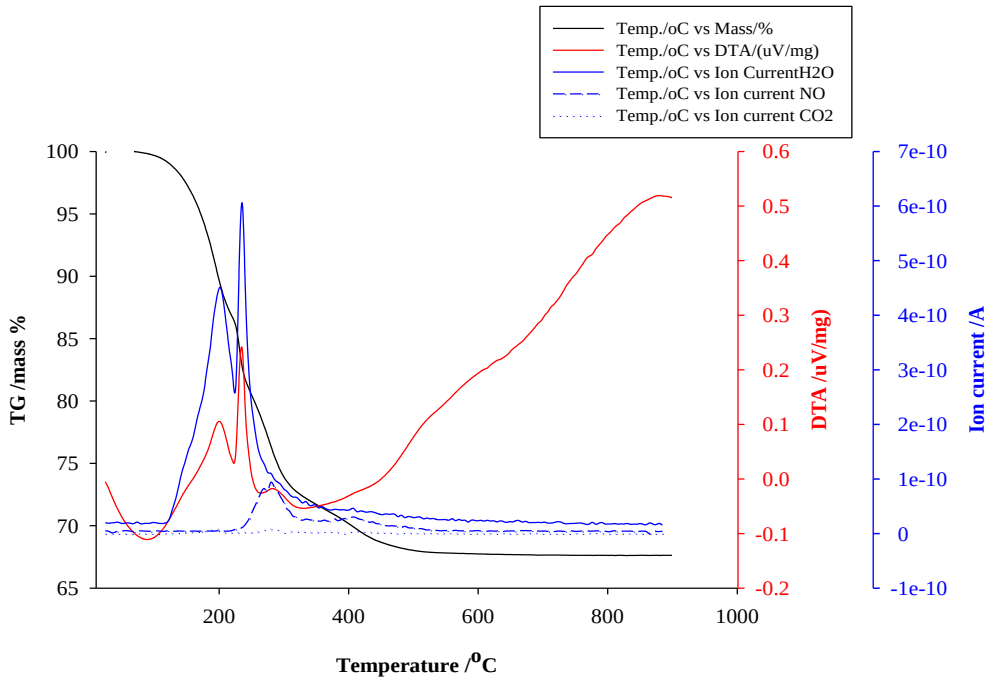

Fig.3.31: TG, DTA and gas evolution ion current curves of Zn_4AlNO_3 HTlc

These samples basically show similar thermal behaviour as those of previous samples with thermal curves typical of hydrotalcites with ZnAl in the layers. The total weight losses at 900°C are 36.7%, 35.2% and 32.4% for Zn_2AlNO_3, Zn_3AlNO_3 and Zn_4AlNO_3 respectively. The DTA curve of Zn_2AlNO_3 showed two endothermic peaks, one sharp and intense at 246°C (with a bump at the base to the left) and another smaller one centered at 355°C. This may mean that the amount of nitrate anion intercalated into the galleries of Zn_2AlNO_3 hydrotalcite is comparably smaller than its $MgAlNO_3$ counterpart. However the mass spectrometry analysis showed elimination of water at 240 and 352°C and NO at 352°C. For Zn_3AlNO_3, the first weight loss accounting for 13.3% wt. loss showed on the DTA curve at ca. 211°C and the ion current curve for m/z equivalent to 18 signifying H_2O loss which corresponds to the removal of interlamellar water molecules. The second weight loss step centered at ca. 241°C occurred in stages

with removal of water at ca. 236°C and NO and residual CO_2 at 282/413°C and 282°C respectively (dehydroxylation of the metal hydroxide layers occurring simultaneously with the decomposition of nitrate plus residual carbonate anions). This second weight loss step accounts for 22% wt. loss. As the Zn/Al mole ratio further increases to 4:1, the temperature of the two weight loss steps decreases due to decreased charge density. This is also evident in the temperature of evolution of H_2O, NO and CO_2. Following this, is the transformation of the collapsed structure into mixed metal oxides between 500- 900°C[159, 160].

3.8.6: Thermal analysis and structural stability of Chloride hydrotalcite-like compounds.

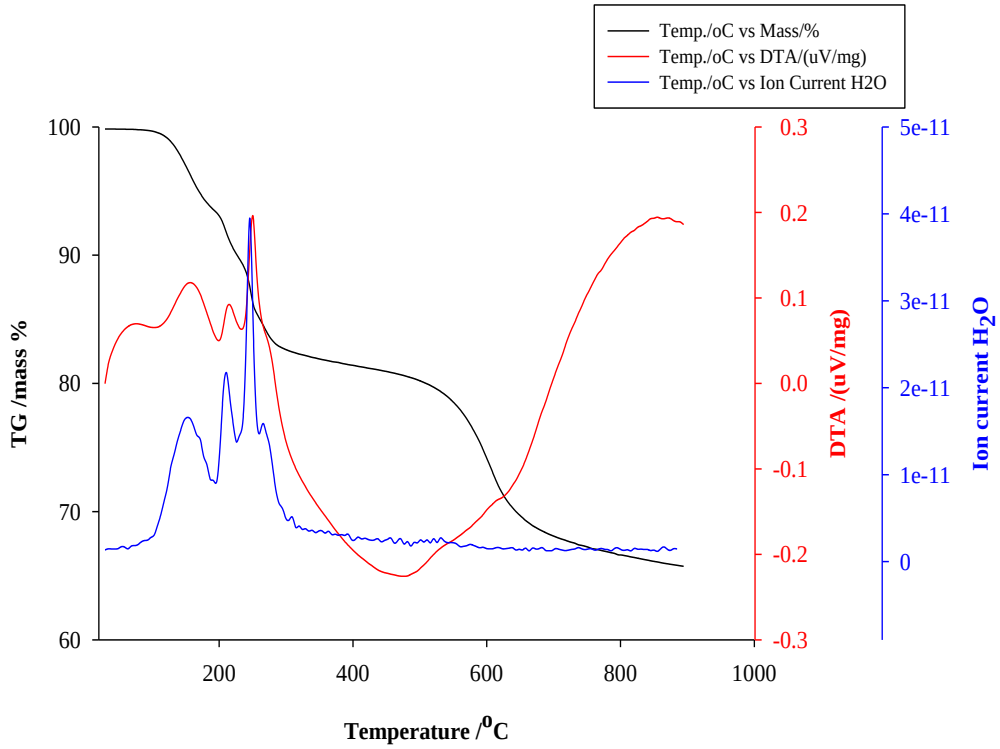

Fig3.32: TG, DTA and gas evolution ion current curves of Zn_2AlCl HTlc

Fig.3.32-35 illustrates the thermal curves of some of the chloride hydrotalcites. They exhibit similar thermal behaviour peculiar to hydrotalcites. Zn_2AlCl is characterised by endothermic effects noted at 76^{o}C, 157^{o}C, 215^{o}C and about 280^{o}C, with the first three associated with dehydration due to removal of surface physisorbed on the surface of the hydrotalcite and water from the inside of the galleries. The mass spectrometry analysis showed elimination of water at 150^{o}C and 210^{o}C. The second mass loss can be attributed to the abstraction of water from the metal hydroxide layers which usually occurs in most hydrotalcites together with decomposition of the interlayer anion resulting into a collapse of the structure, although, the mass spectrometry analysis of outflowing gases did not detect chloride release. This may be due to the low set temperature of the QMS furnace (200^{o}C). However it is possible that chloride was given off at higher temperature but the form could not be ascertained. Miyata[82] in their thermal decomposition study of MgAlCl HT, stated that elimination of OH and Cl^- occurred at 430^{o}C and 480^{o}C respectively and Barriga et al[161] showed in their thermal analysis of ZnAlCl with Zn/Al mole ratio 2 and 3, that chloride ion is removed as HCl at above 600^{o}C alongside dehydroxylation of the hydroxide layers at between 400-600^{o}C. Heat treatment up to 900^{o}C gave a total mass loss of 34.3% with respect to the initial sample weight. The other chloride hydrotalcites showed similar behaviour.

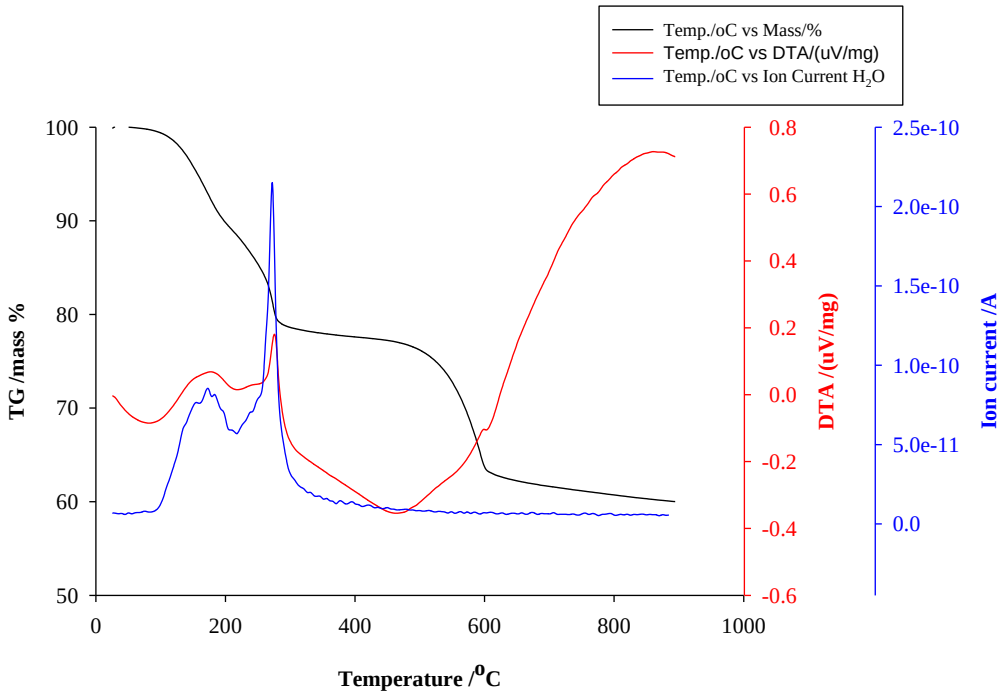

Fig.3.33: TG, DTA and gas evolution ion current curves of Zn_3AlCl HTl

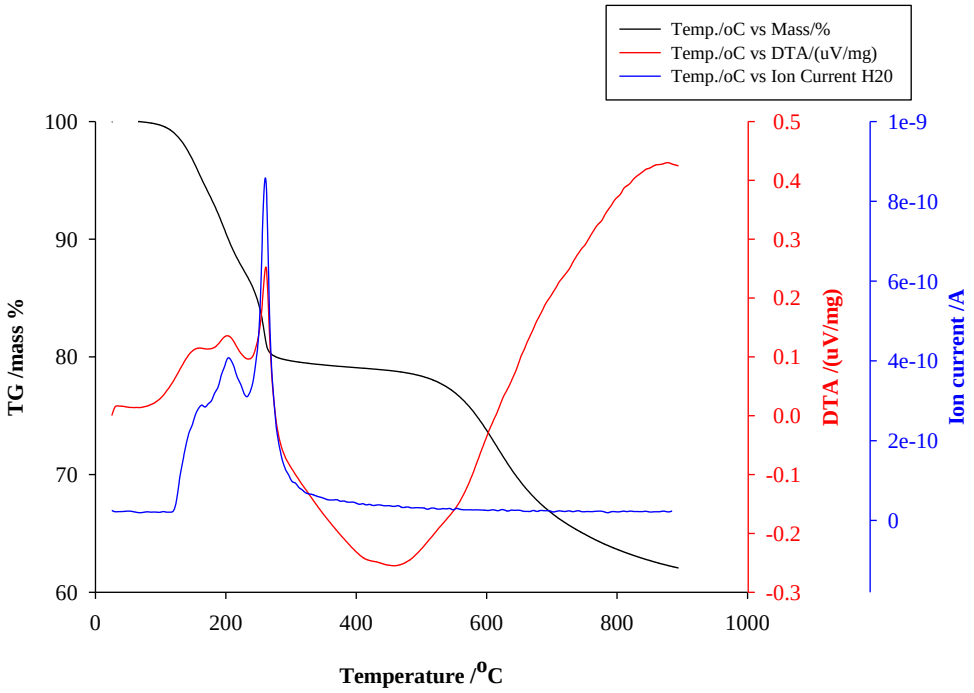

Fig.3.34: TG, DTA and gas evolution ion current curves of Zn_4AlCl HTl

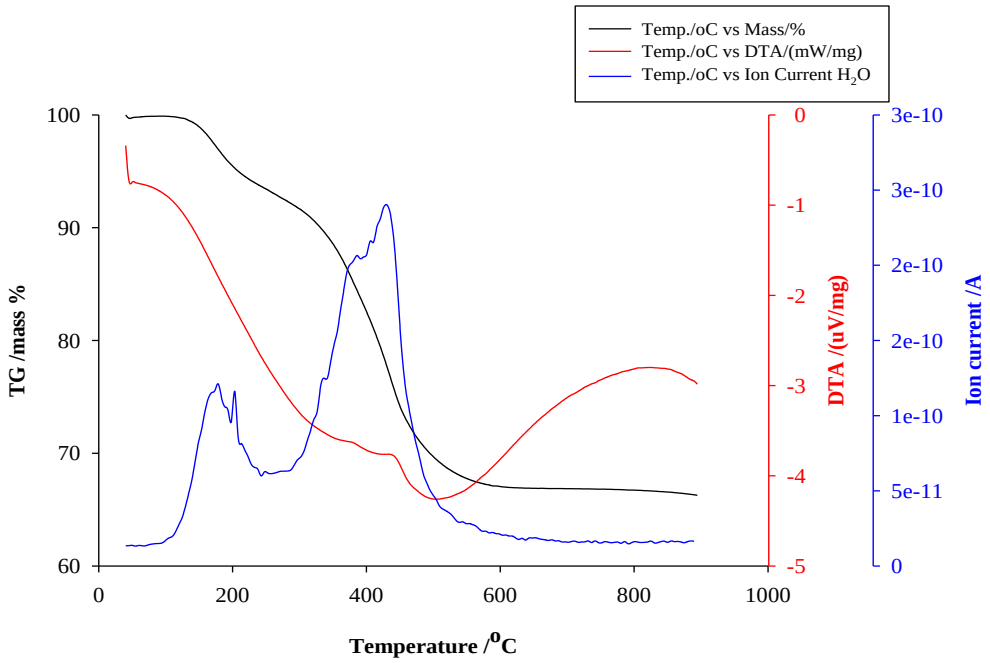

Fig.3.35: TG, DTA and gas evolution ion current curves of Mg_2AlCl HTlc

3.9: Scanning Electron Microscopy (SEM) results

The SEM images of some of the hydrotalcites are shown in Figs 3.36-3.38. The carbonate intercalated hydrotalcites displayed in Fig.3.36 all show thick broken hexagonal particles which are not uniform in size and distribution. Figs.3.36b and 3.36e, Mg_3AlCO_3 HTlc and Zn_3AlCO_3 show bigger particles that are non-homogenously distributed. This may indicate that the samples are more crystalline and this ties with XRD result.

The grinding done on the sample before storage could have affected the differences in particle sizes besides synthetic method. However, Oh et al [65] showed that, the size of hydrotalcite crystals or particles can be controlled by influencing some synthetic parameters like aging time and reaction temperature, in addition to metal ion concentration. They prepared hydrotalcites by two methods, urea hydrolysis plus hydrothermal synthesis and co-precipitation method, and they showed that, the size of hydrotalcite crystals or particles was influenced by aging time and reaction temperature. They explained that, while fixing other parameters but varying aging time and reaction temperature, that hydrotalcite with larger particles could be obtained from urea method of synthesis at longer time of aging (30hrs) as shown in Fig.3.36' below. This may be attributed to the slow rate of hydrolysis of urea resulting to low degree of supersaturation ratio which caused a decreased nucleation rate leading to larger particles.

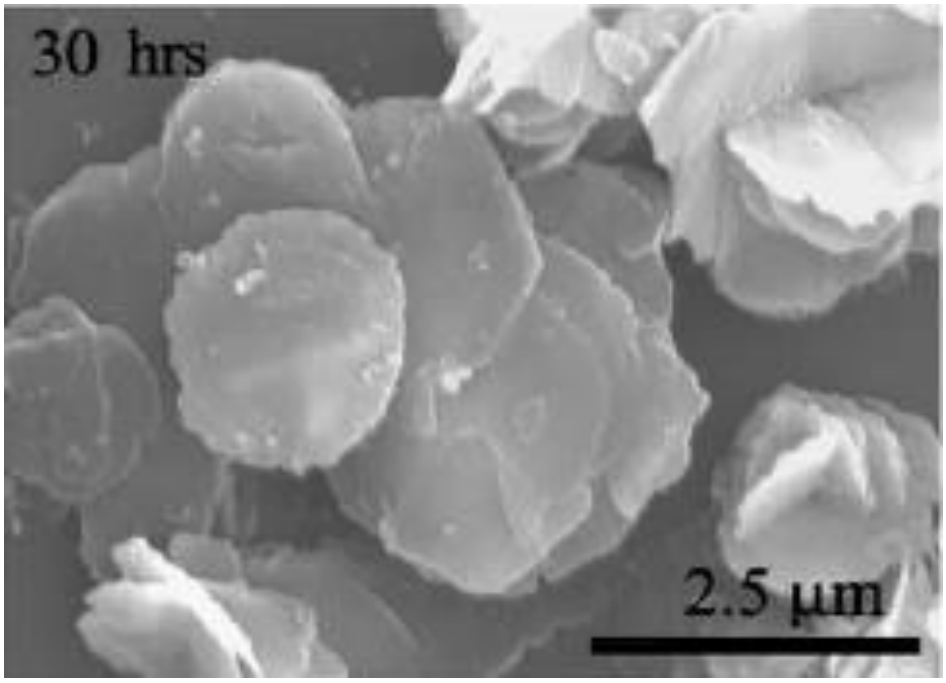

Fig.3.36': Mg_2AlCO_3 HTlc by Urea method at 30hrs aging time, taken from[65]

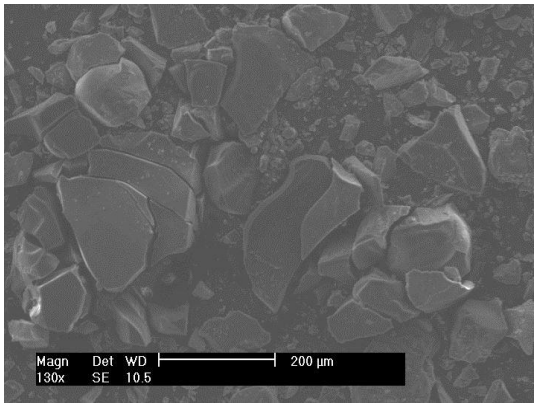

(a) Mg_2AlCO_3 by co-ppt

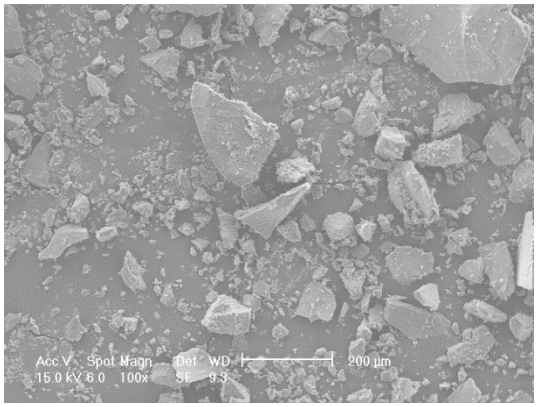

(b) Mg_3AlCO_3 by co-ppt

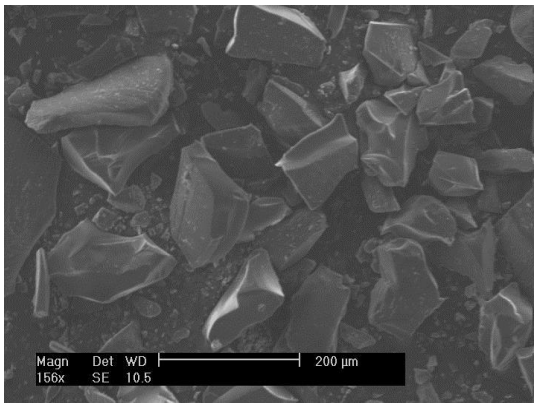

(c) Mg_4AlCO_3 by co-ppt

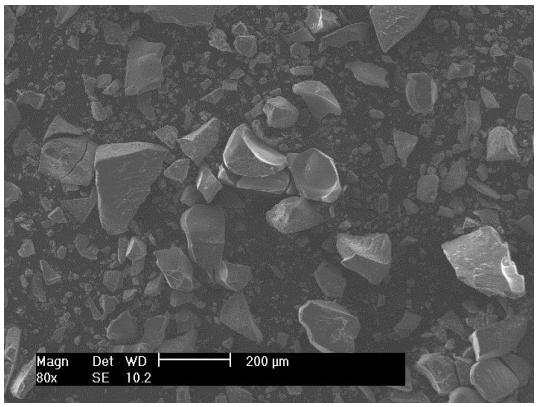

(d) Zn_2AlCO_3 by co-ppt

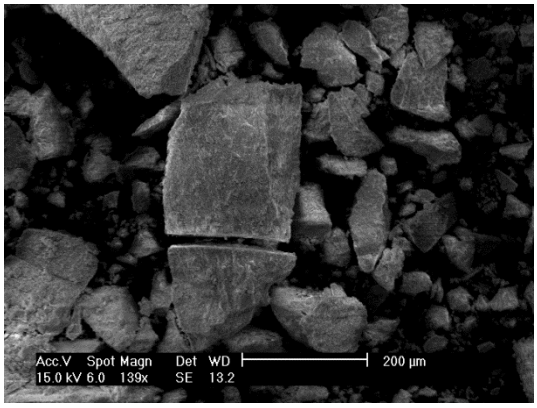

(e) Zn_3AlCO_3 HTlc

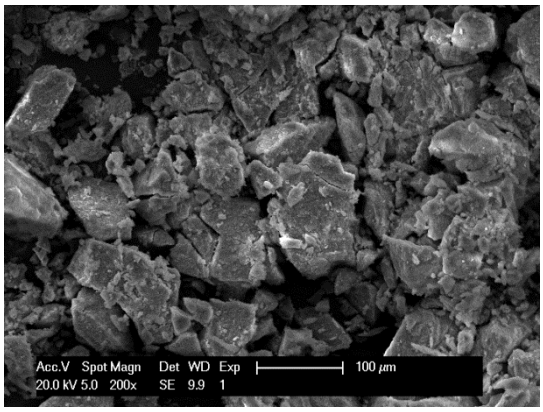

(f) Zn_4AlCO_3 HTlc

Fig.3.36: SEM results for the CO_3^{2-} -HTlcs

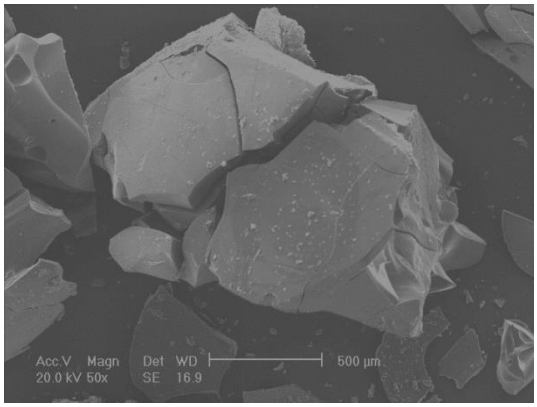

(a) Mg_2AlNO_3 HTlc

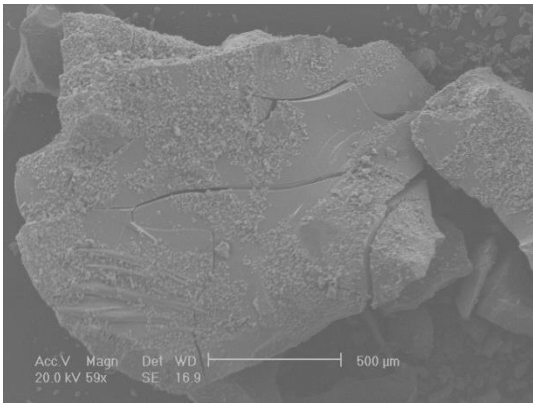

(b) Mg_3AlNO_3 HTlc

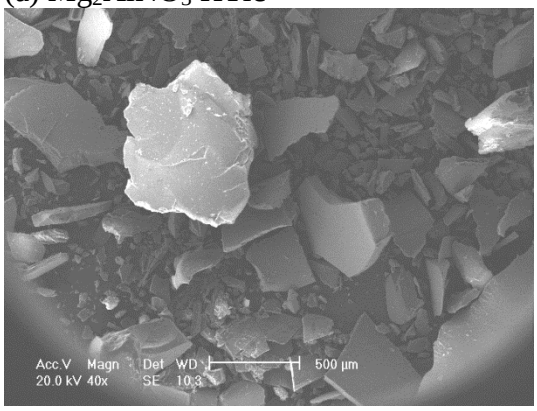

(c) Mg_4AlNO_3 HTlc

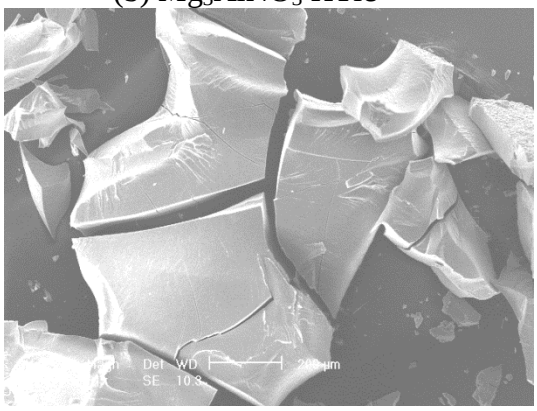

(d) Zn_2AlNO_4 HTlc

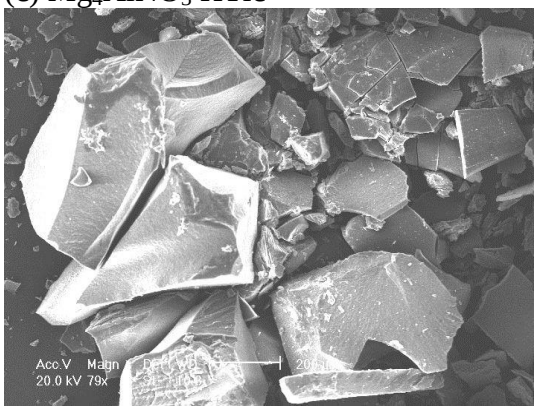

(e) Zn_3AlNO_4 HTlc

Fig.3.37: SEM results for the NO_3^- -HTlcs

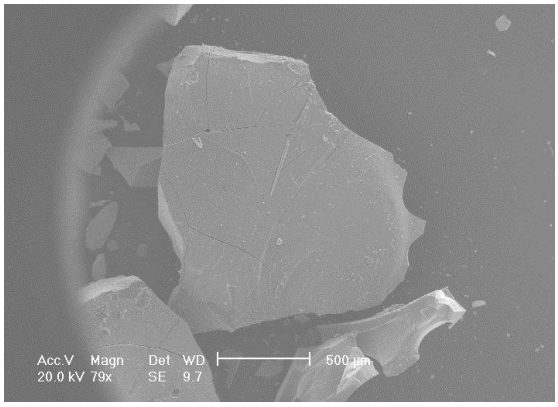

(a) Zn_2AlCl HTlc

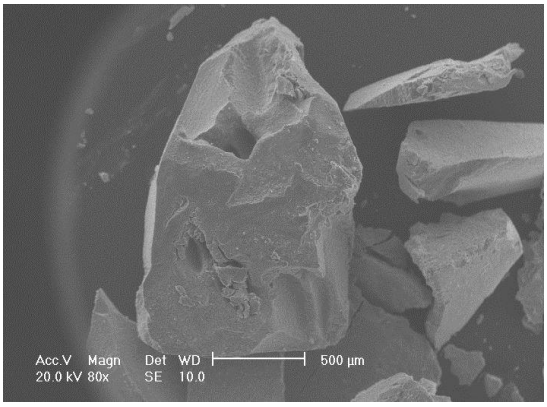

(b) Zn_3AlCl HTlc

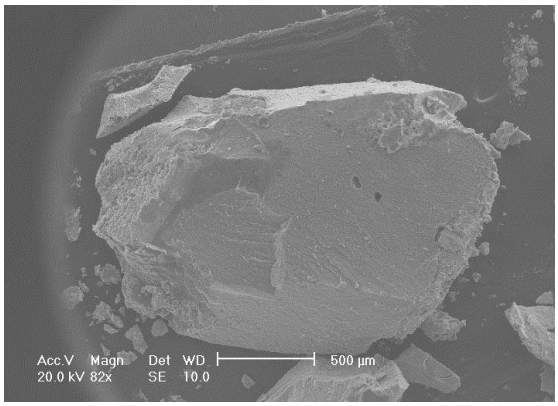

(c) Zn_4AlCl HTlc

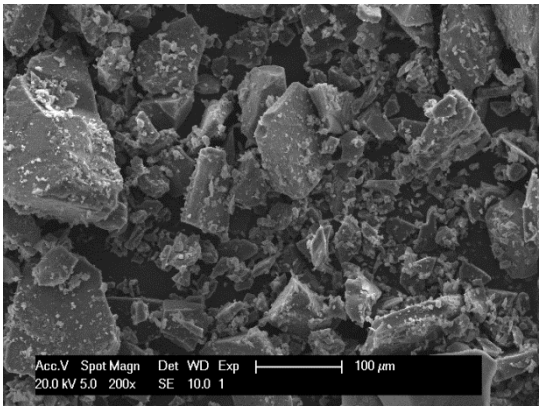

(d) Mg_2AlCl HTlc

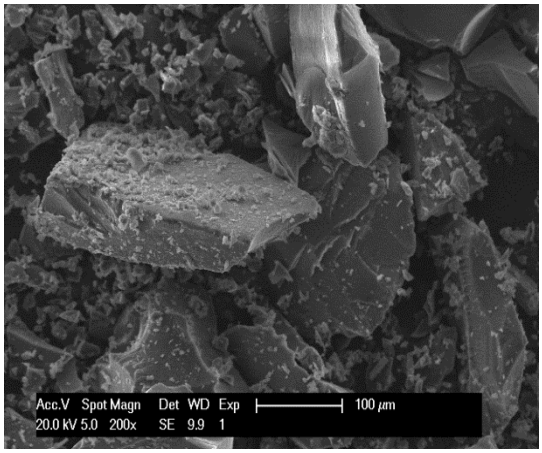

(e) Mg_3AlCl HTlc

Fig.3.38: SEM results for the Chloride HTlcs

3.10 Conclusions

Hydrotalcites with $Mg^{2+}Al^{3+}$ and $Zn^{2+}Al^{3+}$ cations in the layers with M^{2+}/M^{3+} mole ratio of 2-4 have been successfully synthesised. Different anions such as carbonate, nitrate and chloride have been intercalated into their galleries. It was observed that, varying the ratios of M^{2+}/M^{3+} cations in the layers resulted into distinguishing properties, for example, charge density, crystallinity, amount and orientation of anions in the interlayers and morphology

The influence of layer cations and interlayer anions influences the crystallinity and thus can affect the stability of hydrotalcites and could have effect on the overall properties of the hydrotalcites.

.

CHAPTER FOUR

MODIFICATION OF PREFORMED HYDROTALCITES

4.1 Introduction

4.1.1 Background

The previous chapter discussed the synthesis, characterisation and properties optimisation of our as-synthesised hydrotalcite-like compounds (HTlcs). This chapter will focus on the modification of these preformed hydrotalcite-like compounds herein referred to as host HT or HT-SDS and HT-SDBS and their characterisation based on the same procedures that were applied to the preformed or host hydrotalcites. The preformed hydrotalcite-like compounds were modified by ion exchanging the initial inorganic anions in their lamellar region with two anionic surfactants, sodium dodecylsulfate (SDS) and sodium dodecylbenzenesulfonate (SDBS) via intercalation reactions following either a calcination-regeneration route or ion exchange process. An intercalation reaction is one which allows the incorporation of changeable guest species into the host lattice of a compound or material while maintaining the structural integrity of the lattice of the compound. Hydrotalcite can serve as a host compound or material for different anion exchange reactions premised on its layered charged structure and anion exchange capability as discussed earlier. The exchange ability of hydrotalcite permits a variety of anions to be introduced into their gallery space by exchange of the original anions with those of the guest species in aqueous solutions[42, 162, 163]. Different methods can be used to insert these guest anions into the lamellar space of hydrotalcites whereby the guest species replace the anions originally present in the gallery of the

preformed hydrotalcites which now serves as the host. Hydrotalcite is hydrophilic in nature which makes it not very attractive towards anionic organic species, so by intercalation of anionic surfactant guests it may be possible to create materials with more hydrophobic character or surfaces that may be attractive towards co-intercalation of organic species like phenol and chlorophenols. To our knowledge none of the hybrid organo-hydrotalcites that existed has focused on different layers and interlayer compositions to establish the relationship between compositions, with regards to fine-tuning their properties as sorbents to uptake phenol and chlorophenol from wastewater. Several routes can be followed to replace the initial inorganic anions in the interlayer space with the guest organic anions. Generally this can be achieved by three methods[164]: direct synthesis of organo-hydrotalcites by co-precipitation method[165, 166, 167, 168, 169], the reconstruction of calcined preformed hydrotalcites in the presence of the guest anions[170, 171, 172, 173] and ion exchange reaction in which the inorganic anions of the hosts or precursors is exchanged with the guest species of interest from aqueous solution[168, 169, 174, 175]

.

4.2 Experimental

4.2.1 Synthesis of $MgAlCO_3$-SDS, $ZnAlCO_3$–SDS and $MgAlCO_3$-SDBS, $ZnAlCO_3$-SDBS

14.42g of sodium dodecylsulfate (98.5%, Sigma-Aldrich) was dissolved and stirred vigorously in 100cm^3 de-ionised deareated water for 3hrs (equivalent to 0.5M sodium dodecylsulfate (SDS) solution), similarly 6.97g of sodium dodecylbenzenesulfonate (technical grade, Sigma-Aldrich) was also dissolved and stirred vigorously in 100cm^3 de-ionised deareated water for 3-4hrs (equivalent to 0.2M sodium dodecylbenzenesulfonate SDBS) solution). 3.0g of the preformed $MgAlCO_3$ and $ZnAlCO_3$ hydrotalcites with M^{2+}/M^{3+} ratio = 2, 3 & 4 were heated at a ramp rate of 5^oC/min to 500^oC and 350^oC respectively (temperature predetermined from variable temperature XRD and TGA) and held at that temperature for 5 hrs. This is to convert the preformed hydrotalcites into their oxide forms which were named as calcined HTlc-T. The calcined MgAl and ZnAl hydrotalcites were allowed to cool under nitrogen before 1.0 g of each of the MgAl and ZnAl oxide precursors were dispersed in 50cm^3 of the 0.5M sodium dodecylsulfate or 0.2M sodium dodecylbenzenesulfonate solutions prepared previously. The mixtures were stirred continuously for 24 hrs under nitrogen atmosphere at room temperature. After 24 hrs, the resulting colloidal suspensions were centrifuged and the precipitate washed several times with deionised, deareaeted water. The resultant residues were dried in an oven at 50^oC for a further 24hrs. The obtained solids were gently powdered and stored in sealed containers for further use. The $ZnAlCO_3$ series of samples were initially contacted with the surfactant solution under the conditions stated above but we were unable to obtain single phase products.

Therefore the pH of the SDS and SDBS solutions for $ZnAlCO_3$ hydrotalcites series were adjusted to bring the pH of the suspension down to ca.6 using aqueous HNO_3 acid (70%, analytical reagent grade, Fishers scientific, UK). To achieve this, typically 15 to 20 drops of HNO_3 acid was added to the 0.2M or 0.5M surfactant solution to bring the pH to 2.06 (SDBS) and 2.0 (SDS) from initial pH of ca. 7.89 and 8.96 respectively. A pH meter was immersed into the reaction flasks to monitor the pH of the reaction mixtures during exchange. The pH of the $ZnAlCO_3$ hydrotalcites series at the start of reaction was ca. 12, while at the end was about ca. 6.8 and typically ca. 1g of product was obtained. For the $MgAlCO_3$ series the pH was about 13 at the completion of the reaction and ca. 2g of product was typically obtained. These samples are denoted as HTlc-DS and HTlc-DBS.

4.2.2 Synthesis of Mg_2AlNO_3-SDS, Zn_2AlNO_3–SDS and Mg_2AlNO_3-SDBS, Zn_2AlNO_3-SDBS

3.0g of the preformed $MgAlNO_3$ and $ZnAlNO_3$ with Mg/Al and Zn/Al ratio equivalent to 2 were calcined under stated conditions in 4.2.1 above. 1.0g of the calcined Mg_2Al and Zn_2Al hydrotalcites (after allowing cooling under nitrogen) were dispersed in $50cm^3$ of 0.5M sodium dodecylsulfate or 0.2M Sodium dodecylbenzenesulfonate solutions. The pH of the SDS and SDBS solutions were adjusted as in 4.2.1 with few drops of aqueous HNO_3 prior to contacting them with the hydrotalcite system. This is to reduce the pH of the suspension containing $ZnAlNO_3$ hydrotalcite to about 6-7. The mixtures were stirred under nitrogen atmosphere and room temperature for 24 hrs. The resulting colloidal suspensions were centrifuged to isolate the precipitates formed which were thereafter washed and dried following the same procedure in 4.2.1.

4.2.3 Synthesis by direct ion exchange

A few samples were made by the direct ion-exchange method. In a typical experiment, 1.0g powder of the preformed chloride or nitrate Mg-Al and Zn-Al HTlc hosts without calcining were stirred directly in aqueous solutions of SDS and SDBS of same concentrations as in previous sections. The suspensions were allowed to stir under nitrogen atmosphere for 24hrs and room temperature. As with the previous samples, when using ZnAl hydrotalcites, the pH of the SDS and SDBS aqueous solutions were adjusted by adding 15 or 20 drops of HNO_3 acid to bring the pH of the suspension down to between 6-7. The process of isolating the solid, washing and drying followed the same procedure as above. The obtained solids were gently crushed and stored in sealed container and labelled as Mg_2AlNO_3-DS_IE, Mg_2AlNO_3-DBS_IE and Zn_2AlNO_3-DS_IE, Zn_2AlNO_3-DBS_IE or Mg_2AlCl-SDS_IE, Mg_2AlCl-SDBS_IE, Zn_2AlCl-SDS_IE and Zn_2AlCl-SDBS_IE.

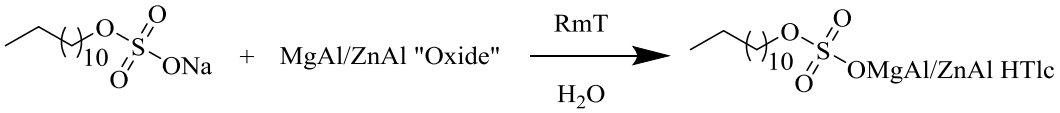

Fig.4.1: Reaction scheme for the synthesis of HT-SDS

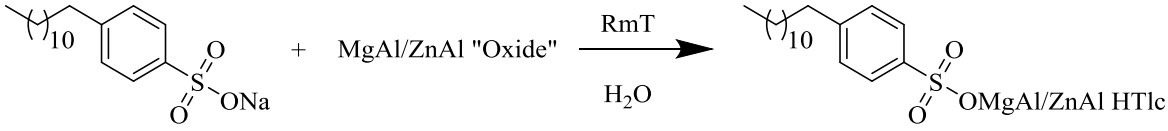

Fig.4.2: Reaction scheme for the synthesis of HT-SDBS

4.3 Characterisation of the modified hydrotalcite-like compounds

A different diffractometer was required to be used because of the large d-spacings expected and low angles to which it was necessary to record the XRD data. Hence, X-ray diffraction analysis for characterization and identification was performed on the as-synthesised organo-hydrotalcites, HTlc-DS and HTlc-DBS at ambient temperature using a D5005 Siemen diffractometer with $CuK\alpha_1$ radiation ($\lambda = 1.5406$Å) operating at 40KV and 30mA, in reflection mode. Randomly oriented powdered samples were scanned employing counting time of 0.33s per step. Generally, the XRD patterns of the hybrid organo-hydrotalcites (modified hydrotalcites) showed a shift of peak positions to lower $2\theta^o$ with expanded d-spacing suggesting that the surfactant anions, dodecycylsulfate (DS) and dodecylbenzenesulfonate (DBS) have been intercalated into the interlayer space of the preformed hydrotalcite-like compounds. The peak positions were determined using Eva software (Materials Data, Inc.). The basal spacing of the various hybrid organo-hydrotalcites were calculated from the *(003)* reflection and where possible the unit cell parameter *a* was determined from the *(110)* reflection using Bragg's equation. The gallery height was calculated from the relationship: gallery height = basal spacing (d) – thickness of the layer, while the inclined angle (ϕ) was calculated using trigonometric analysis. XRD measurements were also carried out at variable temperatures by heating the hydrotalcites within the sample holding unit of Bruker D8 X-ray diffractometer in 2 theta reflection geometry under nitrogen at a temperature interval of 50^oC

Fourier Transform Infrared analysis was then performed on the samples to obtain additional information. The spectra obtained showed appearance of bands confirming the intercalation of DS and DBS into the structure.

The chemical analysis data for Al, Zn and Mg were then obtained by using X-ray Fluorescence Spectrometry. The XRF analysis was carried out under the same conditions used for the preformed host hydrotalcites to find out if the molar ratios of the divalent/trivalent cation pairs (M^{2+}/M^{3+}) in the modified hydrotalcites are consistent with the stoichiometry of the preformed hydrotalcites that were modified. The fused beads method was used for this determination just like the host precursors, except that the ratio of sample to flux was reduced from 0.35g to 0.2g sample to 4.0g flux after several beads breakages were encountered. The presence of DS and DBS affected the interlinking of the flux that stabilised the glass bead formation under supercooling conditions so the beads formed were breaking. In order to prevent this, the proportion of sample was reduced since lithium tetraborate melts have sufficient internal structure to form a stable glass by themselves.

TGA-DTA was performed under same conditions as the parent samples under nitrogen environment at the heating rate of 5^{o}C/min using the same Netzsch STA 449 FI Jupiter® apparatus, connected to a quadrupole mass spectrometer (Netzsch QMS 403 Aëolus®) instrument as was with the host HTs. The thermal analysis was carried out between 25 - 900^{o}C.

Scanning Electron Microscopy was carried out as with the parent hydrotalcites.

4.4 Results and discussion

4.4.1 Powder XRD

The powder X-ray diffraction (XRD) patterns of Mg_2AlCO_3-HTlc (pattern c in black), Mg_2AlCO_3-500^oC, calcined host hydrotalcite (pattern d in olive green), Mg_2AlCO_3-SDS which is the sodium dodecylsulfate (SDS) regenerated hydrotalcite (pattern a in red) and Mg_2AlCO_3-SDBS, the sodium dodecylbenzenesulfonate (SDBS) regenerated hydrotalcite (pattern b in blue) are illustrated in Fig.4.3. The host hydrotalcite (Mg_2AlCO_3-HTlc) shows diffraction peaks at 7.76Å $d_{(003)}$, 3.88 Å $d_{(006)}$, 2.57 Å $d_{(012)}$, 1.52 Å $d_{(110)}$ and 1.49 Å $d_{(113)}$. The XRD patterns of the regenerated hydrotalcites appear to exhibit the characteristic reflections similar to the host hydrotalcite from which they have been made with resemblance of a number of (00*l)* peaks. However the (00*l)* reflections are broadened with decreased intensities when compare to the host hydrotalcite that was modified and some have almost disappeared. The broadening of the reflections may be an indication of reduced crystallinity or low degree of exchange in the regenerated hydrotalcites. The regenerated hybrid organo-hydrotalcites show a series of reflections with high orders which may signify a relatively well ordered structures of the HT-SDS and HT-SDBS with layered double hydroxide structure restored. This is supported by the presence of *(00l)* reflections to several orders in all the SDS and SDBS intercalated hydrotalcites which shows that the crystalline layers were regenerated without structural deformation. The host hydrotalcite showed a d-spacing of 7.76Å. Calcining the host in the stated conditions produced the pattern with diffraction peaks matching the metal oxide phase with destruction of the crystal structure of hydrotalcite evidenced by the disappearance of the $d_{(003)}$ and $d_{(006)}$ peaks at this point

(Fig.4.3d) due to dehydration, dehydroxylation of the layers and loss of anions. Most of the carbonate anions or any other anions and water in the interlayer have been removed. When the calcined hydrotalcite (e.g Mg_2AlCO_3-500^oC) is rehydrating in sodium dodecylsulfate (SDS) and sodium dodecylbenzenesulfonate (SDBS) solutions, the hydrotalcite structure is reformed intercalating dodecylsulfate and dodecylbenzenesulfonate anions within the galleries showing increased d-spacings (patterns a and b). The shift of the $d_{(003)}$ plane peak towards lower 2θ°[178, 179] is an indication that the guest anions, dodecylsulfate (DS), and dodecylbenzenesulfonate (DBS) have been successfully intercalated into the gallery of the organo-hydrotalcite structure giving an expanded basal spacing. This expanded basal spacing depends on the nature of the functional group of intercalated surfactant, the amount intercalated and the size and the length of the surfactant type.

The calcination of the as-synthesised preformed Mg_2AlCO_3 hydrotalcite (host HT) at the intermediate temperature of 500^oC gave rise to a mixed metal oxide that has a memory of the original hydrotalcite. Therefore it was possible to reconstruct the hydrotalcite structure without layer degradation, showing that the selected intermediate temperature is appropriate for the hydrotalcite composition. The $d_{(003)}$ plane peak of modified hydrotalcites shifted towards lower 2 theta angle, for example Mg_2AlCO_3 HTlc shifted to give increased basal spacing from 7.76Å to 30.47 Å and 30.50 Å with DS and DBS intercalation respectively. Considering the thickness of the hydrotalcite layer of 4.78 Å[42, 180] and the end to end lengths of the DS = 20.80 Å and DBS = 20.30 Å (calculated from the chemical structure assuming an all trans configuration in the alkyl chain), the gallery heights for each of the compounds is calculated by subtracting the thickness of the hydroxide layer to obtain approximately 26Å for both. This

observation matches bilayer packing with opposite DS and DBS anions arranged with a tilted angle of 52° to the hydroxide layer. The surfactant ions may have self-assembled themselves to a slanting bilayer orientation in the interlayer spaces with the alkyl chains arranged in opposite direction.

The same order of magnitude of $d_{(003)}$ is observed in the other series such as Mg_3AlCO_3-DS, Mg_3AlCO_3-DBS and Mg_4AlCO_3-DS, Mg_4AlCO_3-DBS. Their powder XRD patterns are shown in Figs 4.4 and 4.5 respectively. Mg_3AlCO_3-DS and Mg_3AlCO_3-DBS show gallery heights of 23.71 Å and 26.41 Å respectively while Mg_4AlCO_3-DS and Mg_4AlCO_3-DBS organo-hydrotalcites show gallery heights of 25.33 Å and 26.45 Å, which conforms to interpenetrated bilayer orientation with tilt angles of ca. 55° and ~ 51° for the Mg_3AlCO_3-DS and Mg_3AlCO_3-DBS, and a tilt angle of ~51° and 50° for the Mg_4AlCO_3-DS and Mg_4AlCO_3-DBS. This is consistent with the findings of Zhao and Nagy, 2004 who reported increased basal spacing from 7.74 Å to 25.8 Å (Mg_2AlCO_3-HT to Mg_2AlCO_3-DS) giving a monolayer packing mode. Similarly, Bouraada and co-workers [178] observed an increased basal spacing of 7.53 Å to 26.24 Å and 29.47Å for Mg_2AlCO_3-SDS and Mg_2AlCO_3-SDBS respectively which they ascribed to interdigitated monolayer and tilted bilayer orientation of the anions respectively. According to Zhao and Nagy [116], dodecylsulfate intercalated hydrotalcites having basal spacing equivalent to 26Å form perpendicular monolayer while those with d-spacing greater than 26Å can either form perpendicular bilayers with some degrees of overlap or form tilted bilayers. This agrees with the literature[42, 46].

Pattern (a) in Fig.4.3 shows a peak corresponding to d-spacing of 7.73Å which may be due to some carbonate anions co-intercalated within the interlayer space of the Mg_2AlCO_3-SDS due to incomplete replacement[181] despite observing an increase in

basal spacing. This may be due to high charge density of Mg_2AlCO_3-HT. It is also possible that CO_2 may have been re-absorbed from air during the separation and washing steps, which reconstructed carbonate in the interlayer. Moreover due to high electrostatic interaction that existed between the CO_3^{2-} and the OH groups of Mg_2AlCO_3 hydrotalcite layers, CO_3^{2-} can easily co-inhabit the interlayer space of Mg_2AlCO_3-SDS. Furthermore, the $ZnAlCO_3$-SDS and SDBS series displayed similar behaviour as their $MgAlCO_3$-SDS and SDBS counterparts. Representatives of the powder XRD patterns are shown in Fig.4.6 with bilayer packing modes observed for both DS and DBS intercalated hydrotalcites with tilt angles of 57.4° and 56.3° respectively observed. These results are similar to those reported previously[42, 46, 116, 174, 179, 182, 183, 184].

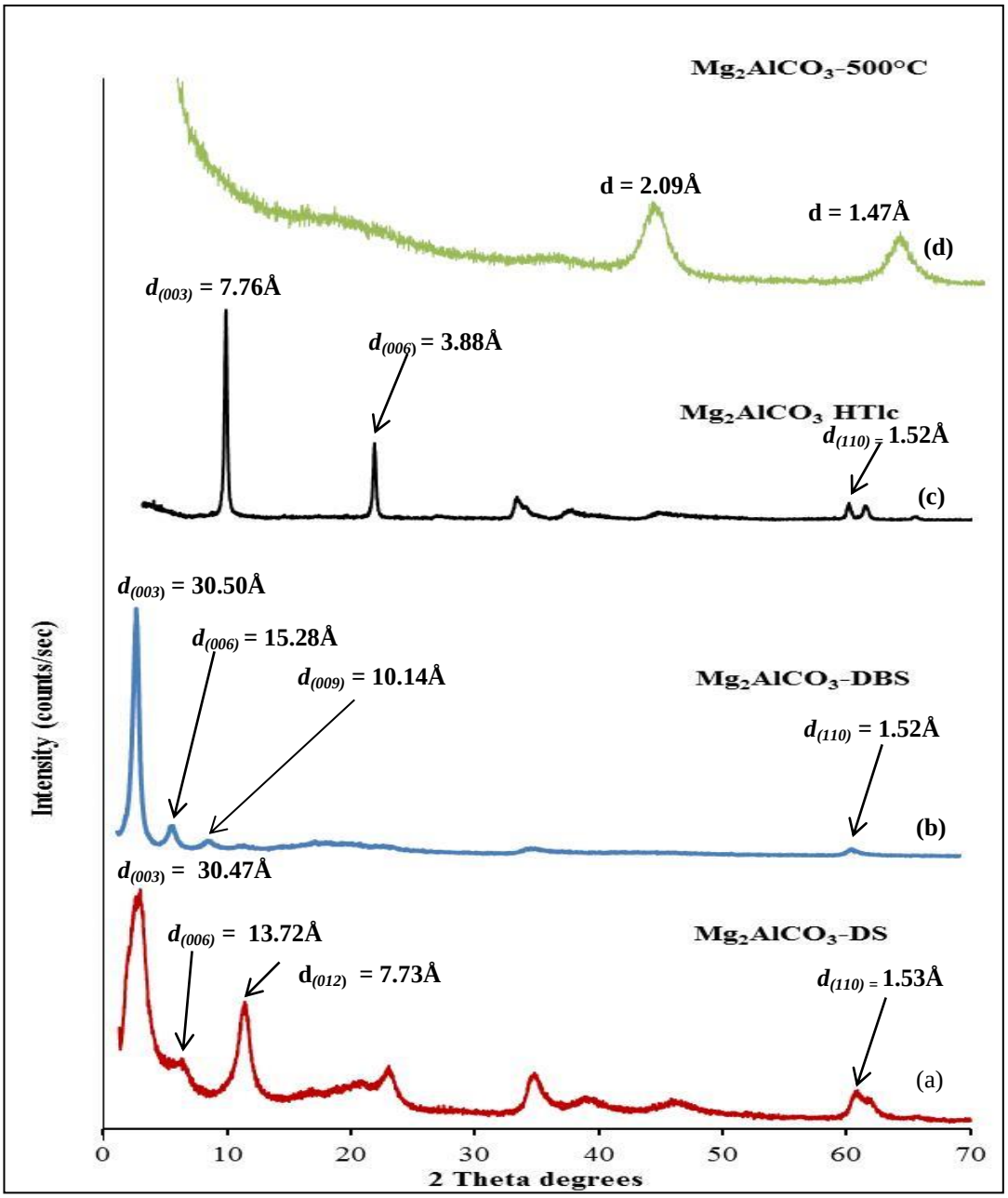

Fig.4.3: Powder XRD patterns of (a) Mg_2AlCO_3-DS (dodecylsulfate-intercalated hydrotalcite (red pattern), (b) Mg_2AlCO_3-DBS (dodecylbenzenesulfonate-intercalated hydrotalcite (blue pattern), (c) as-synthesised Mg_2AlCO_3 HTlc (Host Mg_2AlCO_3 hydrotalcite (pattern in black) and Mg_2AlCO_3-500^oC (calcined host hydrotalcite at 500^oC, olive green pattern).

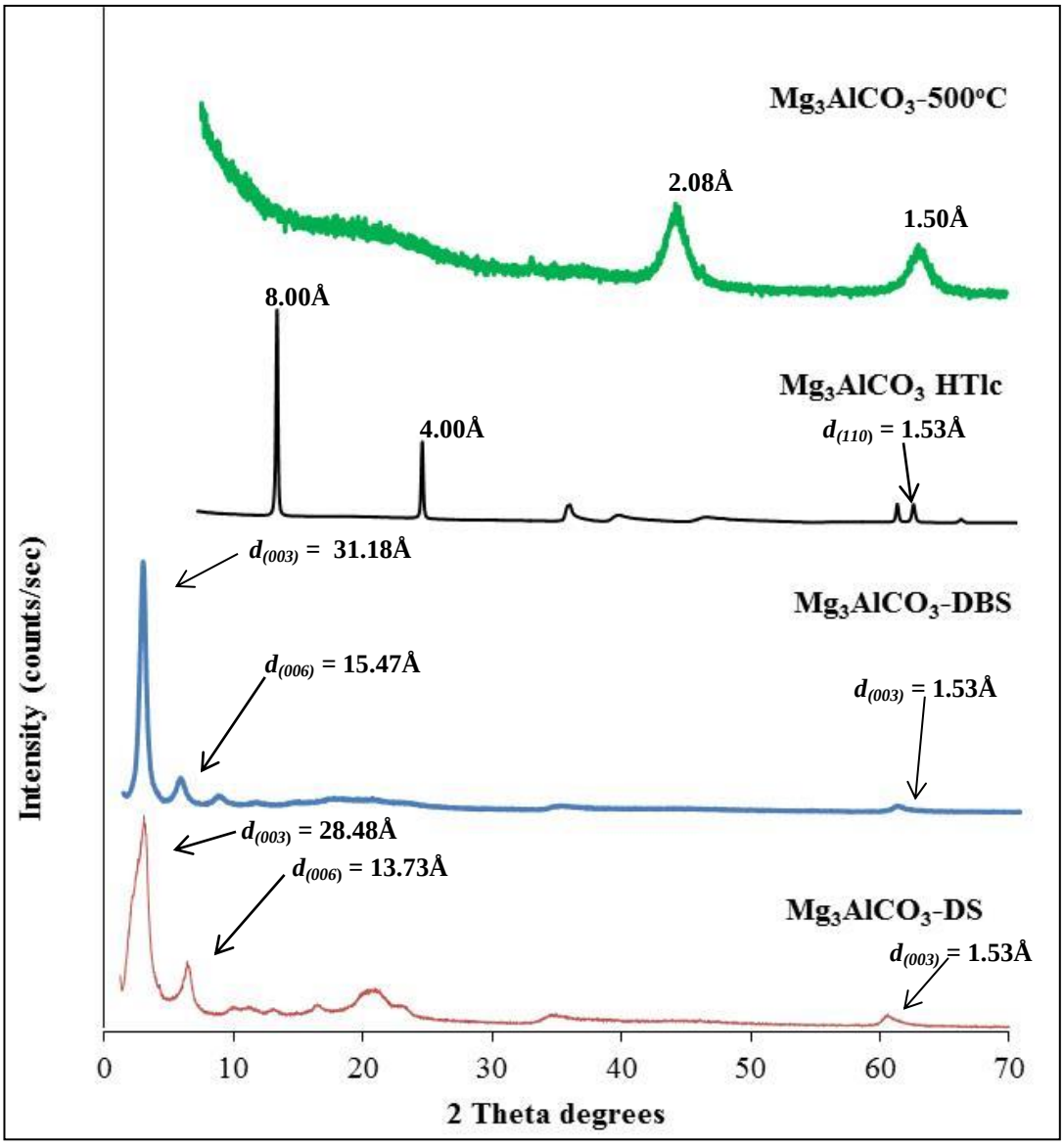

Fig.4.4: Powder XRD patterns of as-synthesised Host Mg_3AlCO_3 HTlc (pattern in black), its Calcined derivative (green pattern) plus dodecylsulfate-intercalated (DS) and dodecylbenzenesulfonate-intercalated (DBS) derivatives red and blue patterns respectively.

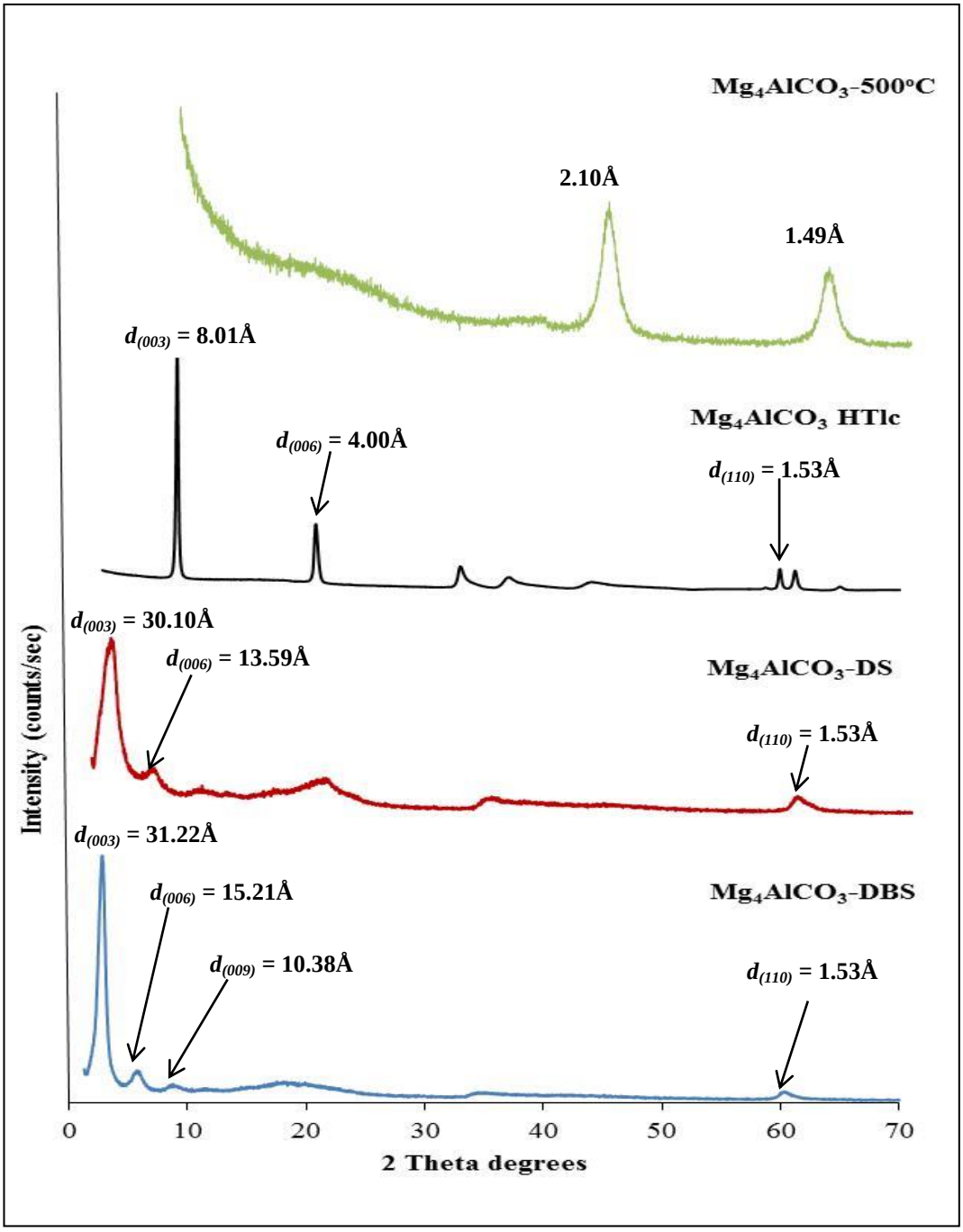

Fig.4.5: Powder XRD patterns of as-synthesised Host Mg_4AlCO_3 HTlc (Black)), Mg_4AlCO_3-DBS (dodecylbenzenesulfonate-intercalated hydrotalcite (Blue)), Mg_4AlCO_3-DS (dodecylsulfate-intercalated hydrotalcite (red)) and Mg_4AlCO_3-500^oC (calcined parent hydrotalcite at 500^oC (olive green)).

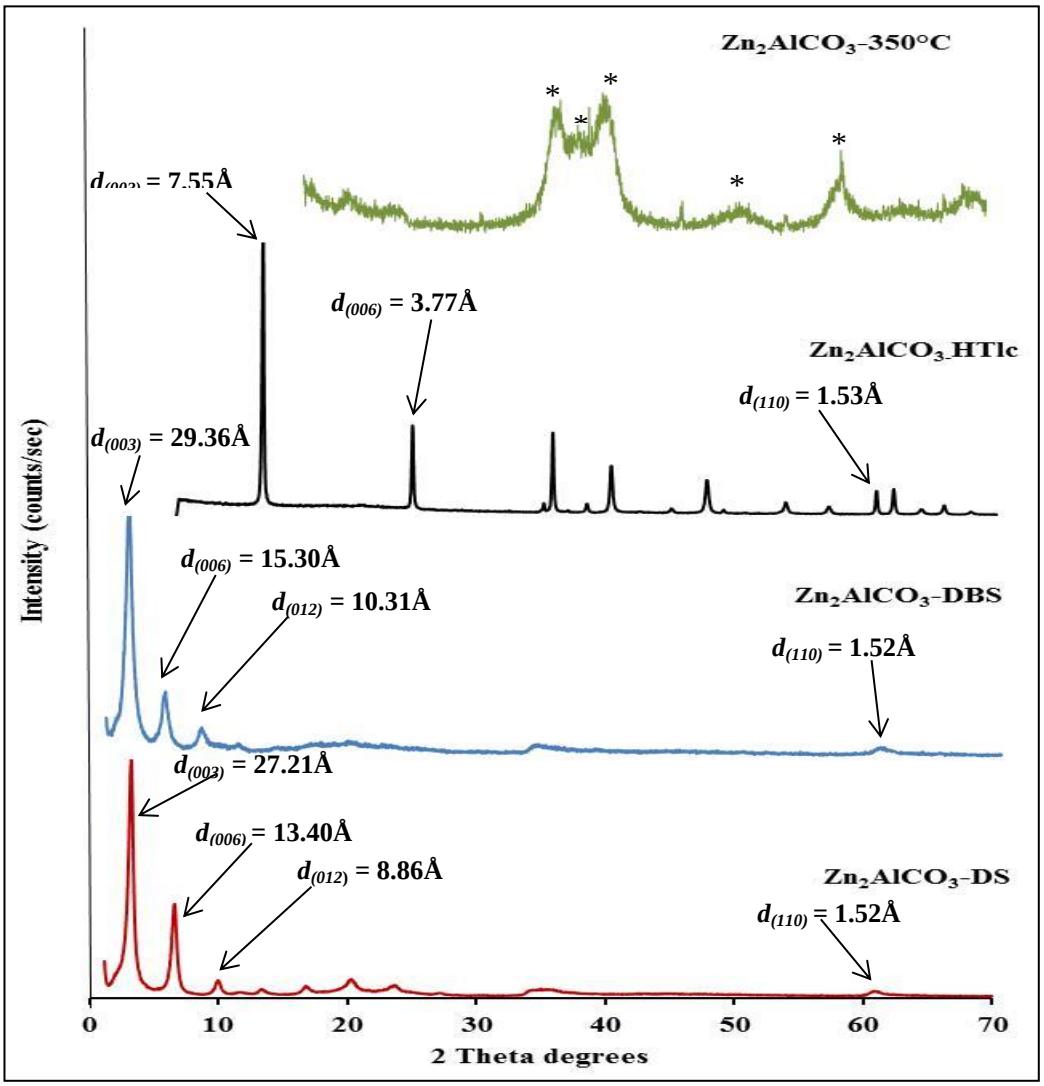

Fig.4.6: Powder XRD patterns of dodecylsulfate-intercalated hydrotalcites (Zn_2AlCO_3-DS (red), Zn_2AlCO_3-DBS ((blue)), Host Zn_2AlCO_3-preformed HT(black) and calcined Zn_2AlCO_3-preformed HT (olive green)).The asterisks are ZnO peaks.

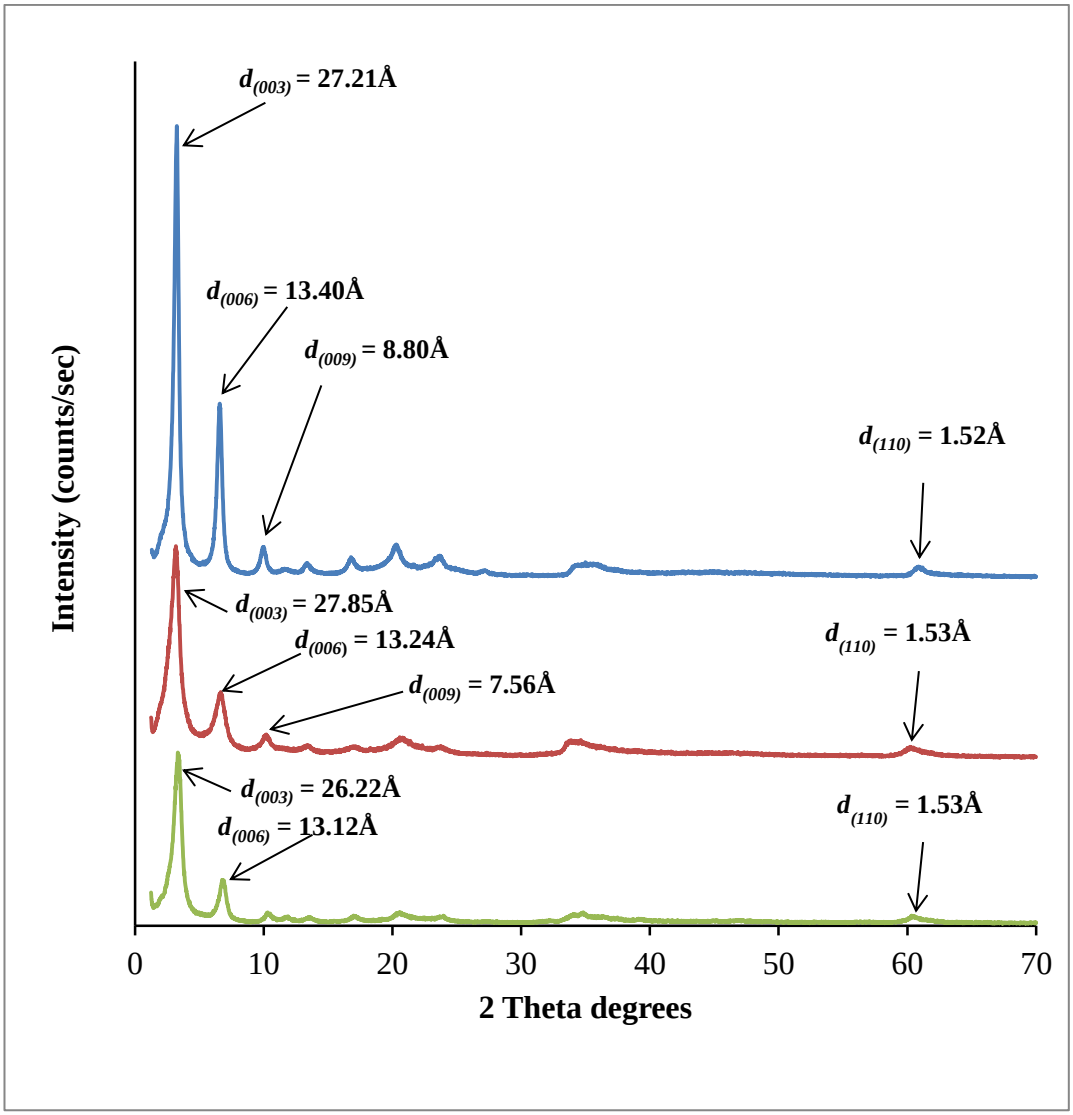

Fig.4.7: Powder XRD patterns of dodecylsulfate-intercalated hydrotalcites (Zn_2AlCO_3-DS (Blue), Zn_3AlCO_3-DS (red), Zn_4AlCO_3-DS (Olive green)).

Fig.4.7 shows the powder XRD patterns of dodecylsulfate-intercalated hydrotalcites with different molar ratios of Zn/Al. Intercalation of DS ions into their interlayer spaces gave increased basal spacings similar to those previously considered in this study. No direct trend appears to exist between $d_{(003)}$ spacing and Zn/Al ratio. However, a slight increase in basal spacing is noted with decreased charge density; Zn_2AlCO_3-DS showed a slightly lower $d_{(003)}$-spacing (27.21 Å) than Zn_3AlCO_3-DS ($d_{(003)}$-spacing of 27.85 Å).

Nevertheless they both gave bilayer orientation of the DS anions within the galleries while Zn_4AlCO_3-DS gave the lowest $d_{(003)}$-spacing of (26.22Å) with a possibility of monolayer arrangement of the DS anions within the interlayer. The *a* lattice parameter, attributed to the crystallographic repeat length within the mixed metal hydroxide layers is determined from the (110) reflection and was found to be the same (3.04 Å) as in the parent $MgAlCO_3$ HTlc showing that the integrity was maintained.

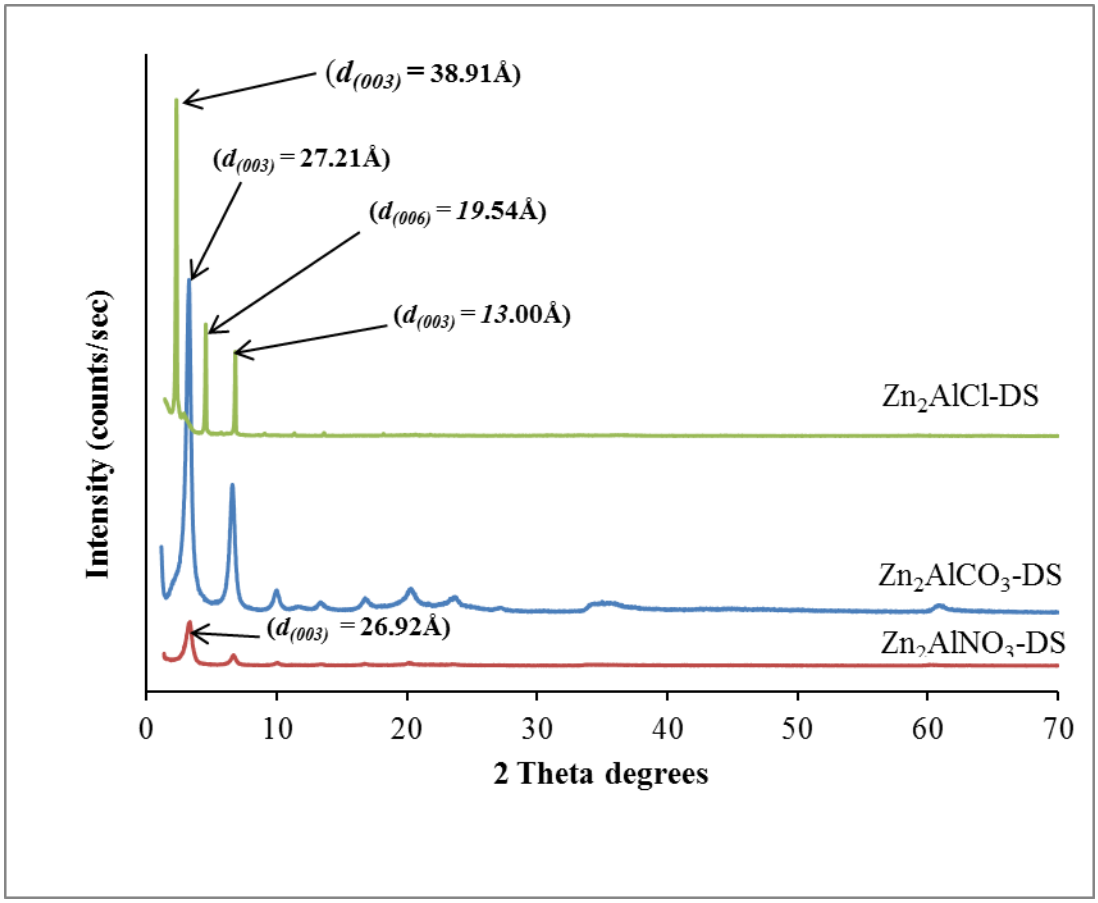

Fig.4.8: Powder XRD patterns of (dodecylsulfate-intercalated hydrotalcites with different anions in the host hydrotalcites.) (a) Zn_2AlCl-DS (green, prepared by ion exchange route IE) (b) Zn_2AlCO_3-DS (blue),) and (c) Zn_2AlNO_3-DS (red) prepared by IE.

Fig.4.8 shows the powder XRD patterns of organo-hydrotalcites with the same layer composition but different interlayer composition comprising of Zn_2AlCl-DS and Zn_2AlNO_3-DS (prepared by ion exchange) and Zn_2AlCO_3-DS. All three samples show

typical hydrotalcite phase with ordered and regularly stacked sheets. Zn_2AlCl-DS shows peaks at 2θ° = 2.269°, 4.519°, 6.793°, and 9.020° corresponding to 38.91Å $d_{(003)}$, 19.54Å $d_{(006)}$, 13.00Å $d_{(009)}$, and 9.80Å. Zn_2AlCO_3-DS and Zn_2AlNO_3-DS also show similar results. The Zn_2AlCl-DS shows a shift of $d_{(003)}$, from 7.86 Å to 38.91 Å. Similarly Zn_2AlNO_3-DS show a shift from 8.98 Å to 26.92 Å $d_{(003)}$ and Zn_2AlCO_3-DS show a shift from 7.58 Å to 27.21 Å. This is an indication that the surfactant dodecylsulfate anions have been intercalated into the interlayers of these various Zn_2Al-hydrotalcite hosts. Of these three, Zn_2AlCl-DS synthesised by ion exchange showed the sharpest and most intense peaks which may suggest better ordering. Also the basal spacing of Zn_2AlCl-DS is higher than that of Zn_3AlCO_3-DS and Zn_4AlNO_3-DS. From the basal spacing and considering the width of the hydroxide layer (4.78Å), the height of the gallery results are 34.13 Å for Zn_2AlCl-DS, 22.43 Å and 22.14 Å for Zn_2AlCO_3-DS and Zn_2AlNO_3-DS respectively. The dodecylsulfate (DS) anion may have formed a tilted interdigitated bilayer between the Zn_2AlCl-DS interlayer space with a tilt angle of 55° while in the interlayer spaces of Zn_2AlCO_3-DS and Zn_2AlNO_3-DS, the dodecylsulfate chain may be packed in slanting bilayer mode with slant angles of 33 and 32° respectively. The basal spacing of Zn_2AlCl-DS is highest which may indicate a dependence on the nature of the inorganic anion present in the original host hydrotalcite and synthetic route which in turn may have affected the orientation of the guest species in the interlayer. The different arrangement of the guest species (DS) in interlayer of organo-hydrotalcites may be affected by several factors such as the identity of the metals, M^{2+}/M^{3+} ratio, pH, method of preparation, the size and functional group of the guest species, level of exchange/intercalation and the presence of water. These results are in agreement with past reports. According to Guo and co-workers[185] basal spacings

of between 26.9 Å and 27.1 Å result in a structure in which the sodium dodecylsulfate chains orient themselves either in a perpendicular or interdigitated monolayer within the gallery of the organo-hydrotalcite. Therefore the surfactant chain may assume interdigitated bilayer arrangement when the basal spacing is larger than the sum of the size of the surfactant molecule and the thickness of one hydrotalcite layer, and/or tilted monolayer arrangement when the basal spacing is smaller. Several authors support this argument[168, 181, 186]. Zn_2AlCl-SDS hydrotalcite shows relatively sharper and more intense peaks indicating better order and crystallinity than the other samples in the series and may also possess better degree of exchange. These observations are true for all the other members of $MgAlCO_3$-DS organo-hydrotalcites series.

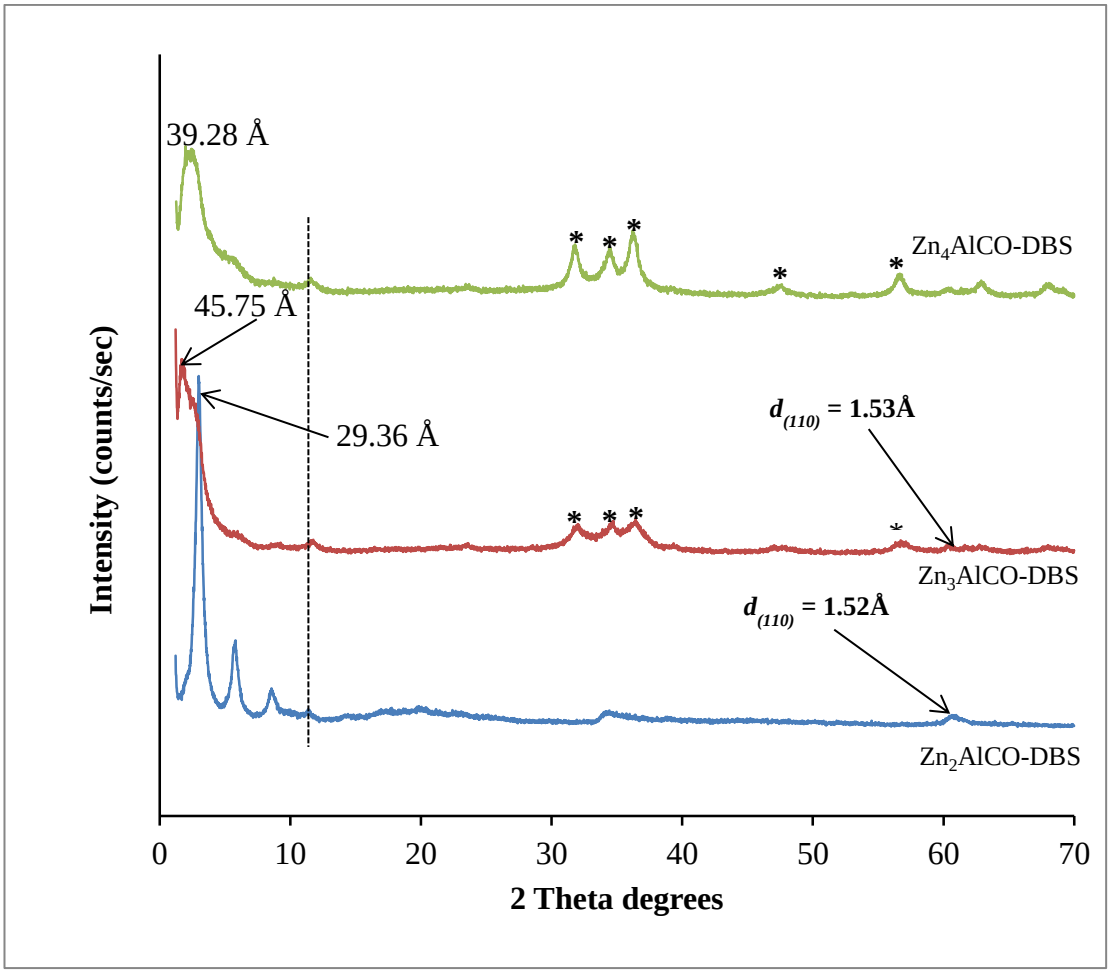

Fig.4.9: Powder XRD patterns of dodecylbenzenesulfonate-intercalated hydrotalcites (a) Zn_2AlCO_3-DBS ((Blue)), (b) Zn_3AlCO_3-DBS (red and (c) Zn_4AlCO_3-DBS (Olive green)). The asterisks peaks are ascribed to ZnO peaks.

Fig.4.9 shows the powder XRD patterns of dodecylbenzenesulfonate-intercalated hydrotalcites with different Zn^{2+}/Zn^{3+} ratios. The intercalation of the dodecylbenzenesulfonate anions resulted in basal spacings of 29.36, 45.75 and 39.28Å for Zn_2Al-DBS, Zn_3Al-DBS and Zn_4Al-DBS organo-hydrotalcites respectively. This is an indication that the dodecylbenzenesulfonate has expanded the galleries by 24.58, 40.97 and 34.50 Å. It was observed that the dodecylbenzenesulfonate anions assumed

similar packing modes in the interlayer spaces of the three organo-hydrotalcites, despite differences in the layer composition, but with different tilt angles. The dodecylbenzenesulfonate is intercalated into the gallery of Zn_2AlCO_3-DBS possibly forming slanting bilayer arrangement with a tilt angle of 37° (Fig.4.11), while based on the XRD data may suggest Zn_3AlCO_3-DBS formed a vertical end to end bilayer arrangement[83, 174] (Fig.1.13 (left)) and the Zn_4AlCO_3-DBS form bilayer arrangement also with a tilt angle of 58° (Fig.4.10). However, the XRD data for both the Zn_3Al and Zn_4Al sample is poorer quality and both show the presence of an impurity of ZnO. This indicates that as the proportion of zinc is increased, the stability of the inorganic layer is reduced, and the structure is lost. Hence, regeneration with DS and DBS anions was less successful for the Zn_2Al sample. The orientation of DBS anions in the interlayers of these hybrid hydrotalcites with varying layer composition may have influenced the interlayer spacing. The water content of each may also have a significant contribution. Of the three hydrotalcites, better crystallinity was shown by the Zn_2AlCO_3-DBS due to its sharper and more intense peaks than the Zn_3AlCO_3-DBS and Zn_4AlCO_3-DBS, where the 1/2 and 1/3 height harmonics show very low intensities compared to Zn_2AlCO_3-DBS. The basal spacing observations are consistent with reports of [42, 167, 186]. Increasing the Zn^{2+}/Al^{3+} mole ratio led to increasing basal spacing but it did not show a clear trend. For Zn_3AlCO_3-DBS and Zn_4AlCO_3-DBS, ZnO is present as an impurity (increasing in amount) as the Zn:Al ratio increases. This could be due to a part of ZnAl Oxide precursor (from calcination) also regenerating which may have contributed to the reduced crystallinity in these samples as compared to the Zn_2AlCO_3-DBS organo-hydrotalcite which shows no appearance of any zinc oxide phase. The marked

reflections or peaks in Fig.4.9 are attributed to a small portion of residual carbonate anion in all three samples.

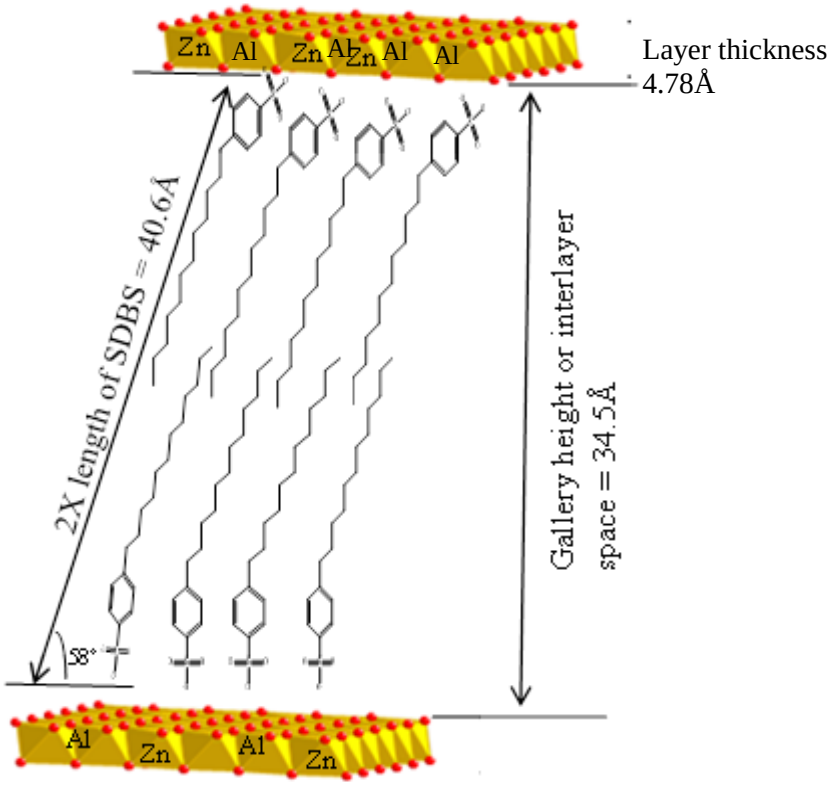

Fig.4.10: Schematic illustration of an almost perpendicular interpenetrated bilayers with tilt angles of 58° within the 3:1 interlayers of dodecylbenzenesulfonate Zn/Al organo-hydrotalcite.

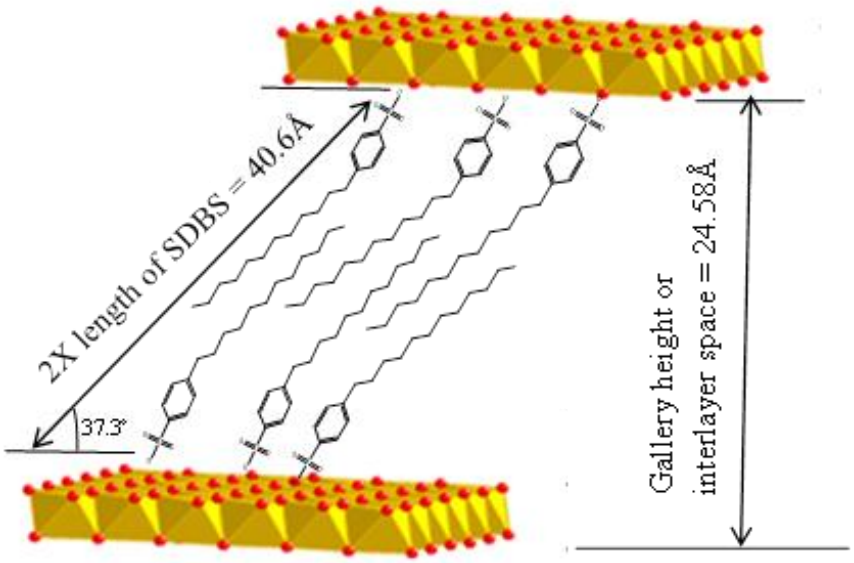

Fig.4.11: Schematic illustration of slanting interpenetrated bilayers with tilt angles of 37° within the 4:1 interlayers of dodecylbenzenesulfonate intercalated Zn/Al organo-hydrotalcite

4.4.2 Fourier Transform Infrared (FT-IR)

Fourier Transform Infrared (FT-IR) spectra displayed in Fig.4.12 show the absorption bands of the host hydrotalcite (Mg_2AlCO_3 HT spectrum in red), Mg_2AlCO_3-SDS (spectrum in blue) and Mg_2AlCO_3-SDS (spectrum in olive green). Comparing the spectra of SDS and SDBS regenerated hydrotalcites with the host HT, all three spectra show broad OH band around 3430 – 3460 cm^{-1}, typically 3434 cm^{-1} for the host HT, 3452 cm^{-1} for the Mg_2AlCO_3-SDS and 3461 cm^{-1} for Mg_2AlCO_3-SDBS, and OH bending vibration bands at 1633 cm^{-1} for the host HT, 1627 cm^{-1} for the Mg_2AlCO_3-SDS and 1628 cm^{-1}, 1603 cm^{-1} for the Mg_2AlCO_3-SBDS intercalated hydrotalcite which are characteristic bands of hydrotalcite-like compounds. The intercalation of the surfactants SDS and SDBS into the host hydrotalcite interlayer is confirmed by the appearance of the C-H stretching vibration bands at 2955 cm^{-1}, 2919 cm^{-1}, 2851 cm^{-1} with 2919cm^{-1}

and 2851cm^{-1} ascribed to the asymmetric and symmetric CH_2 stretch, and the C-H bending vibration band at 1467 cm^{-1}. The sulfate S=O stretching vibration bands at 1200 and 1060 cm^{-1} denote the $V_{S=O}$ symmetric and $V_{S=O}$ asymmetric vibrations. The spectrum in green is the infrared spectrum of Mg_2AlCO_3-SDBS. It also shows evidence of the presence of dodecylbenzenesulfonate anions in the interlayer of Mg_2AlCO_3-DBS hydrotalcite. Aside from the bands due to OH stretching in layer and interlayer water, C-H vibrations are seen in the spectrum of the dodecylsulfate intercalated hydrotalcite (spectrum in blue). This spectrum also reveals vibration bands characteristic of the sulfonate groups at 1174, 1129, 1037, 1010 and 830 cm^{-1} and the aromatic C=C stretching vibration at 1459 cm^{-1} and 1408 cm^{-1}. The regions 800 - 1000 cm^{-1} denote the metal-oxygen bonding vibration. The sharp absorption bands of carbonate around 1365 - 1377 cm^{-1} is an indication that some carbonate anions co-inhabit the gallery regions of the DS and DBS intercalated hydrotalcites. The FT-IR observations of the other series are similar to these. Fig.4.13 shows the FT-IR spectra of Zn_2AlCO_3 host hydrotalcite and its sodium dodecylsulfate and sodium dodecylbenzenesulfonate modified derivatives.

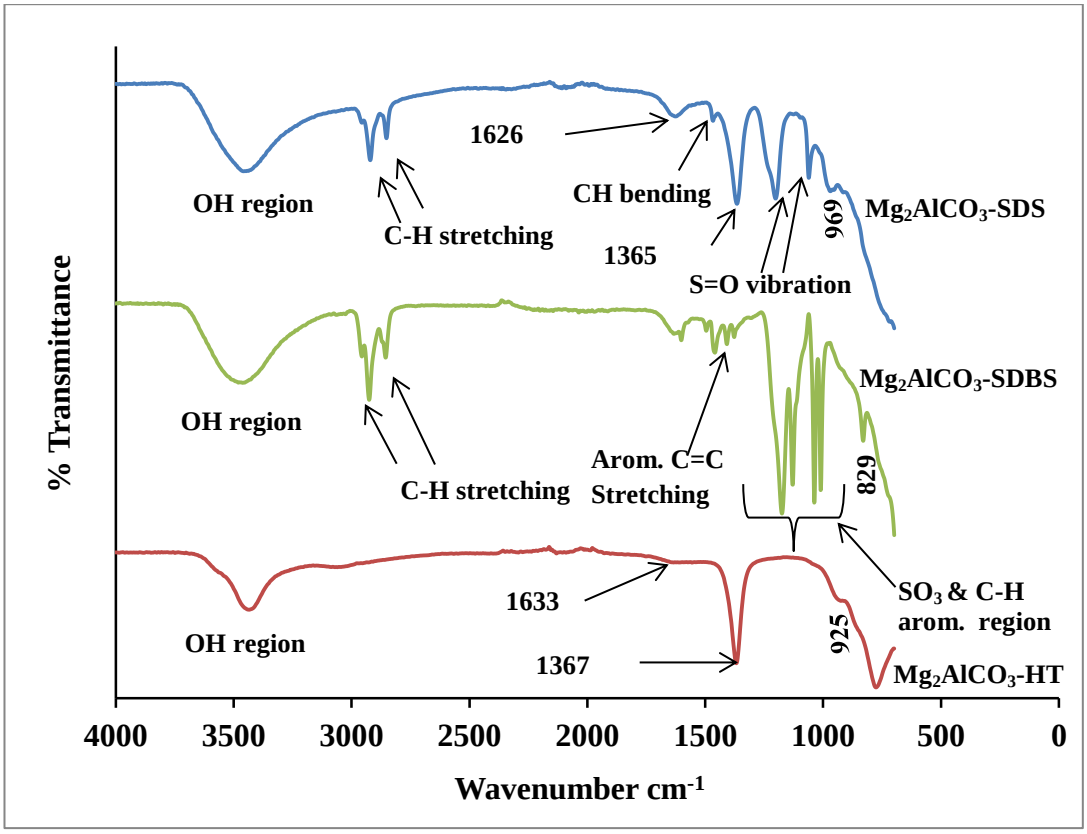

Fig.4.12: FT-IR spectra of Mg_2AlCO_3 hydrotalcite (Host HT-CO3), Mg_2AlCO_3-DS (dodecylsulfate-intercalated hydrotalcite) and Mg_2AlCO_3-DBS (dodecylbenzenesulfonate-intercalted hydrotalcite.

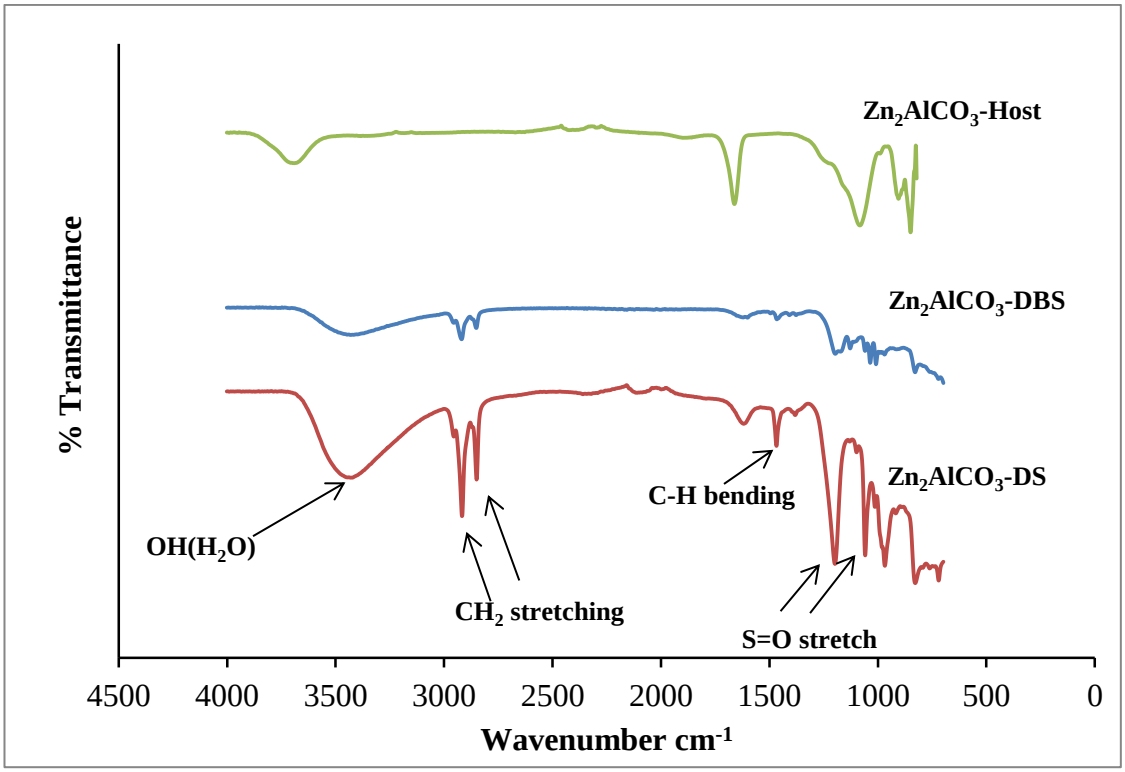

Fig.4.13: FT-IR spectra of Zn_2AlCO_3 hydrotalcite (Host HT-CO3), Zn_2AlCO_3-SDS (dodecylsulfate-intercalated hydrotalcite) and Zn_2AlCO_3-SDBS (dodecylbenzenesulfonate-intercalted hydrotalcite)

Fig.4.13 shows the FT-IR spectra of the host Zn_2AlCO_3-HTlc, Zn_2AlCO_3-DS and DBS organo-hydrotalcites. The broad band within the region 3300 - 3600cm^{-1} centered at 3384cm^{-1} for the host hydrotalcite, 3430 cm^{-1} for SDS intercalated derivative and 3429cm^{-1} for the SDBS derivative are due to the OH stretching vibration of the hydroxide layer and the gallery water molecules[166, 181, 187]. The shift to lower frequency from the host hydrotalcite to the surfactant intercalated hydrotalcite derivatives may be due to different interactions of the DS and DBS anions within the ZnAl hydroxide layer. For the SDS derivative, bands ascribed to CH_2 and OSO_3^- are seen at 2849, 2912 and 1198, 1058cm^{-1} respectively. For the SDBS derivative, bands ascribed to C-H, C-H aromatic, C=C aromatic and SO_3^- are apparent at 1492 cm^{-1}; 1127, 1059cm^{-1}; 1465,

1059 cm^{-1} and 1193, 1035, 1059, 1008cm^{-1} respectively. This demonstrates the intercalation of dodecylsulfate and dodecylbenzenesulfonate anions into the host Zn_2AlCO_3 hydrotalcite interlayer. The peaks with wavenumber of 700 - 1000cm^{-1} are assigned to metal–oxygen vibrations and this is common to all of them suggesting that the DS and DBS modified hydrotalcites maintained the hydrotalcite structure. These results are in agreement with reports of previous researchers[166, 181] who observed similar vibration bands.

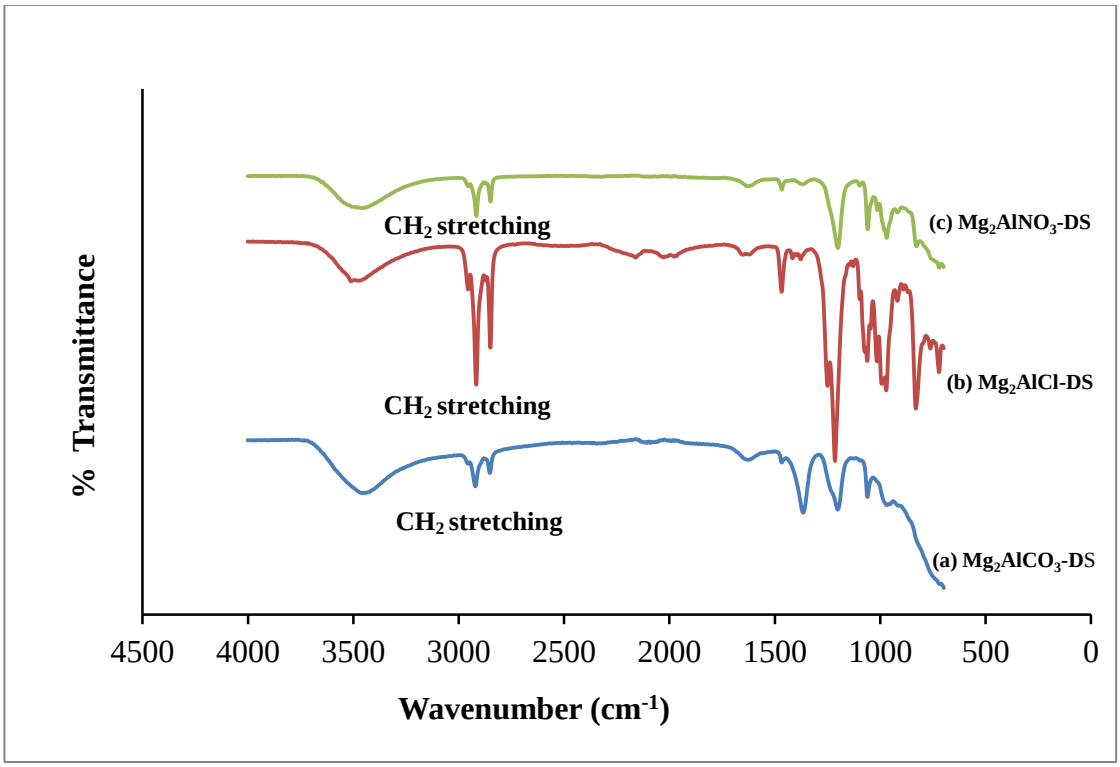

Fig.4.14: FT_IR spectra of (a) $CO_3^{2-}Mg_2Al$-SDS, (b) Cl^-Mg_2Al-SDS and (c) $NO_3^-Mg_2Al$-SDS

The presence of the dodecylsulfate anion in the interlamellar structure of Mg_2AlCO_3-DS, Mg_2AlCl-DS and Mg_2AlNO_3-DS, organo-hydrotalcite were also verified by FT-IR spectroscopy (Fig.4.14). The main frequencies and assignments are summarized in

Table 4.2. The presence of C-H stretching vibration, C-H bending vibration bands and the sulfate S=O stretching vibration bands confirms the intercalation of dodecylsufate into the interlayer of these DS intercalated hydrotalcites.

Table 4.1 Observed FT-IR shifts and assignments for Mg_2AlCO_3 -SDS, Mg_2AlCl -SDS and Mg_2AlNO_3 -SDBS organo-hydrotalcites

Peaks (cm^{-1})		**Designation**	
Mg_2AlCO_3-DS	Mg_2AlNO_3-DS	Mg_2AlCl-DS	
3458	3461	3492	OH stretch
1625	1626		OH bending
2920, 2851	2916, 2849	2916, 2849	CH_2 stretch
1467	1467	1467	C-H bending
1201, 1060	1200, 1059	1214, 1061	S=O (asym & sym.)
968, 719	917, 827	918, 830	M-O lattice

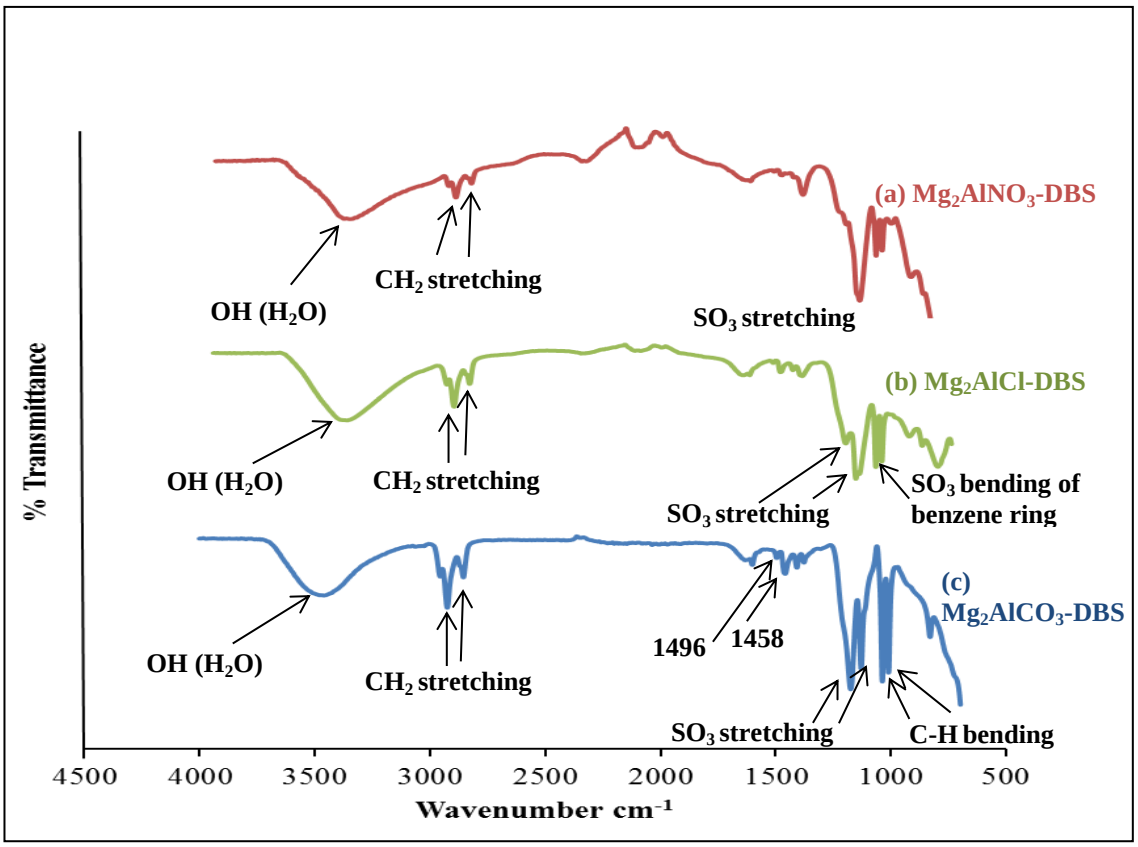

Fig.4.15: FT_IR spectra of (a) NO_3^- Mg_2Al-SDBS, (b) Cl^- Mg_2Al-SDBS and (c) CO_3^{2-} Mg_2Al-SDBS.

Fig.4.15 shows vibration bands that also indicate the intercalation of DBS anions into the interlayers of the various hydrotalcites. The three spectra showed C-H stretching and bending modes, bands due to SO_3 group confirming the presence of dodecylbenzenesulfonate anions in the interlayers of the various hybrid organo-hydrotalcites. The appearance of the sulfonate group is observed at 1174, 1129 cm^{-1} (Mg_2AlCO_3-DBS); 1174, 1120 cm^{-1} (Mg_2AlCl-DBS) and 1200, 1097cm^{-1} (Mg_2AlNO_3-DBS) ascribed to the asymmetric and symmetric bands of SO_3. The C-H bending vibration due to benzene ring are observed at 1036, 1009 $cm^{-1}$for (Mg_2AlCO_3-DBS);

1038, 1010 cm^{-1} (Mg_2AlCO_3-DBS) and 1059, 1013 cm^{-1} for the (Mg_2AlNO_3-DBS). The C-H bending vibrations are seen in the region 1467- 1496cm^{-1}. The slight shift in frequencies may be to the variation in the effect of the inorganic anions present in the various host hydrotalcites. These results confirm the successful intercalation of DBS into the interlayer of these hydrotalcites.

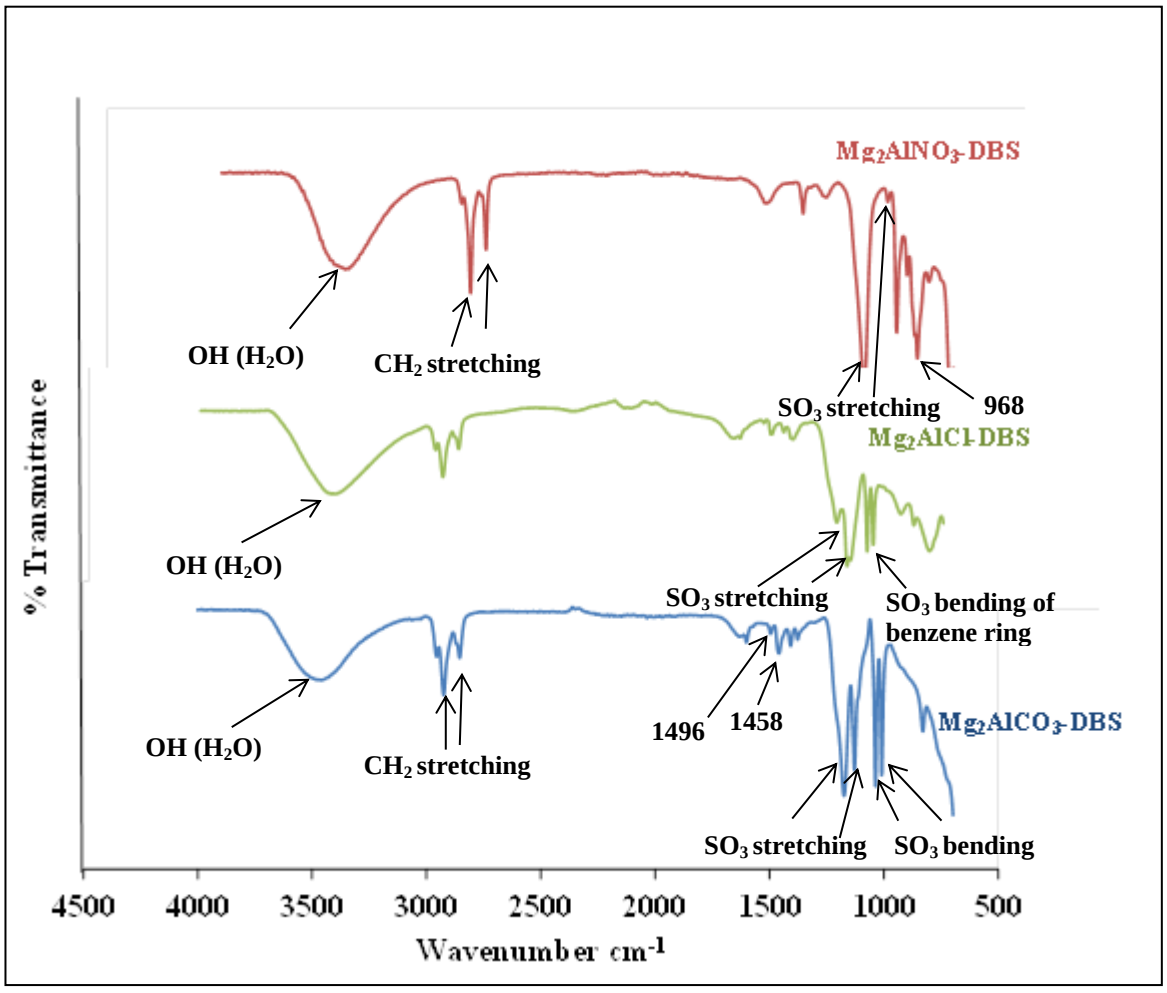

Fig.4.16: FT-IR spectra of (a) NO_3^--Mg_2Al-SDBS, (b) Cl^--Mg_2Al-SDBS and (c) CO_3^{2-} -Mg_2Al-SDBS

Table 4.2 Observed FT-IR shifts and assignments for Mg_2AlCO_3-DBS, Mg_2AlCl-DBS and Mg_2AlNO_3-DBS organo-hydrotalcites

Peaks (cm^{-1})			Designation
Mg_2AlCO_3-DBS	Mg_2AlNO_3-DBS	Mg_2AlCl-DBS	
3449	3401	3410	OH stretch
2954, 2924, 2854	2954,2916, 2849	2954, 2925, 2854	CH_2 stretch
1460	1467	1467	C-H bending
1400	1407	1405	CH_3 stretch
1036,1009	1200, 1097	1174, 1128	Aromatic C-H bend
1174, 1129,	1059, 1013	1036, 1009	SO_3- group
826	968, 917, 719		M-O lattice

4.4.3 XRF Analysis

Table 4.4 shows elemental analysis data and mole ratios of some modified hydrotalcites (organo-hydrotalcites).The compositions of Mg, Zn and Al in the modified hydrotalcites gives similar Mg/Al and Zn/Al ratio to those of the host hydrotalcites that were modified. This suggests that, the SDS and SDBS regenerated hydrotalcites retained their integrity. Following issues discussed previously (section 4.3) which meant that it proved not possible to prepare beads for some of the samples, so we are unable to present data for the full range of hybrid organo-hydrotalcites. However from the results that we have, it is likely that the others will be similarly consistent with their parent hydrotalcite

Table 4.4 Selected elemental analysis data and mole ratios of SDS and SDBS modified hydrotalcites

Hydrotalcite type	Wt % MgO	Wt % Al_2O_3	Wt % ZnO	Molar ratio Mg/Al	Molar ratio Zn/Al
Mg_2AlCO_3-SDS	26.2	13.5	-	2.45	-
Mg_2AlCO_3-SDBS	19.0	9.62	-	2.50	-
Mg_3AlCO_3-SDS	30.5	11.9	-	3.24	-
Mg_3AlCO_3-SDBS	16.1	6.72	-	3.03	-
Mg_4AlCO_3-SDBS	18.2	5.69	-	4.05	-
Zn_2AlCO_3-SDS	-	6.66	24.88	-	2.34
Mg_2AlNO_3-SDS	17.1	10.4	-	2.08	-
Mg_2AlCl-SDS	6.75	4.05	-	2.11	-
Mg_2AlCl-SDBS	30.7	12.0	-	2.32	-
Mg_2AlNO_3-SDBS	6.97	4.05	-	2.18	-

4.4.4 Thermal analysis

The thermal behaviour of the organo-hydrotalcites is similar to that of the host hydrotalcites from which they were derived. The thermal behaviour is described by two thermal transitions depending on the charge density which in turn depends on the aluminium content of the organo-hydrotalcites. In addition to thermal effects due to dehydration of the interlayer space and dehydroxylation of the metal hydroxide layers noted in the host hydrotalcites, the organo-hydrotalcite thermal behaviour show some other effects due to combustion of the dodecylsulfate and dodecylbenzenesulfonate anions.

Fig.4.15 shows the TG-DTA of Mg_2AlCO_3-DS organo-hydrotalcite. It is apparent from the TGA and DTA that this material presented similar endothermic peaks as those of the host hydrotalcite discussed in section 3.9, although the changes are not as sharply defined, and the % weight loss at each stage is different. The differences may be ascribed to the combustion and decomposition of the dodecylsulfate anion, resulting in release of H_2O and CO_2 which were detected by mass spectrometry, and in some cases SO_2 evolution was also observed. Like the host precursor, the TGA profile is characterised by two weight loss steps. The first weight loss step centred at 158^oC accounting for a wt. loss of ca.18.5% from the initial sample weight which, is due to the release of water in stages at 157^oC and 222^oC through desorption of physisorbed water and dehydration of the interlayer space; these two processes are not resolved on the TGA trace. The wt. loss step occurring between the temperature ranges of 360^oC-580^oC, ascribed to 14.7% wt. loss, is accompanied by release of water at 417^oC and release of CO_2 at 422^oC. This step accounts for dehydroxylation of the metal hydroxide layers and combustion of the dodecylsulfate anion leading to loss of water and CO_2 (plus removal of any residual carbonate). No further weight loss steps are observed above *ca*. 600^oC, in contrast to the host precursor Mg_2AlCO_3- HTlc for which the weight loss was complete at *ca*. 440^oC. The endothermic transition observed above 600^oC relates to the phase transformation to the spinel, which is not accompanied by any further weight change. The temperature of the second step is higher in Mg_2AlCO_3-DS organo-hydrotalcite than the host Mg_2AlCO_3- HTlc (section 3.9). The total weight loss at 900^oC is 33.6%.

Fig.4.16: shows the TGA-DTA of Mg_2AlCO_3-DBS organo-hydrotalcite showing similar decomposition processes with differences in the temperature at which the various

weight changes occurred. The first weight loss is centered at 150^{o}C embracing a weight loss of 12% and encompassing the release of water at ca.137^{o}C and 215^{o}C. The second weight loss is centred at ca.416^{o}C leading to a wt. loss of 38% releasing water at a temperature range of 280-580^{o}C in two steps having maxima at ca.405^{o}C and at 474^{o}C on the ion current curve (m/z = 18). CO_2 is also removed between 350 - 560^{o}C in two steps at ca.405^{o}C and 483^{o}C. This stage is attributed to the dehydroxylation of the hydroxide layers and the decomposition of the dodecylbenzensulfonate anions. The first weight loss step occurs at a slightly lower temperature than the DS intercalated sample while the second step has shifted to higher temperature. This may be due to the effect the benzene ring conferred on this sample. The weight loss is complete at *ca*. 600^{o}C, while ca.575^{o}C for Mg_2AlCO_3-DS and ca.440^{o}C for the host Mg_2AlCO_3-HTlc. This organo-hydrotalcite showed a total weight loss of 49.5% at 900^{o}C.

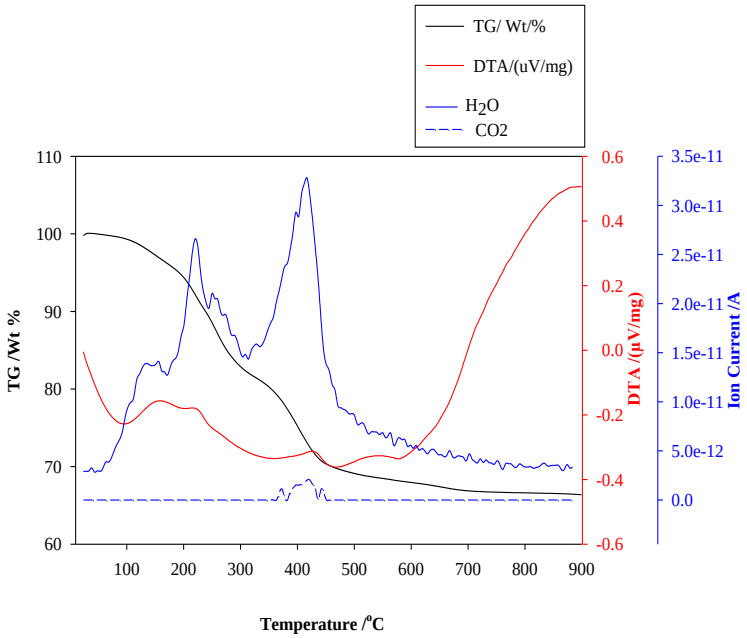

Fig.4.17: TGA-DTA of Mg_2AlCO_3-DS (Mg_2Al-CO_3 hydrotalcite intercalated with sodium dodecylsulfate anion).

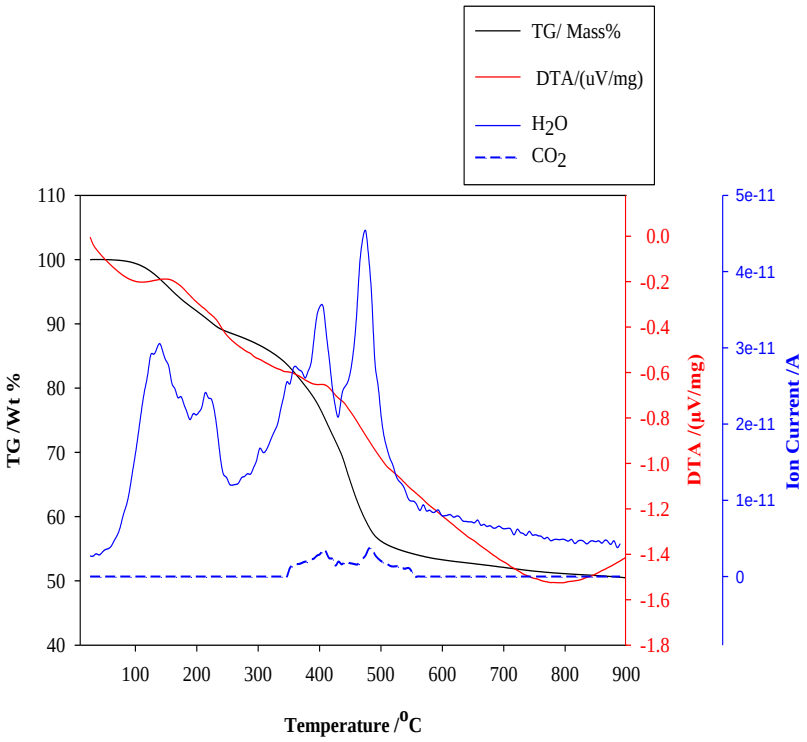

Fig.4.18: TGA-DTA of Mg_2AlCO_3-DBS (Mg_2Al-CO_3 hydrotalcite intercalated with sodium dodecylbenzenesulfonate anion).

The thermogravimetric analysis of the Mg_3AlCO_3-DS organo-hydrotalcite is shown in Fig.4.19. The TG curve shows two weight loss steps embracing 46.13% and 27.2% wt. loss due to similar effects discussed previously. The DTA curve representing the first wt. loss is suggesting two processes occurring consecutively at ca.152^oC and 238^oC accompanied by the removal of CO_2 between 150- 250^oC and water at ca. 244^oC, which may be due to decomposition of the organo-hydrotalcite. The decomposition of the dodecylsulfate anion occurred at a higher temperature releasing H_2O at ca.420^oC, CO_2 at ca.601^oC and SO_2 at ca.610^oC. This sample showed a total weight loss of 62% at 900^oC.

The amount of water removed in the first step is larger than that removed in the second step which may indicate a smaller amount of dodecylsulfate anion incorporation into the

sample. The temperatures at which H_2O and CO_2 is released is comparatively higher than those in the Mg_2AlCO_3-DS/ Mg_2AlCO_3-DBS. In addition, the CO_2 was eliminated in two steps: at low temperature, the release of residual carbonate starts as early as 150°C and continues till 250°C, and the release at high temperature at 525-650^oC. This may be due to an increase in Mg^{2+}/Al^{3+} mole ratio. The weight loss is complete at ca.650^oC and no further weight loss steps occurred above this temperature. However, like the Mg_2AlCO_3-DS the endothermic transition observed above 650^oC relates to the phase transformation forming the spinel and was not accompanied by any further weight change either.

The TGA profile of Mg_3AlCO_3-DBS organo-hydrotalcite is displayed in Fig.4.18. The DTA profile shows four endothermic peaks as the amount of Mg intercalated into the material increased. The first DTA peak at ca.158^oC corresponding to the release of water at 154^oC encompasses a weight loss of 4% from the initial sample weight. This may be attributed to the elimination of physically adsorbed water. The sharp DTA peak with maximum at 346^oC reveals a 10.3%wt. loss on the TG and corresponds to removal of interlayer water. The DTA profile shows two processes occurring between 420-540^oC which shows as a degradation step leading to a wt. loss of ca.38% on the TG curve. The processes occurring here are dehydroxylation of the Mg_3AlOH layer, combustion of the dodecylbenzenesulfonate and decomposition of residual carbonate anion. The temperature at which the various transitions occurred is slightly higher than those of Mg_3AlCO_3-DS organo-hydrotalcite due to same reason discussed previously.

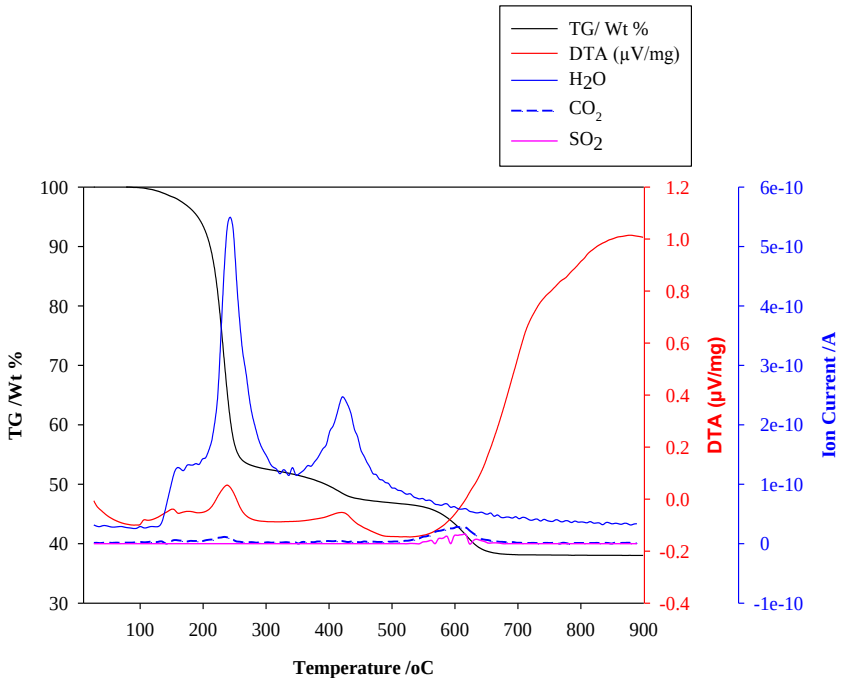

Fig.4.19: TGA-DTA of Mg_3AlCO_3-DS (Mg_3Al-CO_3 hydrotalcite intercalated with sodium dodecylsulfate anion).

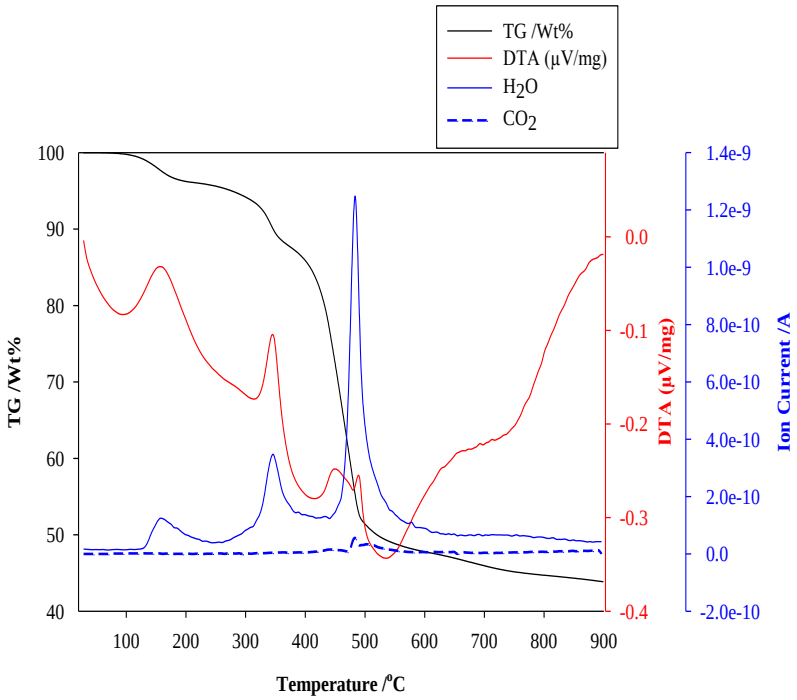

Fig.4.20: TGA-DTA of Mg_3AlCO_3-DBS (Mg_3Al-CO_3 hydrotalcite intercalated with sodium dodecylbenzenesulfonate anion).

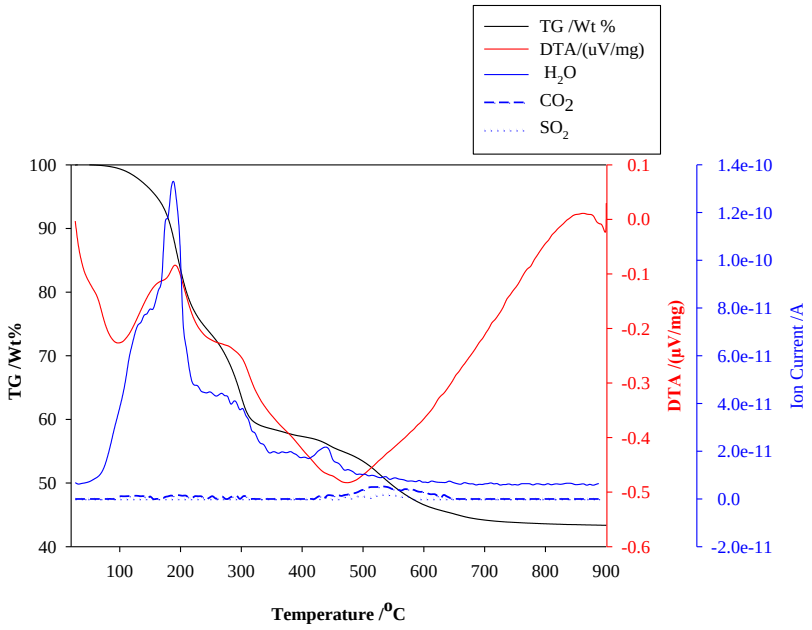

Fig.4.21: TGA-DTA of Zn_2AlCO_3-DS (Zn_2Al-CO_3 hydrotalcite intercalated with sodium dodecylsulfate anion).

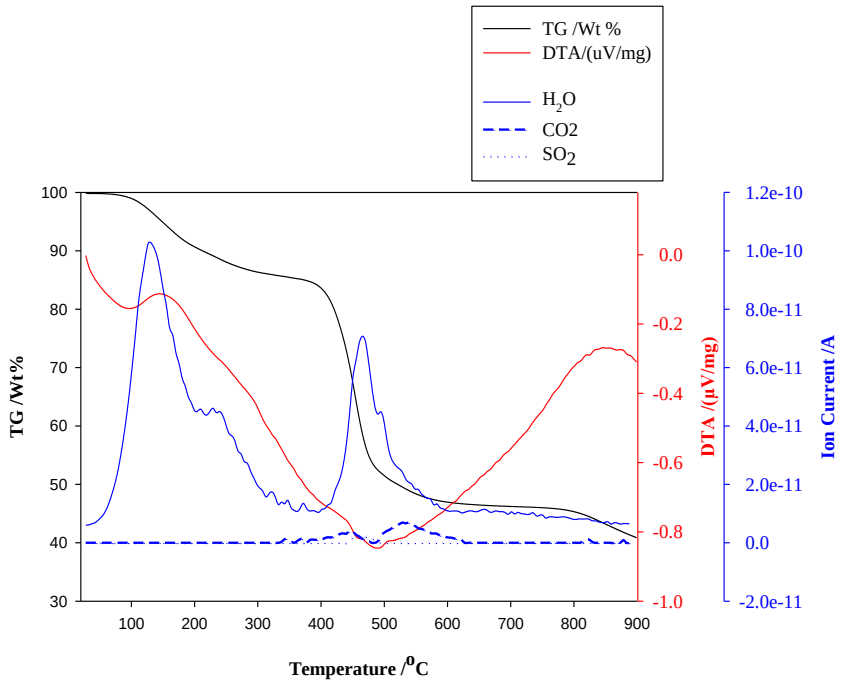

Fig.4.22: TGA-DTA of Zn_2AlCO_3-DBS (Zn_2Al-CO_3 hydrotalcite intercalated with sodium dodecylbenzenesulfonate anion).

Fig.4.21 and Fig.4.22 show the thermal analysis profiles of Zn_2AlCO_3-DS and Zn_2AlCO_3-DBS organo-hydrotalcites. The two materials show thermal transitions

similar to the previous samples with variations in the temperatures associated with the transition steps and the weight changes. Both samples differ from each other by the fact that the transition steps are not clearly resolved in the Zn_2AlCO_3-DS organo-hydrotalcite. This may be due to the strength of interaction between the surfactant anions and the Zn_2AlOH layers. The total weight loss at 900^oC is 57% in Zn_2AlCO_3-DS and 59% in Zn_2AlCO_3-DBS.

Fig.4.23 and 4.24 display the TGA, DTA and ion current profiles of Mg_2AlNO_3-DS and Mg_2AlCl-DS organo-hydrotalcites. Mg_2AlNO_3-DS organo-hydrotalcite exhibits three stages of degradation: The first occurred (in stages) at low temperature below 200^oC ascribed to the removal of surface physiosorbed water and water in the gallery between the Mg_2Al hydroxide layers. The second (occurred below 300^oC and shown on DTA curve with a maximum at 234^oC) is ascribed to the dehydroxylation of the Mg_2Al hydroxide layers plus removal of the carbonate contaminant around 200^oC and the third is the removal of the dodecylsulfate anion due to combustion, and occurred around 600^oC. The temperatures at which each of these stages begins and finishes vary from those of Mg_2AlCO_3-DS discussed earlier and Mg_2AlCl-DS. This sample shows a total weight loss of 58.5% at 900^oC.

The thermal behaviour of Mg_2AlCl-DS organo-hydrotalcite displays TGA-DTA profiles showing various thermal changes leading to evolution of water (in stages at 111^oC, 200-270^oC and around 388^oC), CO_2 (also at ca. 269^oC and ca. 598^oC) and Cl at 260^oC. The evolutions at low temperatures are due to the decomposition of the Mg_2AlCl-DS organo-hydrotalcite while those at high temperatures are due to combustion of the dodecylsulfate. The sample showed a total weight loss of 69.5% at 900^oC. This sample shows a total weight loss of 58.5% at 900^oC.

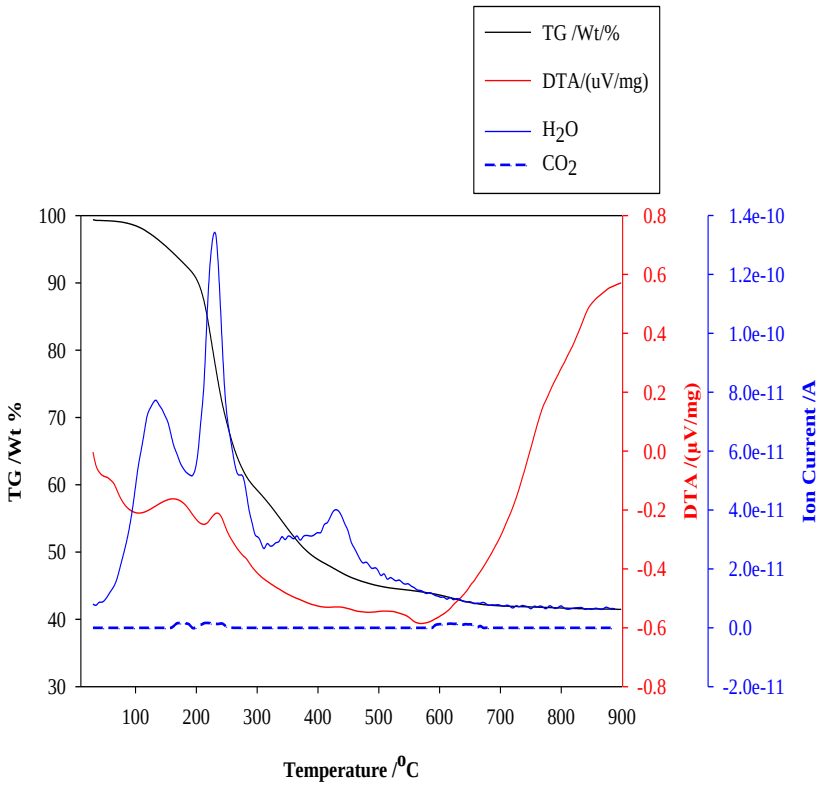

Fig.4.23: TGA-DTA of Mg_2AlNO_3-DS (Mg_2Al-NO_3 hydrotalcite intercalated with sodium dodecylsulfate anion).

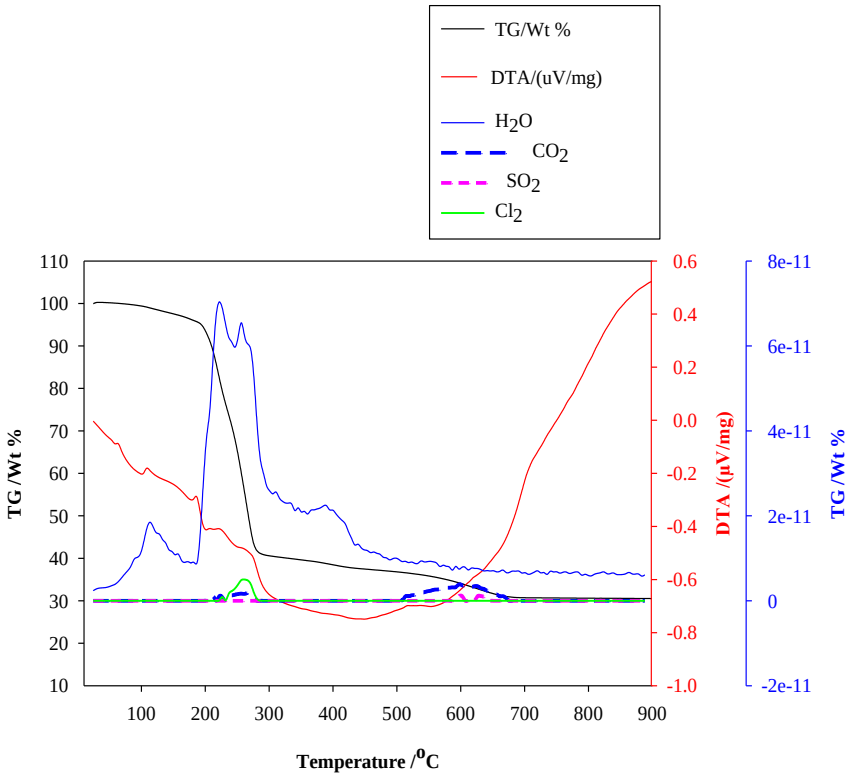

Fig.4.24: TGA-DTA of Mg_2AlCl-DS (Mg_2Al-Cl hydrotalcite intercalated with sodium dodecylsulfate anion).

4.4.5 Scanning Electron Microscopy (SEM)

The SEM images of the synthesised hydrotalcites and the surfactant (SDS and SDBS) intercalated derived hybrid organo-hydrotalcites are shown in Figs 4.25 – 4.34. It can be seen that the host hydrotalcites are thick hexagonal plate-like crystal with non-homogenous crystals. The sizes are not uniform. The modified counterparts show the same morphology as the host precursors, but many of the particles have broken down into smaller pieces, as a result of both the dehydration/dehydroxylation pre-treatment and regeneration with organic anions.

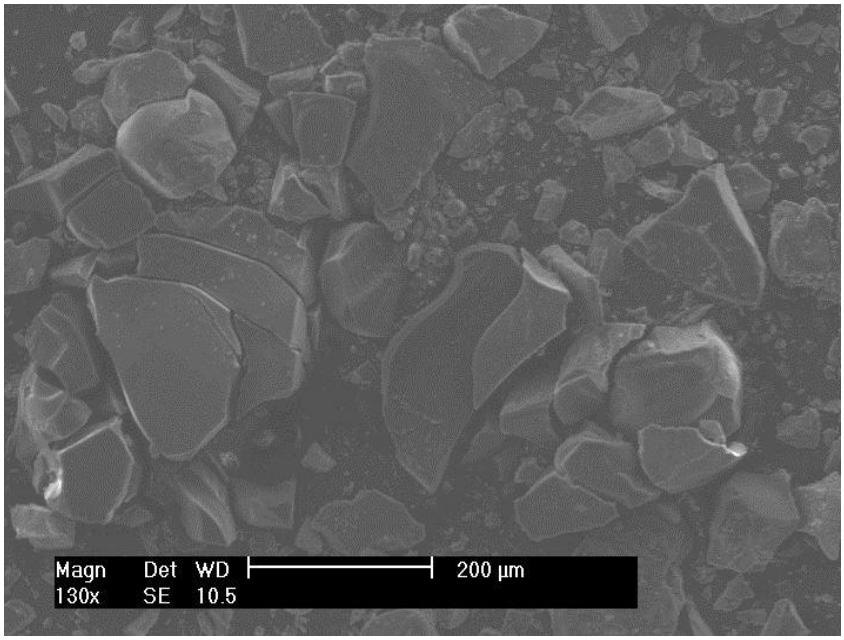

Fig.4.25a: SEM image of Mg_2AlCO_3-HTlc

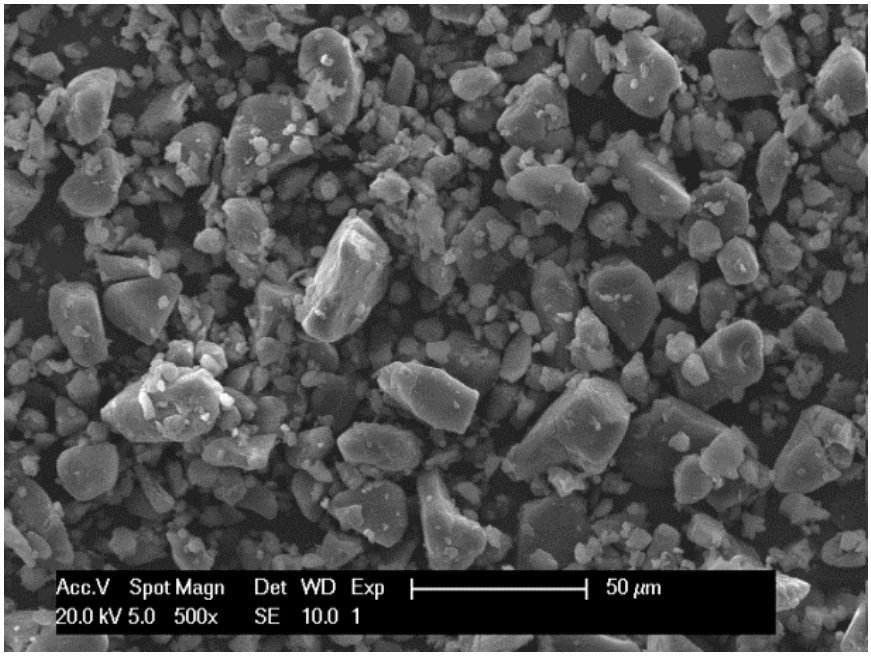

Fig.4.25b: SEM image of Mg_2AlCO_3-DS

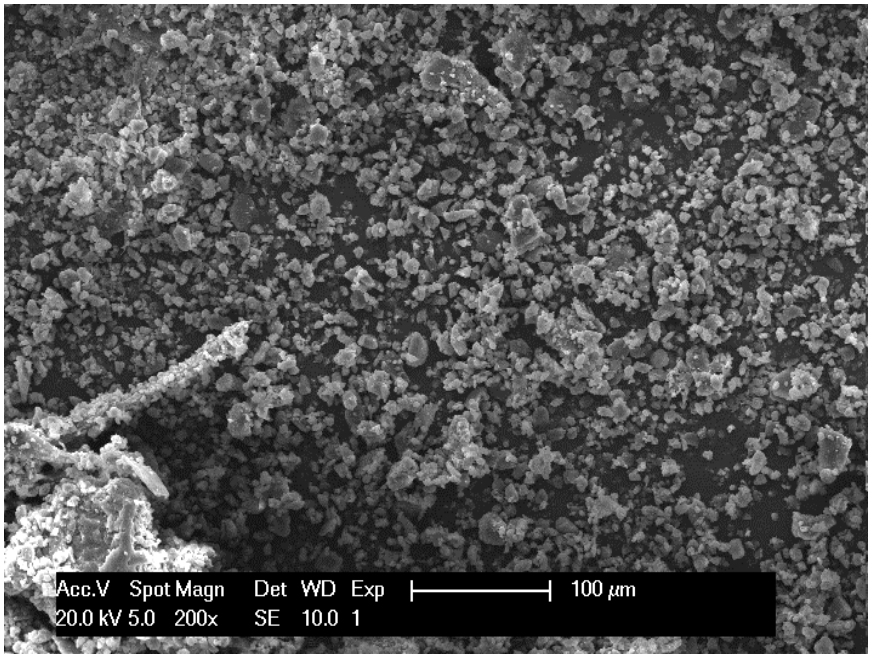

Fig.4.25c: SEM image of Mg_2AlCO_3-DBS hybrid organo-hydrotalcites

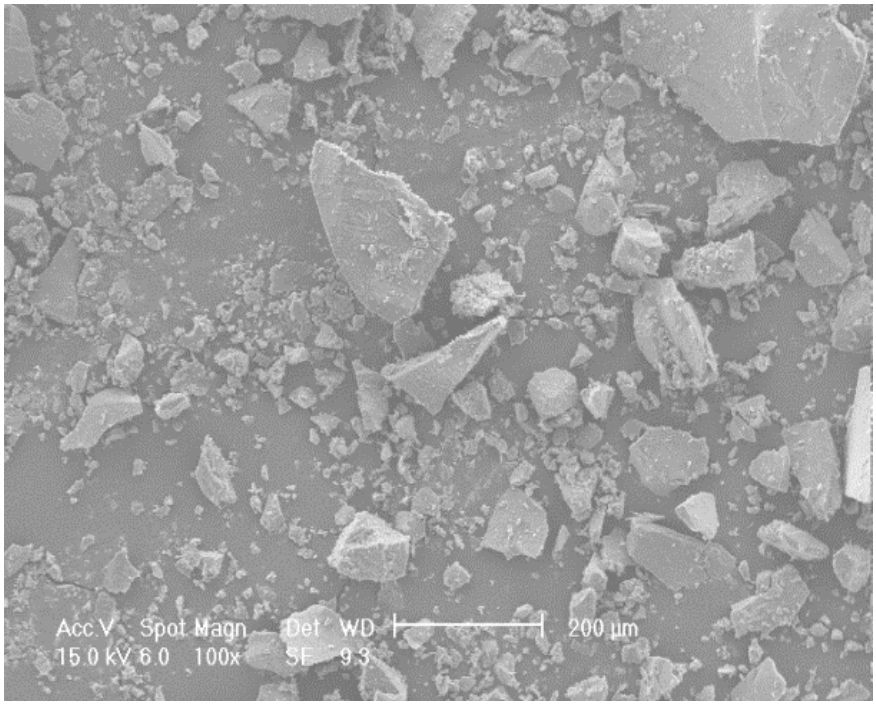

Fig.4.26a: SEM image of Mg_3AlCO_3-HTlc

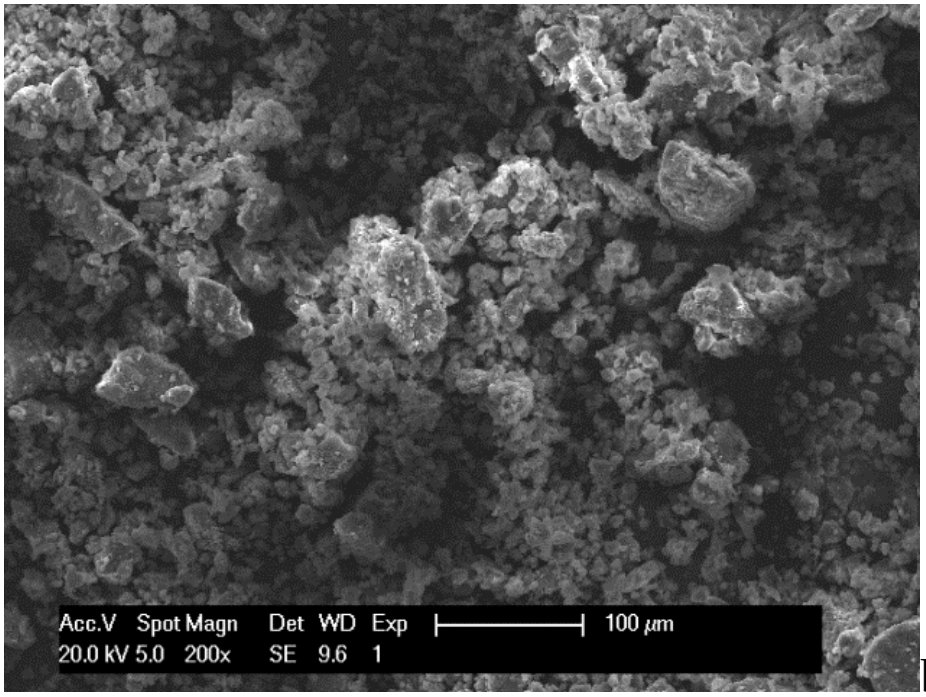

b

Fig.4.26b: SEM image of Mg_3AlCO_3-DS

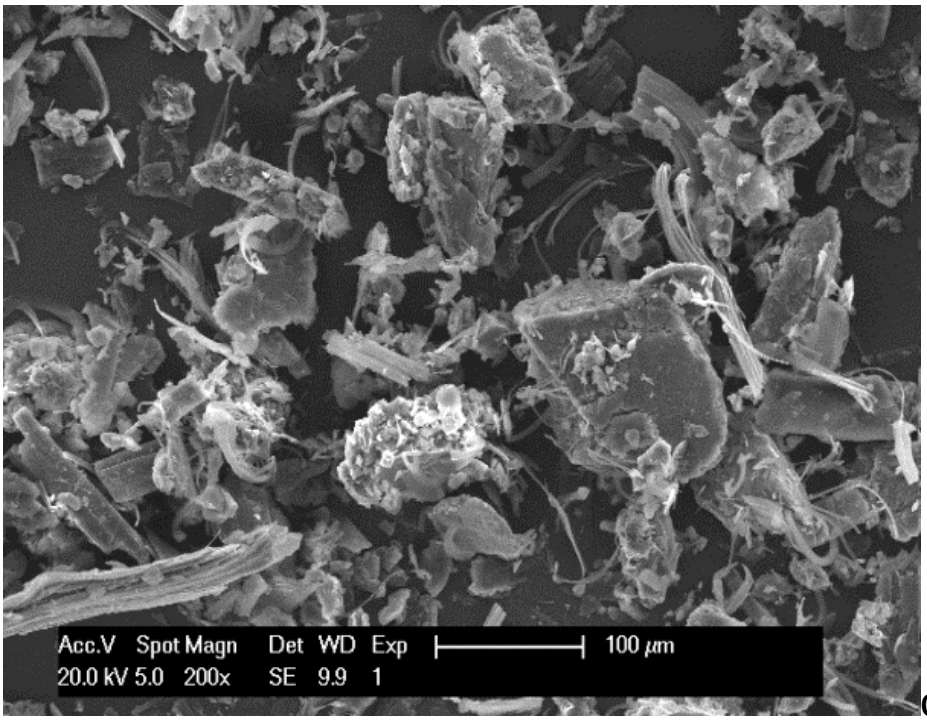

c

Fig.4.26c: SEM image of Mg_3AlCO_3-DBS hybrid organo-hydrotalcites

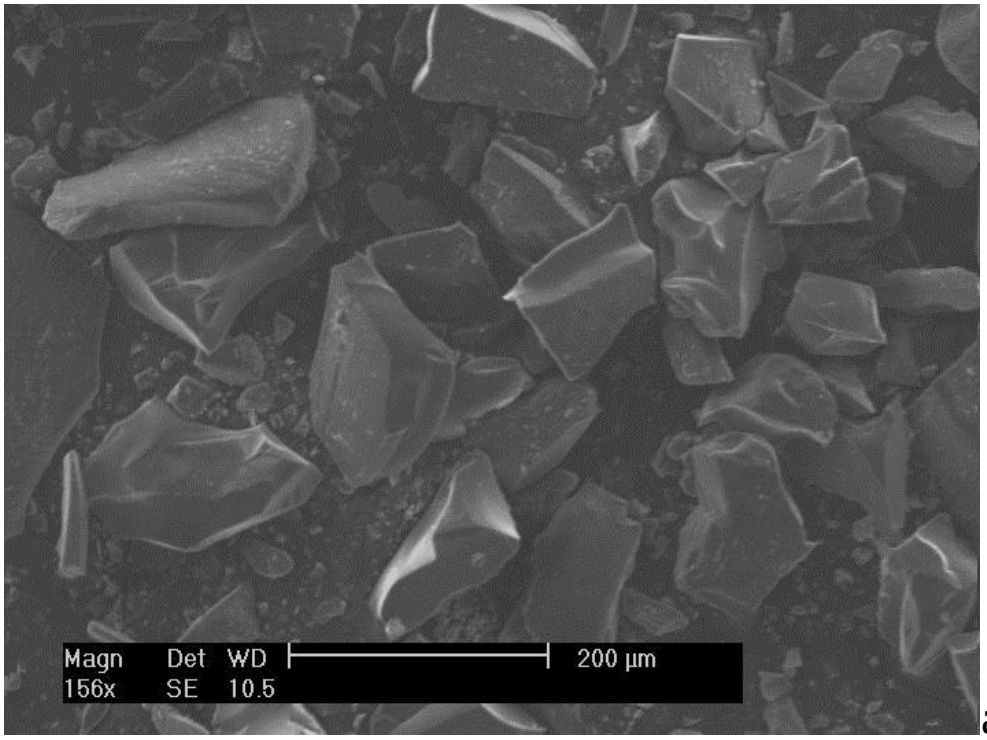

a

Fig.4.27a: SEM image of Mg_4AlCO_3-HTlc

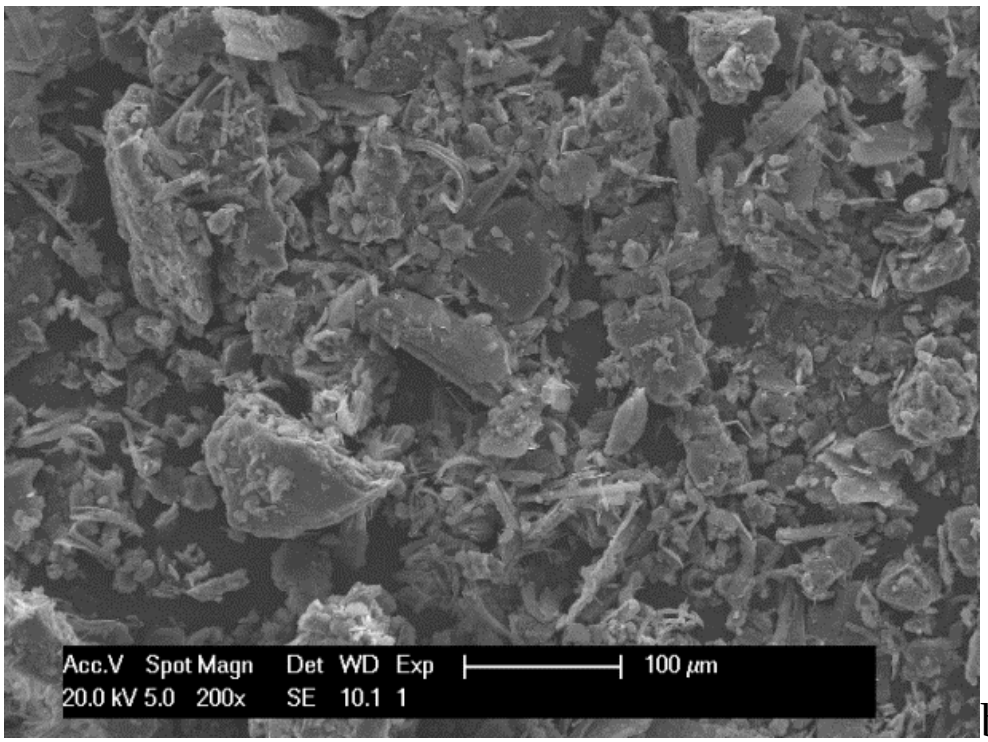

b

Fig.4.27b: SEM image of Mg_4AlCO_3-DS

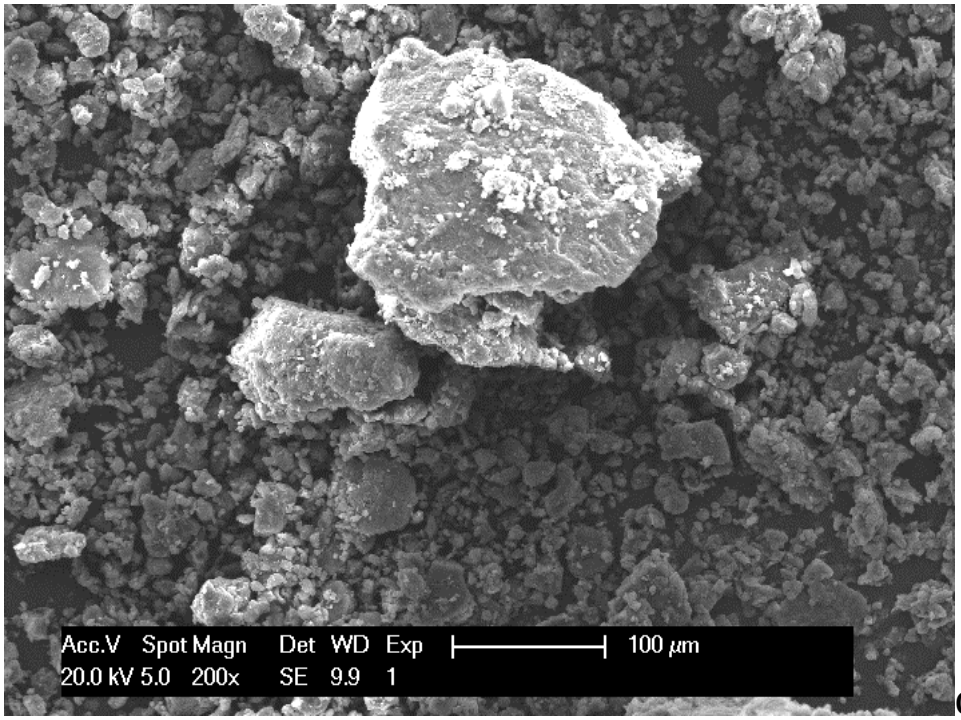

c

Fig.4.27c: SEM image of Mg_4AlCO_3-DBS hybrid organo-hydrotalcites

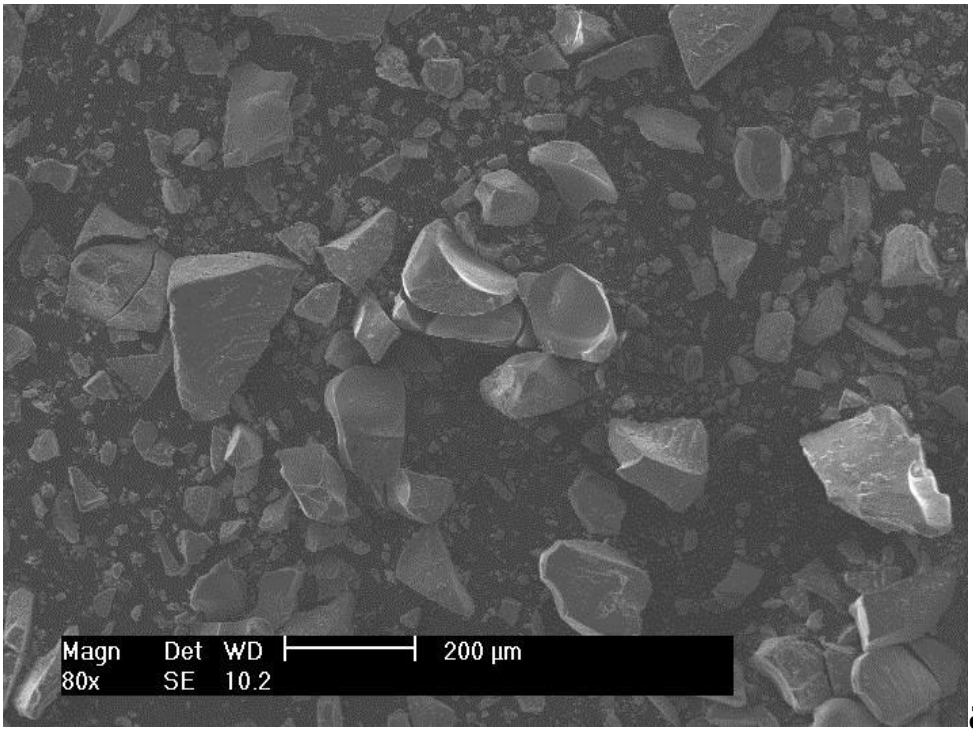

a

Fig.4.28a: SEM image of Zn_2AlCO_3-HTlc,

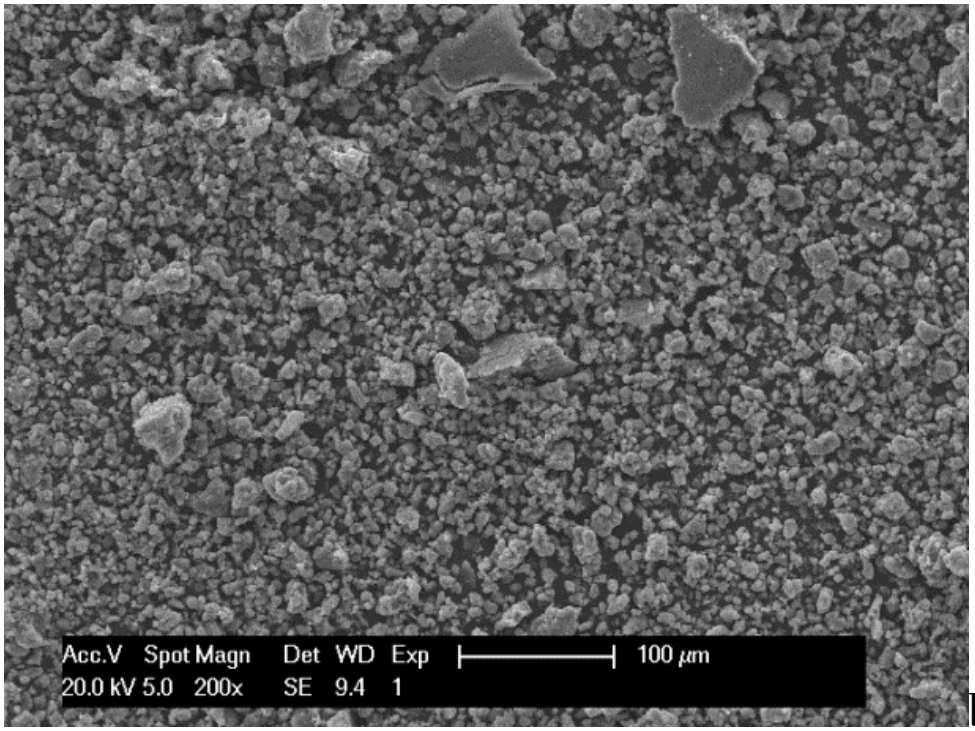

b

Fig.4.28b: SEM image of Zn_2AlCO_3-DS

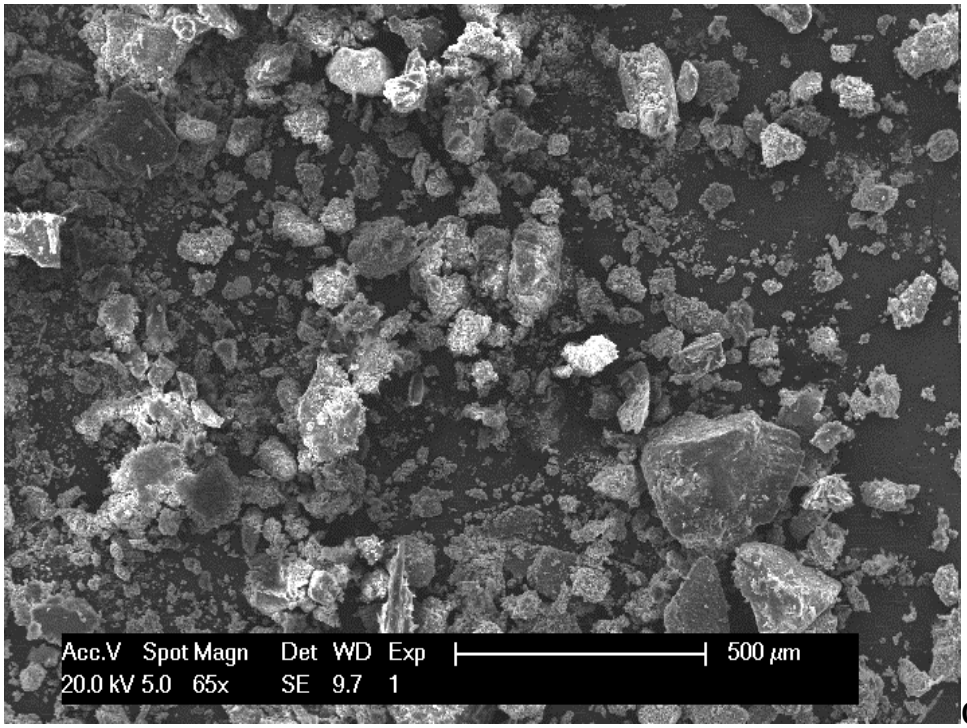

c

Fig.4.28c: SEM image of Zn_2AlCO_3-DBS hybrid organo-hydrotalcites

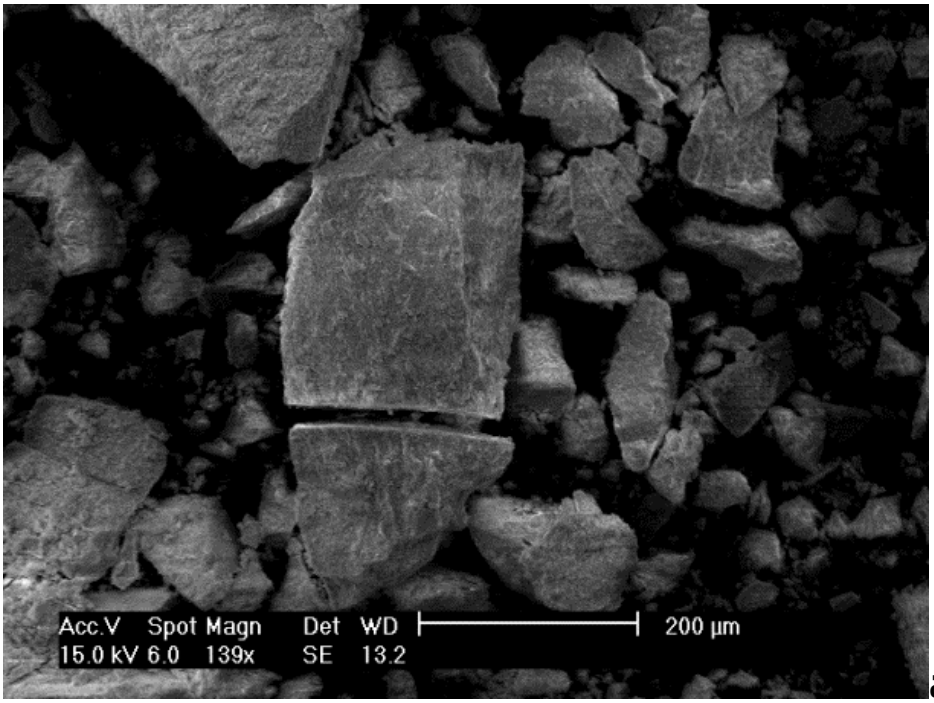

a

Fig.4.29a: SEM image of Zn_3AlCO_3-HTlc

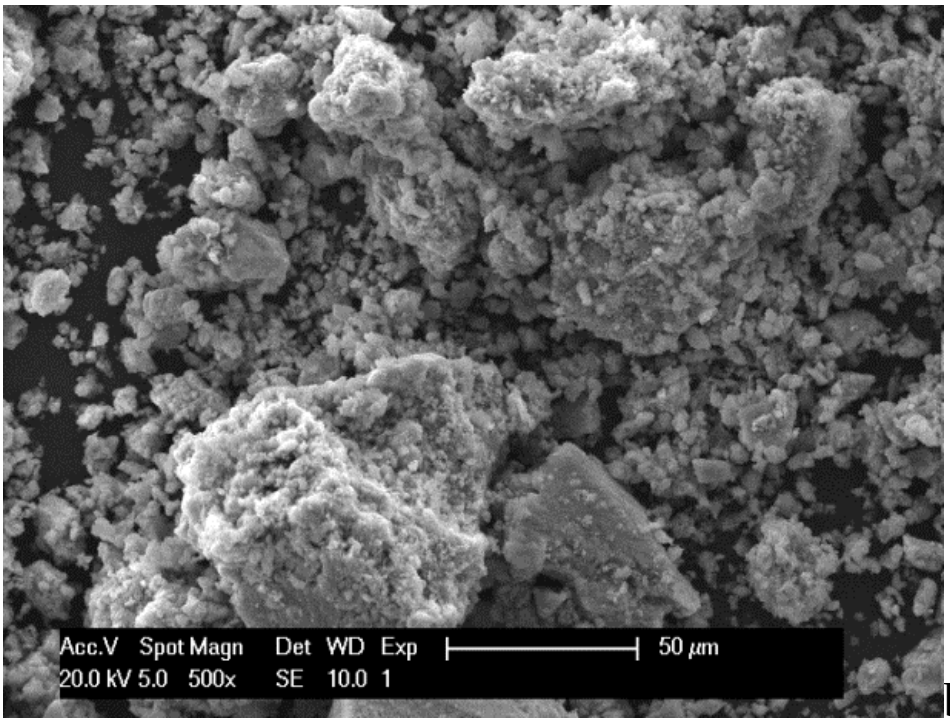

b

Fig.4.29b: SEM image of Zn_3AlCO_3-DS

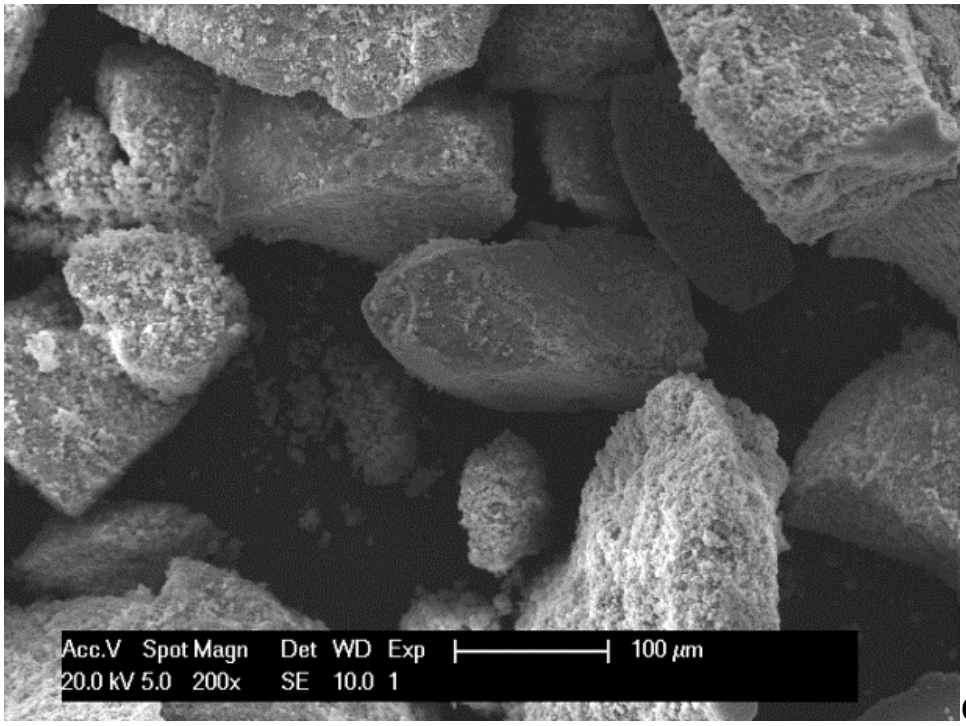

c

Fig.4.29c: SEM image of Zn_3AlCO_3-DBS hybrid organo-hydrotalcites.

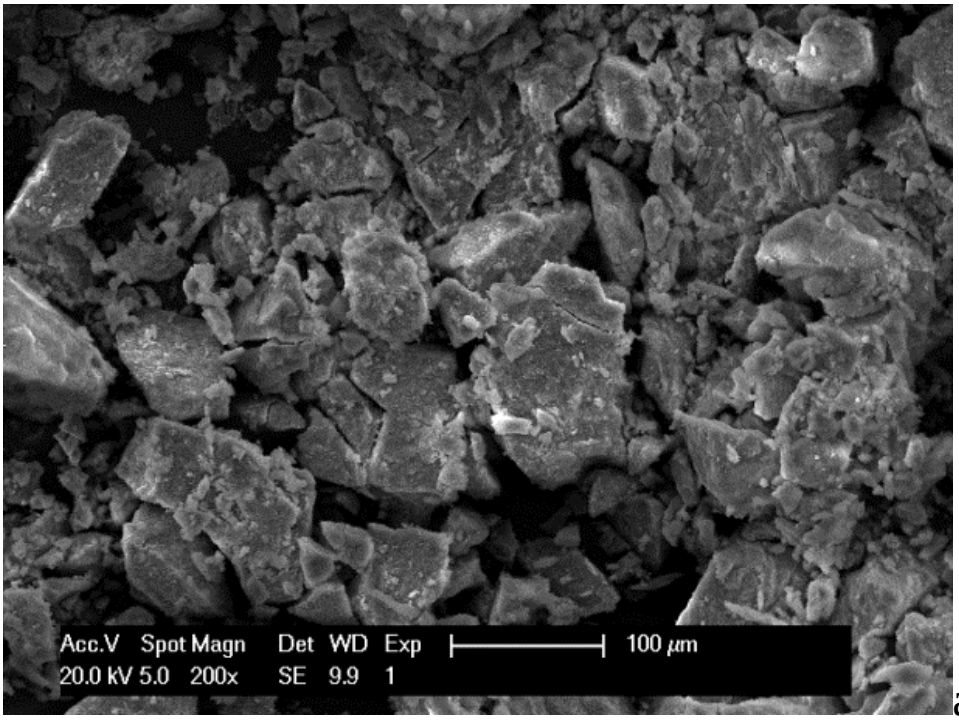

a

Fig.4.30a: SEM image of Zn_4AlCO_3-HTlc

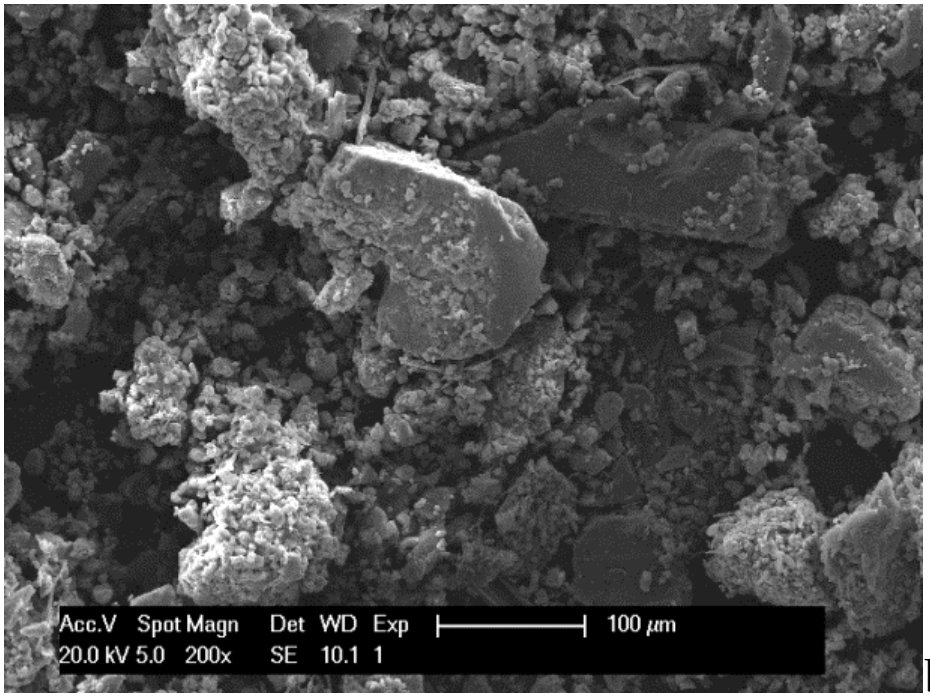

b

Fig.4.30b: SEM image of Zn_4AlCO_3-DS

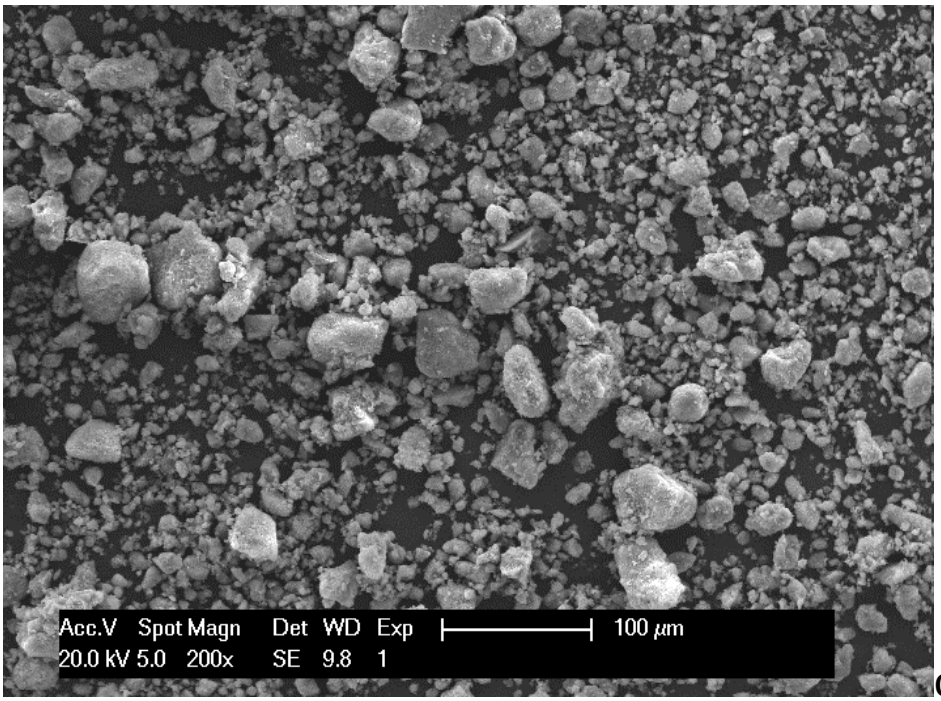

c

Fig.4.30c: SEM image of Zn_4AlCO_3-DBS hybrid organo-hydrotalcites.

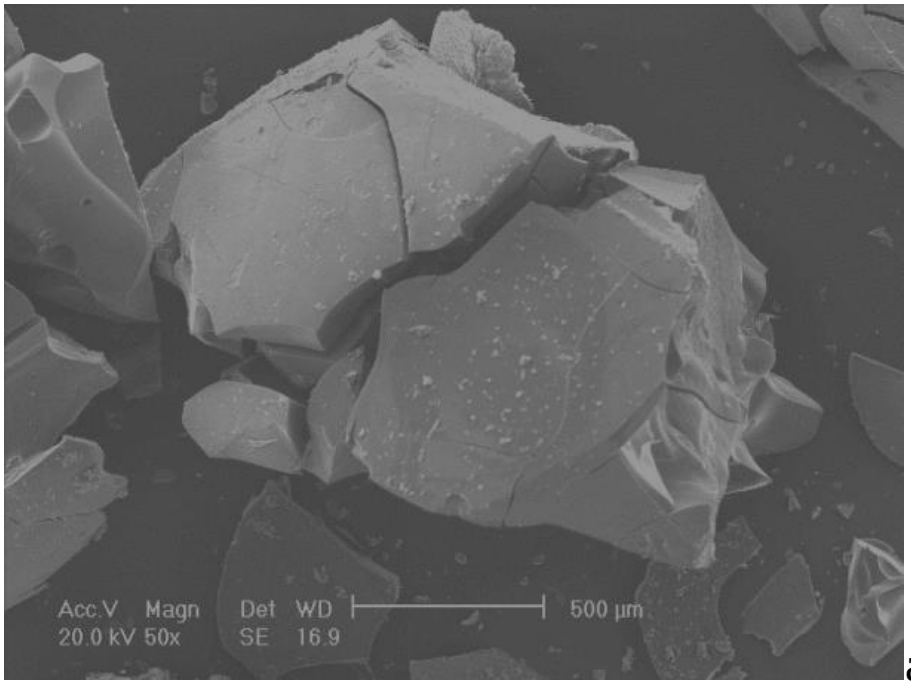

a

Fig.4.31a: SEM image of Mg_2AlNO_3-HTlc

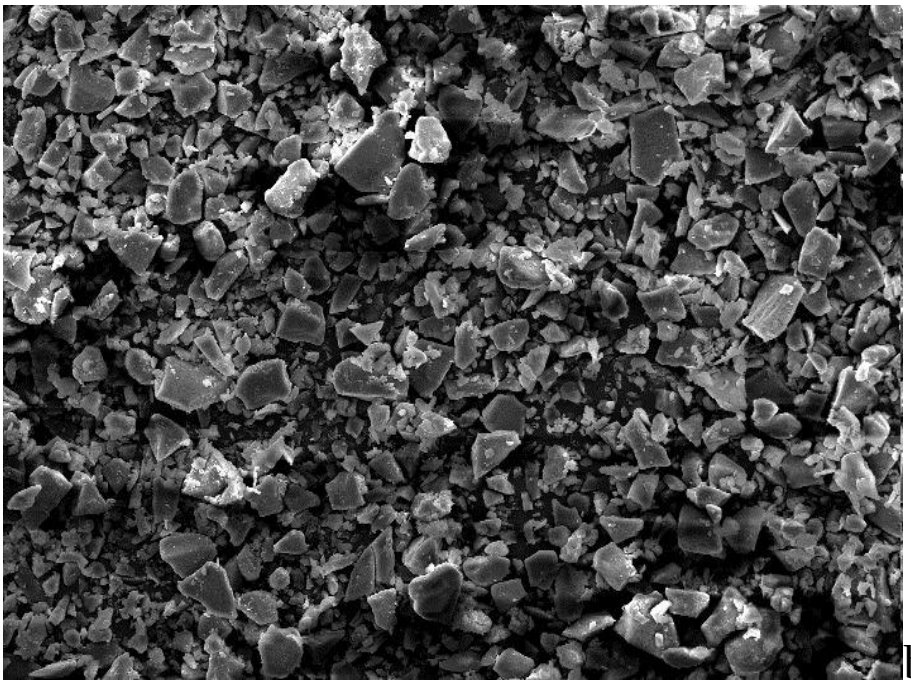
b

Fig.4.31b: SEM image of Mg_2AlNO_3-DS

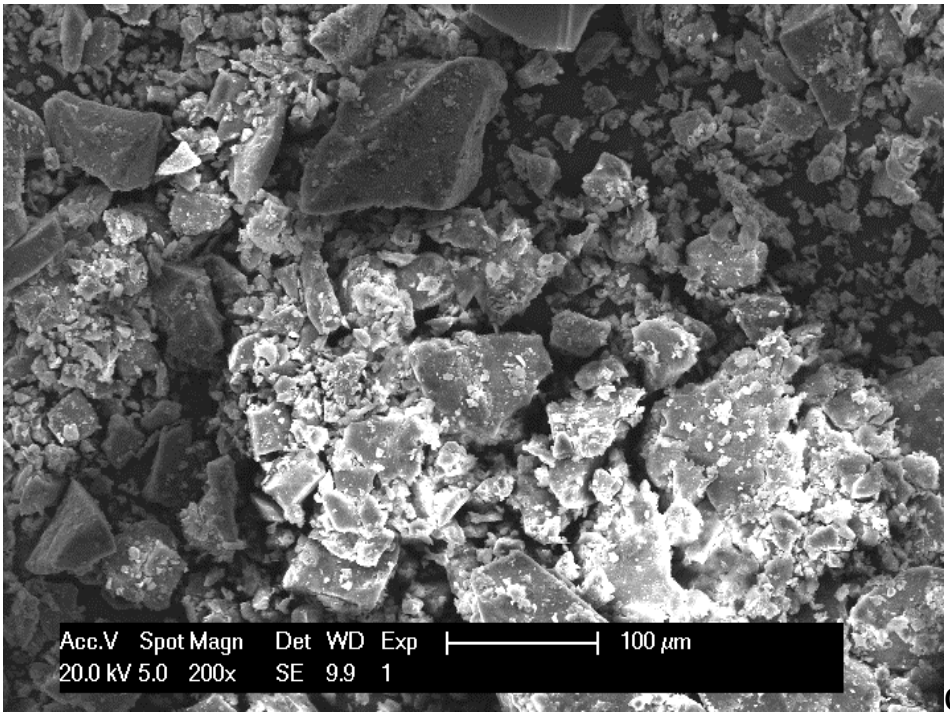

c

Fig.4.31c: SEM image of Mg_2AlCO_3-DBS hybrid organo-hydrotalcites.

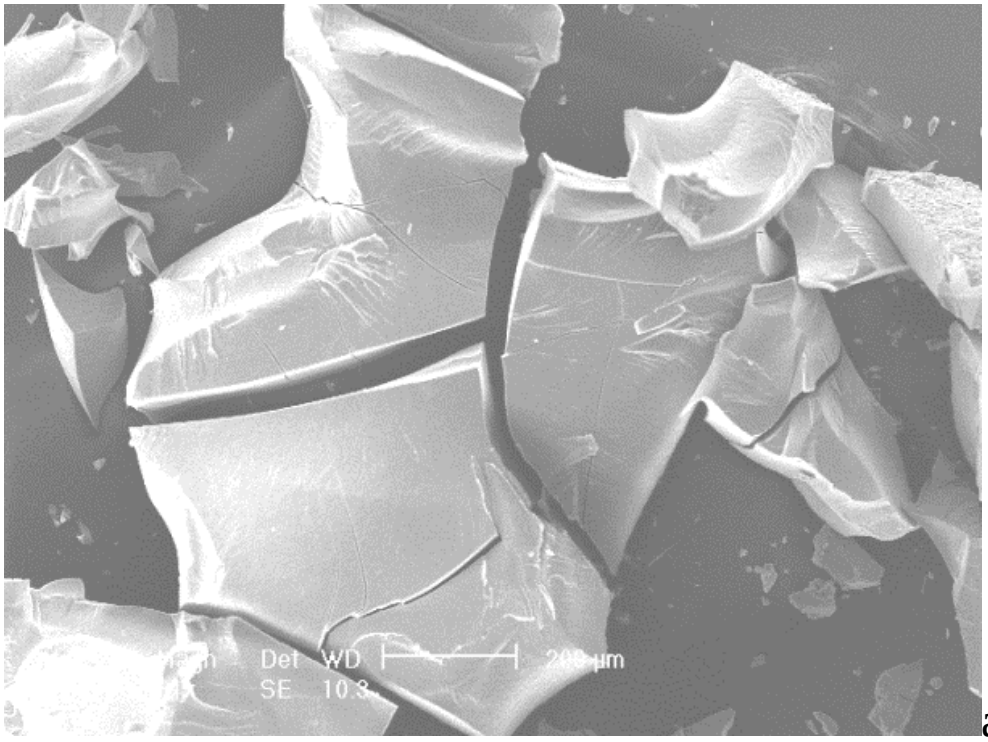

a

Fig.4.32a: SEM image of Zn_2AlNO_3-HTlc

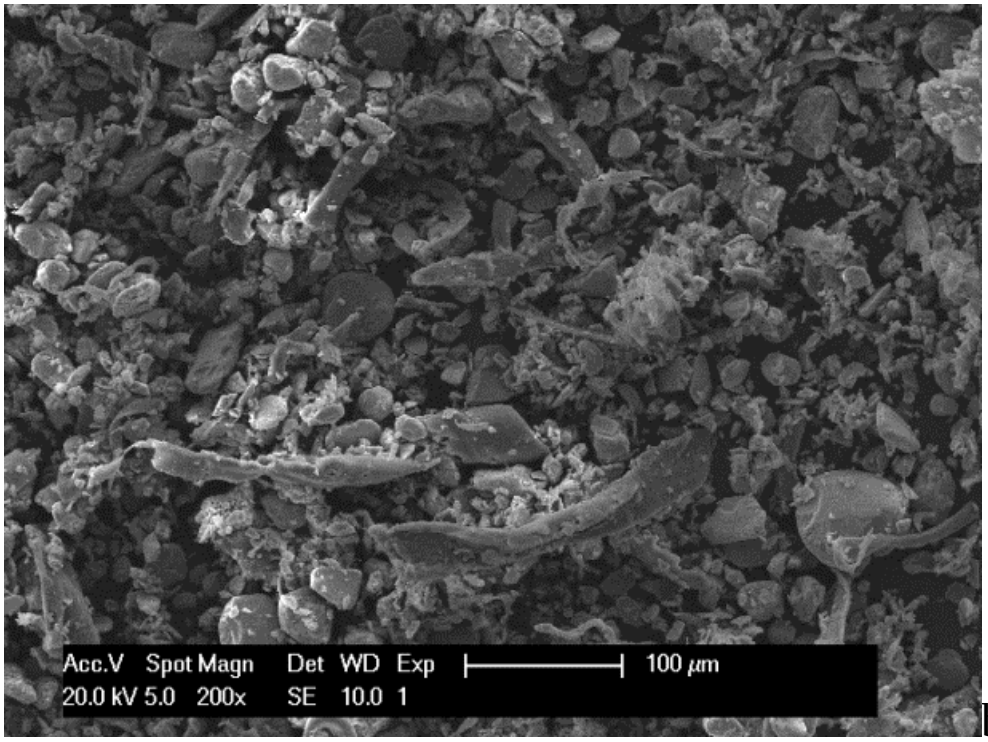

b

Fig.4.32b: SEM image of Zn_2AlNO_3-DS

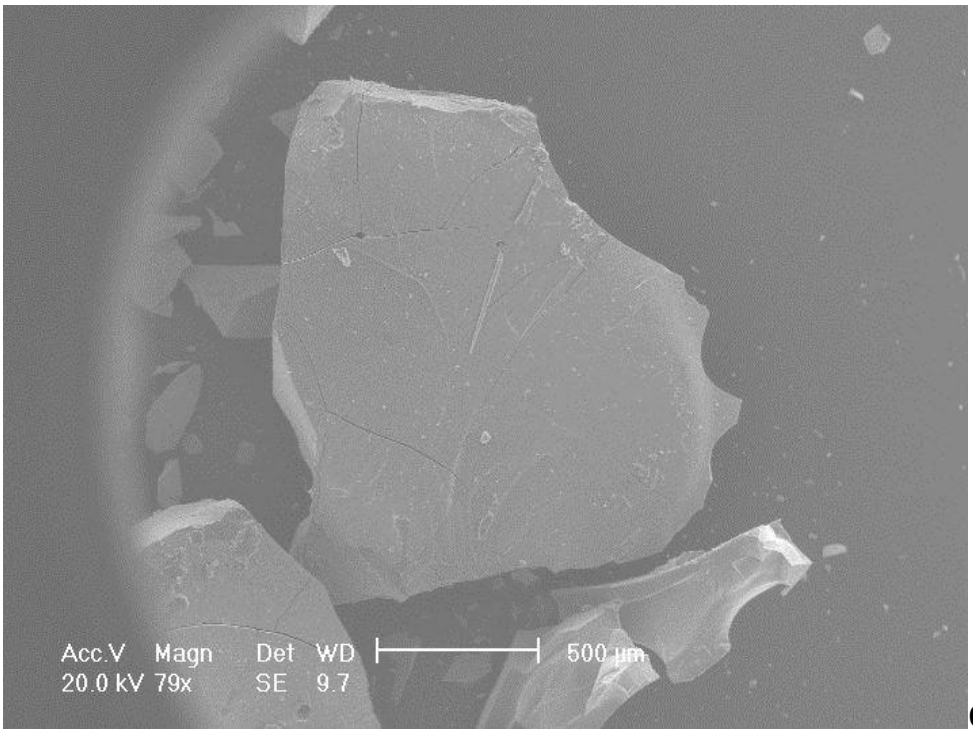

c

Fig.4.32c: SEM image of Zn_2AlCl-HTlc

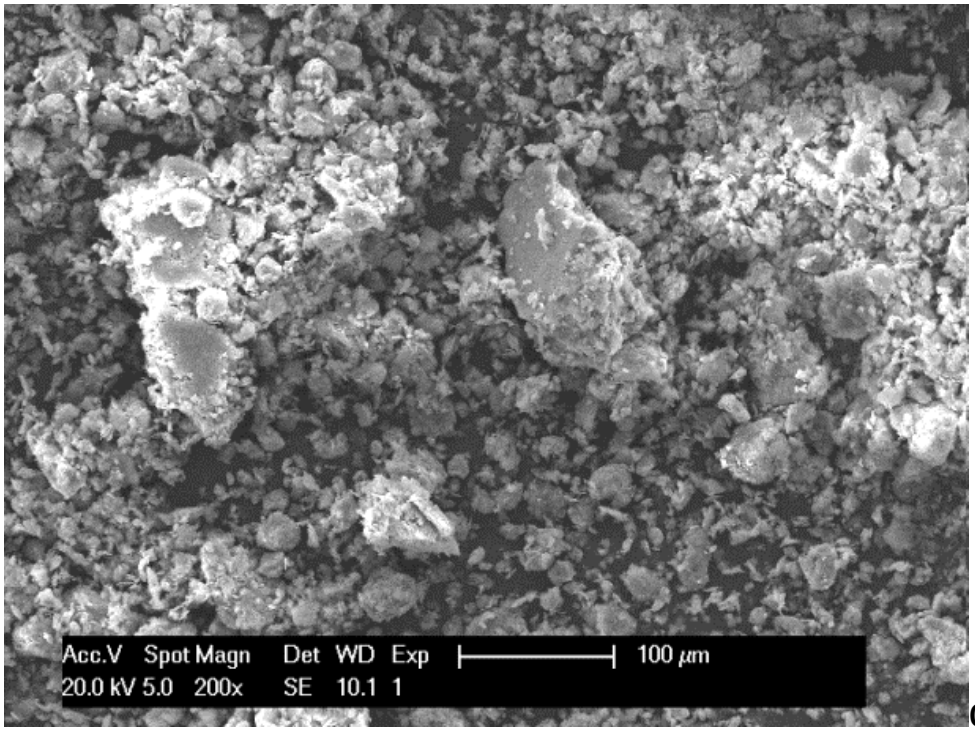

d

Fig.4.32d: SEM image of Zn_2AlCl-DS hybrid organo-hydrotalcites

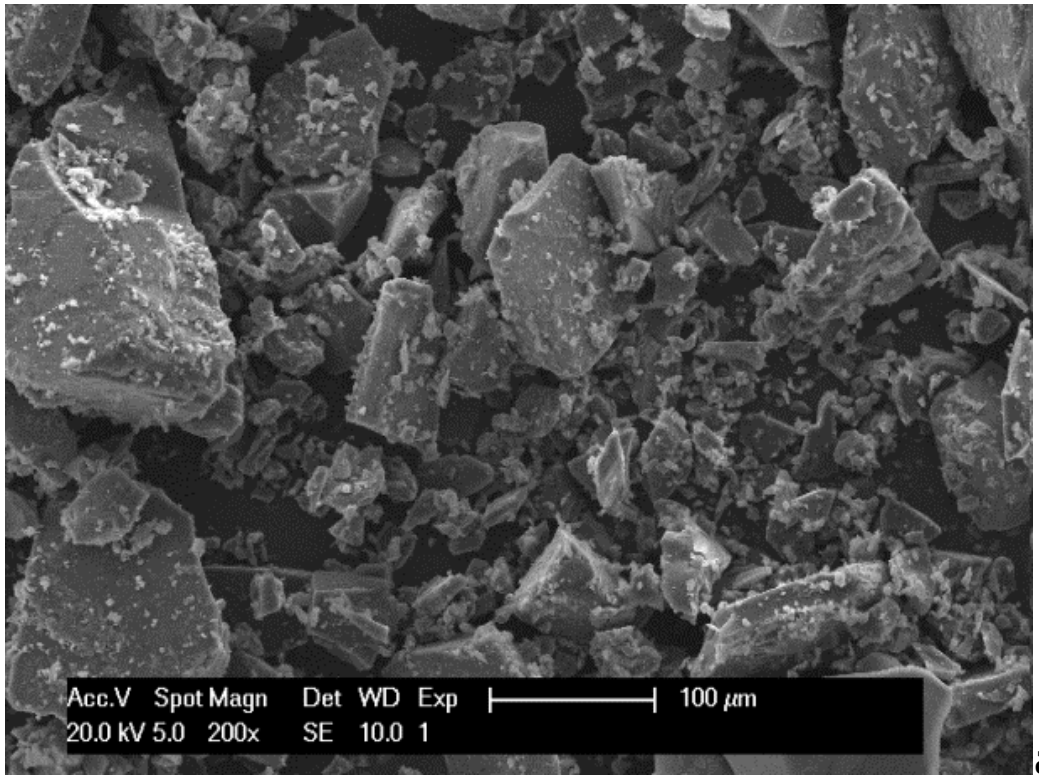

a

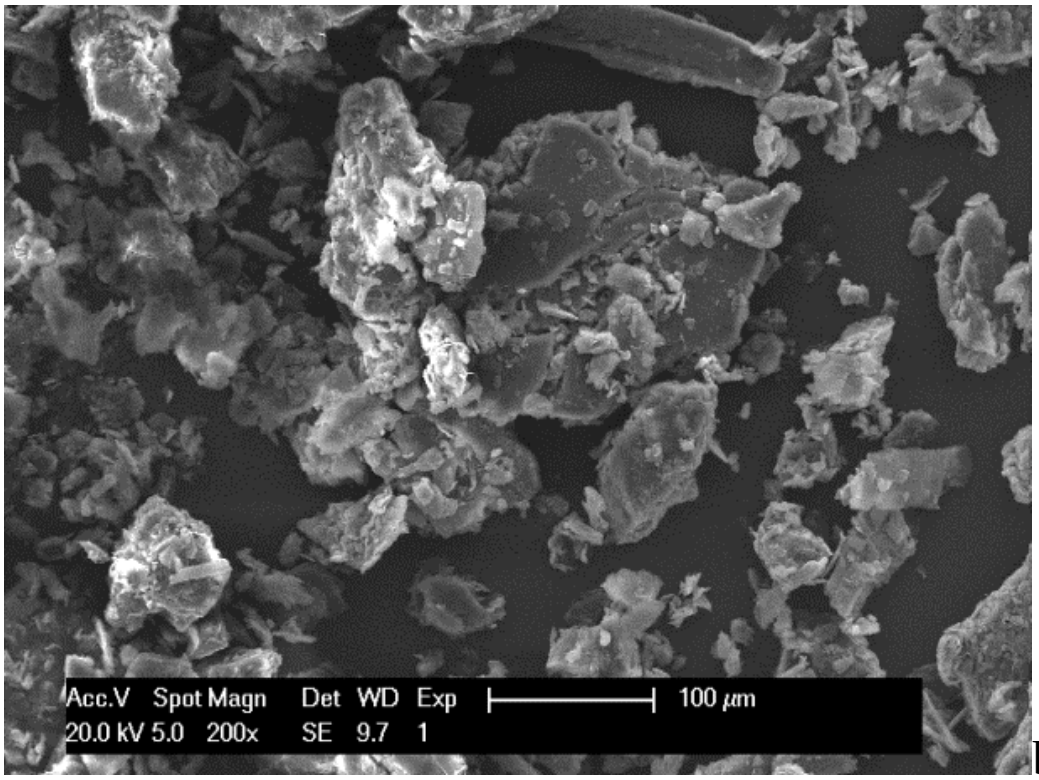

b

Fig.4.33: SEM image of (a) Mg_2AlCl-HTlc and (b) Mg_2AlCl-DS

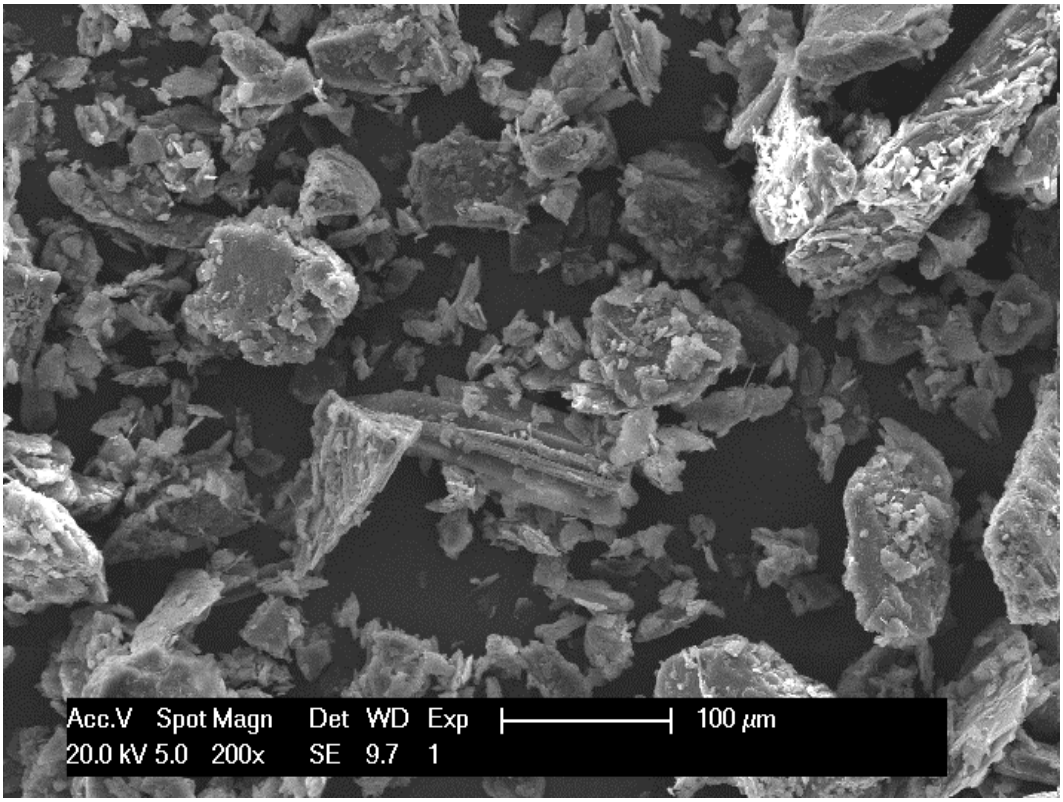

Fig 4.34: SEM image of Mg_2AlCl-DS

4.5 Conclusion

Dodecylsulfate and dodecylbenzenesulfonate anions were intercalated into the galleries of preformed MgAl and ZnAl hydrotalcites with interlayer anions CO_3^{2-}, NO_3^- and Cl^-. The derived hybrid organo-hydrotalcites properties were studied and analysed by XRD, TGA, XRF, FT_IR, SA and SEM. These demonstrate that intercalation of SDS and SDBS has been successfully achieved with the hydrotalcite structure maintained and the interlayer space expanded suggesting that intercalation of other organic compounds or other surfactants may be possible. The dodecylsulfate and dodecylbenzenesulfonate anions in the interlayer may be arranged in various ways depending on the d-spacing of the hybrid organo-hydrotalcites and probably the synthesis conditions. These derived hybrid organo-hydrotalcites have well-ordered layered structures, divalent/trivalent

mole ratios that are close to those of the host precursors, lower specific surface areas and hydrophobic properties due to the amphiphilic nature of the DS and DBS in the interlayer. They show thermal transitions that are comparable to the host hydrotalcites, for instance exhibiting three decomposition steps but with an increase in the temperature at which weight loss is completed.

CHAPTER FIVE

UPTAKE OF PHENOL AND CHLOROPHENOL BY ORGANO-HYDROTALCITES

5.1 Introduction

Man has always wanted to live luxuriously and comfortably hence his quest for development, which has resulted in the recent rapid industrialisation and increased commercial development, which in turn has brought about improved living conditions. Ironically this has created environmental issues for man to address. Large amounts of hazardous and toxic waste are being generated by industries globally and released into the environment. The majority of these toxic wastes are rich in organic compounds such as phenolic compounds. Phenolic compounds are generated by industrial sectors of steel, dye, timber, petroleum, plastic, pesticide and refineries to mention but a few. Phenolic compounds, for instance phenol and chlorophenols, are hazardous and toxic pollutants which are harmful to organisms even at low concentrations. They are non-biodegradable, recalcitrant and thus have potential to bioaccumulate in the environment. Therefore phenol and chlorophenol have been classed by US Environmental Protection Agency (EPA), European Environmental Agency (EEA) and World Health Organisation (WHO) as priority pollutants. The (USEPA) and (WHO) has set the allowable limit at 1.0mg/L[189, 190]. For humans, phenol and chlorophenols are of concern because of their toxicity, carcinogenic potency and ability to cause harmful effect at low concentration. They can commonly affect vital organs like the kidney,

liver, eyes, skin and central nervous system. Therefore the removal of these compounds is a current environmental issue that needs to be addressed. Consequently researchers have directed efforts towards developing effective treatment technologies and/or effective, cheap and environmentally friendly scavengers for these toxic pollutants. Dutta et al.,[191, 192] identified two major treatment categories for phenolic wastewater, which are destructive oxidation and recuperative processes. The latter of these involves adsorption into porous solids, membrane separation and solvent extraction. Adsorption is one of the most popular and most effective methods for removal of organic compounds from water, process effluents, wastewater and aqueous solution. In recent years, a lot of work has been driven towards obtaining new adsorbents, and hydrotalcite (HT) is a promising adsorbent for undesirable inorganic and organic compounds. The previous chapter dealt with modifying the synthesised hydrotalcite compounds in this study by intercalating organic compounds, SDS (sodium dodecylsulfate) and SDBS (sodium dodecylbenzenesulfonate), into their interlayer spaces to alter their nature from hydrophilic to hydrophobic and then study their properties by characterising with various techniques. This chapter focuses on the use of these modified hydrotalcites, herein known as organo-hydrotalcites, to uptake phenol and chlorophenol from aqueous solution.

5.2 Experimental

5.2.1 Materials

The various organo-hydrotalcites were those prepared in this study. The 2-chlorophenol (99% purity) was obtained from Sigma-Aldrich Chemical Corporation and used without further purification. The phenol (99% purity) was obtained from Alfa Aesar chemical

company and also used without further purification. Table 5.1 summarises some relevant physical properties of these compounds. Nitric acid (70%, Fisher scientific), hydrochloric acid (36%, Fisher scientific), and sodium hydroxide (analytical grade, obtained from Fishers Scientific UK) were also used as received.

5.2.2 Development of sorption procedure

Prior to staring sorption studies, it was necessary to develop and optimise the methods to be used to analyse the samples/solutions in order that reliable results could be obtained. Our initial plan was to use high performance liquid chromatography (HPLC) to analyse samples and a great deal of time was spent running standards to try to develop a reliable process. The solutions from trial adsorption experiments were measured along with the standards, and calibration curves were produced which were used to determine the concentration of PhOH and 2-CP in the unknown solutions.

Typically, approximately 47.06mg phenol was accurately weighed out into a 500mL volumetric flask and HPLC-grade water (previously sparged with helium) was added to the mark to make an approximately 1mmol/L solution. 125mL of the solution was diluted to 250mL to make another 0.5mmol/L phenol stock solution. Seven standards were prepared from this stock solution by serial dilution, each in a 50mL volumetric flask. Seven concentrations of 0.053, 0.106, 0.159, 0.266, 0.319, 0.372 and 0.425mmol/L were made based on a linear regression analysis performed to determine the sensitivity of the method and concentrations, which showed a sensitivity of up to 0.531mmol/L. Data were obtained on a Shimadzu LC2010. The phenol solutions prepared were stored in brown glass bottles to prevent photo-oxidation. All pH adjustments were carried out with either 0.1M HCl or HNO_3 along with 0.01M NaOH solutions. Standards were measured along with the unknown sample solutions and the

calibration curve used to determine the concentration of PhOH in the adsorption solutions.

Different solvent systems were trialled to run the HPLC analysis in order to find the most appropriate eluent: water/methanol and water/acetonitrile mixtures in different ratios were tested, using typically 100ml of solvent and a 60min injection time. Despite extended tests and refinement of parameters to optimise adsorption, reproducible results were not obtained. Furthermore, particulates in the solutions caused some blocking of the column, which interfered with the HPLC method.

Because reliable and reproducible results could not be obtained from HPLC, focus was shifted to using Uv/vis spectrometry as an alternative. Trials were also carried out to establish suitable concentration ranges for test and standard solutions along with optimum adsorption parameters. Initially again, results obtained were inconsistent, with some undesirable artefacts appearing in the UV spectra recorded of our reaction solutions. This was traced to a problem with the removal of particulates, via the filtration process, which has the effect of increasing the observed absorbance. Alternative procedures including centrifugation, and different filters and membranes were tested until a suitable membrane (0.2μm, PTFE) was found to give consistent results.

The method described in the following section outlines the refined procedure that was used for the remainder of the project to study the uptake of phenol and 2-CP for all HTlc samples, which enables direct comparison of the results.

5.2.3 Sorption of phenol by Mg_2AlCO_3-SDS and Mg_3AlCO_3-SDS

The uptake capacity of our organo-hydrotalcites was studied by using some of them, typically, Mg_2AlCO_3-SDS and Mg_3AlCO_3-SDS to remove phenol from aqueous solution at different pH and at room temperature. The effect of time variation was examined. Two separate experiments were performed and the values shown are the average of both experiments. In a typical batch adsorption study, 0.1g of the hydrotalcites was stirred with 200mL of 0.159mmol/L phenol solution in a reaction vessel at room temperature. The pHs of the phenol solution had been adjusted appropriately between 7 -11. The mixture was stirred gently at about 150rpm for 6hrs. At end of the different time, 5, 15, 30, 45, 60, 90, 120, 180 and 360mins, 10ml of the suspension were siphoned out with a syringe and filtered through a 0.2µm syringe filter membrane. The concentration of the phenol in the filtrates was measured using a Uv-vis spectrophotometer (M550 double beam Uv-vis scanner for absorbance measurements). The adsorbed quantities were then determined from the difference between the initial and final concentrations following the equation: $q_t = (Co - Ct)\ V/m$

Where Co = the initial phenol concentration (mmol/L) and m is the mass (g) of organo-hydrotalcites used. C_t is the concentration (mmol/L) of phenol at time *t*, while Volume is equivalent to the volume (L) of aqueous phenol solution and q_e is the adsorption capacity in (mmol/g). This procedure was repeated using independent sample to obtain average values that were used for calculation of adsorbed quantities. This was due to constrain of time and cost.

5.2.4 Kinetics of the 2-CP sorption by the various organo-hydrotalcites

The kinetic experiments for uptake of 2-CP by organo-hydrotalcites composed of varying layer composition and derivatives of two different surfactant modifications were carried out with adsorbent dose of 0.5g/L at varying pH of 6-11. The concentration of 2-CP was set at 0.078mmol/L. 2-chlorophenol solution of concentration 0.078mmol/L was prepared from 1mM stock solution which was made by drawing 1.04ml from 2-chlorophenol reagent bottle into 100ml volumetric flask. Decarbonated deionised (DD) water was added, swirled and made up to mark. Then 1ml of it was taken into another 100ml flask and made up to mark with DD water to make 1mM 2-chlorophenol solution. The pH was measured (pH = 6.5) at room temperature. 7 standard solutions were made from this stock solution.

The adsorption isotherm was carried out using batch equilibrium techniques. For each isotherm, 200ml of 2-CP solution of 0.078mmol/L were measured into a round bottom flask. Then 0.1g of the organo-hydrotalcites were weighed and dispersed in the solution. The mixtures were stirred at about 120rpm on a magnetic stirrer at room temperature. The pHs of the 2-CP solutions were varied between 7-11 and the adsorption reactions were carried out at different time intervals. The suspensions were held stirring at the different time, 5mins to 24hrs. At the end of each time 5, 15, 30, 45, 60, 90, 120, 180, 360, 540, 720 and 1440mins, 10ml of the suspension were siphoned out with a syringe and filtered through a 0.2µm syringe filter membrane (PTFE). The concentration of the 2-CP in the filtrates were measured using a Uv-vis spectrophotometer (M550 double beam Uv-vis scanner for absorbance measurements). The adsorbed quantities were then determined from the difference between the initial and final concentrations. Each adsorption isotherm was determined in duplicate using two independent samples. The

adsorption abilities/kinetics of the different organo-hydrotalcites (18 samples) was compared. The 2-CP adsorption capacity (mmol/g) was obtained from the equation:

$$q_e = (Co - C_t)\, V/m \qquad (1)$$

Where Co = the initial 2-chlorophenol concentration (mmol/L) and m is the mass (g) of organo-hydrotalcites. C_t is the concentration (mmol/L) of 2-CP at time *t*, while Volume is equivalent to the volume (L) of aqueous 2-CP solution and q_e is the adsorption capacity in (mmol/g). This procedure was also repeated using independent sample to obtain average values that were used to calculate adsorbed quantities. Constrain of time and cost limited the number of times the experiments were repeated. The calibration curve showed a linear variation.

Table 5.1 Physicochemical properties of phenol and 2-chlorophenol

Compound	**Abbreviation**	**λmax(nm)**	**Water Solubility(g/L)**	**Density/cm^3**	**m.pt (^{o}C)**	**b.pt(^{o}C)**	**pKa**
Phenol	PhOH	271	8.3 (20^{o}C)	1.07	40.5	181.7	9.95
2-chlorophenol	2-CP	273, 292	20 (20^{o}C)	1.263	9.4	174.9	8.56

5.3 Results and discussion

5.3.1 Effect of contact time and pH on 2-chlorophenol (2-CP) uptake

The adsorption of 2-CP by the derived organo-hydrotalcites was studied at various pH and time. The time variation of 2-CP uptake by dodecylsulfate and dodecylbenzenesulfonate intercalated Mg_2Al hydrotalcites is shown in Figs.5.1-5.2. The effect of contact time on the uptake of 2-CP on Mg_2AlCO_3-DS and Mg_2AlCO_3-DBS at various pH of the solution was examined. Both plots showed that adsorption of 2-CP is pH dependent; it increases with longer agitation time and reaches equilibrium after 6hrs for each of the three pHs and samples studied. At the beginning of the reaction, the adsorption occurred rapidly, before slowing at later time (3 hrs) during the reaction. The rapid adsorption on initial contact may be due to the availability of physiosorbed DS and DBS molecules on the surfaces of Mg_2AlCO_3-DS and Mg_2AlCO_3-DBS adsorbents, while the later slower rate of 2-CP uptake may be due to slow adsolubilisation of 2-CP into the interior structure of Mg_2AlCO_3-DS and Mg_2AlCO_3-DBS adsorbents. During the intercalation of the surfactants, SDS and SDBS into the galleries of the host Mg_2AlCO_3, the alkyl groups of these surfactants form a hydrophobic region in the galleries as they self-assemble into bilayers between the layers of these hydrotalcites, while some additionally aggregated on the outside surfaces of the clay particles, thereby changing their nature from hydrophilic to hydrophobic. The adsorption of 2-CP by Mg_2AlCO_3-DS and Mg_2AlCO_3-DBS involves adsolubilisation of the 2-CP into this organic phase. Fig.5.3 illustrates the intercalation of the organic ions leading to the formation of organic phase in the gallery which perform as adsolubilisation substance. The

Mg_2AlCO_3-DS and Mg_2AlCO_3-DBS organo-hydrotalcites adsorb the 2-CP with the negatively charged head group orienting towards the hydroxide layers. Assessing the adsorption capacities of both organo-hydrotalcites, the adsorption ability is Mg_2AlCO_3-DBS > Mg_2AlCO_3-DS due to effect of benzene ring resulting from the added effect of the π-π interaction of the 2-CP and the dodecylbenzenesulfonate anions which adds stability. Both samples show increased adsorption capacity from pH6 to pH10.

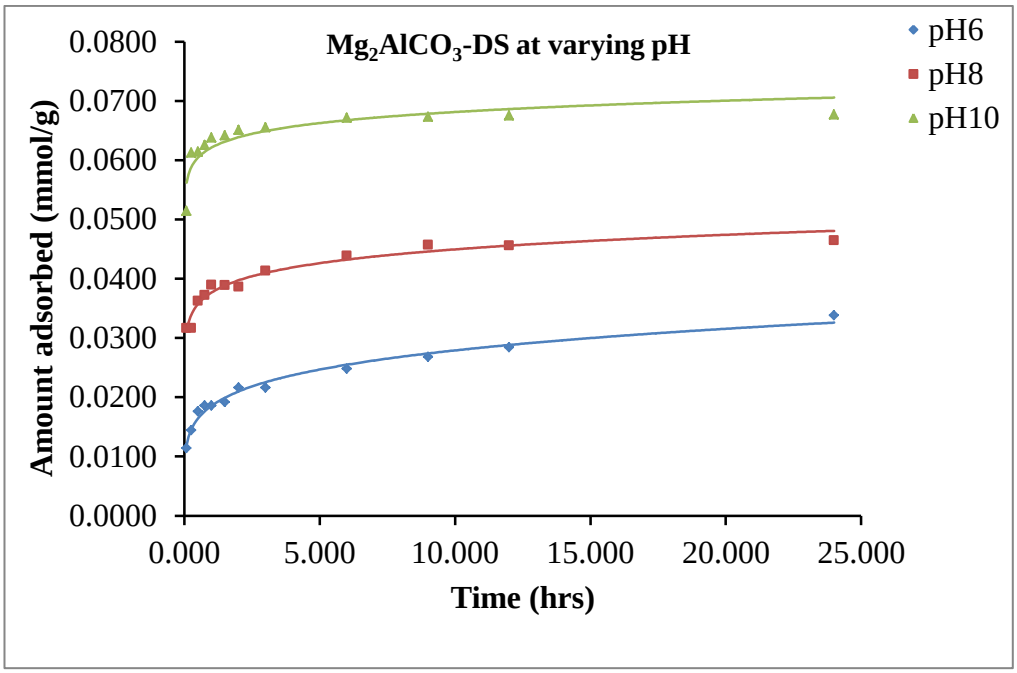

Fig.5.1: Uptake of 2-CP by Mg_2AlCO_3 HTlc modified with sodium dodecylsulfate (SDS) at varying pH. (Uncertainty is within the rang 7.07×10^{-5} – 2.83×10^{-4}, so error bars are within the limit of the dimension symbols)

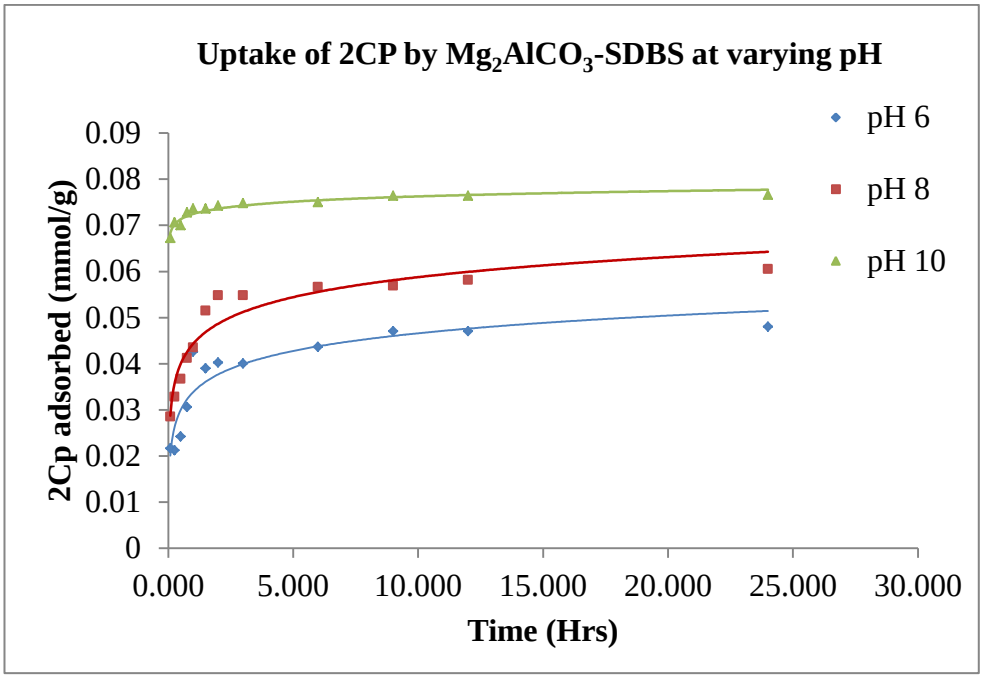

Fig.5.2: Uptake of 2-CP (mmol/g) by Mg_2AlCO_3-DBS (Mg_2AlCO_3 HTlc modified with sodium dodecylbenzenesulfonate) at varying pH. (Error bars are within the limit of the dimension symbols)

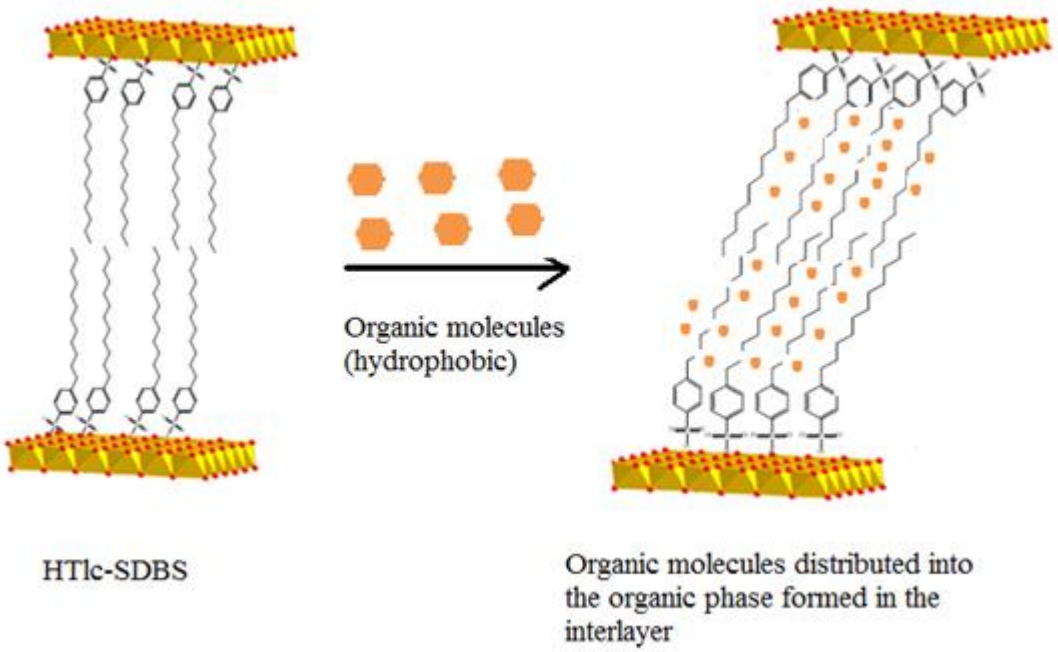

Fig.5.3: Schematic diagram illustrating the suggested sorption characteristics and mechanism for 2-CP uptake by HTlcs.

The plots also show the effect of pH on adsorption capacity and it increases from pH6 to pH10 for Mg_2AlCO_3-DS. In order to explain this it is important to consider the dissociation of 2-CP for which the pK_a is 8.56; hence at pH 10, some of the 2-CP has been deprotonated and is present as phenolate ions, which can interact through electrostatic forces of attraction with the positively charged layers of Mg_2AlCO_3-DS. While this would give the potential for increased sorption, in the case of hosts containing DBS, the loss of aromaticity in the phenolate ions (due to resonance effects) could result in weaker π–π interactions which would have a negative influence on the sorption capacity. However, the overall effect of these different factors still results in an increased capacity at high pH.

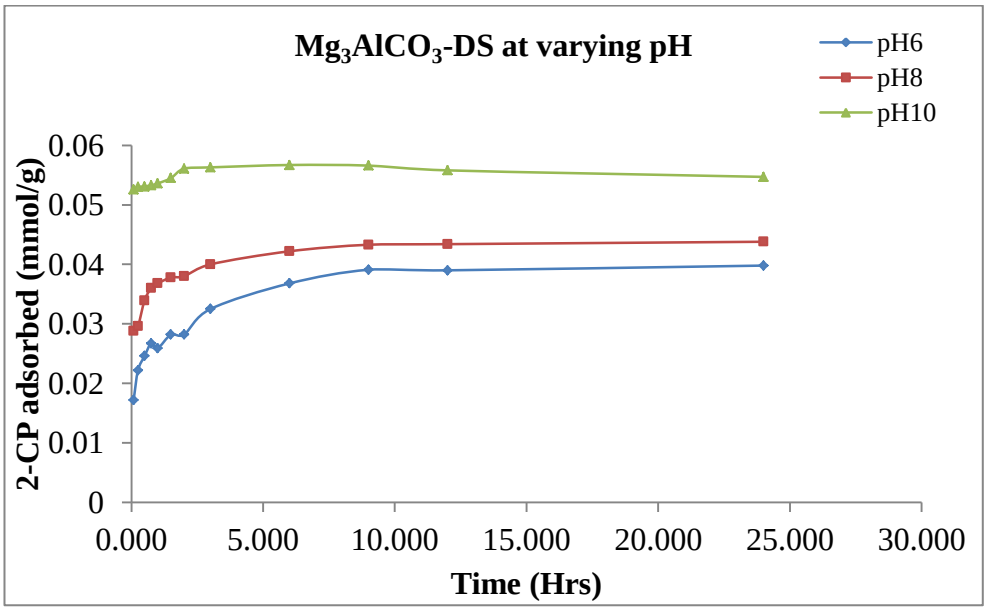

Fig.5.4: Uptake of 2CP by Mg_3AlCO_3 HTlc modified with sodium dodecylsulfate (SDS) at varying pH, (Error bars are within the limit of the dimension symbols)

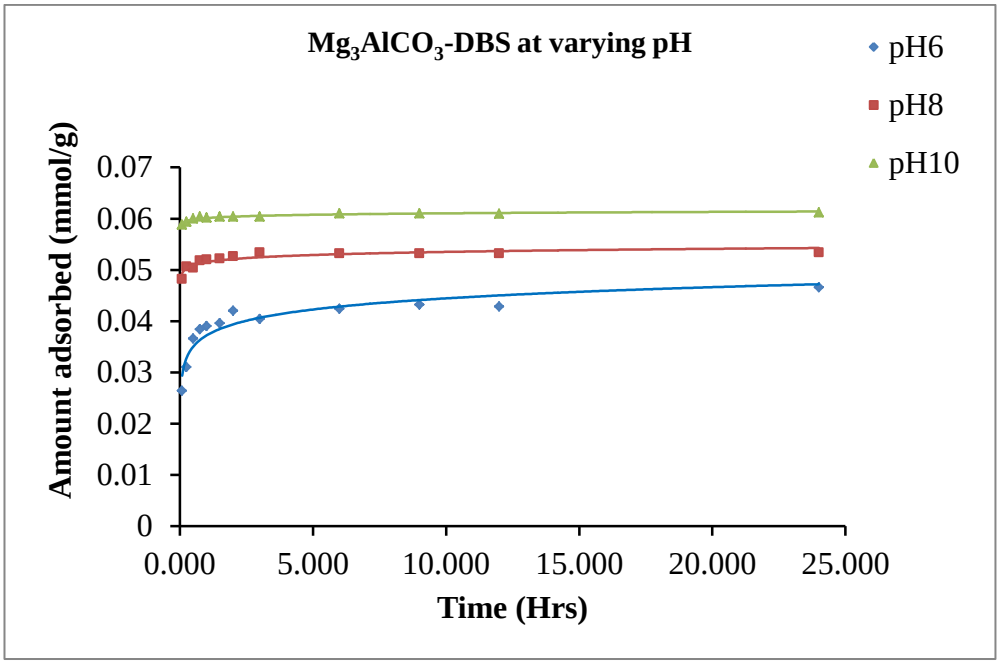

Fig.5.5: Uptake of 2CP (mmol/g) by Mg_3AlCO_3-DBS (Mg_3AlCO_3 HTlc modified with sodium dodecylbenzenesulfonate) at varying pH.(Error bars are within the limit of the dimension symbols

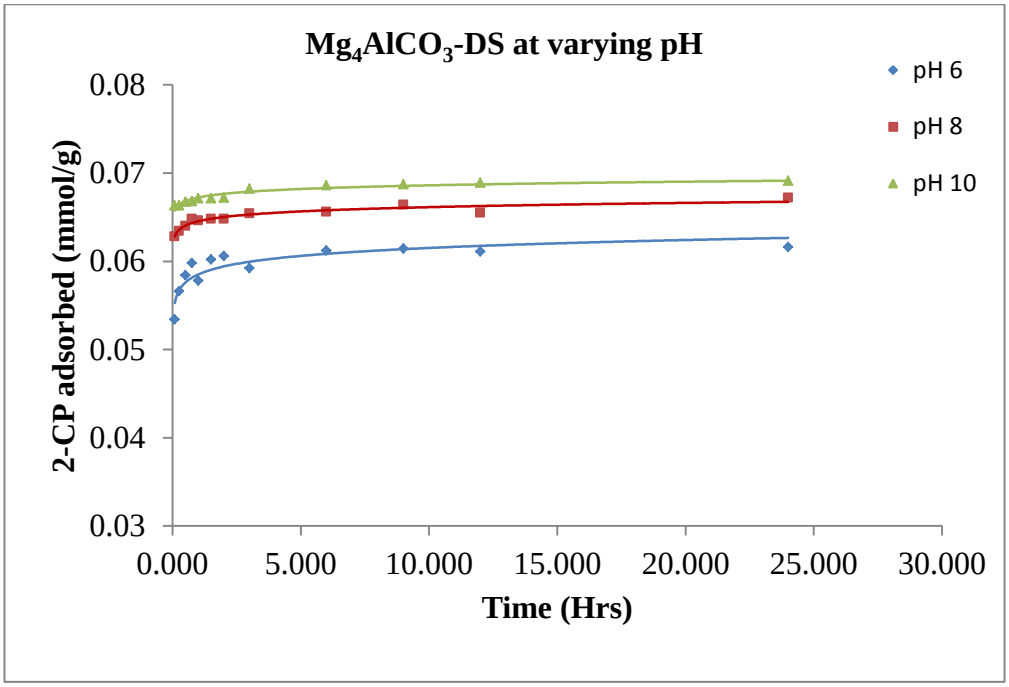

Fig.5.6: Uptake of 2CP by Mg_4AlCO_3 HTlc modified with sodium dodecylsulfate (SDS) at varying pH.(Error bars are within the limit of the dimension symbols)

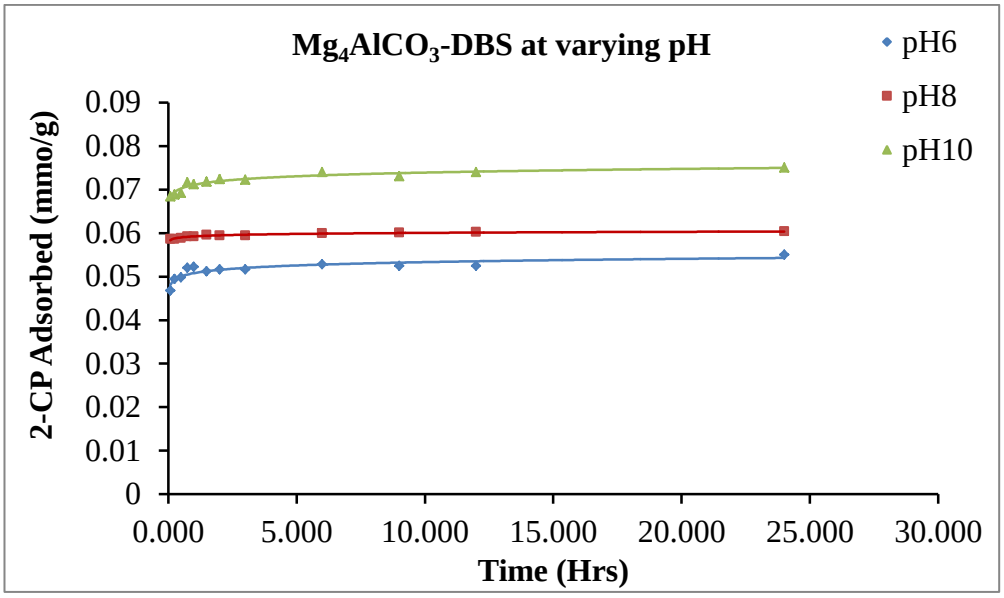

Fig.5.7: Uptake of 2CP by Mg_4AlCO_3 HTlc modified with sodium dodecylbenzenesulfonate (SDBS) at varying pH.(Error bars are within the limit of the dimension symbols

Figs.5.4 - 5.7 show that, the uptake of 2-CP increases with increasing Mg^{2+}/Al^{3+} ratios, with a slight exception seen in the 3:1 of both samples containing DS and DBS. The increasing uptake capacity down the series may be attributed to the combined effect of increased charge density as Mg^{2+}/Al^{3+} ratios increases and thus influencing the amount and packing of anions within the interior of the galleries, and degree of hydrophobicity.

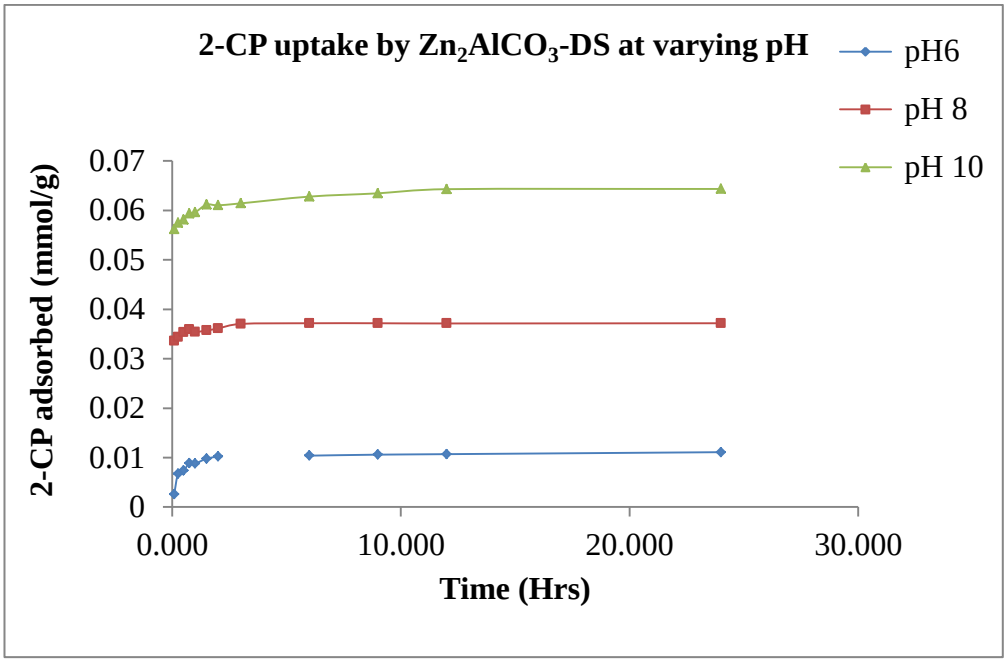

Fig 5.8: Uptake of 2CP by Zn_2AlCO_3 HTlc modified with sodium dodecylsulfate (SDS) at varying pH.(Error bars are within the limit of the dimension symbols)

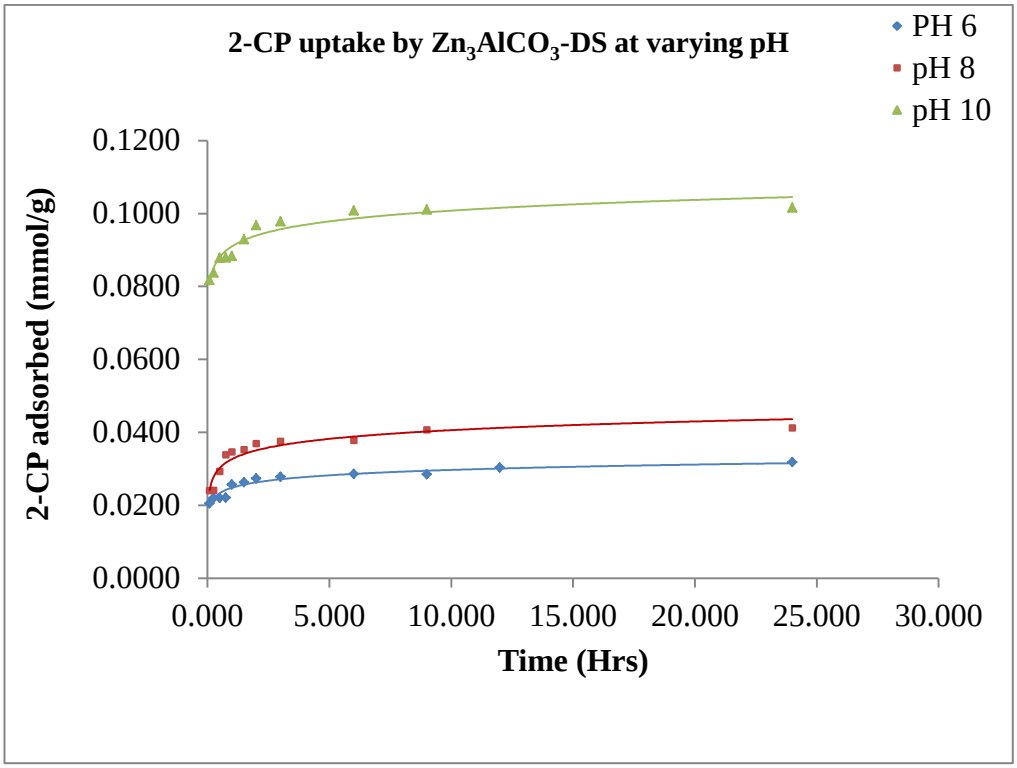

Fig.5.9: Uptake of 2CP by Zn_3AlCO_3 HTlc modified with sodium dodecylsulfate (SDS) at varying pH(Error bars are within the limit of the dimension symbols).

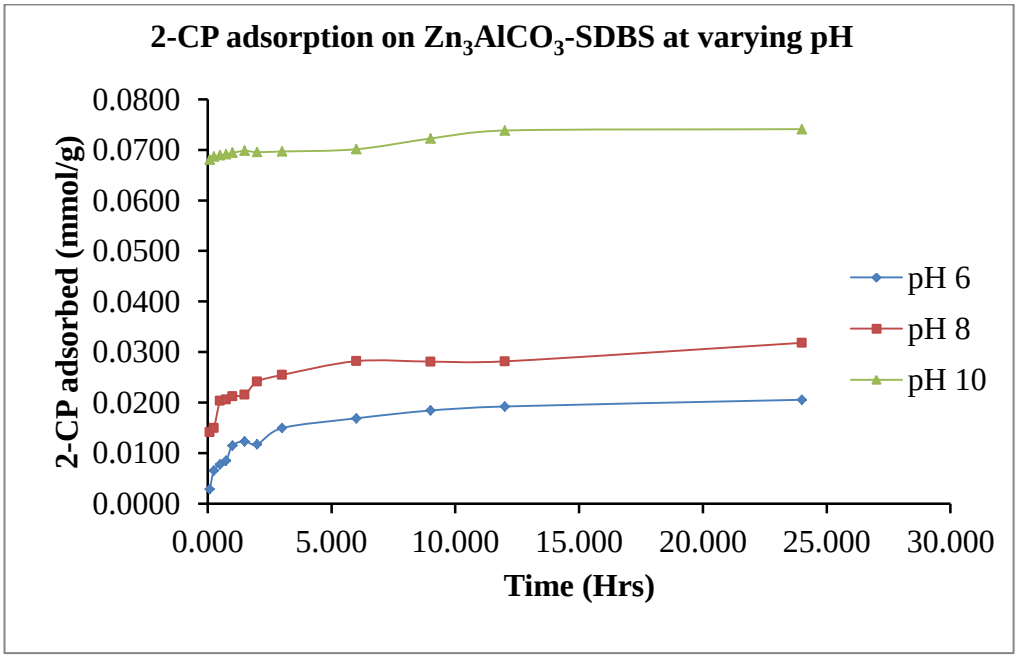

Fig.5.10: Uptake of 2CP by Zn_3AlCO_3 HTlc modified with sodium dodecylbenzenesulonfate (SDBS) at varying pH. (Error bars are within the limit of the dimension symbols.)

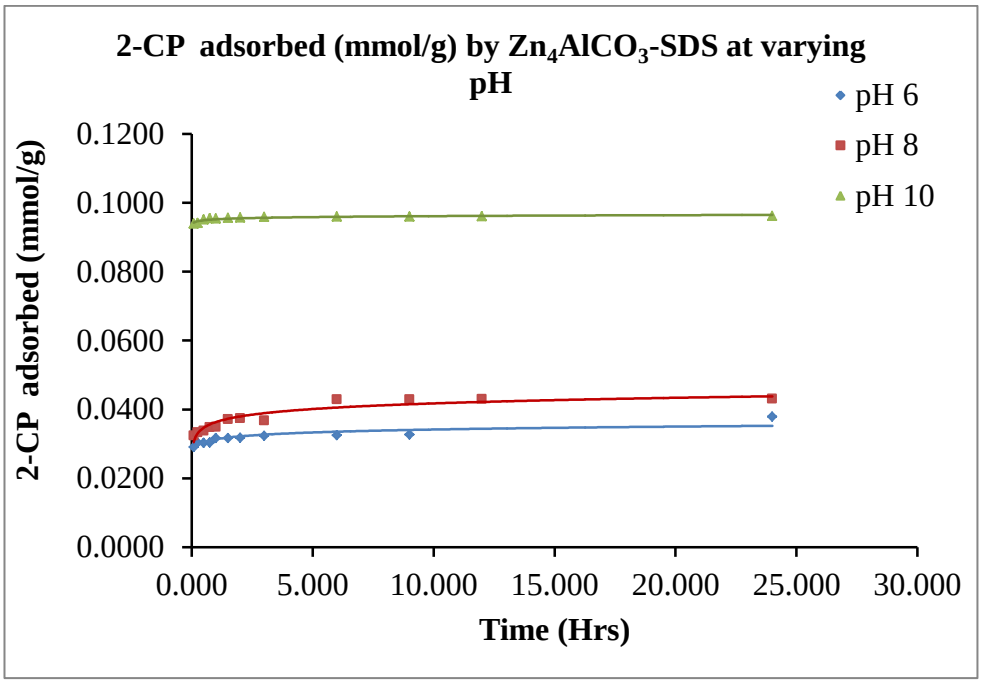

Fig.5.11: Uptake of 2CP by Zn_4AlCO_3 HTlc modified with sodium dodecylsulfate (SDBS) at varying pH. (Error bars are within the limit of the dimension symbols).

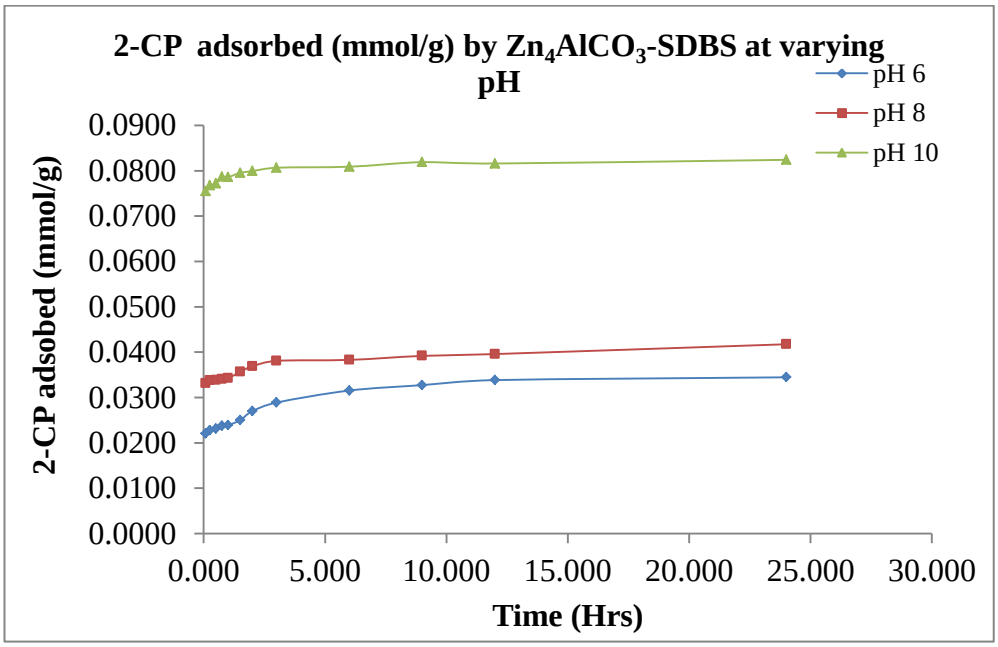

Fig.5.12: Uptake of 2CP by Zn_4AlCO_3 HTlc modified with sodium dodecylbenzenesulonfate (SDBS) at varying pH. (Error bars are within the limit of the dimension symbols).

The hydrotalcites with ZnAl in their layer are displayed in Fig.5.8-5.12 and they also show that sorption equilibrium was reached after 6 hrs, and the removal of 2-CP depended on pH of the solution. At high pH, the increased solubilty or ionisation of 2-CP leads to the increased availability of the phenolate ions which by electrostatic interaction are sorbed on the positively charged layers of the organo-hydrotalcites. The added advantage of the hydrophobic nature conferred on the clay based materials by the incorporation of SDS and SDBS also contributed to the adsorption capacities of these materials at high pH.

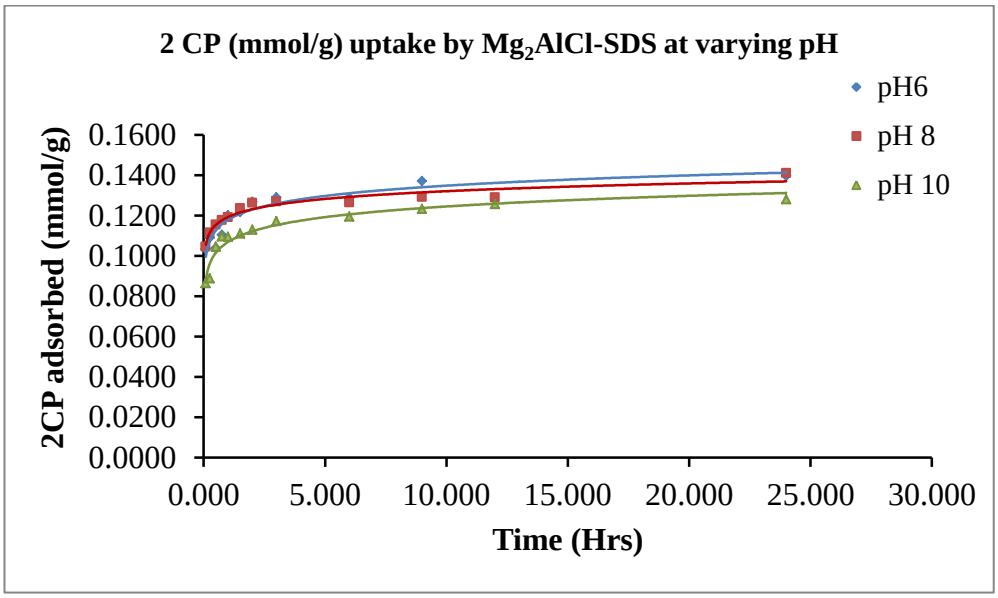

Fig.5.13: Uptake of 2CP by Mg_2AlCl HTlc modified with sodium dodecylsulfate (SDS) at varying pH. (Error bars are within the limit of the dimension symbols).

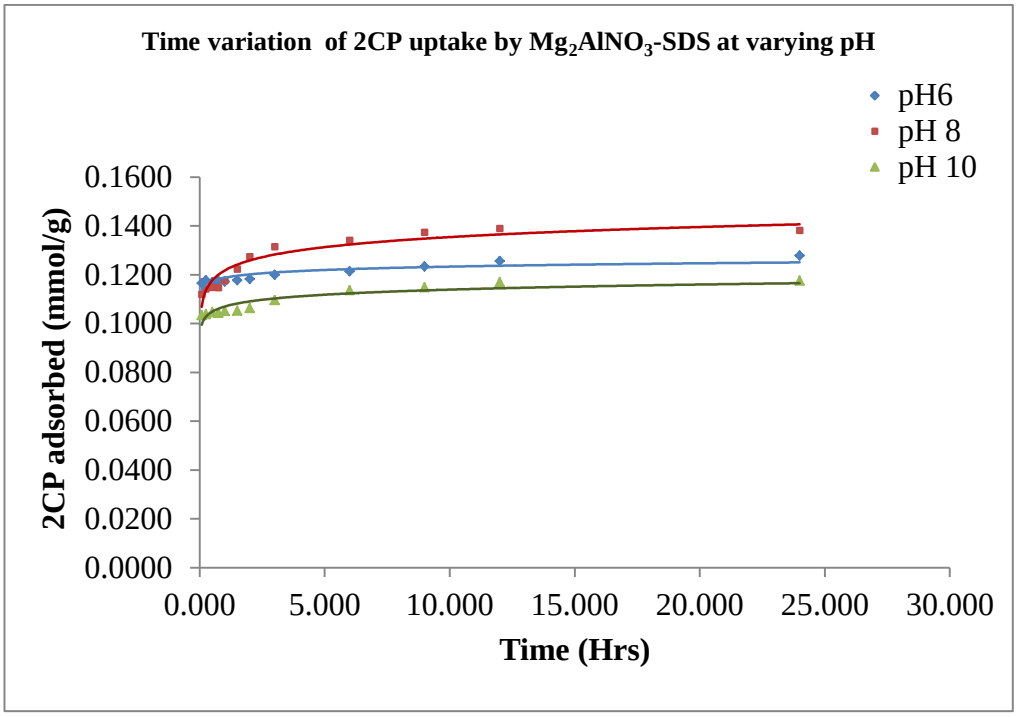

Fig.5.14: Uptake of 2CP by Mg_2AlNO_3 HTlc modified with sodium dodecylsulfate (SDS) at varying pH. (Error bars are within the limit of the dimension symbols).

Comparing the uptake of 2-CP by Mg_2AlCl-SDS and Mg_2AlNO_3-SDS, it is shown that while Mg_2AlCl-SDS adsorbed slightly more 2-CP than Mg_2AlNO_3-SDS, they were both very similar and nearly twice the capacity (in mmol/g) was achieve compared to the carbonate materials.

5.3.2 Effect of contact time and pH on Phenol uptake

Fig.5.15-5.17 shows the uptake of phenol by Mg_2AlCO_3-SDS, Mg_3AlCO_3-SDS and Mg_4AlCO_3-SDS. The results obtained for the removal of phenol with time at different pH of the solution show that adsorption capacity of these materials increased with increasing pH and the sorption reached equilibrium around 90mins. This increasing adsorption with pH may be attributed to the reliance of phenol ionisation or dissociation on pH value. Phenol adsorbed to a greater extent at high pH because it dissociates into the ion at pH ≥ 10 for which its pKa is 9.95. Therefore at pH 11, some of the phenol has been deprotonated and are present as the phenolate ions which by electrostatic forces interacted with the positively charged layers of the organo-hydrotalcites. In addition, the hydrophobic nature impacted upon the organo-hydrotalcites by the intercalation of SDS would have added some effect.

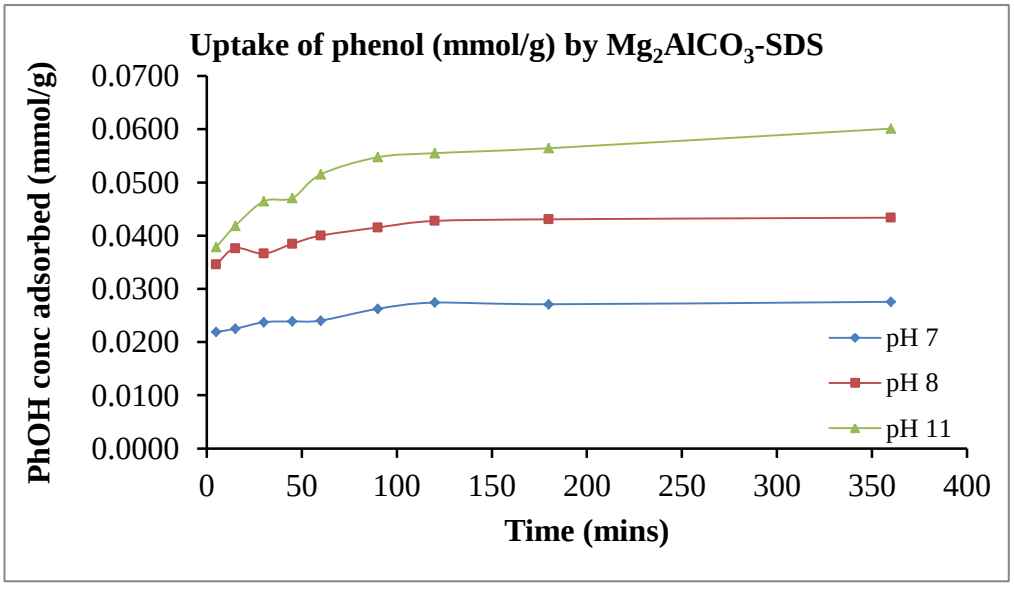

Fig.5.15: Uptake of phenol by Mg_2AlCO_3 HTlc modified with sodium dodecylsulfate (SDS) at varying pH.(Error bars are within the limit of the dimension symbols)

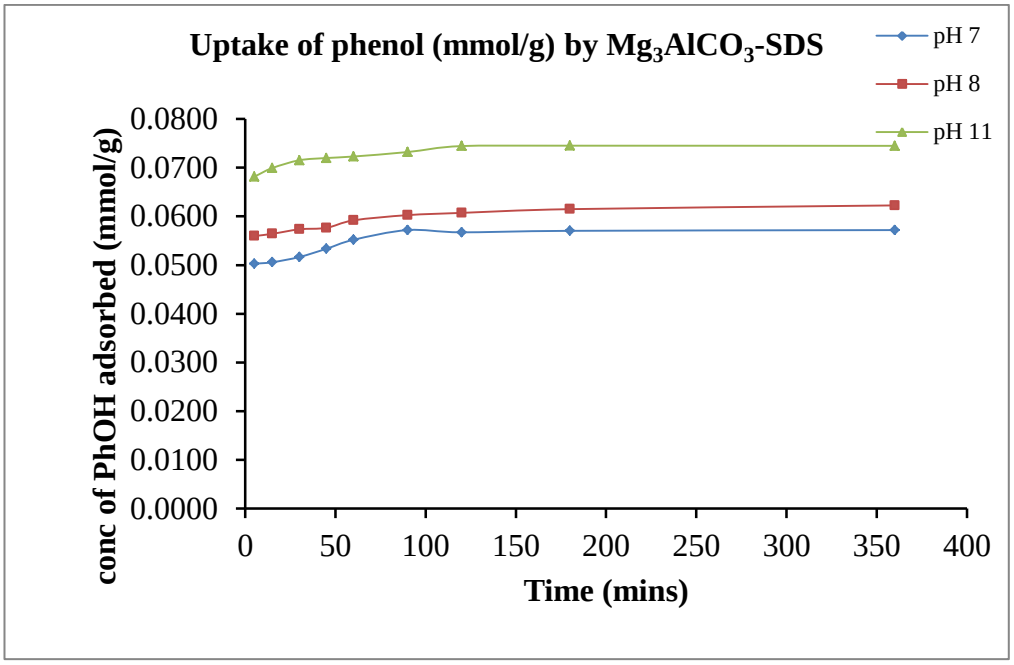

Fig.5.16: Uptake of phenol by Mg_3AlCO_3 HTlc modified with sodium dodecylsulfate (SDS) at varying pH. (Error bars are within the limit of the dimension symbols).

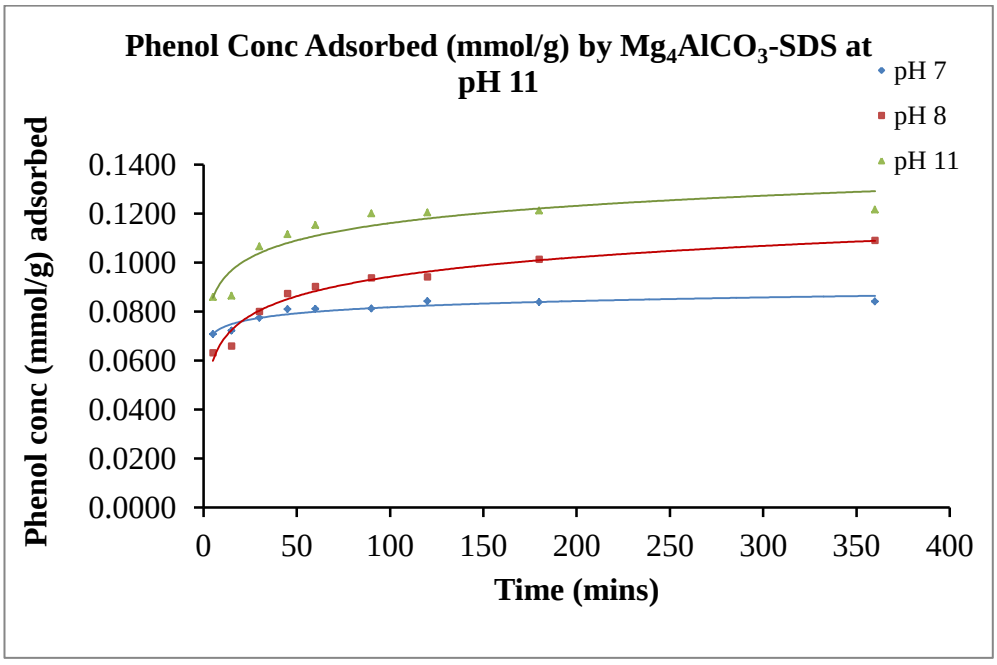

Fig.5.17: Uptake of phenol by Mg_4AlCO_3 HTlc modified with sodium dodecylsulfate (SDS) at varying pH.(Error bars are within the limit of the dimension symbols.)

5.3.3 Adsorption kinetic modelling

Two different types of kinetic models, most popularly used in the literature to predict the mechanism involved in sorption process, were used to test the experimental data. They are the Lagergren first order and pseudo second order equations. The Lagargren is presented in the form:

$$\frac{dq}{dt} = K_i(q_e - q_t) \quad (1)$$

Where q_t and q_e (mmol/g) are the amounts of sorbed or uptaken phenol or 2-CP molecules at time t and at equilibrium. $K_1(min^{-1})$ is the first order rate constant. Integrating equation (1) by applying the conditions $q_t = 0$ at $t = 0$ and $q_t = q_t$ at $t = t$. it becomes:

$$ln\ (q_e - q_t) = ln q_e - K_1 t \quad (2)$$

Where q_t (mmol/g) is the amount of absorption at time t (mins) and K_1 is the rate constant of the equation in (min^{-1}) and q_e is the amount of adsorption at equilibrium (mmol/g). The rate constant K_1 of the adsorption can be obtained by plotting ln $(q_e - q_t)$ against time t. These parameters were calculated for some of the organo-hydrotalcites in this study. Typical plots are shown in Fig.5.18 and the calculated parameters displayed in a table 5.2.

The second order model is described by the following equation:

$$\frac{dq}{dt} = k_2(q_e - q_t)^2 \quad (3)$$

Integrating by applying the condition $q_t = 0$ at $t = 0$ and $q_t = q_t$ at $t = t$, equation (3) becomes $t/q_t = \frac{1}{k_2 q_e^2} + \frac{t}{q_e}$ (4)

Where K_2 (g $mmol^{-1}$ min^{-1}) is the rate constant of the second order reaction rate equation, q_t (mmol g^{-1}) is the amount of adsorption at time t (min) and q_e is the amount of adsorption at equilibrium (mmol/g). Like the first order model, plotting t/q_t vs t gives a straight line graph with slopes of $1/q_e$ and intercept of $1/k_2q_e^2$. The rate constant k_2 and equilibrium sorption capacity q_e can be obtained from these parameters.

The values obtained from the pseudo first order kinetic model show that, the experimental values fitted poorly with the calculated results. It reveals a large difference between the experimental and calculated values of the equilibrium sorption capacities. Therefore we inferred that the first order kinetic model was not suitable to describe this sorption process. The pseudo second order kinetic model was applied and better correlation with experimental data was observed and this suggests a chemisorption mechanism which supports the argument that the alkyl chain of SDS and SDBS aggregated and form an organic phase that furnished the distribution medium for 2-CP in the interlayer. Typical plots for Mg_3AlCO_3-SDS and Mg_3AlCO_3-SDBS are displayed in Fig.5.18 for the first and second order reactions and the values of the rate constant, k and k_2, the equilibrium sorption capacity, q_e and the associated linear regression calculated coefficient R^2 for the different organo-hydrotalcites are reported in Table 5.2.

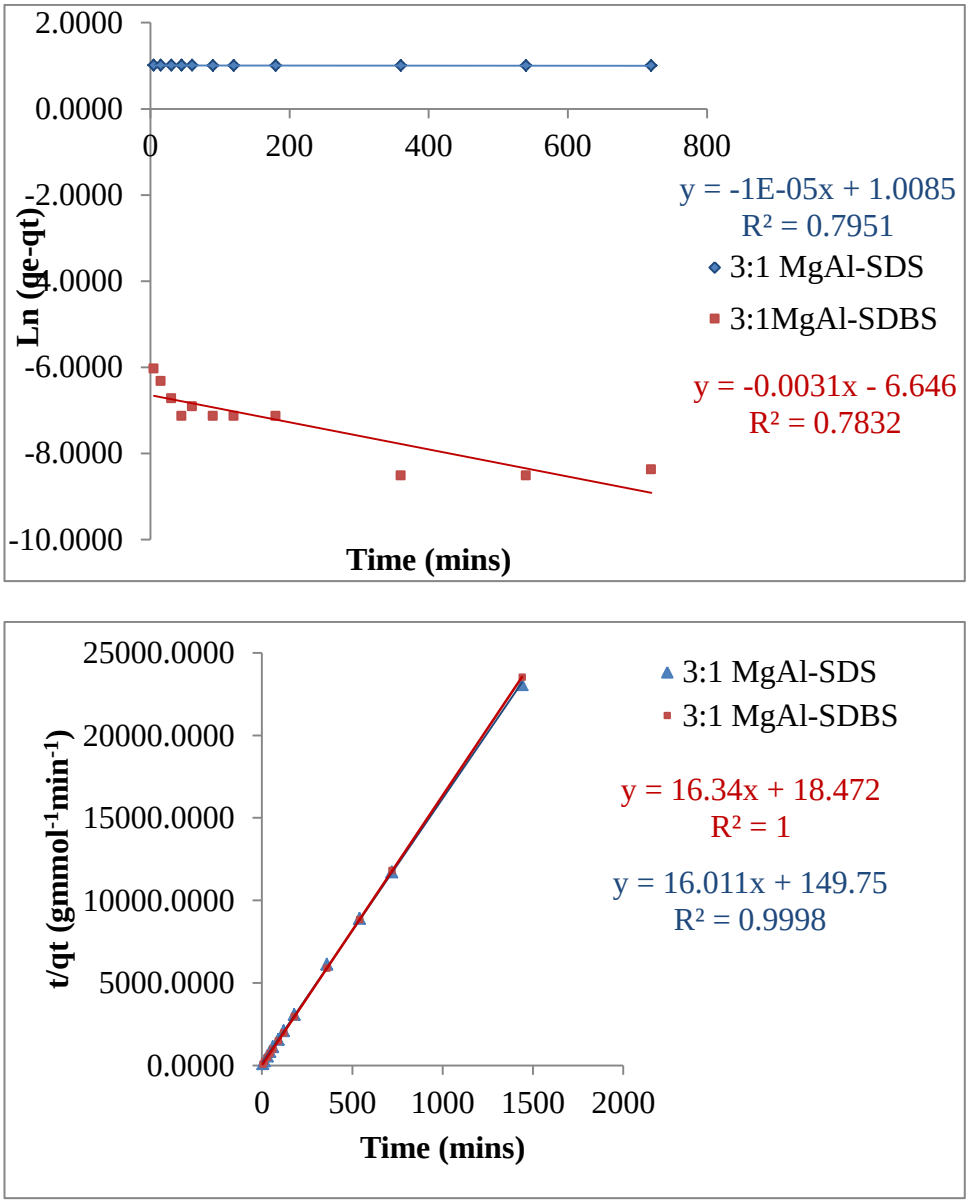

Fig.5.18: Pseudo-first order (upper) and second order (lower) reactions for 2-CP ions adsorbed onto Mg_3AlCO_3-SDS and Mg_3AlCO_3-SDBS.

Table 5.2 Kinetic models parameters obtained on the adsorption of 2-CP on SDS and SDBS HTlcs

Sample	**Lagargren first order**			**q_e exp (mmol/g)**	**Pseudo second order**		
	q_{ecal} (mmol/g)	$K_1(min^{-1})$	R^2		q_{ecal} (mmol/g)	K_2 $gmmol^{-1}min^{-1}$	R^2
Mg_2AlCO_3-SDS	0.0056	0.0038	0.9284	0.0677	0.0678	3.941	1.0000
Mg_2AlCO_3-SDBS	0.0057	0.0051	0.9114	0.0766	0.0767	14.138	1.0000
Mg_3AlCO_3-SDS	2.7415	$1x10^{-5}$	0.7951	0.0624	0.0625	$2.61x10^{-5}$	0.9998
Mg_3AlCO_3-SDBS	0.0013	0.0031	0.7832	0.0612	0.0621	14.04	1.0000
Mg_4AlCO_3-SDS	0.0026	0.0037	0.9599	0.0691	0.0690	9.3691	1.0000
Mg_4AlCO_3-SDBS	0.0046	0.0023	0.7249	0.0750	0.0749	3.2691	0.9999
Zn_2AlCO_3-SDS	0.0067	0.0034	0.9532	0.0643	0.0642	3.6233	0.9998
Zn_2AlCO_3-SDBS	0.0300	0.0019	0.8364	0.0617	0.0506	0.9918	0.9896
Zn_3AlCO_3-SDS	0.0170	0.0073	0.9504	0.1016	0.1020	1.6637	0.9998
Zn_3AlCO_3-SDBS	0.0066	0.0034	0.8059	0.0741	0.0741	2.1546	1.0000
Zn_4AlCO_3-SDS	0.0011	0.0033	0.7741	0.0962	0.0960	0.0029	1.0000

Mg_2AlNO_3-SDS	0.0161	0.0040	0.9683	0.1175	0.1178	1.0737	0.9999
Mg_2AlCl-SDS	0.0270	0.0034	0.9133	0.1281	0.1283	0.6308	0.9997

Table 5.3 Kinetic models parameters obtained on the adsorption of PhOH on SDS HTlcs

Sample	**Lagargren first order**			**q_e (exp) (mmol/g)**	**Pseudo second order**		
	$q_e$cal (mmol/g)	K_1 (min-1)	R^2		$q_e$cal (mmol/g)	K_2 (gmmol-1min-1)	R^2
Mg_2AlCO_3-SDS	0.0194	0.0108	0.9106	0.0600	0.0610	1.7055	0.9989
Mg_3AlCO_3-SDS	0.0089	0.0307	0.8554	0.0745	0.0748	10.6791	1.0000
Mg_4AlCO_3-SDS	0.0349	0.0265	0.9534	0.1217	0.1233	2.0702	0.9998

5.4 Conclusion

In this study we prepared materials with dodecylsulfate and dodecylbenzenesulfonate anions, which render the interlayer region more hydrophobic in nature providing the potential for further intercalation/adsorption of other organic species. Dependent on the charge density on the metal hydroxide layers, the density of packing of these organic anions can be controlled with most resulting in tilted bilayers of anions being present.

Adsorption studies were carried out to investigate the properties of the organo-hydrotalcites in the uptake of phenol and 2-chlorophenol compounds from aqueous solution. For each hydrotalcite sample, the uptake was found to be pH dependent with higher pH (10 for 2-CP) and (11 for phenol) leading to greater capacity of uptake, which could be attributed in part to the deprotonation of the phenolic compounds and the potential for ionic interaction of the phenolate formed. The uptake for 2-CP was found to be higher for DBS-intercalated compounds than for DS-intercalated compounds, which may be due to the potential for π-π stacking interactions to increase the strength of binding interactions between host and guest species.

The trends in sorption capacity as the Mg^{II}:Al^{III} ratio changes are less clearcut, but the variation can be explained by the competing factors of the degree of hydrophobicity in the interlayer region with the number of organosulfate/sulfonate anions available to interact, balanced against the space potentially available between anions in the interlayer (which is greatest for the 4:1 materials due to less dense anion packing), as well as the pH. The inorganic anions initially present in the host hydrotalcites from which the organo-hydraotalcites were derived seems to have influence on the properties of these organo-hydrotalcites.

The kinetics of the adsorption process was modelled, with both first and second order processes and the data did not fit well to a first order reaction, but proved to fit extremely well to a pseudo second order adsorption process. From the results obtained in this study, these clay based materials have clearly demonstrated potential as adsorbents for phenol and 2-chlorophenol, and may be extended to other phenolic compounds. However, further fine-tuning of the anion intercalation stage, with respect to the surfactant loading in order to control the number of organosulfate/sulfonate anions available to interact with the host hydrotalcites, will lead to better control of the degree of hydrophobicity in the interlayer region, and optimisation of sorption capacities.

CHAPTER SIX

CONCLUSION AND FUTURE WORK

6.1 Conclusion

In this research, clay minerals have been selected as the starting material to derive sorbents for environmental management because of their expansive surfaces often having anions or cations depending on clay type. Hydrotalcite-like compounds of Mg^{2+}/Al^{3+} and Zn^{2+}/Al^{3+} cations in the layer at different mole ratios with different anions, carbonate, chloride and nitrate in the galleries were successfully synthesised. Two methods, the urea hydrolysis and the co-precipitation methods were used to synthesise the parent materials. The urea method yielded less dense materials of higher structural order and crystallinity than the denser materials from the co-precipitation method. However the urea hydrolysis method could only be used to prepare materials containing carbonate as the intercalated anion, and with a ratio of M^{2+}:M^{3+} of 2:1. The co-precipitation method enabled variance of the M^{2+}:M^{3+} ratio and the generation of materials containing different anions within the interlayer region - the variation of the layer cations and the interlayer anions have influence on the specific properties of these hydrotalcites as revealed by the range of techniques employed to characterise them. Generally the carbonate containing materials were more crystalline, and the decomposition temperatures were higher than for the nitrate and chloride containing materials.

Thermal treatment was applied to all HTlcs prepared to obtain intermediate mixed metal oxide structures which maintained a memory effect of the starting structure, which enable regeneration of hydrotalcite-like phases from contacting with a solution

containing different anions. In this study we prepared materials with dodecylsulfate and dodecylbenzenesulfonate anions, which render the interlayer region more hydrophobic in nature providing the potential for further intercalation/adsorption of other organic species. Dependent on the charge density on the metal hydroxide layers, the density of packing of these organic anions can be controlled with most resulting in tilted bilayers of anions being present.

Adsorption studies were carried out to investigate the properties of the organo-hydrotalcites in the uptake of phenolic compounds from aqueous solution. The uptake was found to be higher for Mg-containing compounds than for Zn-containing compounds. The materials derived from the parent nitrates and chloride phases proved better than those derived from carbonates. This is an interesting observation, as the inorganic anion is removed in the thermal treatment step, yet has an influence on the properties of the final organo-hydrotalcite.

For MgAl HTlcs, as the Mg^{2+}:Al^{3+} ratio is changed the adsorption capacity is also modified, but not necessarily as would have been predicted. Generally, the 3:1 materials show lowest uptake with the 2:1 slightly higher and the 4:1 compounds demonstrating greatest capacity. The explanation for this non-linear trend could be explained by the fact that adsorption is a balance between the degree of hydrophobicity in the interlayer region and the number of organosulfate/sulfonate anions available to interact with (both of which are greater for the 2:1 materials), balanced against the space potentially available between anions in the interlayer (which is greatest for the 4:1 materials due to less dense anion packing).

For ZnAl HTlcs, the capacity increases as the Zn^{2+}:Al^{3+} ratio increases for all values.

pH also proved a key factor in the adsorption, with higher pH (10) leading to greater capacity for 2-chlorophenol uptake, which could be attributed in part to the deprotonation of the phenolic compound and the potential for ionic interaction of the phenolate formed. Compounds containing DBS anions showed higher sorption capacities than the corresponding DS-containing compounds, which is believed to be due to the potential for π- π stacking interactions to increase the strength of binding interactions between host and guest.

The kinetics of the adsorption process was modelled, with both first and second order processes being considered. The data did not fit well to a first order reaction, but proved to fit extremely well to a pseudo second order adsorption process.

These clay based materials (organo-hydrotalcite-like compounds) have exhibited a capacity to sorb organic compounds and so can function as sorbents for environmental remediation. Therefore, they have the potential for being used in environmental applications in the treatment of water and wastewater to remove organic pollutants.

6.2 Future Work

From the results obtained to date, clearly the potential of these materials as sorbents has been demonstrated. There is however more that can be done to fine-tune the control of the anion intercalation stage, particularly with respect to the ZnAl HTlcs where the side product of zinc oxide is difficult to eliminate.

For the sorption studies, further work is required to fully understand the equilibrium, kinetics and thermodynamics of the adsorption process, and the work could also be

readily expanded to look into other organic substrates e.g. toluene derivatives, and if there is selectivity for specific substrates where present in solutions containing more than one organic species. In this respect, the presence of aromatic (benzylsulfonate) groups may be important in effecting any selectivity due to the different interactions possible.

Further studies to investigate the recoverability of the organic contaminants following sorption would also be of interest, in order to examine the re-use and recycling of the sorbents. This would be an important step before any use of these materials in real environmental applications.

REFERENCES

1. Grim, R. E., *Clay Minearology*. McGraw-Hill: New York, 1968.

2. Velde B., *Origin and Mineralogy of Clays.* Velde, B., Ed. Springer-Verlage: New York, 1995.

3. Bhattacharyya, K. G.; Gupta, S. S., *Adv. Colloid Interface Sci.* **2008,** *140*, 114.

4. Coston, J. A.; Fuller, C. C.; Davis, J. A., *Geochim. Cosmochim. Acta.* **1995,** *59*, 3535.

5. Hendershot, W.; Lavkulich, L., *Soil Sci. Soc. Am. J.* **1983,** *47*, 1252.

6. Schwertmann, U.; Taylor, R. M., *Soil Sci. Soc. Am., Madison W1* **1977**, 145.

7. Corneli, A.; Laszlo, P., *Jans. Chim. Acta* **1990**, 83.

8. Carrado, K. A., In *Handbook of Layered Materials*, Auerbache, S. M.; Carrado, K. A.; Dutta, P. K., Eds. CRC Press: New York, Vol.1.,2004.

9. Worrall, W. E., *Trans. Brit. Ceram. Soc.* **1963,** *62*, 477.

10. Velde, B.; Brusewitz, A. M., *Clays Clay Miner.* **1986,** *34*, 651.

11. Butruille, J.; Pinnavaia, T. J., In *Comprehensive Supramolecular Chemistry*, Atwood, J. L., et al, Ed. Oxford: Pergamon, 1996.

12. Vaccari, A., *Catal. Today* **1998,** *41*, 53.

13. Lvov, Y. M.; Shchukin, D. G.; Mohwald, H.; Price, R. R., *ACS Nano.* **2008,** *2*, 814.

14. Ross, C. S.; Kerr, P. F., U.S Geo. Survey Prof. Paper. **1934,** *185-G*.

15. Jepson, W. B., *Philos. Trans. R. Soc. London, A* **1984,** *311*, 411.

16. Carretero, M. I., *Appl. Clay Sci.*, **2002,** *21*, 155-163.

17. Carretero, M. I.; Gomes, C. S. F.; Tateo, F., Clays and Human Health. In *Developments in Clay Science*, Bergaya, F.; Theng, B. K. G.; Lagaly, G., Eds. Elsevier: Vol. 1, 2006.

18. Velde, B., *Introduction to Clay Minerals: Chemistry, Origin, Uses and Environmental Significance.* Chapman and Hall: London, 1992.

19. Poppe, L. J.; Paskevich, V. F.; Hathaway, J. C.; Blackwood, J. C. Individual Clay Minerals. (online), U. S. Geological Survey Open-File Report 01-041, 2001. http://pubs.usgs.gov/of/2001/of01-041/htmldocs/clays/illite.htm (accessed 25 February).

20. Moore, D. M.; Reynolds Jr, R. C., *X-ray diffraction and the Identification and Analysis of Clay Minerals*. Oxford University Press (OUP): New York, 1989.

21. Hounslow, A. W., *Water Quality Data: Analysis and Interpretation*. CRC press: USA, 1995.

22. Cavani, F.; Trifirò, F.; Vaccari, A., *Catal. Today* **1991,** *11*, 173.

23. Trifiro, F.; Vaccuri, A., *Comprehensive Supramolecular Chemistry*. Pergamon press: Oxford, 1996.

24. Reichle, W. T., *Solid State Ionics* **1986,** *22*, 135.

25. Allmann, R., *Chimia* **1970,** *24*, 99.

26. Kovanda, F.; Kovácsová, E.; Koloušek, D., *Collect. Czech. Chem. Commun.* **1999,** *64*, 1517.

27. Pavan, P. C.; Crepaldi, E. L.; Valim, J. B., *J. Colloid Interface Sci.* **2000,** *229*, 346.

28. Oswald H. R.; Asper R., In *Physics and Chemistry of Materials with Layered Structures*, R. M. A. Leith, Ed. Reidel D. Publishing Company: Dordrecht, Netherlands. Vol. 1, 1977.

29. Rives, V., *Layered Double Hydroxides: Present and Future*. Nova Publishers: New York, 2001.

30. Braterman, P. S.; Xu, Z. P.; Yarberry, F., Layered Double Hydroxides. In *Handbook of Layered Materials*, Auerbach, S.M., Carrado, K. A., Dutta P.K., Eds. Marcel Dekker: New York, USA, 2004.

31. Evans, D. G; Slades, R.C.T., Structural Aspects of Layered Double Hydroxides. In *Layered Double Hydroxides, Structure and Bonding, 119,* Springer: 2006.

32. Jirátová, K.; Čuba, P.; Kovanda, F.; Hilaire, L.; Pitchon, V., *Catal. Today* **2002,** *76*, 43.

33. Ditris, V. A.; Sokolova, T. N.; Sokolova, G. V.; Cherkashin, V. I., *Clays Clay Miner.* **2006,** *35*, 401.

34. He, J.; Wei, M.; Li, B.; Kang, Y.; Evans, D. G.; Duan, X., Preparation of Layered Double Hydroxides. In *Layered Double Hydroxides, Structure and Bonding, 119,* Springer: 2006.

35. Othman, M. R.; Helwani, Z.; Fernando, W. J. N., *Appl. Organomet.Chem.,* **2009,** *23,* 335.

36. Pérez-Ramírez, J.; Overeijnder, J.; Kapteijn, F.; Moulijn, J. A., *Appl. Catalysis B: Environ.,* **1999,** *23,* 59.

37. Serna C. J.; Rendon J. L.; Iglesias, J. E., *Clays Clay Miner.,* **1982,** *30*, 180.

38. Thiel S. P.; Chiang C. K.; Poeppelmier, K. R., *Chem. Mater.,* **1993,** *5*, 297.

39. Wen Z. Y.; Lin Z. X.; Chen, K. G., *J. Mater. Sci. Lett.,* **1996,** *15*, 105.

40. Velu, S.; Suzuki, K.; Kapoor, M.; Tomura, S.; Ohashi, F.; Osaki, T., *Chem. Mater.,* **2000,** *12*, 719.

41. Tichit, D.; Das, N.; Coq, B.; Durand, R., *Chem. Mater.*, **2002,** *14*, 1530.

42. Meyn, M.; Beneke, K.; Lagaly, G., *Inorg. Chem.*, **1990,** *29*, 5201.

43. A de Roy, C.; Forano, K.; El Malki, J.; Besse, P., Synthesis of Mesoporous Matterials. In *Expanded Clays and other Microporous Solids*. Ocelli M.L., Robson, H., Eds. Van Nostrand- Reinhold: New York, 1992.

44. Mascolo, G.; Marino, O., *Miner. Magaz.*, **1980,** *43*, 619.

45. Zhao, H. T.; Vance, G. F., *Clays Clay Miner.*, **1998,** *74*, 712.

46. Kopka, H.; Beneke, K.; Lagaly, G., *J. Colloid Interface Sci.*, **1988,** *123*, 427.

47. Miyata, S., *Clays Clay Miner.*, **1983,** *31*, 305.

48. Xu, Z. P.; Zeng, H. C., *J. Phys. Chem. B.*, **2001,** *105*, 1743.

49. Drits, V. A.; Sokolova, T. N.; Sokolova, G. V.; Cherkashin, V. I., *Clays Clay Miner.*,**1987,** *35*, 401.

50. Auerbache, S. M.; Carrado, K. A.; Dutta, P. K., *Handbook of Layered Materials*. New York, 2004.

51. Vaysse, C.; Guerlou-Demourgues, L.; Demourgues, A.; Lazartigues, F.; Fertier, D.; Delmas, C., *J. Mater. Chem.*, **2002,** *12*, 1035.

52. Thomas G.S.; Rajamathi M.; Kamath P.V.; Vishnu, P., *Clays Clay Miner.*, **2004,** *52*, 693.

53. Drits, V. A.; Bookin, A., In *Layered Double Hydroxide - Present and Future*, Nova Science publishers: New York, 2001.

54. Khan, A. I.; O'Hare, D., *J. Mater. Chem.*, **2002,** *12*, 3191.

55. Bookin, A. S.; Drits, V. A., *Clays Clay Miner.*, **1993,** *41*, 551.

56. Bookin, A.; Drits, V., *Clays Clay Miner.*, **1993,** *41*, 551.

57. Bookin, A. S.; Cherkashin, V. I.; Drits, V. A., *Clays Clay Miner.*, **1993,** *41*, 558.

58. Feitknecht, W., *Helv Chim Acta.*, **1938,** *21*, 766.

59. Ogawa, M.; Kaiho, H., *Langmuir* **2002,** *18*, 4240.

60. De Roy, A.; Forano, C.; El Malki, K.; Besse, J.-P., In *Expanded Clays and other microporous solids*, Springer: 1992.

61. Vogel, A. I.; Jeffery, G. H., *Vogel's textbook of quantitative chemical analysis*: Pearson Education Ltd, England. 1989.

62. Costantino, U.; Marmottini, F.; Nocchetti, M.; Vivani, R., *Euro. J. Inorg. Chem.*, **1998,** *10*, 1439.

63. Kustrowski, P.; Sulkowska, D.; Chimiellaz, L.; Rafalsaka-Lasocha, A.; Dudek, B.; Dziembaj, R., *Micropor. Mesopor. Mater.*, **2005,** *78*, 1.

64. Rao, M. M.; Reddy, B. R.; Jayalakshmi, M.; Jaya, V. S.; Sridhar, B., *Mater. Res. Bul.*, **2005,** *40*, 347.

65. Oh, J. M.; Hwang, S. H.; Choy, J. H., *Solid State Ionics* **2002,** *151*, 285.

66. Erickson, K. L.; Bostrom, T. E.; Frost, R. L., *Mater. Lett.*, **2005,** *59*, 226.

67. Marchi, A. J.; Apesteguia, C. R., *Appl. Clay Sci.*, **1998,** *13*, 35.

68. Rocha, J.; de Archo, M.; Rives, V.; Ulibarri, M. A., *J. Mater. Chem.*, **1999,** *9*, 2499.

69. Stanimirova, T. S.; Kirov, G.; Dinolova, E., *Mater. Sci. Lett.*, **2001,** *20*, 453.

70. Aloisi, G. G.; Costantino, U.; Elisei, F.; Latterini, L.; Natalia, C.; Nocchaetti, M., *J. Mater. Chem.* ,**2002,** *12*, 3316.

71. Vaccari, A., *Appl. Clay Sci.*, **1999,** *14*, 161.

72. Kooli, F.; Rives, V.; Ulibarri, M. A., *Inorganic Chemistry* **1995,** *34*, 5114.

73. You, Y.; Zhao, H.; Vance, G. F., *J. Mater. Chem,*. **2002,** *12*, 907.

74. Aisawa, S.; Hirahara, H.; Ishiyama, K.; Ogasawara, W.; Umetsu, Y.; Narita, E., *J. Solid State Chem.*, **2003,** *174*, 342.

75. Oriakhi, C. O.; Farr, I. V.; Lerner, M. M., *Clays Clay Miner.*, **1997,** *45*, 194.

76. Carlino, S.; Hudson, M. J.; Husain, S. W.; Knowles, J. A., *Solid State Ionics* **1996,** *84*, 117.

77. Kagunya, W.; Chibwe, M.; Jones, W., *Mol. Cryst. Liq. Cryst.*, **1994,** *224*, 155.

78. Martin, M. J. S.; Villa M.V.; Sanchez-Camazano, M., *Clays Clay Miner.*, **1999,** *47*, 777.

79. Del Arco, M.; Gutierrez, S.; Martin, C.; Rives.V., *Inorg. Chem.*, **2003,** *42*, 4232.

80. Li, L., Luo, Q. S.; Duan, X., *J. Mater. Sci. Lett.*, **2002,** *21*, 439.

81. Ukrainczyk, L.; Chibwe, M.; Pinnavaia, T. J.; Boyd, S. A., *J. Phys. Chem.*, **1994,** *98*, 2668.

82. Miyata, S., *Clays Clay Miner.*, **1975,** *23*, 369.

83. Drezdzon, M. A., *Inorg. Chem.*, **1988,** *27*, 4628.

84. Newman, S. P.; Jones, W., *New J. Chem.*, **1998,** *22*, 105.

85. Veniale, F.; Barberis, E.; Carcangiu, G.; Morandi, N.; Setti, M.; Tamanini, M.; Tessier, D., *Appl. Clay Sci.*, **2004,** *25*, 135.

86. Okamoto, M.; Ray, S. S., *Prog. Polym. Sci*,. **2003,** *28*, 1539.

87. Ferrario, J. B.; Byrne, C. J.; Cleverly, D. H., *Environ. Sci. Technol.*, **2000,** *34*, 4524.

88. Sanchez-Martin, M. J.; Rodriguez-Cruz, M. S.; Andrades, M. S.; Sanchez-Camazano, M., *Appl. Clay Sci.*, **2006,** *31*, 216..

89. Constantino V.R.L.; Pinnavaia, T. J., *Catal. Lett.*, **1994,** *23*, 361.

90. Corma, A.; Formes, V.; Fey, F.; Cervilla, A.; Liopis, E.; Riberia, R., *J. Catal.*, **1995,** *152*, 237.

91. Tichit, D.; Coq, B., *Cattech* **2003,** *7*, 206.

92. Aguzzi, C.; Cerezo, P.; Viseras, C.; Caramella, C., *J. Appl. Clay Sci.*, **2007,** *36*, 22.

93. Huh, I. K.; Song, D. I.; Jeon, Y. W., *Sci. Technol.*, **2000,** *35*, 243.

94. Mastral, A. M.; Garcia, T.; Murillo R.; Callen, M. S.; Navarro, M. V.; Galban, J., *Energy Fuels* **2001,** *15*, 1.

95. Irha, N.; Teinemaa, E., *Polycyclic Aromat. Compd.*, **2002,** *22*, 663.

96. Tsai, W. T.; Lai, C. W.; Su, T. Y., J. *Hazard. Mater.*, **2006,** *134*, 169.

97. Hernández, M.; Fernández, L.; Borrás, C.; Mostany, J.; Carrero, H., *Anal. Chim. Acta* **2007,** *597*, 245.

98. Najim, I. N.; Snoeyink, V. L.; Suidan, M. T.; Lee, C. H.; Richard, Y., *J.AWWA.*, **1990,** *82*, 65.

99. Pibazari, M.; Badriyha, B. N.; Kim, S. H.; Miltner, R. J., *J.AWWA.*, **1992,** *84*, 83.

100. Robinson, T.; Chandran, B.; Nigam, P., *Bioresources Technol.*, **2002,** *85*, 119.

101. Batzia, F. A.; Sidiras, D. K., *J. Hazard. Mater.*, **2007,** *141*, 668.

102. Ghosh, D.; Bhattacharyyra, K. G., *J. Appl. Clay Sci.*, **2002,** *20*, 295.

103. Dasauziers, G. K.; Anand, S.; Das, R. P.; Muir, D. M.; Senanayake, G.; Singh, P.; Hefter, G., *Canadian Inst. Min. Metall. and Petroleum, Montreal.* **1997,** *1*, 471.

104. Zhao, H. T.; Vance, G. F., *J. Incl. Phenom. Mol. Recogn. Chem.*, **1998,** *31*, 305.

105. You, Y.; Zhao, H.; Vance, G. F.,. *Colloids and Surf. A: Physico. Engr. Aspects* **2002,** *205*, 161.

106. Dutta, P. K.; Robins, D. S., *Langmuir* **1994,** *10*, 1851.

107. Jakupca, M.; Dutta, P. K., *Chem. Mater.*, **1995,** *7*, 989.

108. Villa, M. V.; Sanchez-Martin, M. J.; Sanchez-Camazona, M., *J. Environ. Sci. Health Part B* **1999,** *34*, 509.

109. Celis, R.; Koskinen, W. C.; Hermosín, M. C.; Ulibarri, M. A.; Cornejo, J., *J. Soil Sci. Soc. Am.*, **2000,** *64*, 36.

110. You, Y. W.; Vance, G. F.; Zhao, H. T., *Appl. Clay Sci.*, **2001,** *20*, 23.

111. Kang, M. J.; Rhee, S. W.; Moon, H., *Radiochim. Acta* **1996,** *75*, 169.

112. Kang, M. J.; Chun, K. S.; Rhee, S. W.; Do, Y., *Radiochim. Acta* **1999,** *85*, 57.

113. Goswamee, R. L.; Sengupta, P.; Bhattacharyya, K. G.; Dutta, D. K., *Appl. Clay Sci.*, **1998,** *13*, 21.

114. Fetter, G.; Ramos, E.; Olguin, M. T.; Bosch, P.; Lopez, T.; Bulbulian, S., *J. Radioanal. Nucl.Chem.*, **1997,** *21*, 63.

115. Hermosin, M. C.; Pavlovic, I.; Ulibarri, M. A.; Cornejo, J., *J. Environ. Sci. Health A* **1993,** *28*, 1875.

116. Zhao, H.; Nagy, K. L., *J. Colloid Interface Sci.*, **2004,** *274*, 613.

117. Dekany, I.; Berger, F.; Imrik, K.; Lagaly, G., *Colloid and Polymer Sci.*, **1997,** *275*, 681.

118. Esumi, K.; Yamamoto, S., *Colloids Surf.s A: Physico. Engr. Aspects* **1998,** *137*, 385.

119. Bruna, F.; Pavlovic, I.; Barriga, C.; Cornejo, J.; Ulibarri, M. A., *Appl. Clay Sci.*, **2006,** *33*, 116.

120. Pecharsky, V. K.; Zavalij, P. Y., *Fundamentals of powder diffraction and structural characterization of materials*. Springer: New York, **2005**.

121. Tilpler, P. A., *Physics for Scientists and Engineers*. 4th edition ed.; W.H. Freeman and Company: New York, 1999.

122. West, A. R., *Basic Solid State Chemistry*. John Wiley & Sons: England, 2011.

123. Smart, I. L. E.; Moore, E. A., *Solid State Chemistry: An Introduction*. 3rd ed.; Taylor & Francis: Boca Raton, **2005**.

124. Kittel, C., *Introduction to Solid State Physics*. 8th edition; John Wiley & Sons: USA, 2005.

125. Bragg, W. L. In *The Diffraction of Short Electromagnetic Waves by a Crystal*, Proceedings of the Cambridge Philosophical Society, 1913; 43.

126. Whiston, C., X-ray Method. 1st edition; John Wiley & Sons: USA, **1987**.

127. Datye, A. K.; Hansen, P. L.; Kelveg, S., *Handbook of heterogeneous catalysis*. 2nd edition; Wiley: VCH, 2008.

128. Skoog, D. A.; West, D. M.; Holler, J. F.; Crouch, S. R., *Fundamental of Analytical Chemistry*. 8th edition; David Harris: USA, 2004.

129. Alemi, A.; Joo, S.; Khademinia, S.; Dolatyari, M.; Bakhtiari, A.; Moradi, H.; Saeidi, S., *Int. Nano. Let.,* **2013,** *3*, 1.

130. Yun, S. K.; Constantino, V. R. L.; Pinnavaia, T. J., *Clays Clay Miner.*, **1995,** *43*, 503.

131. Yun, S. K.; Pinnavaia, T. J.,. *Chem. Mater.*, **1995,** *7*, 348.

132. Lin, Y. H.; Lin, D.; Evans, D. G.; Duan, X., *Polym. Degrad. Stab.* **2005,** *88*, 286.

133. Xu, Z.; Fan, J.; Zheng, S.; Ma, F.; Yin, D., *J. Environ. Qual.* **2009,** *38*, 1302.

134. Comparelli, R.; Fanizza, E.; Curri, M. L.; Cozzoli, P. D.; Mascolo, G.; Agostiano, A., *Appl. Catal. B - Environ.* **2005,** *60*, 1.;

135. Seftel, E. M.; Popovici, E.; Mertens, M.; Witte, K.; Tendeloo, G.; Cool, P.; Vansant, E. F., *Micropor. Mesopor. Mater.,* **2008,** *113*, 296.

136. Evans, D.; Slade, R. T., Structural Aspects of Layered Double Hydroxides. In *Layered Double Hydroxides*, Duan, X.; Evans, D., Eds. Springer Berlin Heidelberg: Vol. 119, 2006.

137. Forano, T.; Hibino, F.; Leroux, F.; Taviot-Guého, C., Layered Double Hydroxide. In *Handbook of Clay Sience*, F. Bergaya; Theng, B. K. G.; Lagaly, G., Eds. Elsevier Ltd: 2006.

138. Brindley, G. W.; Kikkawa, S., *Am. Miner.,* **1979,** *64*, 836.

139. Thiel, S. P.; Chiang, C. K.; Poeppelmier, K. R., *Chem. Mater.,* **1993,** *5*, 297.

140. Tichit, D.; Das, N.; Coq, B.; Durand, R., *Chem. Mater.,* **2002,** *14*, 1530.

141. Frost, R. L.; Reddy, B. J., T *Spectrochimica Acta Part A: Mol. Biomol Spectros.* **2006,** *65*, 553.

142. Allmann, R., *Chimia* **1970,** *24*, 99.

143. Labajos, F. M.; Rives, V.; Ulibarri, M. A., *J. Mater. Sci.*, **1992,** *27*, 1546.

144. Cheng, X.; Huang, X.; Wang, X.; Sun, D., *J. Hazard. Mater.,* **2010,** *177*, 516.

145. Parida, K. M.; Sahoo, M.; Singha, S.,. *J. Mol. Catal. A - Chem.,* **2010,** *329*, 7.

146.(a) Kovanda, F.; Balek, V.; Dornicak, V.; Martinec, P.; Maslan, M.; Bilkova, L.; Kolousek, D.; Bountsewa, I. M., *J. Therm. Anal. Calorim.,* **2003,** *71*, 727.

(b) Kovanda, F.; Grygar, T.; Dornicak, V., *Solid State Sci.*, **2003,** *5*, 1019.

147. Hibino, T. K., K; Tsunashima, A., *Clays Clay Miner.* **1996,** *44*, 151.

148. Crepaldi, E. L.; Pavan, P. C.; Valim, J. B., *J. Brazilian Chem. Soc.* **2000,** *11*, 64.

149. Frost, R. L.; Musumeci, A. W.; Bostrom, T.; Adebajo, M. O.; Weier, M. L.; Martens, W., *Thermochim Acta* **2005,** *429*, 179.

150. Frost, R. L.; Erickson, K. L., *J. Therm. Analys. Calorim.,* **2004,** *76*, 217.

151. Pesic, L.; Salipurovic, S.; Markovic, V.; Vucelic, D.; Kagunya, W.; Jones, W., *J. Mater. Chem.,* **1992,** *2*, 1069.

152. Malherbe, F.; Besse, J. P., *J. Solid State Chem.,* **2000,** *155*, 332.

153. Faweett, T. G., Faber, J., Kabbekodo, S., McClune, F., Rafaja, D.:, "PDF-4+ Material Identification Database" *Microstructure analysis in Material Science* **2005**, *Freiburg* (1–3), June 15.

154. Velu, S.; Ramkumar, V.; Narayanan, A.; Swamy, C. S., . *J. Mater. Sci.,* **1997,** *32*, 957.

155. Guimarães, J. L.; Marangoni, R.; Ramos, L. P.; Wypych, F., *J. Colloid Interface Sci.,* **2000,** *227*, 445.

156. Padmasri, A. H.; Venugopal, A.; Durga Kumari, V.; Rama Rao, K. S.; Kanta Rao, P., *J. Molecular Catal. A: Chem.,* **2002,** *188*, 255.

157. Kloprogge, J. T.; Hickey, L.; Frost, R. L., *Appl. Clay Sci.*, **2001,** *18*, 37.

158. Frost, R. L.; Martens, W.; Ding, Z.; Kloprogge, J. T., *J. Therm. Anal Calorim.,* **2003,** *71*, 429.

159. Tichit, D.; Lhouty, M. H.; Guida, A.; Chiche, B. H.; Figueras, F.; Auroux, A.; Bartalini, D.; Garrone, E., *J. Catal.*, **1995,** *151*, 50.

160. Tichit, D. B., M. N.; Figueras, F.; Ruiz, J.R., *Langmuir* **1998,** *14*, 2086.

161. Barriga, C.; Jones, W.; Malet, P.; Rives, V.; Ulibarri, M. A., *Inorg. Chem.,* **1998,** *37*, 1812.

162. Chibwe, K.; Jones, W., *J. Chem. Soc. Chem. Commun.*, **1989,** 14, 926.

163. Chibwe, K.; Jones, W., *Chem. Mater.*, **1989,** *1*, 489.

164. Newman, S., *New J. Chem.,* **1998,** *22*, 105.

165. Carlino, S.; Hudson, M. J., *J. Mater. Chem.,* **1995,** *5*, 1433.

166. Wang, B.; Zhang, H.; Evans, D. G.; Duan, X., *Mater. Chem. Phys.*, **2005,** *92*, 190.

167. Trujillano, R.; Holgado, M. J.; González, J. L.; Rives, V., *Solid State Sci.*, **2005,** *7*, 931.

168. Iyi, N.; Tamura, K.; Yamada, H., *J. Colloid Interface Sci.*, **2009,** *340*, 67.

169. Ayala-Luis, K. B.; Koch, C. B.; Hansen, H. C. B., *Appl. Clay Sci.*, **2010,** *48*, 334.

170. Sato, T.; Okawaki, A., *Solid State Ionics* **1991,** *45*, 43.

171. Saber, O.; Tagaya, H., *J. Inclus. Phenom. Macrocyclic Chem.*, **2003,** *45*, 107.

172. Kameshima, Y.; Yoshizaki, H.; Nakajima, A.; Okada, K., *J. Colloid Interface Sci.*, **2006,** *298*, 624.

173. Costa, F. R.; Leuteritz, A.; Wagenknecht, U.; Jehnichen, D.; Häußler, L.; Heinrich, G., *Appl. Clay Sci.*, **2008,** *38*, 153.

174. Clearfield, A.; Kieke, M.; Kwan, J.; Colon, J.; Wang, R.-C., *J. Inclusion Phenom. Mol. Recognit. Chem.*, **1991,** *11*, 361.

175. Costantino, U.; Nocchetti, M.; Sisani, M.; Vivani, R., *Zeit. Krist.*, **2009,** *224*, 273.

178. Bouraada, M.; Lafjah, M.; Ouali, M. S.; de Menorval, L. C., *J. Hazard. Mater.*, **2008,** *153*, 911.

179. Zhang, P.; Qian, G.; Cheng, H.; Yang, J.; Shi, H.; Frost, R. L., . *Spectrochimica Acta Part A: Molec. Biomol. Spectros.*, **2011,** *79*, 548.

180. Smyth, J. R.; Bish, D. L., *Crystal structures and cation sites of the rock-forming minerals*. Allen & Unwin Boston: 1988.

181. Anbarasan, R.; Lee, W.; Im, S., *Bull. Mater. Sci.*, **2005,** *28*, 145.

182. Lagaly, G.; Beneke, K., *Colloid and Polymer Sci.*, **1991,** *269*, 1198.

183. You, Y. W.; Zhao, H. T.; Vance, G. F., *Colloids Surf. A-Physicochem. Engr. Aspects* **2002,** *205*, 161.

184. Liang, L. V.; Wang, Y.; Wei, M.; Cheng, J., *J. Hazard. Mater.*, **2008,** *152*, 1130.

185. Guo, Y.; Zhang, H.; Zhao, L.; Li, G. D.; Chen, J. S.; Xu, L., *J. Solid State Chem.*, **2005,** *178*, 1830.

186. Xu, Z. P.; Braterman, P. S., *J. Phys. Chem. C* **2007,** *111*, 4021.

187. Chuang, Y. H.; Tzou, Y. M.; Wang, M. K.; Liu, C. H.; Chiang, P. N., *Industr. Engr. Chem. Research* **2008,** *47*, 3813.

188. Herrero, M.; Labajos, F. M.; Rives, V., *Appl. Clay Sci.*, **2009,** *42*, 510.

189. Copeland, C. Toxic Pollutants and the Clean Water Act: Current Issues. http://digital.library.unt.edu/ark:/67531/metacrs89/ : 1993, (accessed February 6).

190. U.S.; Environmental protection Agency, Water Science and Technology, Priority Pollutants. . Appendix A to 40 CFR Part 4231: Washington D.C, 1992.

191. Dutta, N. N.; Patil, G. S.; Brothakur, S., *Separation Sci. Technol.*, **1992**, *27*, 1435.

192. Dutta, N. N.; Brothakur, S.; Baruah, R., *A Water Environ. Research* **1998**, *70*, 4.

Appendix

Oral Presentation

University of Illinois: 50th Anniversary Annual Meeting of the Clay Mineral Society, USA. .